Title
First-Principles Computational Approaches to Advancing Green Chemistry and Technology

Author
Rossomme, Elliot Conner

Publication Date
2022

Peer reviewed|Thesis/dissertation

First-Principles Computational Approaches to Advancing Green Chemistry and Technology

by

Elliot Conner Rossomme

A dissertation submitted in partial satisfaction of the

requirements for the degree of

Doctor of Philosophy

in

Chemistry

in the

Graduate Division

of the

University of California, Berkeley

Committee in charge:

Professor Martin Head–Gordon, Chair
Associate Professor Eric Neuscamman
Associate Professor Lin Lin

Fall 2022

First-Principles Computational Approaches to Advancing Green Chemistry and Technology

Abstract

First-Principles Computational Approaches to Advancing Green Chemistry and Technology

by

Elliot Conner Rossomme

Doctor of Philosophy in Chemistry

University of California, Berkeley

Professor Martin Head–Gordon, Chair

The American Chemical Society defines Green Chemistry in terms of a visionary set of principles that encourage rethinking of the material and chemical economy to reduce waste, decrease hazard, and innovate towards a sustainable future. While Green Chemistry, like all chemistry, is ultimately an empirical science, computational efforts lend significant support to implementation of greener frameworks. The present work is divided into two parts, each describing work in first-principles quantum chemistry to address pressing problems in Green Chemistry. The first concerns the development of predictive models for catalysis applications, specifically the carbon dioxide reduction reaction (CO2RR). In this, we utilize high-level electronic structure theory to analyze the nature of the metal–carbon monoxide (M−CO) chemistry, the fundamental interaction in the electrocatalytic CO2RR. In this, we provide detailed description of the physical and chemical contributions toward M−CO bonding, significantly deepening understands of these bonds. We also characterize errors associated with the use of pseudopotentials for modeling relevant chemical systems, finding that these represent an often overlooked but significant inhibitor to accurate systems modeling. The second part of this work examines the mechanism of action for *p*-phenylenediamine (PPD) antidegradants, which are ubiquitous in tire manufacturing globally. While these compounds protect rubber against degradation due to surface ozone (O_3), one of their key transformation products is acutely toxic to aquatic life. Through application of modern density functional theory, we determine a detailed mechanism for the ozonation of these compounds, which was hitherto absent from the literature. This mechanism also provides key insights into the particularly high O_3 reactivity of PPDs, and could help guide future efforts to identify non-toxic alternatives for tire manufacturing.

Contents

Contents **i**

List of Figures **iii**

List of Tables **vii**

1 Electronic Structure Theory for Green Chemistry **1**
1.1 The problem of electronic structure theory . . . 3
1.2 Hartree–Fock theory: A mean-field solution to the electronic problem . . . 5
1.3 Correlated wave function approaches . . . 11
1.4 Density functional theory . . . 20
1.5 Scope of the present work . . . 26

I Insights into modeling difficulties for metal–carbon interactions and the physics and chemistry that underpin them **28**

2 Pseudopotential inconsistency errors **29**
2.1 Introduction . . . 29
2.2 Methods . . . 37
2.3 The scale of basis set incompleteness error . . . 41
2.4 The good: Barrier heights and non-bonded interactions . . . 42
2.5 The bad: Transition metal reaction energies . . . 45
2.6 The ugly: Main-group bond breaking . . . 47
2.7 Summary and conclusions . . . 48

3 Energy decomposition analysis of MCOs **51**
3.1 Computational methods . . . 56
3.2 Validation of density functional theory . . . 58
3.3 Bonding in MCO complexes . . . 63
3.4 Anomalous behavior in MCO compounds . . . 74
3.5 Conclusions . . . 85

II Progress towards salmon-safe tires: Identifying the mechanism of ozonation for rubber and 6PPD **87**

4 Ozonation of rubber and PPDs **88**
4.1 Introduction 88
4.2 Computational methods 92
4.3 Benchmarking methods for modeling O_3 chemistry 95
4.4 EDA of radical ion complexes 104
4.5 Mechanisms of natural rubber ozonation 106
4.6 Mechanisms of PPD ozonation 107
4.7 Implications for non-toxic PPD design 115

Bibliography **117**

A Additional Work **154**

List of Figures

2.1 Basis set incompleteness error (BSIE) for all-electron def2-TZVPP results is within chemical accuracy for most systems: (a) BSIE relative to interaction energy indicates small errors across system size and (b) base-ten logarithm of magnitude of BSIE shows most errors are in the 0.1–1 kcal mol^{-1} range. Chemical accuracy is achieved by points within the gray band in panel (a) and below the gray line in panel (b). (c) Root-mean-squared BSIE satisfies chemical accuracy across methods for the S22, W4-11, and TMD10 data sets, except HF for W4-11, where large errors for FOO and ClOO dominate. Omission of these species lowers HF RMSE to 1.0 kcal mol^{-1}. 40

2.2 Pseudopotential errors (kcal mol^{-1}) for the S22 dataset of intermolecular interactions versus the value of the interaction energy. The errors are defined as deviations between (left) fit-CRENBL/def2-QZVPPD and (right) SRLC/def2-QVZVPPD PP calculations relative to all-electron calculations, for each of the 6 DFAs listed. Errors for all data points are within the chemical accuracy threshold of 1 kcal mol^{-1}, and vary linearly with the size of the interaction. 43

2.3 Pseudopotential errors [kcal/mol] for (a) def2-ECP, (b) fit-CRENBL, (c) GTH-PBE, and (d) PAW-PBE for the TMC34 data set of transition metal containing energy changes. TMC34 contains 3 subsets: barrier heights (TMB; crosses), reaction energies (MOR; circles) and dimer bond strengths (TMD; diamonds). Errors generally increase from TMB to MOR to TMD. Gray bands correspond to chemical accuracy of ± 1 kcal mol^{-1}. Outliers and other aspects of the data are discussed in the text. 44

2.4 Errors (kcal/mol) in the W4-11 total atomization energies relative to all-electron def2-QZVPPD results. PP errors for each methodology are indicated by the left-hand side of each violin. Inclusion of element-specific atomic corrections significantly improves performance in all cases (right violins), indicating a large degree of systematic PP error. Violins are decorated with root-mean-squared pseudpotential errors (RMSEs). 46

3.1 Dominant orbital interactions in the Dewar–Chatt–Duncanson model of metal-carbonyl binding: (a) forward donation from the CO σ orbital into unoccupied metal orbitals of appropriate symmetry (in this case $3d_{z^2}$); (b) back donation from occupied metal d orbitals (here, $3d_{xz}$) into the unoccupied CO π^* orbital. Orbitals pictured here obtained using COVP analysis on VCO^-. 52
3.2 Comparison of experimental and computational CO frequency shifts in MCO complexes of different charge. ωB97X-V (solid circles) performs well against CCSD(T) (open squares) and experimental frequency shifts (solid line) for species of different charge. Computations performed using the def2-TZVPD basis set. The experimental value for $MnCO^+$ has been corrected for matrix effects following Ref. 341. 62
3.3 Binding energy of isolated CO relative to that at the equilibrium bond length, plotted with the absolute dipole moment of CO, both as a function of distance. Results using ωB97X-V/def2-TZVPD (solid) and CCSD(T)/def2-TZVPD (dashed) are compared. The dipole moment vector is oriented from O to C, such that a positive dipole moment corresponds to the localization of negative charge on the carbon atom. Vertical black lines indicate bond lengths where CO exhibits no permanent electric dipole. Energies, dipole moments, and bond lengths are in units of kcal/mol, debye, and angstom, respectively. 64
3.4 Frozen, polarized, and unconstrained potential energy surfaces for MCO anions considered in this study. The energetic zero is defined as the energy of infinitely separated M^- and CO fragments. Missing data for the POL surfaces of $TiCO^-$ and $NiCO^-$ are due to SCF convergence errors. 65
3.5 Potential energy surfaces for VCO^- dissociation at different values of r_{C-O}. All dissociations are rigid in the C−O bond length. The energetic zero for solid lines is defined as infinitely separated V^- and Co fragments, where the isolated fragment value for r_{C-O} is given by the colors in the legend. Dashed lines are rescaled such that the energetic zero corresponds to infinitely separated V^- and CO with $r_{C-O} = 1.126\,\text{Å}$. 67
3.6 Coupled occupied-valence pair (COVP) analysis for selected transition metal monocarbonyls. Energy stabilization due to charge transfer is separated into contributions from forward- (CO → M) and back-donation (M → CO). 69
3.7 COVP orbitals for $\pi^* \leftarrow 4p$ back-donation from M to CO for (a) $CuCO^-$ and (b) ZnCO. This is the dominant CT interaction in these systems. 76
3.8 Potential energy surfaces for the energy decomposition analysis of (a) NiCO and (b) MnCO. In both cases the most tightly bound MCO complex is formed through the interaction of an electronically excited metal atom and ground state CO. See text for discussion of the discontinuity and asymptotes in $^1\Sigma^+$ NiCO dissociation and the absence of FRZ and POL surfaces for bound MnCO. 77
3.9 Molecular orbital diagram for POL surface of ^{1}NiCO (*cf.* Figure 3.8). The orbitals on the lower and upper surfaces were obtained with $r_{M-C} = 2.7$ and 2.8 Å, respectively. 79

3.10 COVP orbitals for the most significant back-donation interactions in (a) $MnCO^+$ and (b) $FeCO^+$. Metal–carbon bond lengths influence the strength of the interaction and thereby the extent of CT effects on ΔE_{bind} (Table 3.4) and $\Delta\omega_{\text{CO}}$ (Table 3.5). 81
3.11 Most significant COVP orbitals for CrCO: (a) forward-donation and (b)-(d) back-donation. Repulsion between the CO 5σ- and Cr $4s$-electrons alters the complex geometry and orbital interactions. 84

4.1 Ozone charge transfer complexes for (a) natural rubber and (b) 6PPD have been proposed by a number of authors (see text). 91
4.2 Substrates used in modeling ozone reactivity. Primary exploration of potential energy surfaces was completed using **1** and **2**, as surrogates for **NR** and **4**. Select modeling was completed for compound **3** to better understand experimental results for ozonation kinetics. 95
4.3 Definition of conformer labeling for PPD DeMore adducts. R = H (4ADPA), Me (MePPD). 96
4.4 Definition of conformer labeling for PPD-OH DeMore adducts. R = H (4ADPA), Me (MePPD). 97
4.5 Definition of conformer labeling for PPD primary ozonides. R = H (4ADPA), Me (MePPD). 98
4.6 Definition of conformer labeling for hydroxylated PPDs. R = H (4ADPA), Me (MePPD). 98
4.7 Energy decomposition analysis for CT complexes of 2M2B (**1**, top line) and 4ADPA (**2**, bottom line) with O_3. Structural minima for biradical zwitterionic CT complexes could not be found on unconstrained surfaces, where spontaneous charge transfer (indicated by dashed lines) resulted in charge-neutral fragments and the structures shown in the inset. The zero of energy corresponds to the optimal geometry of isolated neutral fragments. 105
4.8 Mechanistic possibilities for the formation of the 2-methyl-2-butene (**1**) primary ozonide (**1c**). In addition to the symmetric addition of O_3 to **1** ($\Delta H_{\text{TS}}^{\text{T}=0\,\text{K}} = 3.5\,\text{kcal mol}^{-1}$) and the true DeMore pathway through **1b** ($\Delta H_{\text{TS}}^{\text{T}=0\,\text{K}} = 4.0\,\text{kcal mol}^{-1}$), two asymmetric additions ($\Delta E^{\ddagger} = 1.8$ and $2.1\,\text{kcal mol}^{-1}$) *without* isolable DeMore intermediates were identified. 106
4.9 Selected reaction pathways for PPDs and ozone. In general, each structure represents a collection of regioisomers. Two sequential additions of ozone to the PPD ring system can afford hydroquinone **g** (R_2 = OH), which is readily oxidized to quinone **q**. R_1 = H, Me, and 1,3-dimethylbutyl correspond to 4-ADPA (**2**), *N*-Me-PPD (**3**), and 6PPD (**4**), respectively. 108

4.10 Vibrationally corrected barrier heights for PPD ozonation pathways compared to the minimum barrier pathway for 2M2B ozonation (**1**, solid black lines). Transition structures are shown for 4-ADPA transformations. For N−H insertion reactions, solid and dashed lines correspond to insertion at terminal and central N atoms, respectively. DeMore (DM) additions of O_3 to the rings of 4-ADPA (**2**), 4-ADPA-OH (**2g**), and MePPD (**3**) are the only transformations that are kinetically competitive with **1** ozonation. DeMore TSs with secondary H-abstraction interactions show additional stabilization. 109
4.11 Vibrationally correct reaction energies ($\Delta H_{\text{rxn}}^{T=0\,\text{K}}$) for steps from 4ADPA (**2**) to 4ADPA-OH (**2g**) at the SC- and AP-ωB97X-V/def2-TZVPP levels. Following the initial ozonation step to form **2c**, both methods indicate a strongly exothermic reaction cascade. 112
4.12 Intrinsic bonding orbitals (IBOs) for (a) MePPD (**3**), showing delocalization of N lone pair stabilized by methyl hyperconjugation and (b) DeMore-like TS for **3** with a secondary interaction between the amine H and O_3. 113
4.13 Reaction pathways for ring ozonation in 4ADPA QDI (**2h**). Neither primary ozonide **2i** nor DeMore intermediate **2j** is likely to result in products conducive to quinone formation. 114

List of Tables

1.1 Performance of classes of DFAs (with dispersion corrections) on Rungs 2-4 across different types of reaction classes as obtained from Ref. 272. Reactions are separated into "easy" and "difficult" categories, following the preceding reference. Ranges are given as 25th and 75th percentiles for root-mean-squared errors (RMSEs) in kcal mol^{-1}. 25

2.1 Core size for each of five pseudopotentials included in this study across all relevant elements. Highlighted blocks correspond to successive rows of the periodict table. 38
2.2 Basis set and pseudopotential combinations used for various computations in this work. Citations for each basis set are found in text. For the TMC34 BSIE results, onlt the TMD10 subset was considered. 39
2.3 Root-mean-squared errors (RMSEs) of W4-11 total atomization energies for basis set and effective core potential combinations relative to def2-QZVPPD (def2-ECP) results across a representative set of density functionals with and without pseudopotential and HF density corrections applied [kcal/mol]. Least-squares energy corrections for each atom result in significant improvement for PP inconsistency errors. 47

3.1 Computational and experimental data for MCO complexes of specified multiplicity (M), organized into isoelectronic series. Geometric parameters and harmonic vibrational frequencies were computed using the indicated method with the def2–TZVPD basis set. Unless noted otherwise, binding energies were determined using def2–QZVPD single-point computations on these geometries and include corrections for vibrational zero-point energies. Binding energies are calculated according to Eq. 3.2, such that a negative value indicates a stable complex, unlike some other conventions. Harmonic frequency shifts are reported relative to isolated CO, and experimental values were obtained from species in Ne matrices and obtained from values in Ref. 441, unless noted otherwise 60
3.2 Electronic, vibrational zero point, and binding energies for first-row transition metal monocarbonyls. Geometries and vibrational frequencies were determined using the def2-TZVPD basis set, and complex single-point energies using bases indicated in the table. Energies in kcal/mol. 61

3.3 Geometric parameters for selected transition metal monocarbonyls of multiplicity M on different adiabatic EDA surfaces. Values obtained using the ωB97X-V density functional with the def2–TZVPD basis set; this theory predicts the bond length of isolated CO to be 1.126 Å. Missing entries indicate a lack of a bound structure on a given surface. 66
3.4 Adiabatic energy decomposition analysis of binding energies (kcal mol^{-1}) for metal monocarbonyls of a specified spin multiplicity (M). FRZ, POL, and CT values are incremental, as defined in Section 3.1.2 of the text, and computations were performed using the ωB97X-V density functional with the def2–TZVPD basis set. Positive binding energies indicate that a complex is metastable with respect to ground state fragments, and missing entries a lack of a bound structure at a given level of theory 70
3.5 Adiabatic energy decomposition analysis of harmonic vibrational frequencies (cm^{-1}) for metal monocarbonyls of a specified spin multiplicity (M). FRZ, POL, and CT values are incremental, as defined in Section 3.1.2 of the text, and computations were performed using the ωB97X-V density functional with the def2–TZVPD basis set. Missing entries a lack of a bound structure at a given level of theory . 71
3.6 Binding energies and frequency shifts for MCO complexes that form from bond prepared metal atoms, computed at the ωB97X-V/def2-TZVPD level of theory. Electronic binding energies (D_e) with respect to both ground ($\Delta E_{\text{bind}}^{\text{grd}}$) and bond-prepared ($\Delta E_{\text{bind}}^{\text{bp}}$) fragments are reported. Experimental CO vibrational frequency shifts ($\Delta\nu_{\text{CO}}^{\text{expt}}$), reproduced from Table 3.1, allow unambiguous identification of experimental species. Energies and frequency shifts are in units of kcal/mol and cm^{-1}, respectively. 75
3.7 CCSD(T) and ωB97X-V bond angles (degree) for bent MCO complexes of multiplicity M 83

4.1 Errors in spin-contaminated (SC) and approximate projection (AP) single-point energies for benchmark ozonation reactions. Reference values are CCSDT(Q) results extrapolated to the CBS limit obtained from Ref. 405. 99
4.2 Effect of regularizer strength (κ) on performance of κ-OOMP2 for benchmark ozonation reactions. Empty columns for approximate projection (AP) results indicate an absence of spin polarization for all relevant species and the given method. CCSDT(Q)/CBS results obtained from Ref. 405 101
4.3 Errors in spin-contaminated (SC) and approximate projection (AP) single-point energies for benchmark van der Waals (vdW) complexation energies. For κ-OOMP2 ($\kappa = 1.45$) results, no spin polarization was observed for O_3 or any vdW complex, so "SC" does not apply and AP corrections are identically zero. Reference values are CCSDT(Q) results extrapolated to the CBS limit obtained from Ref. 405. Highlighted boxes represent the best performing methodology for a given parameter at a given basis set truncation. 103

4.4 Vibrationally corrected barrier heights and reaction energies for PPD ozonation on both SC- and AP-ωB97X-V/def2-TZVPP surfaces. SC energies are more accurate for ΔE_{TS}, while AP energies are more accurate for ΔE_{rxn} (Section 4.3). Results for the lowest energy 2M2B (**1**) ozonation pathway are included for reference. All values are at 0 K. [Units: kcal mol^{-1}] 111

Acknowledgments

It is obvious to start with those whose minds have most directly shaped the content of these pages, though my gratitude is no less sincere for this obviousness. To Martin, for your support and challenge, good humor and guidance over the past five years: thank you. Your mentorship has doubtless shaped the way I think about the problems of the world, but more than anything else I will remember your kindness. It is no small thing. To Eric, thank you for your feedback in shaping the final form of this monograph; it was tremendously helpful. Teaching with you remains one of my favorite experiences in graduate school, and I am grateful to have twice had the opportunity.

Others from Berkeley deserve mention for the ways that they contributed directly to the work that follows (though shortcomings are my own). Beyond those named above, Alex Bell, Kaixuan Chen, Leo dos Anjos Cunha, Billy Hart–Cooper, Teresa Head–Gordon, Wanlu Li, Christianna Lininger, Alexandra McIsaac, Colleen McMahan, and Bill Orts each provided direct support for at least one of the chapters herein. To the Berkeley Center for Green Chemistry, those I have met through it, including Megan Arnett and Meg Schwarzman, I am grateful for the ways you blew wind in the flagging sails of my graduate career some eighteen months ago. Likewise, though touched only briefly, Rachel Clune, Orion Cohen, Avishek Das, and Dipti Jasrasaria were my coconspirators in developing the Berkeley Math Bootcamp, which is one of my two favorite projects in graduate school. Thank you for your excellence, and for making something so challenging seem fun.

It may seem like the pages that follow represent the past five years of my life, but they are but a fraction of how I have spent my time. I am unable to say whether such honesty may be undue or exactly appropriate, but I cannot imagine having stuck around Berkeley long enough to complete this degree if not for the many other ways that I have spent my time. To the Berkeley Institute and its people, thank you for providing respite from the sciences, reminding me that I'll probably always find the true interests of my mind in the humanities. To City Hope, City Church, and the Newbigin House of Studies, thank you for providing avenues for me to remember that the world is bigger than myself and my problems. Thanks, too, for joy.

I reserve my greatest thanks for closest friends and family, whose love and support, not to mention distraction, have been instrumental in all aspects of life to this point. To Cynthia and Randy, as well as Cosette and Cassie, who have never given me too hard a time for moving across the country and have been willing to pick right back up whenever I find my way home again. To Brandon and Maria, who have seen me quite literally through this entire program. To Justin, whose easy nature and resilience makes me better, and who has helped me find joy in life. To Dipti, my confidant through all of it and the only person to be mentioned twice. To Riley, who saw me through the darkest moments of these past five years and Brough laughter. To Kim and Terry, who provided home for me thousands of miles from my family. To David, for the ease you have brought in even the most stressful moments.

In no order at all, to Trisha, Paul, Susan, Lucia, Mandy, Sarah, Jon, Ryan, Jacey, Jackson, Isaiah, Jason, Katherine, Olivia, Hannah, Madison, Alvin, Joey, Caroline, Rachel, Alison, Anne, Josh, Scott, Crystal, Sam, Alex, and Gary: your friendship has been and remains a gift.

The words that fill this book and the person that wrote them would not be what they are today without the support of these many others, both those I have remembered and those I have overlooked. The list above, like all things in life, is incomplete. More than anything else, thanks to all of you for regular reminders that what we accomplish is really only a small part of who we are.

Cheers to life and all it attends.

ECR
San Francisco, California

Chapter 1

Introduction: Modeling for green chemistry through modern electronic structure theory

The American Chemical Society (ACS) defines Green Chemistry very simply as "a different way of thinking about how chemistry and chemical engineering can be done."[373] Following Anastas and Warner,[5] they expand on this definition by enumerating 12 Principles that guide this "new way" to approaching the chemical sciences. These Principles codify an expansive vision of what it means for chemistry to become Green, and they are worth repeating here:

1. Prevention
2. Atom Economy
3. Less Hazardess Chemical Synthesis
4. Designing Safer Chemicals
5. Safer Solvents and Auxiliaries
6. Design for Energy Efficiency
7. Use of Renewable Feedstocks
8. Reduce Derivatives
9. Catalysis
10. Design for Degradation
11. Real-Time Analysis for Pollution Prevention
12. Inherently Safer Chemistry for Accident Prevention

For each of these twelve, the ACS provides an expanded definition, as well as metrics for determining just how green a current practices or protocols is.[372] Though sprawling, these principles are intimately connected, and advancing one goal of Green Chemistry usually serves others as well.[5]

Furthermore, it is clear from the Principles that advancing Green Chemistry requires engagement across the fields of chemistry, including synthesis, materials, engineering, and toxicology. Still, the role of computation in Green Chemistry has gone underappreciated, receiving little to no explicit attention in the published ACS discussion on the topic.[373]

This is not to say that computational chemists have not contributed to the advance of Green Chemistry. Indeed, applications of computational quantum chemistry to solve problems in Green Chemistry were recently reviewed,[378] and they include rational design of catalysts (Principle 9),[388, 418] development of greener solvents (Principle 5),[232, 433] and studies on CO_2 reduction as a renewable source of polymers (Principle 7).[93, 332, 94] Examples are plentiful, and many exciting projects in Green Chemistry are supported by work in computation. Even as this body of work grows, significant challenges remain in developing computational chemistry into a tool to address the most pressing problems of sustainability. While examples are plentiful (see cited literature), we illustrate the factors at play through consideration of one particular case that lives large in the popular imagination.

Perhaps the most famous problem in Green Chemistry, there are many ongoing efforts to address the problems of climate change, which are largely caused by industrial emission of greenhouse gases. While reduction of carbon dioxide (CO_2) emissions is one approach to address this, development of technologies that remove currently present CO_2 from the atmosphere will likely prove essential for meeting emissions reduction targets and mitigating the effects of climate change.[328, 204, 131] While sequestration is one possible fate of harvested CO_2, alternative frameworks that utilize CO_2 are more attractive both from an economic standpoint and from the Green Chemistry principle of advancing renewable feedstocks in the material economy.[372] Among proposed options,[57, 421, 108] electrocatalytic reduction of CO_2 to form small organic molecules is of particular interest.[412, 284, 334] First, the CO_2 reduction reaction (CO2RR) has been experimentally demonstrated in the presence of a variety of metal catalysts.[171, 226, 192, 331, 195] Second, under the right conditions, major products of the CO2RR include ethene (C_2H_4) and ethanol (C_2H_5OH),[99, 172, 142] which are essential feedstocks for the chemical industry.[57, 194, 412] These compounds are currently sourced from refining petroleum,[75, 295, 275] the continued extraction and use of which is a major driver of climate change. Furthermore, as the transition away from fossil fuels as energy sources proceeds, the existing processes for large-scale production of C_2H_4 and C_2H_5OH may become less competitive. Thus, if successful, industrial scaling of the CO2RR would address climate change on two important fronts: (1) removal of CO_2 form a warming atmosphere and (2) diminishing our dependence on fossil fuels for running the chemical economy.

Despite proof-of-concept studies referenced above, there are significant challenges to large-scale implementation of the CO2RR, and this chemistry has not been optimized to a sufficient degree to be economically viable.[208] The complexity of these systems makes this optimization a formidable challenge for experimental work, making this process (and electrocatalysis generally) an attractive target for computationalists.[370, 142, 208] Nevertheless, accurate modeling of systems of this complexity requires significant advances in current modeling capabilities. In broad strokes, these include development and application of highly accurate electronic structure theories (ESTs) for modeling the reactive chemistry[185, 315, 262, 263]; inclusion of molecular solvent and molecular electrolyte[74, 142, 190]; accounting for the non-equilibrium dynamics that pertain in the biased system[40, 250, 415]; and modeling of critical proton and electron transfer steps.[142, 415, 434] While each type of modeling

plays an important role, here we focus on high-performing EST methods for modeling chemical reactions like those implicated in catalysis.

In order to achieve meaningful predictions, an EST model needs to be able to accurately model a number of different types of interactions with comparable fidelity. Once again, the CO2RR indicates the broader challenges nicely. Here, one must be able to successfully treat the reactive substrates of interest (CO_2, CO, C_2H_4, *etc.* in this case), the catalyst, solvent and electrolyte molecules, and the mutual interactions of each of these components. While exact and quasi-exact methods exist for each of these, these are prohibitively expensive for many systems of interest, and various approximation schemes must be employed. As we will see in what follows, approximations that are well-suited for some of these species and interactions may be wholly inadequate for others. Still, work in recent years has begun to bridge this gap, and a convergence between accuracy and tractability is increasingly achieved. Nevertheless, this balancing act can be quite delicate, and an understanding of the factors at play is necessary to appreciate the challenges of modeling complex systems. Thus, in this introduction, we describe the central challenges of electronic structure theory and provide an overview of many common approaches to overcoming them. This discussion sets the stage for the work that follows, which variously employs each of these methods to address problems related to green chemistry.

1.1 The problem of electronic structure theory

As quantum mechanical systems, molecules and their constituent parts are governed by the Schrödinger equation, *viz.*

$$\hat{H}\Psi(\mathbf{x},t) = i\hbar\frac{\partial}{\partial t}\Psi(\mathbf{x},t), \tag{1.1}$$

where $\hbar = h/2\pi$ is the reduced Planck constant, the Hamiltonian $\hat{H}$ defines the energetic components under consideration, and Ψ is the wave function that depends on coordinates $\mathbf{x}$ for all particles in the system and time t. Because electrons are quantum mechanical objects that possess spin, the coordinates $\mathbf{x}$ may be decomposed into Kronecker products of spin and spatial components, *viz.*

$$\mathbf{x} = \mathbf{r} \otimes s. \tag{1.2}$$

It is postulated that $\Psi(\mathbf{x},t)$ contains all physical information of the quantum mechanical system. It is fruitful to consider eigenstates of the operator $\hat{H}$, which are wave functions $\Psi_\alpha(\mathbf{x},t)$ that satisfy

$$\hat{H}\Psi_\alpha(\mathbf{x},t) = E_\alpha\Psi_\alpha(\mathbf{x},t) \tag{1.3}$$

for an eigenvalue E_α. Inserting such a state into Eq. 1.1 yields

$$\hat{H}\Psi_\alpha(\mathbf{x},t) = E_\alpha\Psi_\alpha(\mathbf{x},t) = i\hbar\frac{\partial}{\partial t}\Psi_\alpha(\mathbf{x},t) \tag{1.4}$$

$$\Rightarrow \Psi_\alpha(\mathbf{x},t) = e^{-iE_\alpha t/\hbar}\Psi_\alpha(\mathbf{x},t). \tag{1.5}$$

In words, this equation states that an $\hat{H}$ eigenstate $\Psi_\alpha(\mathbf{x}, \mathbf{t})$ does not evolve in time, the phase factor $e^{-iE_\alpha t/\hbar}$ notwithstanding. As a result, states $\Psi_\alpha(\mathbf{x}, t)$ are sometimes referred to as *stationary states*, and their identification is the fundamental goal of electronic structure theory. Likewise, in this discipline it is common to replace Schrödinger equation Eq. 1.1 with Eq. 1.3, which is sometimes referred to as the time-independent Schrödinger equation.[1] Since we will be concerned with stationary states in what follows, we will drop the dependence on t from all future expressions.

Among all quantum mechanical operators, the Hamiltonian occupies a privileged role due to its place in Eq. 1.1. As a result, specification of $\hat{H}$ for a system of interest is paramount. While more complicated forms of $\hat{H}$ exist depending on the application, work in electronic structure theory generally begins with the (non-relativistic) molecular Hamiltonian

$$\hat{H} = -\sum_{A}^{N_n} \frac{1}{2M_A}\nabla_A^2 - \sum_{i}^{N_e} \frac{1}{2}\nabla_i^2 - \sum_{Ai} \frac{Q_A}{r_{iA}} + \sum_{A<B} \frac{Q_A Q_B}{r_{AB}} + \sum_{i<j} \frac{1}{r_{ij}}. \tag{1.6}$$

Here, a nucleus with mass M_A and charge Q_A is denoted by coordinates A and B, electrons by coordinates i and j, N_e and N_n are the number of electrons and nuclei in the molecule, respectively, and quantities like r_{ij} are distances $|\mathbf{r}_i - \mathbf{r}_j|$. Eq. 1.6 is given in atomic units, where the mass of an electron, the charge of an electron, the permittivity of free space, and the reduced Planck constant are identically unity.

For an N_n nucleus and N_e electron system, we must keep track of many coordinates. To simplify our notation, we therefore define vector quantities

$$\mathbf{X} = (\mathbf{X}_1, \mathbf{X}_2, \ldots, \mathbf{X}_{N_n}) \tag{1.7}$$

$$\mathbf{x} = (\mathbf{x}_1, \mathbf{x}_2, \ldots, \mathbf{x}_{N_e}) \tag{1.8}$$

that contain all of the nuclear and electronic coordinates, respectively. Using these and given the dependence on both nuclear and electronic coordinates in Eq. 1.6, the wave functions of interest will be of the form

$$\Psi = \Psi(\mathbf{X}, \mathbf{x}) \tag{1.9}$$

in the general case. In molecular quantum mechanics, however, it is common to invoke the Born–Oppenheimer approximation,[48] which assumes that the nuclear and electronic coordinates in Eq. 1.9 are separable into nuclear and electronic components, *i.e.*

$$\Psi \approx \Psi_n(\mathbf{X})\Psi_e(\mathbf{x}). \tag{1.10}$$

This separation is generally justified on the basis of a classical-type argument that nuclear masses are significantly larger than the electron mass, and therefore the adjustment of electronic states to nuclear motion is effectively instantaneous. Still, Eq. 1.10 is not applicable

[1] This distinction and its naming are unfortunate. As the presentation above shows clearly, there are not two distinct Schrödinger equations, and Eq. 1.3 instead specifies an algebraic definition of particular states $\Psi_\alpha(\mathbf{x}, t)$ that have trivial evolution in time. The Schrödinger equation 1.1 is fundamentally time-dependent.

to many systems of interest, and Ref. 152 provides a recent and accessible review of non-Born–Oppenheimer methods in quantum chemistry. Under the assumption that Eq. 1.10 is exact, we can think of an electronic wave function Ψ_e as being parameterized by the nuclear coordinates $\{X_A\}$ for $A = 1, 2, \ldots, N_n$, which is effectively saying that we treat the nuclei as classical objects.[111] For a fixed set of nuclei, we separate Eq. 1.6 into terms that depend on electronic coordinates and terms that do not, leaving

$$\hat{H} = \hat{H}_n + \hat{H}_e \tag{1.11}$$

$$\hat{H}_n = -\sum_{A}^{N_n} \frac{1}{2M_A} \nabla_A^2 + \sum_{A<B} \frac{Q_A Q_B}{r_{AB}} \tag{1.12}$$

$$\hat{H}_e = -\sum_{i}^{N_e} \frac{1}{2} \nabla_i^2 - \sum_{Ai} \frac{Q_A}{r_{iA}} + \sum_{i<j} \frac{1}{r_{ij}} \tag{1.13}$$

where $\hat{H}_n$ and $\hat{H}_e$ are the nuclear and electronic Hamiltonians. This additively separable form implies that the eigenstates of $\hat{H}$ will be multiplicatively separable (*cf.* Eq. 1.10), and that they will therefore satisfy

$$\begin{aligned} \hat{H}\Psi_\alpha &= \left(\hat{H}_e + \hat{H}_n\right) \Psi_n(\mathbf{X})\Psi_e(\mathbf{x}) \\ &= \left[E_{\alpha_e}(\mathbf{X}) + \hat{H}_n\right] \Psi_n(\mathbf{X})\Psi_e(\mathbf{x}), \end{aligned} \tag{1.14}$$

for the electronic eigenvalue E_{α_e}, which is parameterized by the nuclear coordinates $\{\mathbf{X}_A\}$. Under the Born–Oppenheimer assumptions, the electronic eigenvalue problem becomes[111]

$$\hat{H}_e \Psi_e(\mathbf{x}) = E_{\alpha_e} \Psi_e(\mathbf{x}; \mathbf{X}), \tag{1.15}$$

where $\hat{H}_e$ is given by Eq. 1.13. Use of the Born–Oppenheimer product (Eq. 1.10) through Eq. 1.14 defines the most common problem in electronic structure theory, which is the solution of Eq. 1.15 for a specified set of nuclear coordinates. In what follows, we will drop the subscripts for electronic coordinates, assuming that energies, wave functions, and operators all correspond to these unless otherwise specified. We will also drop the α annotations from energies and wave functions, reintroducing similar subscripts when distinctions between different states are needed. In this new notation, our fundamental equation becomes

$$\hat{H}\Psi(\mathbf{x}) = E\Psi(\mathbf{x}), \tag{1.16}$$

and we now turn to discuss its solution.

1.2 Hartree–Fock theory: A mean-field solution to the electronic problem

Even under the non-relativistic and Born–Oppenheimer approximations that were referenced above, solution for the stationary states of the Schrödinger equation 1.1 *via* Eq. 1.16 is non-

trivial for all but the simplest symptoms. More specifically, in any atomic or molecular system with more than one electron, the presence of the electron-electron repulsion term

$$\hat{V}_{\text{ee}} = \sum_{i<j} \frac{1}{r_{ij}} = \sum_{i<j} \frac{1}{|\mathbf{r}_i - \mathbf{r}_j|} \tag{1.17}$$

means that analytic solutions for E and Ψ cannot be obtained.[385] As a result, the use of additional approximation schemes is necessary to obtain results for virtually all systems of chemical interest.

The difficulties imposed by Eq. 1.17 stem from a general inability to analytically solve many-body problems due to the mutual interactions of three or more objects. Mean-field approaches, where the interactions between particles in the system are included in an average way, represent one path forward. For our electronic problem, this assumption implies that the many-particle wave function $\Psi(\mathbf{x}_1, \mathbf{x}_2, \ldots, \mathbf{x}_N)$ may be decomposed into a *Hartree product* of one-electron wave functions[154]

$$\Psi^{\text{HP}}(\mathbf{x}_1, \mathbf{x}_2, \ldots, \mathbf{x}_N) \approx \prod_{i}^{N} \chi_i(\mathbf{x}_i), \tag{1.18}$$

where $\chi_i(\mathbf{x}_i)$ is the normalized one-electron orbital for the ith electron in the system. These orbitals are eigenfunctions of the one-electron, mean-field Hamiltonian

$$\hat{f}_i(\mathbf{x}_1) = -\frac{1}{2}\nabla_i^2 + \sum_{A}^{N_n} \frac{Q_A}{r_{iA}} + \sum_{j \neq i} \hat{V}_j^{\text{MF}}(\mathbf{x}_1), \tag{1.19}$$

where $\hat{V}_{\mathbf{x}_2}^{\text{MF}}(\mathbf{x}_1)$ corresponds to the interaction between the ith electron and the mean-field potential generated by the jth electron, given by

$$\hat{V}_j^{\text{MF}}(\mathbf{x}_1) = \int d\mathbf{x}_2 \, \frac{\chi_j^*(\mathbf{r}_2)\chi_j(\mathbf{r}_2)}{|\mathbf{r}_1 - \mathbf{r}_2|} - \hat{K}_j, \tag{1.20}$$

for the electron in the jth orbital, where the integral on the right-hand side of this expression is the classical Coulomb repulsion due to the electron in the jth orbital and $\hat{K}_j$ is a non-classical term that will be described below. We will write the remaining terms in Eq. 1.19 as the operator

$$\hat{h}_i = -\frac{1}{2}\nabla_i^2 + \sum_{A}^{N_n} \frac{Q_A}{r_{iA}}. \tag{1.21}$$

This definition leaves a full mean-field, Hartree–Fock (HF) Hamiltonian, $\hat{H}_{\text{HF}}$, for an N-electron system is then written as a sum of these one-electron operators

$$\hat{H}_{\text{HF}} = \sum_{i}^{N} \left(\hat{h}_i + \frac{1}{2} \sum_{j \neq i}^{N} \hat{V}_j^{\text{MF}}(\mathbf{x}_i) \right), \tag{1.22}$$

where the prefactor for the second sum corrects for double counting the interaction between electrons i and j. We emphasize that the sum of one-electron operators $\hat{f}_i$ is equivalent to neither $\hat{H}_{\rm HF}$ nor the physical Hamiltonian of Eq. 1.6, due to the double-counting of electron-electron interactions and the mean-field approximation for $\hat{V}_{\rm ee}$, respectively. Nevertheless, if we choose one-electron orbitals χ_i that are eigenfunctions of the one-electron operators $\hat{f}_i$, the Hartree product wave function Eq. 1.18 will be an eigenfunction of the overall mean-field Hamiltonian (albeit with different eigenvalues).

Still, Hartree product states given by Eq. 1.18 do not satisfy the basic quantum mechanical requirement that electronic wave functions be antisymmetric with respect to electron exchange.[306] It is therefore helpful to generalize our wave functions into a normalized sum of Hartree product wave functions that satisfies this condition. In the two-electron case, this may be achieved *via.*

$$\Psi_{\rm as} = \frac{1}{\sqrt{2}} \left[\chi_1(\mathbf{x}_1)\chi_2(\mathbf{x}_2) - \chi_1(\mathbf{x}_2)\chi_2(\mathbf{x}_1) \right], \tag{1.23}$$

where it is clear that exchange of electronic coordinates changes the overall sign of $\Psi_{\rm as}$. Eq. 1.23 can also be written as the determinant

$$\Psi_{\rm as} = \frac{1}{\sqrt{2}} \begin{vmatrix} \chi_1(\mathbf{x}_1) & \chi_2(\mathbf{x}_1) \\ \chi_1(\mathbf{x}_2) & \chi_2(\mathbf{x}_2) \end{vmatrix}. \tag{1.24}$$

The form of this *Slater determinant*[371] generalizes to the N-electron case, where we have

$$|\Psi_{\rm SD}\rangle = \frac{1}{\sqrt{N!}} \begin{vmatrix} \chi_1(\mathbf{x}_1) & \chi_2(\mathbf{x}_1) & \dots & \chi_N(\mathbf{x}_1) \\ \chi_1(\mathbf{x}_2) & \chi_2(\mathbf{x}_2) & \dots & \chi_N(\mathbf{x}_2) \\ \vdots & \vdots & \ddots & \vdots \\ \chi_1(\mathbf{x}_N) & \chi_2(\mathbf{x}_N) & \dots & \chi_N(\mathbf{x}_N) \end{vmatrix}. \tag{1.25}$$

Wave functions with the form of $\Psi_{\rm SD}$ will be eigenfunctions of the mean-field Hamiltonian Eq. 1.22, that satisfy the antisymmetry requirement.

The task at hand then becomes determining the set of orbitals $\{\chi_i(\mathbf{x})\}$ that will provide the optimal mean-field description for the N-electron system. In other words, we wish to determine the form of the orbitals χ_i that may be used to minimize the expectation value of our Slater determinant with respect to Eq. 1.22,

$$\langle \Psi_{\rm SD} | \hat{H}_{\rm HF} | \Psi_{\rm SD} \rangle = E_{\rm HF}, \tag{1.26}$$

where the matrix element on the left-hand side of this equation is defined as

$$\langle \Psi_{\rm SD} | \hat{H}_{\rm HF} | \Psi_{\rm SD} \rangle = \int d\mathbf{x}_1 \, d\mathbf{x}_2 \, \dots d\mathbf{x}_N \; \Psi^*_{\rm SD}(\mathbf{x}_1, \mathbf{x}_2, \dots, \mathbf{x}_N) \hat{H}_{\rm HF} \Psi_{\rm SD}(\mathbf{x}_1, \mathbf{x}_2, \dots, \mathbf{x}_N). \tag{1.27}$$

Using the form of $\hat{H}_{\rm HF}$ from Eq. 1.22, we expand Eq. 1.27 as

$$\langle \Psi_{\rm SD} | \hat{H}_{\rm HF} | \Psi_{\rm SD} \rangle = \sum_i^N \langle \Psi_{\rm SD} | \hat{h}_i(\mathbf{x}_i) | \Psi_{\rm SD} \rangle + \frac{1}{2} \sum_i^N \sum_{j \neq i}^N \langle \Psi_{\rm SD} | \hat{V}_j^{\rm MF}(\mathbf{x}_i) | \Psi_{\rm SD} \rangle . \tag{1.28}$$

To evaluate the first term on the right-hand side of Eq. 1.28, we remember that the Slater determinant $|\Psi_{\text{SD}}\rangle$ is a sum of Hartree products. These terms will therefore only be non-zero when they couple Hartree products of the same spin-orbitals and coordinates. Since electrons are indistinguishable, there are N ways that χ_i may be coupled with $\hat{h}_i$ across this matrix element (one for each of the electron coordinates), and within these $(N-1)!$ permutations of the other spin-orbitals χ_j for $j \neq i$, resulting in a total of $N!$ such terms for each spin-orbital χ_i.[385] These cancel the pre-factor in the Slater determinant (*cf.* Eq. 1.25). Without loss of generality, we evaluate the matrix elements of $\hat{h}$ for the electron with coordinates $\mathbf{x}_1$, leaving

$$\sum_i \langle \Psi_{\text{SD}} | \hat{h}_i(\mathbf{x}_i) | \Psi_{\text{SD}} \rangle = \sum_i^N \langle \chi_i | \hat{h}(\mathbf{x}_1) | \chi_i \rangle \,. \tag{1.29}$$

Treatment of the second sum in Eq. 1.27 is more complicated, but the same general procedure applies. Here, because $\hat{V}_j^{\text{MF}}(\mathbf{x}_i)$ contains coordinates of two electrons, its matrix element corresponds to the two-electron integral

$$\langle \Psi_{\text{SD}} | \hat{V}_j^{\text{MF}}(\mathbf{x}_i) | \Psi_{\text{SD}} \rangle = \iint d\mathbf{x}_1 \, d\mathbf{x}_2 \; \Psi_{\text{SD}}^*(\mathbf{x}_1, \mathbf{x}_2, \ldots, \mathbf{x}_N) \frac{1}{|\mathbf{r}_i - \mathbf{r}_j|} \Psi_{\text{SD}}(\mathbf{x}_1, \mathbf{x}_2, \ldots, \mathbf{x}_N). \tag{1.30}$$

This term will be nonzero when both Hartree products under the integral possess spin-orbitals χ_i and χ_j that are occupied by either of the electrons with coordinates $\mathbf{x}_i$ and $\mathbf{x}_j$ and all other orbital/coordinate pairs in the product are the same. Again, we proceed by evaluating integrals with coordinates $\mathbf{x}_1$ and $\mathbf{x}_2$ and accounting for the other electrons through simple combinatorics. In the case where both Hartree products contain terms like $\chi_i(\mathbf{x}_1)\chi_j(\mathbf{x}_2)$, the contribution to the determinant will be of the form

$$J_{ij} = \iint d\mathbf{x}_1 \, d\mathbf{x}_2 \; \frac{\chi_i^*(\mathbf{x}_1)\chi_j^*(\mathbf{x}_2)\chi_i(\mathbf{x}_1)\chi_j(\mathbf{x}_2)}{|\mathbf{r}_1 - \mathbf{r}_2|} =: \langle ii|jj\rangle \,, \tag{1.31}$$

where we have introduced the common notation for chemists denoting this type of two-electron integral in the final equality. In the alternative nonzero case, where one Hartree product under the integral of Eq. 1.30 contains $\chi_i(\mathbf{x}_1)\chi_j(\mathbf{x}_2)$ and the other $\chi_i(\mathbf{x}_2)\chi_j(\mathbf{x}_1)$, while all other orbital/coordinate pairs are identical, we have

$$K_{ij} = \iint d\mathbf{x}_1 \, d\mathbf{x}_2 \; \frac{\chi_i^*(\mathbf{x}_1)\chi_j^*(\mathbf{x}_2)\chi_j(\mathbf{x}_1)\chi_i(\mathbf{x}_2)}{|\mathbf{r}_1 - \mathbf{r}_2|} = \langle ij|ji\rangle \,. \tag{1.32}$$

The integrals expressed in Eqs. 1.31 and 1.32 are known as Coulomb and exchange integrals, respectively. The former is simply the classical Coulomb repulsion between electrons in orbitals χ_i and χ_j, while the latter is a fundamentally quantum mechanical term that arises from the antisymmetry principle incorporated into our Slater determinant. In the overall matrix element Eq. 1.30, there are N ways to choose the occupation of χ_i (one for each

electron coordinate), $N-1$ ways to choose the occupation of χ_j, and $(N-2)!$ ways to fill the remaining orbitals, once again resulting in $N!$ contributions for each J_{ij} and K_{ij} pair.

Returning to the contribution from the sum of all two-electron terms in Eq. 1.28, we note that the antisymmetric form of $|\Psi_{\rm SD}\rangle$ means that the Hartree products necessary to generate exchange integrals K_{ij} will necessarily have opposite signs. Hence, we can write the energetic contribution from the interaction of the ith electron with all other electrons in the N-electron system as

$$E_i^{ee} = \sum_{j \neq i} \left(J_{ij} - K_{ij} \right). \tag{1.33}$$

It is also clear from Eqs. 1.31 and 1.32 that $J_{ii} = K_{ii}$, and this motivates the definition of the Fock operator[117, 118]

$$\begin{aligned} \hat{H}_0 &= \hat{h} + \sum_j \hat{V}_j^{\rm MF} \\ &= \hat{h} + \sum_j \left(\hat{J}_j - \hat{K}_j \right), \end{aligned} \tag{1.34}$$

where we have defined Coulomb and exchange operators $\hat{J}_j$ and $\hat{K}_j$, defined by their action on the orbital χ_i according to

$$\hat{J}_j \, \chi_i(\mathbf{x}_1) = \int d\mathbf{x}_2 \, \frac{\chi_j^*(\mathbf{x}_2)\chi_j(\mathbf{x}_2)}{|\mathbf{r}_1 - \mathbf{r}_2|} \chi_i(\mathbf{x}_1) \tag{1.35}$$

$$\hat{K}_j \, \chi_i(\mathbf{x}_1) = \int d\mathbf{x}_2 \, \frac{\chi_j^*(\mathbf{x}_2)\chi_i(\mathbf{x}_2)}{|\mathbf{r}_1 - \mathbf{r}_2|} \chi_j(\mathbf{x}_1). \tag{1.36}$$

We can see that the Coloumb operator $\hat{J}_j$ corresponds to the first term in the mean-field potential $\hat{V}_j^{\rm MF}$ (Eq. 1.20), and identify the exchange operator $\hat{K}_j$ with the second term in this expression. The Fock operator $\hat{H}_0$ (Eq. 1.34) differs from the expression for $\hat{f}_i$ in Eq. 1.19 only in that the sum in its final term includes *all* indices $j \in [1, N]$. The form of $\hat{H}_0$ has the advantage that it applies identically for each of the electrons in the N-electron system, which is not the case for the one-electron operators $\hat{f}_i$ (Eq. 1.19). Having developed expressions for each of the terms $\hat{H}_0$, we can obtain the energy E_0 as

$$E_0 = \langle \Psi_{\rm SD} | \hat{H}_0 | \Psi_{\rm SD} \rangle = \sum_i^N \langle \chi_i | \hat{h} | \chi_i \rangle + \sum_{ij}^N \Big(\langle ii|jj\rangle - \langle ij|ji\rangle \Big) \tag{1.37}$$

$$= \sum_i^N \langle \chi_i | \hat{h} | \chi_i \rangle + \sum_{ij}^N \langle ij||ij\rangle, \tag{1.38}$$

where the second expression defines notation combining the Coulomb and exchange integrals into a single expression, $\langle ij||ij\rangle$.

In practice, the spin-orbitals $\{\chi_i\}$ in Eq. 1.37 and preceding expressions are usually determined by projecting these solutions into a basis and utilizing matrix algebra to solve the resulting expressions.[385] The spatial component ψ_i of the spin-orbital χ_i is then written as the linear combination

$$|\psi_i\rangle = \sum_b^{N_b} c_{bi} |\phi_b\rangle , \tag{1.39}$$

for N_b basis functions $|\phi_b\rangle$ and expansion coefficients c_{bi}. We Insert this expansion into the eigenvalue expression for $\hat{f}$ as follows

$$\begin{aligned} \hat{f} |\psi_i\rangle &= \varepsilon_i |\psi_i\rangle \\ \sum_b^{N_b} c_{bi} \left(\hat{f} |\phi_b\rangle \right) &= \sum_b^{N_b} c_{bi} \left(\varepsilon_i |\phi_b\rangle \right) \end{aligned} \tag{1.40}$$

Projection of these equation onto the space of the basis function ϕ_a results in an equation of matrix elements

$$\sum_b^{N_b} c_{bi} \langle \phi_a | \hat{f} | \phi_b \rangle = \varepsilon_i \sum_b^{N_b} c_{bi} \langle \phi_a | \phi_b \rangle . \tag{1.41}$$

Defining $N_b \times N_b$ Fock and overlap matrices with entries F_{ab} and S_{ab} given by the matrix elements

$$F_{ab} := \langle \phi_a | \hat{f} | \phi_b \rangle = \int d\mathbf{x} \, \phi_a^*(\mathbf{x}) \hat{f} \phi_b(\mathbf{x}) \tag{1.42}$$

$$S_{ab} := \langle \phi_a | \phi_b \rangle = \int d\mathbf{x} \, \phi_a^*(\mathbf{x}) \phi_b(\mathbf{x}), \tag{1.43}$$

the HF problem can be rewritten as the matrix equation

$$\mathbf{FC} = \mathbf{SC}\boldsymbol{\varepsilon}, \tag{1.44}$$

where the coefficient matrix C contains the expansion coefficients c_{bi} defined above, and $\boldsymbol{\varepsilon}$ is a diagonal matrix of the eigenvalues ε_i. In practice, the generalized eigenvalue Eq. 1.44 is solved through an iterative, self-consistent procedure to afford the expansion coefficients c_{bi} and the one-electron eigenfunctions of the Fock operator.[153, 117, 118] Since $\mathbf{F}$ is a Hermitian matrix, this system will have N_b solutions, where N_b is the number of basis functions used in the expansion Eq. 1.39. Since N_b is always chosen to be larger than N, the number of electrons in the system, this results in more orbitals than can be occupied in a given system. The N lowest energy orbitals are used to construct a Slater determinant, which is the ground state solution of the Schrödinger equation under the mean-field approximation for the electron-electron repulsion, with energies given by Eq. 1.37.[385]

Recall, however, that the energy E_0 in Eq. 1.38 is obtained as the expectation value of $\hat{H}_0$ for this determinant, *not* that of the mean-field Hamiltonian $\hat{H}_{\text{HF}}$ (Eq. 1.22). Still, it is

straightforward to evaluate the expectation of $\hat{H}_{\mathrm{HF}}$ for our mean-field orbitals, and doing so yields the so-called Hartree–Fock energy[153, 385]

$$E_{\mathrm{HF}} = \sum_{i}^{N} \langle \chi_i | \hat{h} | \chi_i \rangle + \frac{1}{2} \sum_{ij}^{N} \langle ij || ij \rangle \,, \tag{1.45}$$

which differs from E_0 by the factor preceding contributions of electron-electron interactions. Despite the limitations of the mean-field approximation, discussed briefly in what immediately follows, this is an extremely important result in electronic structure theory.

1.2.1 Limitations of HF theory: Omission of electron correlation

In arriving at the working equations for HF theory, we have assumed that each electron experiences the presence of the other electrons in the system only in an average way. Despite this significant approximation, HF solutions are able to capture significant aspects of the interactions in molecules. HF theory can predict bond lengths within fractions of Å and ionization potentials for a number of small molecules within 10–20 $\mathrm{kcal\,mol^{-1}}$ relative to experimental values.[385] While these energy discrepancies are small relative to the total energies of these systems, they are often intolerable for predicting chemical activity, where more accuracy is needed. Indeed, so-called chemical accuracy is generally defined to require predictions with 1 $\mathrm{kcal\,mol^{-1}}$. Hence, while HF computations may be an effective starting point for the electronic problem, they are insufficient for many problems of interest.

The failures of HF theory motivate the definition of the *electron correlation energy* (E_{corr}), which is taken as the difference between the HF energy E_{HF} and the energy E of the true Hamiltonian:

$$E_{\mathrm{corr}} = E - E_{\mathrm{HF}}. \tag{1.46}$$

In absolute terms, E_{corr} is small relative to E_{HF}. Nevertheless, determination of E_{corr} is critically important to improve the predictive power of our methods. Recovering as much of E_{corr} as possible is the principle focus of modern electronic structure theory, and the remainder of this Chapter will describe these endeavors.

1.3 Correlated wave function approaches

While the Hartree–Fock (HF) method developed above proves inadequate for many chemical systems, it is an effective starting point for more exact methods. As a result, it is common to first obtain HF determinants and energies for a system and then determine or approximate E_{corr} on the basis of corrections the HF results. But these methodologies come with a catch, as higher computational costs accompany systematically improved solutions. That is to say, we cannot avoid the fundamental difficulties of the N-body problem in molecules. In practice, the goal then becomes balancing the trade-offs of accuracy and efficiency for a given system. While a great number of correlation schemes have been developed over time,

we emphasize here those that are the most relevant to understanding the key challenges of recovering electron correlation as well as the following Chapters in this work.

1.3.1 Full configuration interaction

The shortcomings of HF theory stem from its attempt to overcome the quantum many body problem by treating each of the electrons in an N-electron system as operating independently in a mean-field of each of the other electrons. This is a departure from the physical picture, where the motion of each electron is inherently correlated with that of all the others. In arriving at the HF solution for the ground state of a system, expansion coefficients for one-electron basis functions ψ_i are optimized to form molecular orbitals χ_i that are eigenfunctions of the Fock operator, and the N orbitals with the lowest energy are used to construct a Slater determinant. In reality, higher energy configurations of our HF orbitals, *i.e.* those constructed with orbitals other than the N lowest energy orbitals, contribute to the picture of the ground state.[160] These excited determinants are normally indexed relative to the ground state, $|\Psi_0\rangle$, using $i, j, \ldots$ to represent HF orbitals that are occupied in the ground state and $a, b, \ldots$ to represent those that are not. A determinant where the electron in spin-orbital χ_i is promoted to one in χ_b is then written $|\Psi_i^a\rangle$, a doubly excited determinant where $\chi_i \rightarrow \chi_a$ and $\chi_j \rightarrow \chi_b$ as $\left|\Psi_{ij}^{ab}\right\rangle$, *etc.*, all the way through determinants with N-tuple excitations. The so-called full configuration interaction (FCI) wave function for the ground state is written as a linear combination of the ground state determinant with all excited determinants, *viz.*[385]

$$|\Psi_{\mathrm{FCI}}\rangle = |\Psi_0\rangle + \sum_i \sum_a C_i^a \left|\Psi_i^a\right\rangle + \sum_{i<j} \sum_{a<b} C_{ij}^{ab} \left|\Psi_{ij}^{ab}\right\rangle + \ldots. \tag{1.47}$$

The coefficients C_i^a, C_{ij}^{ab}, *etc.* in this expression are variationally minimized to obtain the FCI energy for the ground state of the system.

Within the chosen basis set for expansion of the molecular spin-orbitals (Eq. 1.39), the FCI energy gives the best possible expression for the overall energy of the N-electron system. As the basis set is improved to approximate a complete basis for the Hilbert space of the N-electron problem, the FCI solution becomes exact for the non-relativistic Schrödinger eigenvalue problem 1.3. Nevertheless, the number of determinants in Eq. 1.47 quickly becomes quite large, and in the limit of a large closed-shell system with $2N$ electrons and a large number of orbitals N_b, the number of determinants is approximately given by[160]

$$N_{\mathrm{det}} \approx \frac{1}{2N\pi} \left(\frac{N_b}{N}\right)^{2N}. \tag{1.48}$$

This scaling means that the use of the FCI procedure is impractical for all but the smallest systems.

Truncated CI schemes, *i.e.* those where Eq. 1.47 is terminated at some point in the excitation series, are able to avoid the severe scaling of the FCI wave function while recovering

some portion of E_{corr}, and these represent one path forward. Due to Brillouin's theorem,[53] which indicates that the Hamiltonian does not connect the HF wave function to its singly excited determinants,

$$\langle \Psi_0 | \hat{H} | \Psi_i^a \rangle = 0 \quad \forall\ i, a \tag{1.49}$$

the single excitations do not make a direct contribution to the energy of $|\Psi_{\text{FCI}}\rangle$, and the doubly-excited determinants $\left|\Psi_{ij}^{ab}\right\rangle$ generally represent the most important excitations. Because of this, it is common to truncate the series in Eq. 1.47 after the double excitations, to achieve the CI with single and double excitations (CISD) method, which is tractable for many chemical systems with modern computer infrastructures. While CISD recovers a respectable portion of E_{corr}, it and other truncated CI schemes do not treat systems of different size evenly, and they are not used widely.

This problem can be illustrated using the simple case of non-interacting dihydrogen (H_2) molecules, following Ref. 385. For a single H_2, a 2-electron system, the CISD method contains all possible excited determinants, making it equivalent to FCI and exact within a chosen basis. By contrast, the CISD method is no longer exact for the case of two infinitely separated (and therefore non-interacting) H_2 molecules, where excitations involving more than two electrons are omitted. Critically, the configuration where both H_2 molecules are doubly excited is absent from the description, even though it is included by CISD for the system of a single H_2. Omission of the quadruply excited determinant from the composite system means the CISD energy for two infinitely separated H_2 molecules will not be equal to twice the CISD energy of a single H_2. This failure to achieve size-extensivity is exacerbated when treating large systems as well as chemical reactions where the number of electrons in molecular subcomponents changes significantly, and it plagues all truncated CI treatments. As a result, computational chemists usually turn to other methods that do not fail in this way.

1.3.2 Møller–Plesset perturbation theory

Generally speaking, perturbation theories take some approximate scheme, for which the exact solution is known, and derive (hopefully small) corrections to the approximate results.[86] For present purposes, these schemes take the HF energies and wave functions are taken as zeroth-order approximations to the exact solution of the Schrödinger eigensystem, and perturbation series are developed to improve upon them.[162] Theoretically speaking, each subsequent term in a series results in a more accurate solution, though we will see that this does not always hold for particular systems. Thus, in principle, these hierarchies provide a systematic way to improve upon the HF solution for a system of interest. Before discussing the particular use of perturbation theory for the HF expressions, we derive general expressions that apply to any number of formalisms.[385] In the general case, perturbation theories in electronic structure theory attempt to solve Schrödinger equation 1.3 by expanding the Hamiltonian,

wave function, and energies through the expansions

$$\hat{H} = \hat{H}_0 + \hat{H}^{(1)} + \hat{H}^{(2)} + \dots \tag{1.50}$$

$$\Psi_n = \Psi_n^{(0)} + \Psi_n^{(1)} + \Psi_n^{(2)} + \dots \tag{1.51}$$

$$E = E_n^{(0)} + E_n^{(1)} + E_n^{(2)} + \dots, \tag{1.52}$$

where the parenthetical superscripts on Ψ_n and E_n indicate the order of the term in the perturbative series. We have intentionally used different notation ($\hat{H}_0$) for the zeroth-order Hamiltonian in Eq. 1.50 to make explicit reference to Eq. 1.22. In many applications, the series in $\hat{H}$ is terminated after the first-order term, such that the exact Hamiltonian is written

$$\hat{H} = \hat{H}_0 + \hat{H}_1, \tag{1.53}$$

and we follow this convention here. Then, expanding the Schrödinger Eq. 1.3 in each of these elements gives the following result:

$$\left(\hat{H}_0 + \hat{H}_1 + \dots\right)\left(\left|\Psi_n^{(0)}\right\rangle + \left|\Psi_n^{(1)}\right\rangle + \dots\right) = \left(E_n^{(0)} + E_n^{(1)} + \dots\right)\left(\left|\Psi_n^{(0)}\right\rangle + \left|\Psi_n^{(1)}\right\rangle + \dots\right). \tag{1.54}$$

We extract the zeroth-order equation from this expression as

$$\hat{H}_0\left|\Psi_n^{(0)}\right\rangle = E_n^{(0)}\left|\Psi_n^{(0)}\right\rangle, \tag{1.55}$$

and we presume solutions are available for this "unperturbed" eigensystem. Then we have

$$\left\langle\Psi_n^{(0)}\middle|\hat{H}_0\middle|\Psi_n^{(0)}\right\rangle = E_n^{(0)}\left\langle\Psi_n^{(0)}\middle|\Psi_n^{(0)}\right\rangle = E_n^{(0)}, \tag{1.56}$$

where the final equality assumes a normalized zeroth-order wave function $\Psi_n^{(0)}$. The zeroth-order Hamiltonian $\hat{H}_0$ is chosen such that we can obtain an explicit solution for Eq. 1.55. From this, we can develop expressions for higher-order terms.

Collecting the first-order contributions to Eq. 1.54 results in

$$\hat{H}_0\left|\Psi_n^{(1)}\right\rangle + \hat{H}_1\left|\Psi_n^{(0)}\right\rangle = E_n^{(0)}\left|\Psi_n^{(1)}\right\rangle + E_n^{(1)}\left|\Psi_n^{(0)}\right\rangle. \tag{1.57}$$

The perturbation series in the final wave function Ψ_n (Eq. 1.51) makes clear that we cannot have $\langle\Psi_n|\Psi_n\rangle = \left\langle\Psi_n^{(0)}\middle|\Psi_n^{(0)}\right\rangle$ unless all higher-order contributions to $|\Psi_n\rangle$ are zero. We have already taken the zeroth-order to be normalized in arriving at Eq. 1.56, and we now choose the normalization of Ψ_n such that

$$\left\langle\Psi_n^{(0)}\middle|\Psi_n\right\rangle = \left\langle\Psi_n^{(0)}\middle|\Psi_n^{(0)}\right\rangle + \left\langle\Psi_n^{(0)}\middle|\Psi_n^{(1)}\right\rangle + \left\langle\Psi_n^{(0)}\middle|\Psi_n^{(2)}\right\rangle + \dots = 1, \tag{1.58}$$

implying (see Ref. 385)

$$\left\langle\Psi_n^{(0)}\middle|\Psi_n^{(m)}\right\rangle = \delta_{0m} \tag{1.59}$$

Hence, multiplication of Eq. 1.57 by $\left\langle \Psi_n^{(0)} \right|$ gives a simple first-order correction to the energy,

$$E_n^{(1)} = \left\langle \Psi_n^{(0)} \middle| \hat{H}_1 \middle| \Psi_n^{(0)} \right\rangle . \tag{1.60}$$

Furthermore, the zeroth-order wave functions $\{\Psi_n^{(0)}\}$ form a complete basis for the Hilbert space of interest, and we can use this to write the first-order correction $\Psi_n^{(1)}$ as

$$\left| \Psi_n^{(1)} \right\rangle = \sum_{i \neq n} c_{ni} \left| \Psi_i^{(0)} \right\rangle . \tag{1.61}$$

Inserting this expression into Eq. 1.57 gives

$$\sum_{i \neq n} c_{ni} \hat{H}_0 \left| \Psi_i^{(0)} \right\rangle + \hat{H}_1 \left| \Psi_n^{(0)} \right\rangle = \sum_{i \neq n} c_{ni} E_n^{(0)} \left| \Psi_i^{(0)} \right\rangle + E_n^{(1)} \left| \Psi_n^{(0)} \right\rangle . \tag{1.62}$$

We determine a particular coefficient $c_{nk} \equiv \left\langle \Psi_k^{(0)} \middle| \Psi_n^{(1)} \right\rangle$ for $k \neq n$ by projecting on $\left\langle \Psi_k^{(0)} \right|$ to obtain

$$\sum_{i \neq n} c_{ni} E_i^{(0)} \left\langle \Psi_k^{(0)} \middle| \Psi_n^{(0)} \right\rangle + \left\langle \Psi_k^{(0)} \middle| \hat{H}_1 \middle| \Psi_n^{(0)} \right\rangle = \sum_{i \neq n} c_{ni} E_n^{(0)} \left\langle \Psi_k^{(0)} \middle| \Psi_n^{(0)} \right\rangle + E_n^{(1)} \left\langle \Psi_k^{(0)} \middle| \Psi_n^{(0)} \right\rangle . \tag{1.63}$$

Because the zeroth-order eigenstates form an orthonormal set, this becomes

$$\begin{aligned} c_{ki} E_k^{(0)} + \left\langle \Psi_k^{(0)} \middle| \hat{H}_1 \middle| \Psi_n^{(0)} \right\rangle &= c_{ki} E_n^{(0)} \\ \implies c_{ki} &= \frac{\left\langle \Psi_k^{(0)} \middle| \hat{H}_1 \middle| \Psi_n^{(0)} \right\rangle}{E_n^{(0)} - E_k^{(0)}}, \end{aligned} \tag{1.64}$$

and the first-order correction to Ψ_n is

$$\left| \Psi_n^{(1)} \right\rangle = \sum_{i \neq n} \left| \Psi_i^{(0)} \right\rangle \frac{\left\langle \Psi_i^{(0)} \middle| \hat{H}_1 \middle| \Psi_n^{(0)} \right\rangle}{E_n^{(0)} - E_i^{(0)}}. \tag{1.65}$$

Higher-order terms for energies and wave functions are obtained following an analogous procedure, though the expressions quickly become unwieldy.[162] Still, as seen shortly, the second-order correction to the energy is of particular importance, so we develop it here. Following a similar procedure, we obtain the second-order Schrödinger equation as

$$\hat{H}_0 \left| \Psi_n^{(2)} \right\rangle + \hat{H}_1 \left| \Psi_n^{(1)} \right\rangle = E_n^{(0)} \left| \Psi_n^{(2)} \right\rangle + E_n^{(1)} \left| \Psi_n^{(1)} \right\rangle + E_n^{(2)} \left| \Psi_n^{(0)} \right\rangle . \tag{1.66}$$

Based on the orthonormality relationship in Eq. 1.59, we project along $\left|\Psi_n^{(0)}\right\rangle$ and obtain the second-order correction to the energy as

$$E_n^{(2)} = \left\langle \Psi_n^{(0)} \middle| \hat{H}_1 \middle| \Psi_n^{(1)} \right\rangle = \sum_{i \neq n} \frac{\left\langle \Psi_n^{(0)} \middle| \hat{H}_1 \middle| \Psi_i^{(0)} \right\rangle \left\langle \Psi_i^{(0)} \middle| \hat{H}_1 \middle| \Psi_n^{(0)} \right\rangle}{E_n^{(0)} - E_i^{(0)}}$$
$$= \sum_{i \neq n} \frac{\left| \left\langle \Psi_n^{(0)} \middle| \hat{H}_1 \middle| \Psi_i^{(0)} \right\rangle \right|^2}{E_n^{(0)} - E_i^{(0)}}. \tag{1.67}$$

As the final equality shows, the second-order correction to the energy depends only on the zeroth-order wave functions and energies and the perturbation to our Hamiltonian. When the zeroth-order solution is taken to be the HF Hamiltonian and eigensystem, Eq. 1.67 can be used to great effect.

Nearly a century ago, Møller and Plesset first applied the principles of perturbation theory as described above to obtain improved results relative to HF theory.[282] In this, the mean field Hamiltonian $\hat{H}_0$ (Eq. 1.22) takes the place of the zeroth-order Hamiltonian $\hat{H}_0$, whose first- (and final-) order perturbation is given by[86]

$$\hat{H}_1 = \hat{H} - \hat{H}_0 = \sum_{i \leq j} \frac{1}{r_{ij}} - \sum_{i,j} \left[\hat{J}_i(j) + \hat{K}_i(j) \right]. \tag{1.68}$$

This indicates that the first-order Møller–Plesset (MP) correction to the HF energy as obtained through Eq. 1.60 is

$$E_{\mathrm{MP}}^{(1)} = -\frac{1}{2} \sum_{ij} \langle ij||ij \rangle . \tag{1.69}$$

Comparison to Eqs. 1.38 and 1.45 above then indicates that the HF energy is correct through the first-order of the MP expansion.[282] In order to improve upon the HF results, we must consider second-order terms *via* Eq. 1.67.

We will concern ourselves with the second-order MP (MP2) energy expression for the ground state, *i.e.* $E_0^{(2)}$. In this, states Ψ_i for $i \neq n$ in Eq. 1.67 are given by excited HF states. Excited states Ψ_i^a obtained from a single $i \rightarrow a$ excitation do not contribute to this expression,[53] so we include doubly-excited determinants Ψ_{ij}^{ab} in the MP2 expression, yielding

$$E_{\mathrm{MP}}^{(2)} = \frac{1}{4} \sum_{ij} \sum_{ab} \frac{\langle ij||ab \rangle \ \langle ab||ij \rangle}{\varepsilon_i + \varepsilon_j - \varepsilon_a - \varepsilon_b}. \tag{1.70}$$

This expression includes pairwise correlation effects, and as a result generally leads to improvements in energy predictions relative to the mean field treatment of HF theory. Still, because MPPT utilizes HF solutions as a reference system, certain features of the mean-field treatment are imported into MP2 predictions. In light of this, efforts to improve MPPT

predictions through the inclusion of correlation effects into the orbitals have been relatively successful.[257, 292, 240]

Alternatively, many have considered the possibility that inclusion of higher-order corrections to achieve more accurate predictions. Third, fourth, fifth, sixth, and even higher orders of MP perturbation theory (MPPT) have been reported, and these schemes can be highly accurate, especially in systems with localized electron pairs.[88] However, in other systems, even extremely high-order MPPT results leave much to be desired, and the series does not converge even for conceptually simple, closed-shell systems like Ne and Cl^-.[244] Furthermore, the convergence of the MPPT series can exhibit strong dependence on the choice of basis set, and subtle changes like inclusion of diffuse functions can cause the series to diverge.[296] These issues stem from the nature of successive inclusion of electron correlation in the MPPT series. Specifically, each subsequent even term (MP2, MP4, *etc.*) in the series includes new correlation effects due to double, quadruple, *etc.* excitations from the HF reference determinant, while the intervening odd terms (MP3, MP5, *etc.*) couple these pairwise excitations to each other.[86] Hence the series exhibits oscillatory behavior generally, and it is not guaranteed to converge.[244]

Thus, while MP2 methods still enjoy use, especially as highly scalable implementations extend their application to increasingly large systems,[86] they are not typically used for determining molecular properties to the highest degree of accuracy. Instead, alternate formalisms that approach the fully correlated limit more smoothly and consistently have come to represent the standard in molecular quantum chemistry.

1.3.3 Coupled-cluster theory

In the course of the preceding discussion, we have noted that the HF scheme accounts for the majority of the energetic contributions for many-electron wave functions, but that its failure to capture the effects of electron correlation renders it incapable of providing accurate predictions for chemical applications. We then presented FCI as an alternative scheme that is fully exact, but exhibits prohibitively aggressive scaling. Truncated versions of FCI, like CISD, are appealing for small systems, but they quickly introduce intolerable errors for large systems due to size-extensivity errors. This failure mode is addressed by many-body perturbation theories like MP2, but the sometimes erratic behavior of later terms in the MPn series diminishes the prospects of reliably approaching the correlation limit through successively more complex treatments. Methods that address all of these challenges by preserving size-extensivity and smoothly approaching the correlation limit are therefore highly desirable. Coupled-cluster (CC) theory[329] provides one such alternative.

Before introducing the CC formalism, we introduce the notation of creation and annihilation operators

$$\hat{a}_i^\dagger \left|\right\rangle = \left|i\right\rangle \tag{1.71}$$

$$\hat{a}_i \left|i\right\rangle = \left|\right\rangle , \tag{1.72}$$

respectively, which act on reference determinants as defined in the preceding equations. This notation is nearly ubiquitous in the coupled-cluster literature, and detailed descriptions and analysis of these operators can be found elsewhere.[163] For present purposes, we can think of creation operator $\hat{a}_i^\dagger$ acting on a reference determinant to add an electron to the spin-orbital χ_i, and the annihilation operator $\hat{a}_i$ on a determinant to remove an electron from spin-orbital χ_i. Furthermore, these operators are defined in such a way that the action of $\hat{a}_i^\dagger$ on a determinant where χ_i is already occupied and $\hat{a}_i$ on a determinant where χ_i is unoccupied both return zero. We use these operators to define *excitation operators*[161]

$$\hat{\tau}_i^a = \hat{a}_a^\dagger \hat{a}_i \tag{1.73}$$

that act on a reference determinant to excite an electron from χ_i to χ_a. While the operator in Eq. 1.73 corresponds to the excitation of a single electron, we will also consider simultaneous excitations of many electrons. For a two-electron excitation, we have

$$\hat{\tau}_{ij}^{ab} = \hat{\tau}_i^a \hat{\tau}_j^b = \hat{a}_a^\dagger \hat{a}_i \hat{a}_b^\dagger \hat{a}_j, \tag{1.74}$$

and the definitions of simultaneous excitations of three, four, and more electrons generalize from here.

The concept of excitation operators can be extended to include all possible excitations for an N-electron system. In this, we define operators $\hat{T}_k$ that consist of all possible k-electron excitations for the determinant of interest. In the one- and two-electron cases, we have

$$\hat{T}_1 = \sum_{ia} t_i^a \hat{\tau}_i^a \tag{1.75}$$

$$\hat{T}_2 = \frac{1}{2} \sum_{ijab} t_{ij}^{ab} \hat{\tau}_{ij}^{ab} \tag{1.76}$$

respectively, where we have also introduced amplitudes t_I^A and t_{IJ}^{AB}, which are coefficients for each excitation that indicate the importance of each excited configuration, analogous to the CI coefficients described in Section 1.3.1 above. Using this notation, all possible excitations for the N-electron system are represented by the cluster operator

$$\hat{T} = \sum_n^N \hat{T}_n. \tag{1.77}$$

Using the operator of Eq. 1.77 directly would result in the FCI wave function as described in Section 1.3.1 above. Instead, within the CC framework, the exponential of $\hat{T}$ is used to generate excitations in the reference HF determinant,[329] and the CC determinant is given by

$$|\Psi_{\mathrm{CC}}\rangle = \exp\left(\hat{T}_N\right) |\Psi_{\mathrm{HF}}\rangle, \tag{1.78}$$

where the exponential operator is defined *via* its Taylor expansion

$$\exp\left(\hat{T}\right) = 1 + \hat{T} + \frac{1}{2}\hat{T}^2 + \frac{1}{6}\hat{T}^3 + \ldots \tag{1.79}$$

Curious at first, this approach has the benefit that all possible excitations of $|\Psi_{\mathrm{HF}}\rangle$ are included, even in truncated representations of $\hat{T}$.[329, 28] To see this, we can consider the case of coupled-cluster with single and double excitations (CCSD), where we have

$$\hat{T}_{\mathrm{CCSD}} = \hat{T}_1 + \hat{T}_2. \tag{1.80}$$

When exponentiated, this truncated operator generates all single- and double-excitations directly through the second term of Eq. 1.79. Higher-order excitations are indirectly achieved through the subsequent terms in this equation. For instance, the square of $\hat{T}_{\mathrm{CCSD}}$ results in operators of the forms $\hat{T}_1^2$, $\hat{T}_1\hat{T}_2$, and $\hat{T}_2^2$. These products generate double, triple, and quadruple excitations in $|\Psi_{\mathrm{HF}}\rangle$, and the higher powers of $\hat{T}_{\mathrm{CCSD}}$ include additional determinants, up through N-electron excitations. This feature allows truncated forms of the CC operator to exhibit the size-extensivity that was missing from the truncated CI frameworks describe above and outperform these latter methods generally.[77]

Having defined the CC excitation operators, the task becomes determining the amplitudes in Eqs. 1.75, 1.76, and their higher-order analogues, and determining the energy of the resulting state $|\Psi_{\mathrm{CC}}\rangle$. The direct approach of variational minimization used for CI wave functions (Section 1.3.1) is disadvantageous here, and will scale exponentially even for truncated CC wave functions.[161] Instead of solving the Schrödinger equation for Eq. 1.78 directly, we project the resulting expression onto the HF state $|\Psi_{\mathrm{HF}}\rangle$, giving

$$\langle\Psi_{\mathrm{HF}}|\hat{H}\exp\Big(\hat{T}\Big)|\Psi_{\mathrm{HF}}\rangle = E\,\langle\Psi_{\mathrm{HF}}|\exp\Big(\hat{T}\Big)|\Psi_{\mathrm{HF}}\rangle = E, \tag{1.81}$$

where the final equality holds because $|\Psi_{\mathrm{HF}}\rangle$ is normalized and orthogonal to all of its excited determinants. A similar equation holds for projection of the Schrödinger equation for $|\Psi_{\mathrm{CC}}\rangle$ onto each of the excited determinants at a given level of truncation. For CCSD, this means we have[329]

$$\langle\Psi_i^a|\hat{H}\exp\Big(\hat{T}_{\mathrm{CCSD}}\Big)|\Psi_{\mathrm{HF}}\rangle = E\,\langle\Psi_i^a|\exp\Big(\hat{T}_{\mathrm{CCSD}}\Big)|\Psi_{\mathrm{HF}}\rangle \tag{1.82}$$

$$\Big\langle\Psi_{ij}^{ab}\Big|\hat{H}\exp\Big(\hat{T}_{\mathrm{CCSD}}\Big)\Big|\Psi_{\mathrm{HF}}\Big\rangle = E\,\Big\langle\Psi_{ij}^{ab}\Big|\exp\Big(\hat{T}_{\mathrm{CCSD}}\Big)\Big|\Psi_{\mathrm{HF}}\Big\rangle \tag{1.83}$$

for all relevant combinations of i, j, a, and b. These two expressions generate an equation for each of the t-amplitudes in Eq. 1.80 above, and they may be determined through an iterative approach. Once obtained, the CC energy may be obtained through Eq. 1.81. While transformed versions of Eqs. 1.82 and 1.83 are often used in practice,[161] the expressions provided above are sufficient for present purposes of illustrating the underlying theory.

The expression for the CCSD equations can readily be generalized for inclusion of triple excitations (CCSDT), quadruple excitations (CCSDTQ), *etc.*, but these more complete methods quickly become intractable for all but the smallest systems.[363] While CCSD scales as $\mathcal{O}[N^6]$, the power of scaling increases by two for explicit inclusion of each additional level of excitation, resulting in $\mathcal{O}[N^8]$ and $\mathcal{O}[N^{10}]$ scaling for CCSDT and CCSDTQ, respectively.[28] These latter methods are therefore relatively uncommon in practical applications of CC theory.

Nevertheless, with the CCSD result in hand, the effect of triples can be approximately included, resulting in the CCSD(T) method,[333] which has become one of the most widely used methods in electronic structure theory.[28] This method is developed by treating the contribution of triple excitations to the overall energy as a perturbation on the CCSD energy, and can be derived with analogy to the MPn methods discussed above (Section 1.3.2), though this involves higher-order terms which were not discussed above. As such, we present the correction for perturbative inclusion of triples excitations on the energy without derivation. It is[333]

$$\Delta E_{\mathrm{T}}^{\mathrm{CCSD}} = \sum_{dt} \frac{a_d V_{dt}}{E_0 - E_t} \left(\sum_s a_s V_{st} + \sum_{d'} a_{d'} V_{d't} \right). \tag{1.84}$$

Overall, the CCSD(T) method scales as $\mathcal{O}[N^7]$, where an order $\mathcal{O}[N^6]$ iterative process must be used to obtain the CCSD wave function and energies, and then a single $\mathcal{O}[N^7]$ computation of Eq. 1.84 yields the final result. This polynomial is significantly more accessible than the exponentially scaling FCI and preserves size-extensivity, unlike truncated CI schemes.[333, 161] Where it is applicable, CCSD(T) has therefore become the "gold standard" of tools in computational quantum chemistry. Still, for many systems of interest, the scaling of CCSD(T) comes at too high a price, and low-scaling methods with reasonable accuracy are necessary.

1.4 Density functional theory

In Section 1.3, we have shown that there are many approaches to systematically achieving exact or quasi-exact results for N-electron systems, but that the most accurate of these are prohibitively expensive for all but the smallest molecules. As a result, these models cannot be applied to many systems of interest. But these correlated wave function approaches do not represent the only path forward.

At its core, the scaling problem of the wave function approaches discussed above stems from the fact that the various energy expressions depend on the N-electron wave function.[304] It has been known for some time, however, that the ground state energy of a molecular system can be written as a functional of its electron density, ρ:

$$E = E[\rho]. \tag{1.85}$$

This expression has the advantage that the electron density always depends on the three coordinates of physical space, regardless of the system size, signaling the potential to circumvent the scaling problems of the methods described earlier. This energy functional takes a form similar to that seen in HF theory above, given by[304]

$$E[\rho] = E_{\mathrm{T}}[\rho] + E_{\mathrm{ext}}[\rho] + E_{\mathrm{ee}}[\rho], \tag{1.86}$$

where $E_{\mathrm{ext}}[\rho]$ is the energy contribution due to the interaction of ρ with the external potential of the nuclei (fixed under the Born–Oppenheimer approximation), $E_{\mathrm{T}}[\rho]$ is the kinetic energy

density of ρ, and $E_{\text{ee}}[\rho]$ is the energy from electron-electron interactions. Equation 1.85 is formally exact,[169] provided the form of the density functionals $T[\rho]$ and $V_{\text{ee}}[\rho]$ are known. As we shall see below, this is not the case, particularly for components of V_{ee}, such that the primary theoretical work of density functional theory (DFT) is to determine forms of $E[\rho]$ that provide reliable predictions for properties of interest.

The earliest work by Thomas and Fermi[397, 115] used expressions for the kinetic energy of the uniform electron gas to approximate the kinetic energy functional $E_{\text{T}}[\rho]$ as

$$E_{\text{T}}^{\text{TF}}[\rho] = C_{\text{TF}} \int d\mathbf{r}\ \rho^{5/3}(\mathbf{r}), \tag{1.87}$$

where C_{TF} is a constant. By using a form for V_{ee} that neglects electron exchange and correlation, they resulted in an overall form[304]

$$E_{\text{TF}}[\rho] = C_{\text{TF}} \int d\mathbf{r}\ \rho^{5/3}(\mathbf{r}) - \int d\mathbf{r}\ \rho(\mathbf{r})\upsilon_n(\mathbf{r}) + \frac{1}{2}\iint d\mathbf{r}_1 d\mathbf{r}_2\ \frac{\rho(\mathbf{r}_1)\rho(\mathbf{r}_2)}{|\mathbf{r}_1 - \mathbf{r}_2|}. \tag{1.88}$$

While this expression provides reasonable results for extended systems, where the PIB approximation is more applicable to highly delocalized electrons, its performance in molecular contexts is miserable. Indeed, early work showed that it does not predict binding between two atoms.[393] This problem stems from the assumption that assumptions underlying the kinetic energy functional $T_{\text{TF}}[\rho]$ (Eq. 1.87) are inapplicable to molecules. In essence, the concept of molecular orbitals (developed in Section 1.2 above) proved to be necessary for accurate description of chemical systems. As a result, DFT experienced a period of protracted dormancy in molecular applications, where it was regarded as too simplistic.[304] Decades later, quantum chemists' interest in DFT was revived when Hohenberg and Kohn demonstrated what was already stated above: that there is some energy functional $E[\rho]$ that exactly reproduces the energy of an arbitrary N-electron system.[169]

1.4.1 Kohn–Sham density functional theory

Errors in the form of the kinetic energy functional $T[\rho]$ contributed to the failures of the orbital-free DFT, as described above. In light of this, the orbital framework of HF theory and its derivatives is attractive, because here the kinetic energy $\hat{T}$ can be evaluated directly. Motivated by this, Kohn and Sham introduced non-interacting orbitals,[219] which are eigenfunctions of the one-electron operator

$$\hat{H}_{\text{KS}} = -\sum_i \frac{1}{2}\nabla_i^2 + \sum_i^N \upsilon_n(\mathbf{r}_i), + \frac{\delta E_{\text{ee}}[\rho]}{\delta\rho}, \tag{1.89}$$

where the final term is the functional derivative of the energy due to electron-electron repulsion. The Kohn–Sham orbitals, ϕ^{KS}, that form the eigensystem for this (approximate)

Hamiltonian can be obtained exactly, and can be used to construct an N-electron Slater determinant (Section 1.2) Ψ^{KS}. This wave function has a well-defined kinetic energy,

$$E_{\mathrm{T}}^{\mathrm{KS}}[\rho] = -\frac{1}{2}\sum_{i}^{N}\left\langle \phi_i^{\mathrm{KS}}\middle|\nabla^2\middle|\phi_i^{\mathrm{KS}}\right\rangle, \tag{1.90}$$

Because $T_{\mathrm{KS}}[\rho]$ obtains the kinetic energy of a Slater determinant comprised of eigenfunctions for a non-interacting Hamiltonian, it does not represent the exact kinetic energy for the corresponding N-electron wave function with electron-electron interactions. Hence, as described so far, the DFT model of the N-electron system is deficient in its failure to include aspects of both electronic kinetic energy and non-classical contributions to the electron-electron repulsive potential. To correct for this, the Kohn–Sham framework defines the exchange-correlation functional E_{xc} that contains the residual elements of both $E_{\mathrm{T}}^{\mathrm{KS}}[\rho]$ and $\hat{V}_{\mathrm{ee}}$, *viz.*

$$E_{\mathrm{xc}}[\rho] = E_{\mathrm{T}}[\rho] - E_{\mathrm{T}}^{\mathrm{KS}}[\rho] + E_{\mathrm{ee}}[\rho] - E_{\mathrm{J}}[\rho]. \tag{1.91}$$

This affords the Kohn–Sham density functional,[219]

$$E_{\mathrm{KS}} = E_{\mathrm{T}}^{\mathrm{KS}}[\rho] + E_{\mathrm{J}}^{\mathrm{KS}}[\rho] + E_{\mathrm{xc}}[\rho], \tag{1.92}$$

which partitions all of the unknowns in Eq. 1.85 into the exchange-correlation functional E_{xc}. The energy in Eq. 1.92 is analogous to the HF energy obtained with HF theory in Section 1.2 above, except that it incorporates the effects of electron correlation through E_{xc}. While the exact form of E_{xc} remains unknown, this expression is formally exact.

The introduction of orbitals into DFT by Kohn and Sham therefore represents the start of an increasingly successful journey towards accurate modeling of chemical systems at accessible computational costs.[305] Within this framework, the task at hand becomes developing ever-improving implementations of E_{xc} that are able to effectively balance the need for highly accurate models with the constraints of modern computing. In the years since their initial work, approximations of E_{xc} have proliferated into the literature, and there are hundreds of options available today.[272] Many of these efforts have been extremely successful, and there now exist density functional approximations (DFAs) that can rival the accuracy of the wave function schemes discussed in Section 1.3 above at fractions of the computational cost.

1.4.2 Modern density functional approximations

Improvements upon the initial work of Kohn–Sham naturally fall into a hierarchy, where increasing complexity (and computational cost) results in higher accuracy, leading to trade-offs similar to those for correlated wave function approaches (Section 1.3). Here, however, the threshold for achieving accurate results *can* be lower, such that reasonable approximations of E_{corr} can be obtained in systems where the latter are inapplicable in practice. The hierarchy in classes of DFAs has famously (within the field of quantum chemistry, at any rate) been compared to Jacob's ladder, that extends upwards to the proverbial heaven of chemical accuracy.[311] We briefly describe the rungs of this ladder here, emphasizing the overall form of each class, rather than specific descriptions of particular functionals.

Rung 1: Local (spin) density approximations. The most basic class of DFAs, first presented in the original work of Kohn and Sham,[219] contains local (spin) density approximations (L(S)DAs). These functionals cast E_{xc} in terms of simple functions of the electron density, namely

$$E_{\text{xc}}^{\text{LDA}} = \int d\mathbf{r}\ \varepsilon_{\text{LDA}}(\rho)\rho(\mathbf{r}) \tag{1.93}$$

$$E_{\text{xc}}^{\text{LSDA}} = \int d\mathbf{r}\ \varepsilon_{\text{LSDA}}(\rho_\alpha, \rho_\beta)\rho(\mathbf{r}), \tag{1.94}$$

where ρ_α and ρ_β are the α- and β-spin densities in the system. In essence, this form assumes that these spin densities are slowly varying through space, and it is relatively accurate for extended systems.[311] In molecular contexts, however, LDAs generally perform poorly,[193] as was expected from the beginning.[219]

Rung 2: Generalized gradient approximations. Inclusion of gradients of the electron density (or spin densities) into the expression for E_{xc} represents in a natural increase in its complexity, resulting in generalized gradient approximations (GGAs). Dropping individual dependence on the spin densities (though it may be included in the general case), these functionals take the form[55]

$$E_{\text{xc}}^{\text{GGA}} = \int d\mathbf{r}\ \varepsilon_{\text{GGA}}(\rho, \nabla\rho)\rho(\mathbf{r}). \tag{1.95}$$

Given the chemical failures of Rung 1 functionals mentioned above, the development of GGAs was an important step forward for DFT, as these functional reduce errors in bond dissociation errors significantly.[311] The BLYP functional, which combines Becke exchange[34] and Lee–Yang–Parr (LYP) correlation,[238] played an important role in this, and the Perdew, Burke, and Ernzerhof (PBE) functional[310] is also significant.

Rung 3: Meta-generalized gradient approximations. Further expansion of the GGA form to include kinetic energy densities for the KS orbitals,

$$\tau(\mathbf{r}) = \frac{1}{2}\sum_i \left|\nabla\psi_i^{\text{KS}}(\mathbf{r})\right|^2 \tag{1.96}$$

results in meta-GGA density functionals,[326]

$$E_{\text{xc}}^{\text{mGGA}} = \int d\mathbf{r}\ \varepsilon_{\text{mGGA}}(\rho, \nabla\rho, \tau)\rho(\mathbf{r}). \tag{1.97}$$

These functionals are the most complex form that is still fully local in the electron density and various functions of it. Though not uniform across all specific functional pairs, meta-GGAs generally improve the prediction of energetic properties relative to GGAs.[311, 1]

Rung 4: Hybrid density functionals. Each of the preceding forms have utilized fully local approximations to include the effects of electron exchange, even though it is known (from the derivations in HF theory, for instance) that exchange is fundamentally nonlocal. In light of this, hybrid density functionals incorporate a degree of the exact exchange as computed from the KS orbitals, $E_{\mathrm{x}}^{\mathrm{exact}}$, into the overall description of E_{xc}. This gives the form[311]

$$E_{\mathrm{xc}}^{\mathrm{hybrid}} = E_{\mathrm{c}}^{\mathrm{DFA}} + \alpha E_{\mathrm{x}}^{\mathrm{exact}} + (1-\alpha)E_{\mathrm{x}}^{\mathrm{DFA}}, \tag{1.98}$$

where α tunes the amount of exact exchange to incorporate and can be parameterized for a given functional. The B3LYP[34, 238] and PBE0[312] functionals, among the most popular of all, are both hybrids.

The form of Eq. 1.98 can be further generalized to change the amount of exact exchange incorporated at different inter-electronic distances, resulting in range-separated hybrid (RSH) functionals.[52] In these schemes, the error function is used to smoothly interpolate between short-range region, where partial exact exchange is used *à la* Eq. 1.98, to the long-range region, where 100 % exact exchange is employed. Range-separated hybrids improve upon global hybrids, where partial inclusion of exact exchange leads to spurious results for long-range interactions (see 66, 52, and references therein).

Rung 5: Double-hybrid density functionals. In addition to inclusion of exact exchange, the (currently) final rung of the DFA ladder incorporates a degree of the exact correlation energy, usually through MP2 like corrections.[143] The functional form of the correlation energy in double hybrids is therefore similar to what was seen for exchange functionals in Rung 4, such that the overall exchange-correlation functional is

$$E_{\mathrm{xc}}^{\text{double hybrid}} = \alpha E_{\mathrm{x}}^{\mathrm{exact}} + (1-\alpha)E_{\mathrm{x}}^{\mathrm{DFA}} + \beta E_{\mathrm{c}}^{\mathrm{wfn}} + (1-\beta)E_{\mathrm{c}}^{\mathrm{DFA}}, \tag{1.99}$$

where here β tunes the degree of wave function correlation incorporated into E_{xc}. Though the most computationally demanding class of DFA, the best double hybrids represent the most accurate density functionals to date.

1.4.3 Choosing a functional: Tradeoffs in accuracy and cost

As with all of electronic structure theory, the choice of a density functional for a given application is ultimately a trade-off between the accuracy and computational cost of a method. For the best functionals in each class, both generally increase while ascending the DFA ladder. A number of recent to semi-recent reviews provide comprehensive analysis of the accuracy of hundreds of different DFAs,[436, 272, 274] and we provide only a broad-strokes discussion here.

In terms of scaling, the DFAs in Rungs 1–3 will scale as $\mathcal{O}[N^3]$ in the limit of a large number of electrons N, owing to the need to diagonalize a matrix in the Kohn–Sham formalism. The need to evaluate 4-center integrals in evaluating contributions from exact exchange increases the scaling of Rung 4 to $\mathcal{O}[N^4]$, and Rung 5 functionals will scale at the level of their

Table 1.1: Performance of classes of DFAs (with dispersion corrections) on Rungs 2-4 across different types of reaction classes as obtained from Ref. 272. Reactions are separated into "easy" and "difficult" categories, following the preceding reference. Ranges are given as 25th and 75th percentiles for root-mean-squared errors (RMSEs) in kcal mol^{-1}.

Interaction Type	GGA	meta-GGA	Hybrid GGA	Hybrid meta-GGA
Barrier Heights	8.3–10.0	5.9–8.7	4.0–5.4	2.5–5.0
Easy systems				
Non-covalent dimerizations	0.4–0.6	0.4–0.6	0.3–0.5	0.3–0.5
Isomerizations	0.7–0.9	0.5–0.8	0.5–0.7	0.5–0.8
Thermochemistry	6.5–9.0	4.9–6.0	3.7–4.8	3.2–5.5
Difficult systems				
Non-covalent dimerizations	2.5–3.5	2.0–3.1	1.4–2.1	1.2–1.8
Isomerizations	5.2-10.3	5.3–6.7	3.4–6.8	4.2–6.0
Thermochemistry	10.1–15.3	6.4–10.2	5.3–8.7	5.9–8.6

explicit correlation methods, $\mathcal{O}[N^5]$ for MP2. In terms of accuracy, the exact performance depends significantly on both the parameterization of a particular density functional and its end-use application. Assessment of hundreds of DFAs across many different system types is provided in Ref. 272, and the first and third quartiles of performance for Rungs 2–4 from this work are found in Table 1.1. From these results, it is clear that performance improves climbing from GGAs on Rung 2 to meta-GGAs on Rung 3, and then further to hybrids (of both GGAs and meta-GGAs) on Rung 4. Furthermore, performance is uneven, and it varies greatly between "easy" and "difficult" reactions, as defined in Ref. 272. Generally speaking, the errors in Table 1.1 indicate that chemical accuracy (errors $< 1\,\text{kcal mol}^{-1}$) can be statistically achieved for easy dimerization and isomerization energies by many functionals, and further more that this standard is nearly obtained by Rung 3 and 4 functionals for difficult reactions of similar types. There are clearly circumstances where certain DFAs are a reasonable alternative to the wave function approaches of Section 1.3

The preceding results are intended only to give broad impressions of performance, not to be exhaustive. Indeed, presentation of the indicated quartiles excludes the best (and worst) performing funcationals, meaning even more accurate results can be achieved in some cases. Where applicable, specific high performance functionals will be discussed at greater lengths in the Chapters that follow. For present purposes, we simply note that although these classes of DFAs do not consistently outperform highly correlated methods like CCSD(T) and beyond, they represent dramatic improvements over HF theory, despite the same formal expressions for their scaling. These former methods may therefore be applied to recover some degree of E_{corr} in significantly larger systems than CC theory. Nevertheless, in any application of DFAs, it is best to proceed with caution, benchmarking results to higher level methods wherever possible. In this way, there is hope that a marriage between tractability

and accuracy can be achieved, providing both qualitative and quantitative insight into many chemistries of interest.

1.5 Scope of the present work

Herein, we apply methods of electronic structure theory as outline above to problems relevant to green chemistry. These studies range from fundamental developments to characterize and improve the performance of electronic structure theory methods for relevant systems to understanding the basic chemistry and physics of select problems in sustainability. These include developments broadly related to modeling for catalysis systems (Part I) and to the development of non-toxic alternatives for commercial tire products (Part II).

In Chapter 2, evaluate the pseudopotential (PP) approximation, which seeks to reduce the cost of computations by replacing core electrons with simple potentials, for chemical applications of DFT. Despite its long history and wide use, the development of custom PPs has not tracked with the explosion of density functional approximations as briefly described in Section 1.4.2 above. As a result, use of PPs with exchange/correlation functionals for which they were not developed is widespread, though this practice is known to be theoretically unsound. In particular, inconsistent use of PPs was found to be a potentially significant but under-appreciated source of error in work benchmarking the applicability of DFT for catalysis modeling,[254, 248]. Still, the extent of these PP inconsistency errors (PPIEs) has not been systematically explored across the types of energy differences commonly evaluated in chemical applications. We evaluate PPIEs for a number of PPs and DFAs across 196 chemically relevant systems of both transition metal and main group elements as represented by the W4-11, TMC34, and S22 data sets. Near the complete basis set limit, these PPs are found to cleanly approach AE results for non-covalent interactions, but introduce root-mean-squared errors (RMSEs) upwards of $15\,\mathrm{kcal\,mol^{-1}}$ to predictions of covalent bond energies for a number of popular DFAs. We achieve significant improvements through the use of empirical atom- and DFA-specific PP corrections, indicating considerable systematicity of PPIEs. The results of this work have implications for chemical modeling in both molecular contexts as well as for DFA design, which we discuss.

We continue in Chapter 3 by reporting the adiabatic energy decomposition analysis (EDA)[174, 266, 265] of DFA results for metal carbonyls, shedding light on the physical content of binding energies and carbon monoxide (CO) frequency (υ_{CO}) shifts in select first-row transition metal monocarbonyls (MCOs; M = Ti^-, V^-, Cr^-, Co^-, Ni^-, Cu^-, V, Cr, Mn, Ni, Cu, Zn, Cr^+, Mn^+, Fe^+, Cu^+, and Zn^+). This approach allows us to directly consider the physical content of υ_{CO} across different transition metals (TMs), in contrast to previous studies of these systems. Neutral, anionic, and cationic systems are compared, and our results indicate that the relative importance of electrostatic interactions, intramolecular orbital polarization, and charge transfer can vary significantly with the charge and electron configuration of the metal participating in binding. Various anomalous systems are also discussed and incorporated into a general model of MCO binding. Electrostatic interactions

and orbital polarization are found to promote blue shifts in υ_{CO}, while charge transfer effects encourage υ_{CO} red-shifting; experimentally observed values of υ_{CO} are found to be a result of a complex but quantifiable interplay between these physical components. This work also uncovers and explains anomalies in these trends for select species, demonstrating the subtlety of these interactions. Advantages and limitations of this model as an approximation to more complicated systems, like those implicated in heterogeneous catalysis, are discussed.

Finally, we change applications in Chapter 4, where we apply modern DFAs to elucidate the mechanism of activity for 6PPD (*N*-(1,3-dimethylbutyl)-*N*-phenyl-*p*-phenylenediamine), a ubiquitous tire additive that products rubber from degradation due to atmospheric ozone (O_3). This work is motivated by the recent discovery that 6PPD quinone (6PPDQ), a derivative of 6PPD that forms *in situ*, possess acute fatal toxicity to various aquatic species.[399, 398, 166, 54] With reference to highly correlated coupled-cluster results on similar systems, we demonstrate that modern DFAs can achieve chemical accuracy for many ozonation reactions, which are notoriously difficult to model. We examine existing mechanisms of ozonation for 6PPD, finding that they are inadequate to account for the high reactivity of 6PPD with O_3. Instead, we find direct interaction between O_3 and PPD carbon atoms is kinetically accessible, and that this motif is more significant than interactions with PPD nitrogens. The former pathway results in a hydroxylated PPD intermediate, which reacts further with O_3 to afford 6PPD hydroquinone and, ultimately, 6PPDQ. This mechanism directly links the toxicity of 6PPDQ to the antiozonant function of 6PPD. Results relating to the structural features of 6PPD that promote its reactivity toward O_3 are discussed in detail, and these results have significant implications for development of safer alternatives for rubber antiozonants.

While the work in Part I was motivated by applications in catalysis like the CO2RR, it generally advances work in this area on a more fundamental front by analyzing and improving common methods in modeling complicated systems (Chapter 2) and working to elucidate the interactions of abstractions to systems relevant to heterogeneous catalysis (Chapter 3). The work on rubber antiozonants in Chapter 4, by contrast, directly applies the tools of computational quantum chemistry to a recently discovered and pressing problem in green chemistry. All-in-all, these three vignettes illustrate the many levels where computational work is needed to pursue a more sustainable future. In sequence, the contributions of this work include definition and characterization of accurate models, application of these models to understand basic aspects of relevant physics and chemistry, and, ultimately, applying well-demonstrated tools to solve problems of interest and necessity.

Following the presentation of the primary material of this dissertation, Appendix A contains a brief description of additional graduate work completed during my stint at Berkeley.

Part I

Insights into modeling difficulties for metal–carbon interactions and the physics and chemistry that underpin them

Chapter 2

Effective use of pseudopotentials: Inconsistency errors in chemical applications of density functional theory

2.1 Introduction

Since its inception nearly a century ago,[164] the pseudopotential (PP) approximation has been a widespread approach for enabling molecular and particularly condensed matter electronic structure calculations. While PPs initially gained traction for use in solid state physics,[316, 317, 318] their use in chemical applications was not long to follow.[416] In these latter applications, PPs have come to enjoy wide spread use, and they are routine for efficient inclusion of electronic relativistic effects[104] and modeling large, complex systems.[406, 211, 357, 139] PP development has paced alongside broadening applications, resulting in many options for computational chemists.[78, 6, 42, 138, 155, 357, 104]

Strictly speaking, PPs are developed for use in conjunction with particular methods of electron exchange and correlation.[17, 221, 387] For instance, a PBE PP is designed to be used in PBE computations and may not perform well in other contexts.[139, 432, 248] Nevertheless, it is common to report results obtained with mismatched methods and PPs. While these formally inconsistent protocols are relatively benign in some cases,[427, 156, 357, 349] they are not theoretically sound and can lead to significant errors.[157, 349, 123, 96, 348, 2, 432, 47, 339, 426, 248] For instance, previous work from some of us identified PP inconsistency errors as a significant obstacle to accurate modeling of catalysis systems.[248] Others have found inconsistent PP methods result in significant errors in band gap determinations for solids,[387, 432, 47] excitation and bond energies in molecules,[2, 432, 426, 248] and other physical parameters.[426]

Herein, we evaluate the performance of the PP approximation and PP transferability

errors across a variety of commonly used density functional approximations (DFAs). In this work, we consider performance for most of the major classes of PP in routine use for chemical applications, as described in Section 2.1.1. We present all of our computational procedures, including details of benchmark datasets, calculation parameters, and the use of relativistic corrections, in Section 2.2. Results across all electronic structure methods, PPs, and datasets are discussed beginning in Section 2.3, and recommendations for future practice in Section 2.7.

2.1.1 Theory and structure of pseudopotentials

At its core, the PP approximation rests on the assumption that only electrons in some defined valence space are relevant to an application of interest.[139] This can be justified by the relatively small polarizability of core electrons, meaning that their orbitals do not vary much in typical chemical processes (of course exceptions exist, such as core excitations[91]). Ignoring such exceptions, core electrons can be removed from the model, replacing the exact Hamiltonian with a simplified operator that possesses eigenvalues and eigenvectors similar to the exact system, reducing computational complexity in a number of ways.[357] First, by definition, PPs reduce the number of electrons in a system, decreasing its size. As a corollary of eliminating the core electrons, overall pseudo wave functions can be made smoother,[139, 432] and therefore smaller basis sets may be adequate,[155] which provides clear computational benefits, particularly in plane wave calculations.

Though separation of core and valence electrons is, strictly speaking, unphysical (electrons are indistinguishable), we can write a model Hamiltonian ($\hat{H}_v$) that describes the physics of this contrived system. Specifically, for N_v valence electrons (coordinates i, j), of an atom a, we have

$$\hat{H}_v = -\frac{1}{2}\sum_{i}^{N_v}\nabla_i^2 + \sum_{i<j}^{N_v}\frac{1}{r_{ij}} + \sum_{i}^{N_v}V_a^{\mathrm{PP}}(r_i), \tag{2.1}$$

where V_a^{PP} is the atomic pseudpotential.[357] This expression can easily be generalized to a molecular context through inclusion of additional cores and a classical core-core repulsion term. We will not do this here, and we will drop the a subscript in the following equations. While a number of different formalisms for V^{PP} exist, they generally contain both local (V_{loc}) and nonlocal (V_{nl}) components, such that

$$V^{\mathrm{PP}} = V_{\mathrm{loc}} + V_{\mathrm{nl}}. \tag{2.2}$$

The first term in the right-hand side of this equation, the local potential (V_{loc}), corresponds to the long-range Coulomb potential of the eliminated core electrons (and the nucleus they screen). The most straightforward approach for V_{loc} is a perfectly screened Coulomb potential,

$$V_{\mathrm{loc}}(r) = -\frac{Z_{\mathrm{ion}}}{r} \tag{2.3}$$

where Z_{ion} is obtained as the nuclear charge less the charge of the electrons eliminated by the PP. To improve numerical stability, particularly in plane wave codes, Gaussian smearing is often applied to the nuclear charge, resulting in a modified local potential

$$V_{\text{loc}}(r) = -Z_{\text{ion}}\frac{\text{erf}(r/\sigma)}{r}, \tag{2.4}$$

where σ specifies the width of the Gaussian charge distribution.[139] Other terms may be added to V_{loc} as well, depending on the formalism.[138, 155]

While V_{loc} captures important aspects of the physics of the eliminated core, it is inadequate to obtain accurate PP computations.[432] Given the nature of electron exchange, it is unsurprising the inclusion of nonlocal terms improves PP performance significantly,[357] which we represent as V_{nl}. A number of different forms for V_{nl} exist, but they generally decompose the V^{PP} in terms of angular-momentum eigenstates (the spherical harmonics, $Y_{\ell,m}$) to account for the hierarchy of ℓ-shells within the core and to incorporate ℓ-dependent exchange effects.[58] Hence, V_{nl} takes the form of a projector along angular momentum eigenstates scaled by an ℓ-dependent potential, V_ℓ, *viz.*

$$V_{\text{nl}} = \sum_{\ell}^{\ell_{\max}-1} V_\ell P_\ell = \sum_{\ell}^{\ell_{\max}-1}\sum_{m=-\ell}^{\ell} V_\ell \left|\ell m\right\rangle \left\langle \ell m\right|. \tag{2.5}$$

Here, $\ell_{\max}$ is the largest angular momentum represented in the (removed) core orbitals. All valence pseudo orbitals with $\ell \geq \ell_{\max}-1$ experience the same potential $V_{\ell_{\max}}$ that is usually of a similar form to V_ℓ for $\ell < \ell_{\max}-1$.[199] The overall potential V_{nl} can then be written[104]

$$V_{\text{nl}} = V_{\ell_{\max}} - \sum_{\ell}^{\ell_{\max}-1} \left(V_\ell - V_{\ell_{\max}}\right) P_\ell, \tag{2.6}$$

where the exact form of V_ℓ changes with the PP.

This framework can be expanded to include the relativistic effects of core electrons, where they are most important.[215, 230, 104] Because spin–orbit (SO) coupling lifts addition degeneracies in the angular momentum eigenstates, the projection operators become

$$P_{\ell j} = \sum_{m} \left|j\ell m\right\rangle \left\langle j\ell m\right|, \tag{2.7}$$

and Eq. 2.6 contains an additional sum over total angular momentum quantum number j, affording

$$V_{\text{nl}}^{\text{rel}} = V_{\ell_{\max},j_{\max}} - \sum_{\ell}^{\ell_{\max}-1}\sum_{j=|\ell-\frac{1}{2}|}^{\ell+\frac{1}{2}} \left(V_{\ell j} - V_{\ell_{\max},j_{\max}}\right) P_{\ell j}. \tag{2.8}$$

The effects of SO coupling may be treated in an average way to recover a relativistic PP without explicit dependence on the j quantum number for each ℓ-subspace,[113, 146] given by

$$V_\ell^{\text{avg}}(\mathbf{r},\mathbf{r}') = \frac{1}{2\ell+1}\left[\ell V_{\ell-1/2}(\mathbf{r},\mathbf{r}') + (\ell+1)V_{\ell+1/2}(\mathbf{r},\mathbf{r}')\right]. \tag{2.9}$$

The form for the SO term can then be derived[114] as the difference between the full relativistic PP and V_ℓ^{avg}. Properties of the projection operators and the angular momentum eigenstates can be exploited to obtain a simplified expression

$$\Delta V_\ell^{\text{SO}} = \sum_{\ell=1}^{\ell_max-1} \frac{\Delta V_\ell^{\text{rel}}}{2\ell+1} \left[\ell P_{\ell,\ell+1/2} - (\ell+1) P_{\ell,|\ell-1/2|}\right], \tag{2.10}$$

where the difference potential $\Delta V_\ell^{\text{rel}}$ corresponds to the relativistic potential between neighboring $Y_{\ell,m}$ states, *i.e.*

$$\Delta V_\ell^{\text{rel}} = V_{\ell,\ell+1/2}^{\text{rel}} - V_{\ell,|\ell-1/2|}^{\text{rel}}. \tag{2.11}$$

Alternatively, the SO difference potential may be written in a form that is explicit in the SO interaction,

$$\Delta V_\ell^{\text{SO}} = \sum_{\ell=1}^{\ell_{\max}-1} \frac{2\Delta V_\ell^{\text{rel}}}{2\ell+1} P_\ell \left(\vec{\ell}\cdot\vec{s}\right) P_\ell, \tag{2.12}$$

though this form was developed primarily for use with configuration interaction (CI) calculations that do not concern the present work.[322]

Though discussion of common PPs follows shortly, inclusion of one example here aids in understand how PPs are ultimately fit to all-electron results. Perhaps the most conceptually straightforward definition expands each semilocal potential V_ℓ in a set, $\{k\}$, of Gaussian-weighted polynomials,[356, 71, 199] yielding

$$V_\ell(r_i) = \sum_k B_{\ell k} r_i^{n_{\ell k}} e^{-\beta_{\ell k} r_i^2}, \tag{2.13}$$

where $B_{\ell k}$, $n_{\ell k}$, and $\beta_{\ell k}$ are adjustable parameters, is common.[357, 104] Such an expansion may also be applied to the relativistic case to introduce additional parameters $C_{\ell jk}$, $n_{\ell jk}$, and $\gamma_{\ell jk}$ in a similar expansion[357]

$$V_\ell(r_i) = \sum_k C_{\ell jk} r_i^{n_{\ell jk}} e^{-\gamma_{\ell jk} r_i^2}. \tag{2.14}$$

Where applicable, parameterization of the various coefficients in Equations 2.13 and 2.14 (and other expressions for different formalisms) results in PPs that are explicitly fit to results of a particular exchange/correlation method.

2.1.1.1 Desirable properties of pseudopotentials

The ideal PP will reproduce desirable physical properties with high fidelity while lowering the computational cost relative to an all-electron procedure. In order to achieve this, many have advocated for PPs that satisfy a variety of (sometimes competing) theoretical criteria.[150, 216, 367, 395, 137]

Norm conservation. First, many PPs are designed to be norm-conserving.[150] This amounts to requiring charge densities for real and pseudo wave functions agree outside some core radius r_c. Norm-conservation is formally achieved by satisfying the following equations:[150, 432]

$$\tilde{\psi}_i^{(x)}(r) = \psi_i^{(x)}(r) \quad x = 0, 1, 2;\ r \geq r_c \tag{2.15}$$

$$\varepsilon_{\mathrm{PP}} = \varepsilon_{\mathrm{AE}} \tag{2.16}$$

$$\left\langle \tilde{\psi}_i \middle| \tilde{\psi}_i \right\rangle = \langle \psi_i | \psi_i \rangle = 1 \tag{2.17}$$

$$\frac{\partial}{\partial \varepsilon} \left(\frac{d \ln \tilde{\psi}_i}{dr} \right) \bigg|_{\mathrm{R}} = \frac{\partial}{\partial \varepsilon} \left(\frac{d \ln \psi_i}{dr} \right) \bigg|_{\mathrm{R}} \quad R \geq r_c, \tag{2.18}$$

where ψ_i is an all-electron orbital, $\tilde{\psi}_i$ a pseudoorbital, (x) superscripts refer to xth derivatives with respect to r, and ε the valence energy eigenvalues. These criteria have been found to result in better-conditioned PPs that perform evenly across chemical environments for DFT computations.[150, 17] Strict adherence to norm-conservation for HF PPs results in nondecaying tails, and localization schemes are necessary to obtain accurate and well-defined results.[401, 402]

Shape consistency. Early work expanded the pseudoorbital $\tilde{\psi}_i$ as a linear combination of (AE) valence orbital ψ_{v_i} and core orbitals ψ_{c_j}, *viz.*

$$\tilde{\psi}_i = C_{v_i} \psi_{v_i} + \sum_j^{N_c} C_{c_j} \psi_{c_j}, \tag{2.19}$$

where C_{v_i} and C_{c_j} are expansion coefficients for virtual and core orbitals.[317, 198] This formalism spuriously stores valence electron density in the core region,[78] resulting in bond lengths that are too short and potential wells that are too deep.[198] Christiansen, *et al.* proposed a new definition

$$\tilde{\psi}_i = \psi_{v_i} + f_i, \tag{2.20}$$

where f_i is zero for $r \geq r_c$ and is chosen to cancel oscillations in ψ_i for $r < r_c$.[78] This alternate definition corrected the aforementioned core/valence problems and improved PP performance significantly (*vide infra*). Subsequent shape-consistent PPs were developed to improve computational efficiency.[379]

Energy consistency. Instead of fitting to orbital properties, some have opted to parameterize PPs to achieve agreement with energetic properties directly,[103] generally emphasizing that this approach focuses exclusively on observables.[225] Despite not being optimized for this outcome, energy consistent PPs are guaranteed to satisfy Eq. 2.18 and thereby achieve some degree of shape consistency.[400, 104] Energy consistent PPs are usually fit to a number of atomic reference states, and this generally results in strong performance across distinct bonding environments.[104]

2.1.1.2 Common classes of pseudopotentials

Overviews for each of the types of PP used in this study are provided in the following paragraphs, emphasizing PP structure, development, and performance. Various review articles provided more detailed treatments for the interested reader.[318, 104]

CRENB pseudopotentials. The Christiansen–Ross–Ermler–Nash–Bursten (CRENB) pseudopotentials were the first shape-consistent Hartree–Fock pseudopotentials, designed to ensure radial wave functions of main group pseudoorbitals closely mirrored all-electron orbitals in the valence space.[78] The form of these potentials is determined by inverting the radial Schrödinger equation and fitting the core region of the pseudoorbital as a polynomial expansion, with the requirement that the magnitude and first three derivatives of the expansion smoothly transition to the exact valence orbital outside the core. This procedure brought significant improvements for PP predictions of geometric properties and dissociation energies for F_2, Cl_2, and LiCl dimers, where earlier PPs resulted in relative errors of up to 70 %.[198, 158] These PPs were subsequently extended to include relativistic effects and all elements of the periodic table through Rn, including both large and small core variants (CRENBL and CRENBS, respectively).[300, 182, 231, 346] Recent work to restructure the radial form of these potentials has resulted in significant improvements in computational cost without affecting numerical accuracy.[278]

Stuttgart pseudopotentials. In contrast, energy consistent Stuttgart relativistic PPs are designed only to reproduce observable quantities like atomic excitation and ionization energies.[225, 37] Motivation for this approach came from earlier work showing superb agreement between PP and AE results for dissociation energies for a variety of atoms, ions, and dimers.[124, 125, 103, 184, 102, 6, 7] Furthermore, relaxation of the space consistency constraint accommodates a simpler PP with form, *viz.*

$$V_i^{\mathrm{PP}} = -\frac{Z_{\mathrm{ion}}}{r_i} + \sum_{\ell=0}^{\ell_{\max}} \sum_{k} A_{\ell k} \exp\left(-\alpha_{\ell k} r_i^2\right) P_\ell, \tag{2.21}$$

where P_ℓ is a projector onto the subspace with angular momentum ℓ, and $A_{\ell k}$ and $\alpha_{\ell k}$ are parameters that are adjusted to minimize the least-squares error between PP results and all-electron, relativistic HF computations.[103] Generally speaking, fewer Gaussian functions are necessary in SRXC potentials (*i.e.* k is small), resulting in more efficient implementations.[37, 278] Here too, both small core and large core (SRSC and SRLC) formulations exist for many elements. Furthermore, agreement between AE and SRXC radial wave functions in the valence region can be quite good, despite the fact that these PPs are not optimized for this outcome.[225]

Karlsruhe pseudopotentials. The popular Karlsruhe basis sets[420, 417] were developed for use with previously published small-core Stuttgart PPs.[6, 203, 245, 279, 313] Following

the convention of the basis set labeling, this PP set is referred to as def2-ECP. Unlike most PP schemes, core electrons are only removed for the fourth and fifth row elements (Rb-Rd); all-electron computations are used for all other elements. It is interesting to note that basis set convergence for the Karlsruhe series is more rapid for DFT than wave function methods, even though these were parameterized with reference to all-electron HF computations.[313, 417]

Dual-space separable pseudopotentials. In plane wave contexts, it is advantageous to develop PPs with optimal behavior in both real and reciprocal space. This provided the impetus for Goedecker–Teter–Hutter (GTH) PPs.[138] The GTH local potential is obtained by smearing the screened nuclear charge (Eq. 2.4) and adding this to a Gaussian-weighted polynomial, and the non-local potential is given by

$$V_{\mathrm{nl}}(\mathbf{r}) = \sum_{\ell,m,i,j} Y_{\ell,m}(\hat{\mathbf{r}}) p_{\ell,i}(r) h_{i,j} p_{\ell,j}(r') Y_{\ell,m}(\hat{\mathbf{r}}'), \tag{2.22}$$

where $Y_{\ell,m}$ are the spherical harmonics, $p_{\ell,i}$ the Gaussian radial projector for angular momentum ℓ, and $h_{i,j}$ the expansion coefficients for the projectors. Though somewhat obscured by the formalism, these potentials and their Fourier transforms both consist of Gaussian-weighted polynomials, which is advantageous for computational and physical reasons.[138] The parameters in GTH PPs are least-squares optimized to maximize agreement with all-electron charge density and select (occupied and virtual) orbital energy eigenvalues, and this was completed separately for LDA and BLYP functionals in the original publication. Inclusion of relativistic effects results in Hartwigsen–Goedecker–Hutter (HGH) potentials, which have been optimized with the LDA functional for all elements through Rn.[155] Additional parameterizations have been reported for BLYP,[221] BP,[221] PBE[221, 259, 258], B97M-rV,[248] and ωB97X-V[248] density functionals.

Projector augmented waves. The projector augmented wave (PAW) approach[42] is conceptually similar to the PPs discussed above, in that it creates a partition between core/valence electrons. Here, the pseudo total wave function $\tilde{\psi}$ is related to the AE wave function ψ through a linear transformation, such that

$$|\psi\rangle = \left|\tilde{\psi}\right\rangle + \sum_i \left(|\phi_i\rangle - \left|\tilde{\phi}_i\right\rangle\right) \left\langle \tilde{p}_i \middle| \tilde{\psi} \right\rangle, \tag{2.23}$$

where ϕ_i and $\tilde{\phi}_i$ are the partial waves and pseudo partial waves, respectively, and $\tilde{p}_i$ is a projector onto the space of $\tilde{\phi}_i$.[42, 223] As in the case of PPs described above, the index i specifies an atomic center and angular momentum quantum numbers (ℓ, m). The basis of $\tilde{\phi}_i$ functions is complete, such that the expansion in Eq. 2.23 is exact in the infinite limit.[42] In practice, only one or two partial waves $\tilde{\phi}_i$ are used for each set of angular momentum quantum numbers.[139] These projectors are localized to a pre-defined core region,[42] and

the size of this region impacts the accuracy of a computation considerable.[139] As above, the partial wave expansion is fit to results from a particular AE method, and a number of parameterizations have been reported.[145, 382]

2.1.2 Pseudopotential (in)consistency

Regardless of the details in form, each of the preceding PPs undergo some fit procedure to achieve agreement with a particular set of all-electron computations. As a result, a PP computation is only theoretically sound if it employs the same methods of electron exchange and correlation as were used to paramaterize the PP.[427, 432] Indeed, much of the groundbreaking work on PPs for chemical applications anticipated reparameterization with more accurate correlation treatments in the future.[17, 157, 138] This has not, however, always been the case, and errors associated with "inconsistent" use of PPs are well-documented.

It is somewhat common to acknowledge the lack of theoretical footing for inconsistent PP use, but advocate this practice anyway on the basis of empirical results.[349, 427, 156, 357] These studies generally compare geometries and energetic properties for a few (<10) small systems to all-electron results, and conclude that errors incurred by PPs are smaller than those due to other approximations, like basis set truncation and inexact correlation treatments. To be fair, there are certainly cases where inconsistency errors are quite small. For instance, Ref. 349 provides mean absolute errors (MAEs) due to use of HF potentials in DFT computations across six small transition metal complexes; these are 0.4 and $0.6\,\mathrm{kcal\,mol^{-1}}$ for S-VWN and B-LYP density functionals, respectively. However, this same paper reports errors of -7.4 and $-13.2\,\mathrm{kcal\,mol^{-1}}$ for binding energies of TiF_4 and $Ni(CO)_4$ when the S-VWN potential is used with B-LYP and presents these results as tolerable. Similar patterns are present in the other cited sources, where good (even great) performance for a small number of systems is extrapolated to justify inconsistent PP use broadly, despite the fact that performance is not uniform.

Indeed, a number of other studies have reached the opposite conclusion, finding PP reparameterization is necessary to achieve high fidelity to AE computations.[155, 96, 432, 387, 248] To take a recent instance, use of a PBE0 potential in lieu of a PBE one reduced mean absolute relative PP errors from 8 to 4.5 % in comparison to all-electron results.[432] This finding is consistent with other work that indicates methods that employ exact exchange (HF, hybrid DFT) require PPs that incorporate these effects.[96, 387] Likewise, results from Ref. 2 indicate that use of the SRSC potential (fit to HF results[225]) in DFT computations results in inconsistency MAEs ranging from about 1–15 $\mathrm{kcal\,mol^{-1}}$ for lanthanide complexes, depending on the density functional. Additionally, previous work from some of us found that use of the GTH-PBE[138, 221] in B97M-rV and ωB97X-V computations incurred mean absolute PP errors of 5.1 and $4.6\,\mathrm{kcal\,mol^{-1}}$ for binding energies of the first-row transition metal monocarbonyls.[248] Parameterization of new GTH potentials for these functionals reduced these MAEs to 3.5 and $2.4\,\mathrm{kcal\,mol^{-1}}$, respectively.

Despite the long-time recognition of theoretical and practical limitations of inconsistent PP use, systematic exploration of this issue is all-but-absent from the literature. Commend-

able work from Borlido, *et al.* examined inconsistent use of PAW potentials for determination of band gaps for 473 materials with a variety of common density functionals.[47] These researchers found that inconsistent use of PPs increased errors at least three-fold relative to consistent computations, but that these generally incurred MAEs of around 0.1 eV, which are argued to be tolerable in solid state contexts. Even so, errors for individual systems yawned to multiple eV in some instances, and problematic cases could not be identified in any predictable way.[47]

Studies of similar scope for PP consistency errors in properties of chemical interest have not been reported, even as use of PPs in these contexts expand, particularly in *ab initio* molecular dynamics where PPs may be applied to all atoms[406, 212, 227, 254] As discussed above, select results in this domain are mixed, making broad recommendations for practice difficult. In the present work, we address this by evaluating PP inconsistency errors incurred for HF and various forms of the density functional approximation (DFA), including local density approximations, generalized gradient approximations (GGAs), meta-GGAs, and hybrids. We evaluate these errors for fit-CRENBL, SRLC, def2-ECP, GTH-PBE, and PAW-PBE potentials across a diverse set of 196 benchmark energies, including atomization energies for main group elements, non-bonded interactions, and both barrier heights and reaction energies for transition metal dimers and organometallic complexes. These DFAs, PPs, and data sets are described in Section 2.2, and results are presented in each of the subsequent sections.

2.2 Methods

Pseudopotential (PP) errors, including inconsistency errors, were determined in reference to all-electron results across a variety of exchange and correlation methods. We report these errors for three diverse benchmark datasets, described in Section 2.2.1. In order to include a breadth of the PP classes described above, we have employed a number of different electronic structure codes. Essential aspects of each of these computations can be found in Section 2.2.2. For systems involving transition metals, we include scalar relativistic effects through the exact two-component (X2C) framework, [91] which we briefly describe in Section 2.2.3.

2.2.1 Benchmark datasets

Performance was evaluated across a diverse collection of benchmark datasets representing the broad range of interactions relevant to complex chemical systems. Non-bonded interactions were represented by the S22 set of non-covalent dimers, which include a range of intermolecular forces, including hydrogen bonds.[196] The W4-11 set of 140 total atomization energies for small first- and second-row molecules and radicals was used to evaluate performance on main group (MG) thermochemistry.[202] Finally, PP performance for transition metal (TM) chemistry was evaluated using the TMC34 set,[68] which is comprised of

Elements	def2-ECP[a]	fit-CRENBL[b]	SRLC[c]	GTH[d]	PAW[e]
B–F	–	[He]	[He]	[He]	[He]
Al–Cl	–	[Ne]	[Ne]	[Ne]	[Ne]
Sc–V	–	[Ne]	[Ar]	[Ne]	[Ne]
Cr–Mn	–	[Ne]	[Ar]	[Ne]	[Ne] + $3s$
Fe	–	[Ne]	[Ar]	[Ne]	[Ar]
Cu–Zn	–	[Ne]	[Ar]	[Ar]	[Ar]
Y–Mo	[Ar] + $3d$	[Ar] + $3d$	–	[Ar] + $3d$	[Ar] + $3d$
Tc–Rh	[Ar] + $3d$	[Ar] + $3d$	–	[Ar] + $3d$	[Ar] + $3d$ + $4s$
Pd	[Ar] + $3d$	[Ar] + $3d$	–	[Ar] + $3d$	[Kr]
Ag–Cd	[Ar] + $3d$	[Ar] + $3d$	–	[Kr]	[Kr]
Hf–Ta	[Kr] + $4d$ + $4f$	[Kr] + $4d$ + $4f$	–	[Kr] + $4d$ + $4f$	[Kr] + $4d$ + $4f$ + $5s$
W	[Kr] + $4d$ + $4f$	[Kr] + $4d$ + $4f$	–	[Kr] + $4d$ + $4f$	[Kr] + $4d$ + $4f$
Re–Pt	[Kr] + $4d$ + $4f$	[Kr] + $4d$ + $4f$	–	[Kr] + $4d$ + $4f$	[Xe] + $4f$
Au–Hg	[Kr] + $4d$ + $4f$	[Kr] + $4d$ + $4f$	–	[Xe] + $4f$	[Xe] + $4f$

[a] Ref. 8
[b] Refs. 300, 182, 231, 346, 278
[c] Ref. 37
[d] Refs. 138, 155
[e] Ref. 223

Table 2.1: Core size for each of five pseudopotentials included in this study across all relevant elements. Highlighted blocks correspond to successive rows of the periodict table.

three subsets: (a) the TMD10 set of first-row TM dimers with MG elements,[283] (b) the MOR13 set of metal-organic reaction energies for TM complexes,[67] and (c) the TMB11 set of TM barrier heights for reactions in second- and third-row TM complexes.[201, 384, 383, 176, 101]

2.2.2 Computational details

Pseudopotential (PP) errors were evaluated in comparison to all-electron (AE) computations across a variety PPs, including def2-ECP,[8] fit-CRENBL,[300, 182, 231, 346, 278] SRLC,[126, 37] PAW-PBE,[42, 223] and GTH-PBE.[138, 155, 221] Core sizes for each of these PPs are found in Table 2.1, and further descriptions in Section 2.1.1, above. We study the use of these PPs in conjunction with different electron exchange and correlation methods, including Hartree–Fock (HF) theory,[345, 149, 324, 38] and five density functional approximations (DFAs): LDA[413], PBE[309], SCAN[381], B97M-rV[271, 273], and ωB97X-V[269]. For computations involving transition metals, scalar relativistic effects were included through the X2C procedure[91] (Section 2.2.3).

Computations for all-electron results as well as the def2-ECP, fit-CRENBL, and SRLC PPs were obtained using the Q-Chem computational chemistry package.[361] These compu-

All-Electron	S22	W4-11	TMC34
BSIE Ref.	def2-QZVPPD	def2-QZVPPD	def2-QZVPPD
PP Ref.	def2-QZVPPD	def2-QZVPPD	TZVPPall (+X2C)
Truncated basis	def2-TZVPPD	def2-TZVPP	def2-TZVPP
Pseudopotential	S22	W4-11	TMC34
fit-CRENBL	def2-QZVPPD	def2-QZVPPD	def2-TZVPP
SRLC	def2-QZVPPD	def2-QZVPPD	–
GTH-PBE	–	TZV2P	TZV2P
PAW-PBE	–	1000 eV	1000 eV

Table 2.2: Basis set and pseudopotential combinations used for various computations in this work. Citations for each basis set are found in text. For the TMC34 BSIE results, onlt the TMD10 subset was considered.

tations employed one of the def2-TZVPP, def2-TZVPPD, or def2-QZVPPD basis sets,[420, 417, 336] as indicated in Table 2.2 and the discussion below. Unrestricted reference states were employed, and stability analysis was used to ensure that minimum energy states were obtained. Fine (99,590) Lebedev integration grids were used to evaluate integrals of the exchange-correlation (XC) functional.[237, 236] Energy convergence thresholds of at most 1×10^{-8} a.u. were used to terminate self-consistent field (SCF) iterations, though more stringent convergences of 1×10^{-10} a.u. were obtained in the majority of cases. In troublesome systems, explicit excitations into the valence space resulted in lower energy solutions; this procedure was used as necessary to ensure energy comparisons relied on the same electronic state.

Results for PBE and B97M-rV computations with Goedecker–Teter–Hutter (GTH) potentials[138, 155] optimized for PBE[221] and B97M-rV[248] were obtained using the CP2K code[409, 255, 183], in combination with the molecular optimized (MOLOPT) TZV2P basis set[408]. Kohn-Sham orbitals were optimized using the orbital transformation method[407] for molecules or using the traditional diagonalization approach for metal atoms. Computations were performed using a box size of 20 Å × 20 Å × 20 Å, and the energy cutoff was set at 800 Ry for the calculation of electrostatic energy terms. SCF iterations were taken to be converged when energy changes were smaller than 1×10^{-6} a.u..

Finally, VASP[222, 145] was used for PAW-PBE results, obtained with the plane wave (PW) basis set cutoffs indicated in Table 2.2. All calculations were performed at the gamma point with Gaussian smearing using a width of 0.03 eV. Calculations were performed with 12 Å of vacuum between periodic images. For charged systems, we include monopole and dipole corrections to the energy to avoid spurious interaction between charged periodic replicas. We include non-spherical contributions to the gradient correction inside the PAW spheres (LASPH = True) and an additional support grid for the augmentation charges (ADDGRID

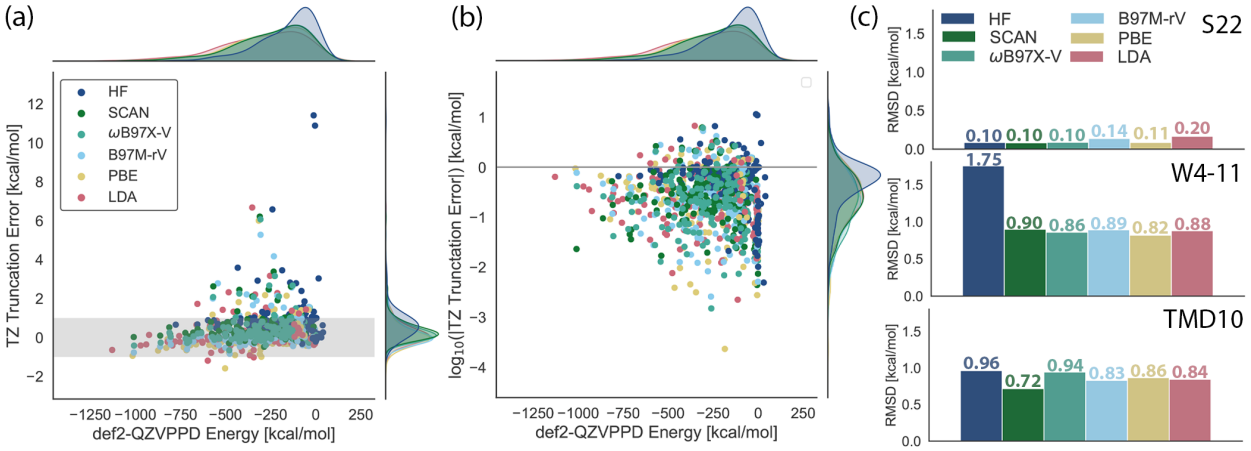

Figure 2.1: Basis set incompleteness error (BSIE) for all-electron def2-TZVPP results is within chemical accuracy for most systems: (a) BSIE relative to interaction energy indicates small errors across system size and (b) base-ten logarithm of magnitude of BSIE shows most errors are in the 0.1–1 kcal mol^{-1} range. Chemical accuracy is achieved by points within the gray band in panel (a) and below the gray line in panel (b). (c) Root-mean-squared BSIE satisfies chemical accuracy across methods for the S22, W4-11, and TMD10 data sets, except HF for W4-11, where large errors for FOO and ClOO dominate. Omission of these species lowers HF RMSE to 1.0 kcal mol^{-1}.

= True), and do not use symmetry (ISYM = 0). The energy convergence criterion was 2.721 14 $\times$ 10^{-9} eV (1 $\times$ 10^{-10} a.u.) for SCAN and PBE functionals and 2.721 14 $\times$ 10^{-8} eV (1 $\times$ 10^{-9} a.u.) for HF and B97M-rV functionals, with the exception of a few difficult to converge systems. 111_b2_W4-11 with B97M-rV has is converged to 1$\times$10^{-8} a.u., TMD12_Co with SCAN is converged to 1 $\times$ 10^{-9} a.u.. Basis set convergence studies suggest basis set errors are <1 kcal mol^{-1} for individual molecules and <0.5 kcal mol^{-1} for all reaction energies, with most systems exhibiting errors lower than those upper bounds.

Throughout this study, PP performance is evaluated in reference to all-electron basis set incompleteness errors (BSIEs), as has been suggested by other authors.[138] In all cases, energies obtained with the def2-QZVPPD basis set were taken as good approximations to the complete basis set (CBS) limit.[417, 336] In the majority of cases, the BSIE associated with use of the def2-TZVPP set was determined as sets of this quality are generally used in production computations.[417] The def2-TZVPPD set was used, however, for computations on the S22 set, as diffuse functions are known to be important for accurate modeling of non-covalent interactions.[302, 303] We do not report BSIEs for the TMB11 and MOR13 subsets of the TMC34, as def2-QZVPPD computations for these systems are intractable.

2.2.3 Relativistic effects for TMC34 benchmarks

All-electron scalar (*i.e.* spin-free) relativistic calculations were performed within the exact two-component (X2C) framework.[256] The X2C model transforms the one-electron Hamiltonian by effectively incorporating information from the solutions of the four-component, one-electron Dirac Hamiltonian.[110, 352, 249] Our implementation of X2C has been previously used to study core-spectroscopy of third period main group elements and first row transition metals[91], where scalar relativistic roles are bound to play a m ajor role. A possible limitation of our relativistic treatment concerns the handling of two-particle interelectronic interactions. Besides being described by a purely coulombic potential, these terms are left unaltered within the simple X2C formalism. For core spectroscopy of transition metals, lack of such effects, known as picture-change effects[352], can lead to large errors in predicting excitation energy[91], but their effect should be minor for valence electrons in first row transition metals and our X2C approach should be adequate for these systems[73]. The same convergence criteria and DFT quadrature grids used in the PP calculations were employed in the all-electron X2C counterparts. For the X2C calculations, the decontracted x2c-TZVPPall basis set [323] was used for all elements. This basis set was specifically designed to be consistent with the the def2 family of basis sets and provides all-electron support for heavy elements whose cores are usually replaced by PPs. Therefore, our all-electron X2C results allow for a straightforward assessment of PP errors for some transition metal complexes.

Results and discussion

2.3 The scale of basis set incompleteness error

The importance of pseudopotential errors (PPEs) in a given calculation should be measured against the scale of other errors in the methodology. It is commonly argued that PPEs are smaller than basis set incompleteness errors (BSIEs)[138] and/or density functional errors (DFEs),[349, 138, 357] and therefore PPEs may be safely ignored. Previous studies have benchmarked DFEs across a range of interactions (*cf.* Mardirossian and Head-Gordon[272] and citations therein), and we do not repeat this work here. We do, however, report BSIEs across the present data sets and for each of the present DFAs as a reference point for later discussion of PP errors in these same systems.

Across all of the present systems, def2-TZVPP BSIEs are generally within the bounds of chemical accuracy ($<1\,\mathrm{kcal\,mol^{-1}}$), regardless of the density functional and the system (Figure 2.1[a]). The logarithm of these BSIEs (Figure 2.1[b]) provides a fuller picture of these data, indicating that the majority of errors fall within the 0.1–1 $\mathrm{kcal\,mol^{-1}}$ range, though even higher accuracy is achieved for many systems. The slight positive slope of the data in Figure 2.1(a) indicates that BSIE varies only slowly with the interaction size, such that chemical accuracy in the BSIEs obtains even for systems with very large transformation

energies. The logarithm plot (Figure 2.1[b]) highlights this structure even more clearly, as seen in the slope of the lower edge of accuracy as we vary the system size.

Summary statistics for BSIEs in these systems are also encouraging across each data set, although as is well known, performance varies considerably from one type of energy difference (and thus one kind of data set) to another (Figure 2.1[c]). Due to favorable error cancellation, BSIEs are generally small for the non-bonded interactions in the S22 set, with RMS errors $\leq$0.2 kcal mol^{-1} for all density functionals. BSIEs are statistically larger for the W4-11 and TMD10 sets, which contain total atomization energies for small main group molecules and first-row transition metal dimers, respectively. Across these results, only HF for the W4-11 fails to achieve chemical accuracy in the BSIEs, and poor performance for two species (FOO and ClOO) dominates this error. Omission of these entries results in an adjusted RMS error of 1.0 kcal mol^{-1}, still slightly larger than BSIEs for the DFAs. In general, HF energies converge more slowly than DFT ones with the Karlsruhe basis sets,[313, 417] so this is unsurprising.

For present purposes, these results define what we consider a tolerable PP error, *i.e.* one that is smaller than the BSIEs in similar systems. In what follows, we evaluate PP errors for these systems using the BSIE benchmark in conjunction with reference to previous results for DFA performance. As seen for the BSIEs, pseudopotential performance is also expected to vary depending upon how well errors cancel in evaluating energy differences. We shall see below that PP errors range from fractions to tens of kcal mol^{-1}.

2.4 The good: Barrier heights and non-bonded interactions

The systems in the S22 set were used in order to assess the validity of common pseudopotential approximations in the context of non-bonded interactions. The benchmarks in this set correspond to the dimerization energy of organic monomers, with computed interaction energies ranging from $-$0.5–21 kcal mol^{-1}.[196] Pseudopotential errors were evaluated relative to all-electron def2-QZVPPD calculations for the fit-CRENBL and SRLC potentials with the same basis set.

As seen in Figure 2.2, PP errors for both fit-CRENBL and SRLC are below the limits of chemical accuracy for all systems in the S22 across all DFAs in this study. These deviations are size-extensive in the magnitude of the interaction, as demonstrated by the clear linearity in the errors. Overall, the methods and systems in Figure 2.2 exhibit average relative errors of about 1–3 %. The largest absolute errors therefore occur in systems with the highest dimerization energies, here the formic acid dimer, the formamide dimer, and the uracil dimer, each of which possess two hydrogen bonds. Still, even the largest absolute error of $-$0.66 kcal mol^{-1} (formic acid dimer, ωB97X-V) is only 3 % of the interaction energy and tolerably small in almost all circumstances.

In addition to being small in absolute terms, fit-CRENBL and SRLC errors are smaller

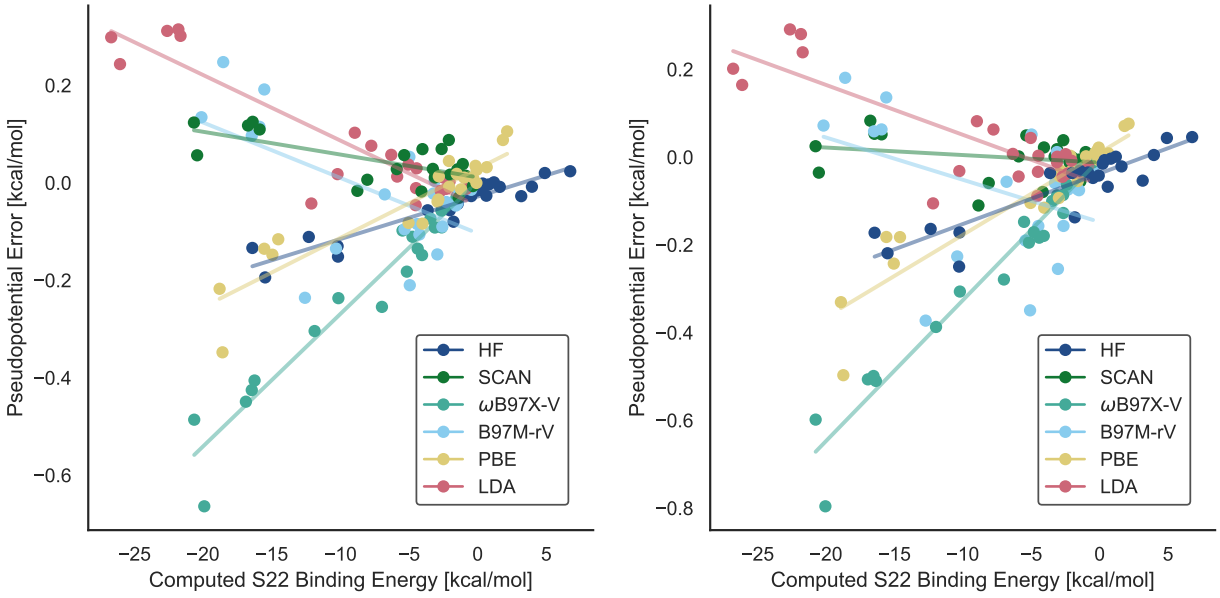

Figure 2.2: Pseudopotential errors ($\mathrm{kcal\,mol^{-1}}$) for the S22 dataset of intermolecular interactions versus the value of the interaction energy. The errors are defined as deviations between (left) fit-CRENBL/def2-QZVPPD and (right) SRLC/def2-QVZVPPD PP calculations relative to all-electron calculations, for each of the 6 DFAs listed. Errors for all data points are within the chemical accuracy threshold of $1\,\mathrm{kcal\,mol^{-1}}$, and vary linearly with the size of the interaction.

than BSIEs for 67 and 59 % of the S22 systems, respectively. Given the size of both types of errors, failures in the DFA correlation scheme will tend to dictate overall model performance for non-bonded interactions. While these results suggest a small degree of caution in systems with extremely strong intermolecular forces, like those with multiple hydrogen bonds, they lend general support to the use of the pseudopotential approximation in non-bonded contexts.

Barrier heights for the transition metal complex reactions of the TMB11 set also generally exhibited small PP errors (Figure 2.3). Still, even here, differences in the quality of various PPs emerges. The def2-ECP exhibits the strongest performance and transferability of all considered PPs, with RMSEs around $0.5\,\mathrm{kcal\,mol^{-1}}$ for all DFAs. In part this is because the def2-ECP is more conservative than the other PPs considered here: def2-ECP is all-electron until the second-row transition metals (*cf.* Table 2.1). The barrier for Mo-catalyzed splitting of a sulfonyl bond reaction represents a clear and single outlier for the HF/def2-ECP combination, with an error of $9.8\,\mathrm{kcal\,mol^{-1}}$ error. If this point is omitted, HF/def2-ECP exhibits the smallest RMSE of all functional/method combinations for the TMB set ($0.26\,\mathrm{kcal\,mol^{-1}}$). The GTH-PBE performs similarly well for PBE computations (RMSE = $0.45\,\mathrm{kcal\,mol^{-1}}$) and exhibits only a small transferability error resulting in a $0.77\,\mathrm{kcal\,mol^{-1}}$

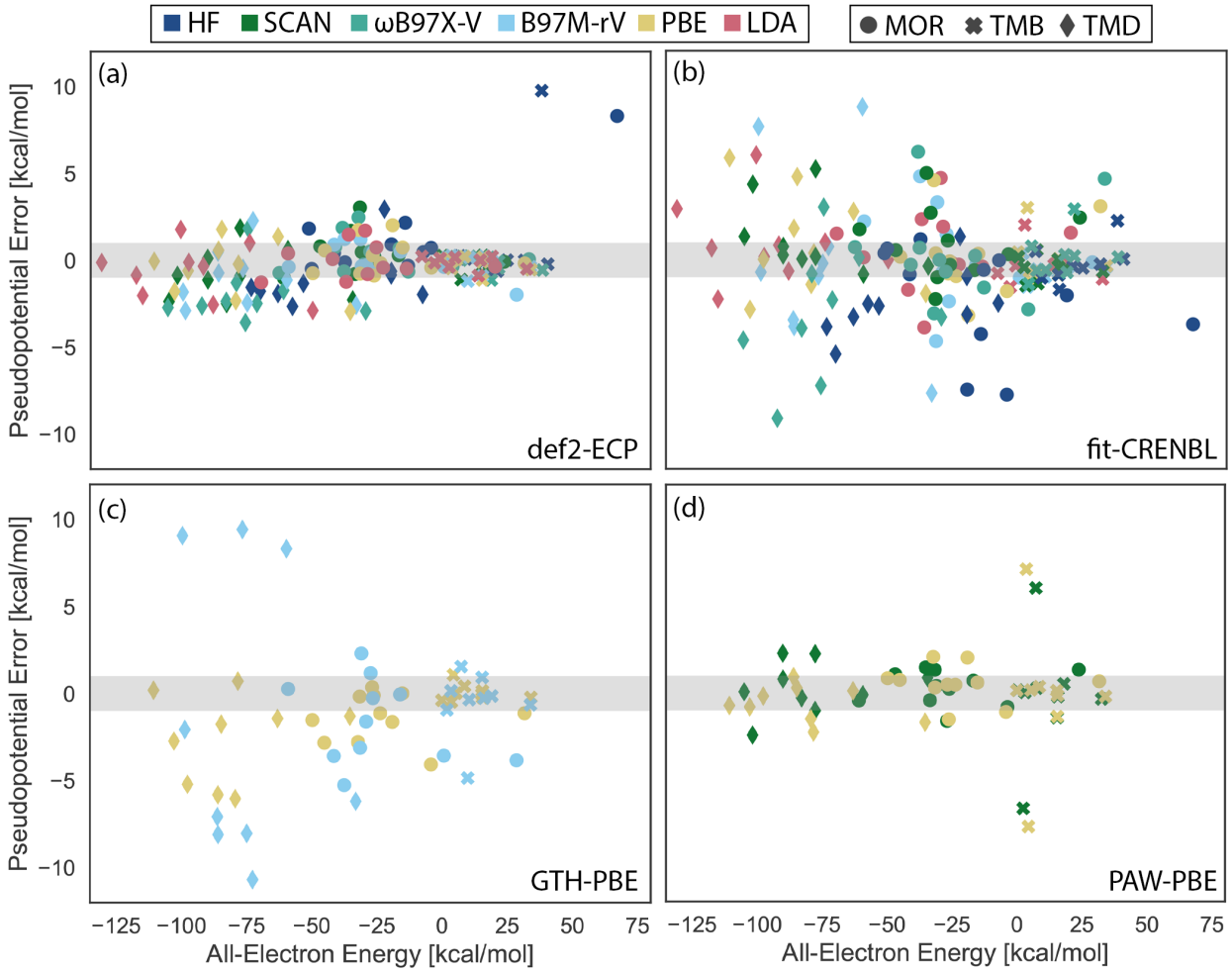

Figure 2.3: Pseudopotential errors [kcal/mol] for (a) def2-ECP, (b) fit-CRENBL, (c) GTH-PBE, and (d) PAW-PBE for the TMC34 data set of transition metal containing energy changes. TMC34 contains 3 subsets: barrier heights (TMB; crosses), reaction energies (MOR; circles) and dimer bond strengths (TMD; diamonds). Errors generally increase from TMB to MOR to TMD. Gray bands correspond to chemical accuracy of $\pm 1\,\mathrm{kcal\,mol^{-1}}$. Outliers and other aspects of the data are discussed in the text.

RMSE upon removal of the same sulfonyl splitting reaction barrier discussed above, which is problematic here as well.

TMB 11 results for the PAW-PBE potential as implemented in VASP are more mixed. If charged systems are omitted, PP errors are in line with the values discussed in the preceding paragraph, with RMSEs of 0.55 and $0.60\,\mathrm{kcal\,mol^{-1}}$ for the PBE and SCAN functionals, respectively. Barrier heights for charged systems are abysmal, shown as the clear outliers

in Figure 2.3(d), but this represents a known challenge for periodic codes,[293, 261] and is not an indictment of the PAW-PBE potential. Finally, of results for the TMB11 set, the fit-CRENBL potential exhibits the worst performance, with DFA-dependent RMS PP errors of 0.8–1.2 kcal mol^{-1}. Once again, Mo-catalyzed sulfonyl splitting exhibits the worst performance for most DFAs, and its omission brings the overall statistics for fit-CRENBL results within chemical accuracy.

Direct comparison to BSIE cannot be made for the TMB11 systems, as many of these reaction complexes are large enough to prohibit near-CBS treatment with the def2-QZVPPD basis. Still, once pathological cases are removed, chemical accuracy is achieved in the majority of cases for all of the DFA/PP combinations considered here. Performance of PPs on transition metal reaction barrier heights and overall energies for non-bonded interactions are similarly strong, and the present results lend support to the use of PPs in such applications.

2.5 The bad: Transition metal reaction energies

Pseudopotential performance degrades when moving from transition metal barrier heights to overall reaction energies for similar systems. Within this category, we include the thermodynamics for the MOR13 TM complex reactions and the dimerization energies of the TMD10. The latter benchmark set is particularly well-suited for differentiating between different PPs, as their performance varies greatly here.

As before, the def2-ECP and PAW-PBE potentials perform well for the MOR13 reaction energies (Figure 2.3). DFA/def2-ECP RMSEs hover around chemical accuracy, ranging from 0.9 kcal mol^{-1} for B97M-rV to 1.2 kcal mol^{-1} for SCAN. As in the TMB11 above, the HF/def2-ECP error is dominated by a single outlier (Pd-catalyzed splitting of C_2H_6), and omission of this point brings the RMSE for this methodology to 1.0 kcal mol^{-1} and does not change the other def2-ECP results significantly. RMSEs for PAW-PBE are similar in overall magnitude for the MOR13, at 1.2 and 1.0 kcal mol^{-1} for the PBE and SCAN functionals, respectively. Perhaps more than any other result in this study, this demonstrates very good transferability of the PAW-PBE potential as the overall error for SCAN is actually less than that of its native PBE. Additionally, each of the def2-ECP and PAW-PBE potentials are able to consistently capture the scalar relativistic effects associated with these systems as approximated by our X2C calculations.

Neither the GTH-PBE nor fit-CRENBL potentials provide as reliable results as def2-ECP or PAW-PBE for the MOR13 reactions. RMS PP errors for fit-CRENBL span 2.0–3.7 kcal mol^{-1} depending on the method, and one cannot clearly attribute these discrepancies to any single outlier (Figure 2.3[b]). Indeed, removal of the largest-error species does not significantly improve the statistical picture for fit-CRENBL across any of the correlation methods. Similar comments can be made for GTH-PBE (Figure 2.3[c]), where errors for PBE and B97M-rV are 1.9 and 2.8 kcal mol^{-1}, respectively. The increase in error magnitudes from PBE to B97M-rV provides a first indication of the sensitivity of GTH potentials to inconsistency errors, as has been noted elsewhere.[138, 155, 221, 248] Still, even when used

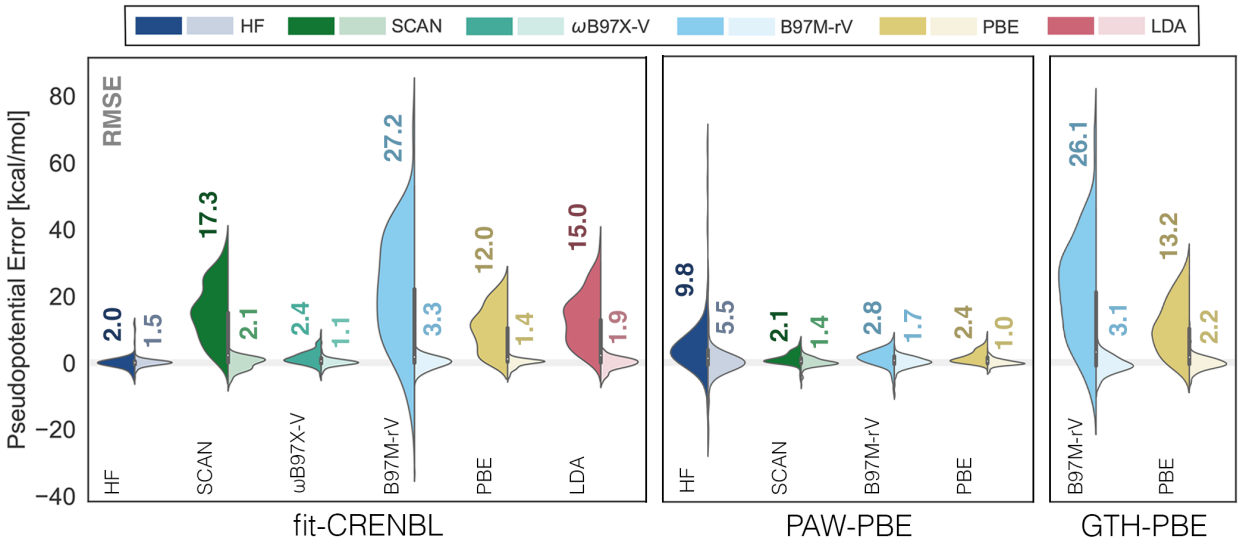

Figure 2.4: Errors (kcal/mol) in the W4-11 total atomization energies relative to all-electron def2-QZVPPD results. PP errors for each methodology are indicated by the left-hand side of each violin. Inclusion of element-specific atomic corrections significantly improves performance in all cases (right violins), indicating a large degree of systematic PP error. Violins are decorated with root-mean-squared pseudpotential errors (RMSEs).

in conjunction with its parent PBE functional, this GTH potential exhibits errors outside of chemical accuracy in all but four of the MOR13 systems. Unlike the treatment of non-bonded interactions and barrier heights, where performance was relatively good for all PPs assessed, the MOR13 subset discriminates between the PPs considered here, with fit-CRENBL and GTH-PBE exhibiting consistently larger errors than def2-ECP and PAW-PBE.

Discrepancies in PP performance become larger in moving to the TMD10 set of dimerization energies for first-row TM–X complexes, where X is a main group element. The best results are obtained with PAW-PBE, where PP RMSEs are 1.2 and 1.4 kcal mol^{-1}, respectively, for PBE and SCAN (Figure 2.3[d]). While included in Figure 2.3(a), TMD10 performance is a poor metric for def2-ECP, as this potential is all-electron for the first-row TM series. Thus def2-ECP errors are largely associated with neglect of relativistic effects, rather than PP success or failure. Still, RMSEs ranging from 1.6–2.5 kcal mol^{-1} for def2-ECP indicate that relativistic effects can be significant even in these systems.

GTH-PBE and fit-CRENBL errors are troubling in these systems. For the latter, RMSEs range from 2.3 kcal mol^{-1} for SCAN to 5.0 kcal mol^{-1} for B97M-rV, and a number of individual fit-CRENBL TMD10 predictions err by over 5 kcal mol^{-1} for each of the tested DFAs. For GTH-PBE, a 3.5 kcal mol^{-1} RMSE for the PBE functional indicates an apparent inadequacy of the GTH procedure, resulting in errors up to 6 kcal mol^{-1} (for MnBr), afford-

Table 2.3: Root-mean-squared errors (RMSEs) of W4-11 total atomization energies for basis set and effective core potential combinations relative to def2-QZVPPD (def2-ECP) results across a representative set of density functionals with and without pseudopotential and HF density corrections applied [kcal/mol]. Least-squares energy corrections for each atom result in significant improvement for PP inconsistency errors.

PP	Basis	HF	LDA	PBE	SCAN	B97M-rV	ωB97X-V
Uncorrected results							
def2-ECP	def2-TZVPP	1.74	0.87	0.81	0.89	0.89	0. 85
fit-CRENBL	def2-QZVPPD	2.00	15.01	11.99	17.25	27.06	2.42
SRLC	def2-QZVPPD	2.51	14.28	11.49	16.94	26.86	2.46
GTH-PBE	TZV2P	–	–	13.19	–	26.13	–
PAW-PBE	PW (1000 eV)	9.82	–	2.40	2.07	2.77	–
With least-squares atomic energy corrections							
fit-CRENBL	def2-QZVPPD	1.49	1.92	1.37	2.09	3.28	1.15
SRLC	def2-QZVPPD	2.02	2.14	1.51	2.57	1.80	1.59
GTH-PBE	TZV2P	–	–	2.22	–	3.07	–
PAW-PBE	PW (1000 eV)	5.50	–	0.98	1.45	1.75	–

ing an RMSE of $3.5\,\mathrm{kcal\,mol^{-1}}$. Transferability errors further plague B97M-rV/GTH-PBE computations, where the *smallest* PP error is $-2\,\mathrm{kcal\,mol^{-1}}$, and over half of these TMD10 errors are in excess of $8\,\mathrm{kcal\,mol^{-1}}$. Refitting GTH potentials for each density functional is therefore necessary but by no means sufficient for obtaining high fidelity results relative to AE computations.

Prediction of dimerization energies between TM and MG atoms therefore represents a challenging problem for PPs, and differences in performance between PAW and GTH/fit-CRENBL are notable. Thus, while PPs introduce few errors for barrier heights of TM complexes and relatively small errors for MOR13 reaction energies, atomization energies present significant challenges for some of the most common types of PPs.

2.6 The ugly: Main-group bond breaking

Pseudopotential errors in dimerization energies for the TMD10 portend further trouble for evaluation of main group atomization eneriges like those of the W4-11 set.[202] Errors for these systems turn out to exhibit an extremely strong dependence on the density functional, with startling error distributions in some cases (Figure 2.4).

Once again, out-of-the-box treatments using the PAW-PBE PP provide most consistently reliable treatment for these systems, with RMSEs of 2.1–$2.8\,\mathrm{kcal\,mol^{-1}}$ for the SCAN, PBE, and B97M-rV DFAs. The greatest range of performance for the W4-11 atomization energies

is found in fit-CRENBL, where PP RMSEs for HF and ωB97X-V are 2.0 and 2.4 kcal mol^{-1}. Meanwhile, fit-CRENBL errors are unacceptably large for each of the other four DFAs (Figure 2.4). For each of SCAN, B97M-rV, and LDA, PP errors are in excess of 1 kcal mol^{-1} for over 95 % of the W4-11 systems. Furthermore, PP errors are larger than def2-TZVPP BSIEs in at least 97 % for each of these three DFAs, as well as PBE. Hence, the general assumption that PP errors are small relative to other computational approximations[349, 155, 357] clearly does not hold here. The difference with ωB97X-V and HF, where about 45 % and 60 % of energies are within chemical accuracy of AE results, is striking, potentially pointing to the importance of exact exchange in the fitting of PPs. This could also explain the larger PAW-PBE errors for HF relative to the tested DFAs. Error distributions for the GTH-PBE approximation in PBE and B97M-rV computations are similar to those for fit-CRENBL: PP errors are significant for both DFAs, but the potential is particularly ill-suited for use with B97M-rV.

Since atomization energies reflect changes in electronic environment between molecules and atoms, it is possible that a significant part of these large errors can be corrected on an atom-by-atom basis. Indeed, at least one previous report on similar datasets has advocated for atomic correction schemes to ameliorate PP errors in these systems.[422] We define atomic corrections δE_{X} for atom X, according to

$$E'_{\mathrm{X}} = E_{\mathrm{X}} + \delta E_{\mathrm{X}}, \tag{2.24}$$

where E_{X} is the uncorrected energy for atom X. Corrections for each DFA/PP pair were optimized by multiple linear regression to minimize the RMSE of the W4-11 and used to recompute TAEs for this set. The errors for corrected PPs are represented by the right-hand distributions of each violin in Figure 2.4, indicating that significant reductions in PP errors are achieved through atomic corrections. Once corrected, nearly uniform performance across all DFA/PP pairs is achieved, and error distributions are roughly normal. These atomic corrections are specifically fit to the W4-11 set, and we do not necessarily recommend their wide use in other systems without further validation. Nevertheless, the success of this approach indicates that the most egregious errors in atomization energies for unmodified PPs are highly systematic, and simple correction schemes can correct for this in native and transferred use of PPs.

While element-specific corrections are clearly valuable for atomization energies, these are not directly applicable to more general types of reaction energies. This highlights the need for more universal correction schemes for PPs. Others have successfully employed non-linear core corrections (NLCCs) to reduce PPEs (though not necessarily PP inconsistency errors) in similar systems,[422] and we are currently exploring their use in these systems.

2.7 Summary and conclusions

The preceding sections have demonstrated that PP errors and PP inconsistency errors are not evenly distributed across all types of molecular energy differences. In particular, we find

it helpful to divide these into three categories:

- *The Good.* These are cases where PP errors are minimal relative to this introduced by other approximations in the computation and/or achieve chemical accuracy. They include non-bonded interactions (like S22 systems[196]) and barrier heights for organometallic reactions (like TMB11 systems[201, 384, 383, 176, 101, 68]). There are select cases where PP errors are greater than $1\,\mathrm{kcal\,mol^{-1}}$ for TMB11 predictions, but even the worst of these is about $5\,\mathrm{kcal\,mol^{-1}}$, and errors are much smaller in a statistical sense.

- *The Bad.* Here we include systems where PP errors are significant for enough systems that chemical accuracy is not achieved statistically. We find this to be the case for transition metal reaction[68, 67]and dimerization[68, 283]energies for most of the classes of PPs studied herein. PAW-PBE and def2-ECP RMS PP errors hover right around $1\,\mathrm{kcal\,mol^{-1}}$, but errors and inconsistency errors for fit-CRENBL and GTH-PBE are 2–3 times this large.

- *The Ugly.* For breaking of main group bonds (the W4-11 systems[202]), PP inconsistency errors can be strikingly bad. The difference between consistent and inconsistent PP use is most striking for the fit-CRENBL potential, whereas GTH potentials result in significant errors regardless of the consistency of the protocol. The PAW-PBE potentials as implemented in VASP exhibit the best performance out of the box, and only with use in HF do errors become notable.

Overall, we find that inconsistent use of PPs represents an often overlooked but potentially serious source of error in modern DFT computations. Based on a relatively small set of results, previous authors have argued that these errors are "much smaller than the errors...introduced by incomplete basis sets"[155] or that "error inherent in the in the (ab initio) electron correlation or density functional procedure is almost always larger than the error produced by the pseudopotential approximation."[357] However, the results presented here indicate that there are many contexts where these conclusions are simply not true. Particular care should be taken when PPs are used in circumstances that break main group bonds, and potentials like def2-ECP, where elements in the first three rows of the periodic table are all-electron, are strongly recommended where possible.

This work has additional implications for the development of PPs and even density functionals. First, results on the W4-11 set indicate that PP inconsistency errors for atomization energies are extremely systematic, and a single energy correction for each atom can remove them almost entirely. Others have come to similar conclusions.[422] There may also be scope for development of generalizations of this approach that permit application to classes of chemical energy differences beyond atomization energies.

However, it is more desirable to instead pursue corrections to the PP formalism itself. Non-linear core corrections (NLCCs) represent one possible path forward,[422, 139] and we are exploring their use in the mitigating inconsistency errors.

Additionally, the results of this study indicate that PP inconsistency errors do not plague all DFAs equally. Specifically, the B97M-rV meta-GGA seems to be particularly susceptible to PP errors. We have not explored the reason for this, but it is possible that the excellent performance of this functional for main group thermochemistry[271, 273] is accompanied by greater sensitivity to the representation of the density. More broadly, differential inconsistency errors between DFAs suggests the possibility that performance in PP calculations be considered in the course of future DFA design; this would be relatively straightforward by including energy differences evaluated with and without use of PPs in training, validation and test sets.

Chapter 3

Energy decomposition analysis determines driving forces behind frequency shifts in transition metal monocarbonyls

This chapter is reproduced from Ref. 347 with permission from the PCCP owner societies.

Transition metal carbonyls possess historical and contemporary interest across a broad range of chemical disciplines. These compounds served as an early and paradigmatic example of synergistic charge transfer interactions in transition metal complexes, and their study elucidates many of the general features of transition metal chemistry.[83] Furthermore, the interaction between transition metals and carbon monoxide (CO) is a critical feature of interactions in catalytic systems.[144, 355, 314] Transition metal chemistry is also regarded as a final frontier in modern electronic structure theory. Computationally tractable methods can now yield reasonable predictions for select transition metal systems, though many difficulties remain.[344, 85, 376, 377, 101, 68] Hence, theoretical study of metal carbonyls serves as a test for state of the art of computational chemistry. Though among the simplest transition-metal systems, controversy has surrounded the electronic structure of bonding in metal carbonyls, and a variety of models have been proposed to explain the properties of these compounds.

3.0.1 The Dewar–Chatt–Duncanson Model

The Dewar–Chatt–Duncanson (DCD) model,[98, 72] originally proposed for metal-olefin systems, is frequently invoked to explain aspects of bonding in molecular metal carbonyls.[167, 366, 33, 443, 3, 26, 276, 319, 45, 120, 92, 386, 260, 121, 100, 441, 181, 321, 423, 220, 341, 51, 343, 430, 424, 267] Within this model, two types of orbital interactions give rise to the bond between the metal atom (M) and CO: (1) electron donation from the slightly antibonding CO 5σ-orbital into unoccupied M orbitals of appropriate symmetry (Figure 3.1a) and (2)

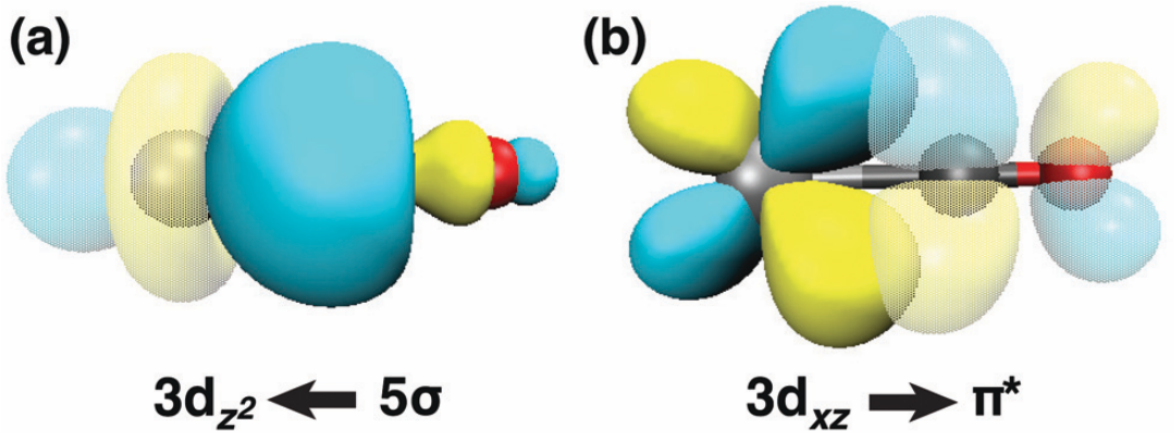

Figure 3.1: Dominant orbital interactions in the Dewar–Chatt–Duncanson model of metal-carbonyl binding: (a) forward donation from the CO σ orbital into unoccupied metal orbitals of appropriate symmetry (in this case $3d_{z^2}$); (b) back donation from occupied metal d orbitals (here, $3d_{xz}$) into the unoccupied CO π^* orbital. Orbitals pictured here obtained using COVP analysis on VCO^-.

electron donation from occupied M orbitals into the unoccupied $2\pi^*$-orbital on CO (Figure 3.1b). These interactions are variously referred to as forward- and back-donation or σ- and π-donation, respectively; we use these terms interchangeably throughout. While both modes of donation are understood to stabilize the MCO complex energetically, they are thought to give rise to competing effects in the properties of the CO adsorbate: the loss of electron density from the (slightly antibonding) 5σ-orbital strengthens the CO bond, decreasing its bond length (r_{CO}) and increasing its vibrational frequency (υ_{CO}), while donation into the $2\pi^*$-orbital weakens this bond, leading to an increase in r_{CO} and a decrease in υ_{CO}. Hence, the DCD model provides a possible, charge-transfer-based explanation for differences in observed CO vibrational frequencies across metal carbonyls in terms of the relative importance of forward- and back-donation in a particular system.

Despite its continued popularity, shortcomings of the DCD model have been well- documented, particularly as it concerns the properties of the C−O bond in the complex, which are evidenced by υ_{CO}. While the DCD model has enjoyed success describing trends in metal carbonyls with red-shifted values of υ_{CO} upon binding,[366, 120, 386, 441] its use in explaining υ_{CO} blue shifts is questionable. Explanations in terms of donation from the slightly antibonding 5σ-orbital once seemed plausible,[168, 386] but subsequent computational studies indicated that electrostatic and polarization effects drive υ_{CO} blue shifts in metal carbonyls, if they are present.[141, 260] As it concerns the complex binding energy (ΔE_{bind}), various studies have indicated that electrostatics, orbital polarization, forward-donation, and

back-donation can all play determining roles depending on the system.[33, 120, 386] Recent experimental accounts of transition metal carbonyls draw on this body of literature to make qualitative explanations of binding phenomena based on both electrostatic effects and orbital interactions.[341, 51, 343]

3.0.2 Alternative Pictures of M−CO Bonds

More detailed quantification of these physical effects in various systems aids in understanding the nature of the metal–carbonyl bond in more complicated and experimentally relevant systems. Previous approaches to this problem can be divided into two broad categories. Some have analyzed computed bond orders and charge migration to evaluate the roles of forward- and back-donation in complexes,[168, 167, 191, 122, 19, 141, 220, 92, 386, 260, 32, 27] while others track complex binding energies to evaluate the importance of various physical components to the overall M−CO bond.[18, 19, 33, 31, 45, 229, 95, 100] These two approaches have led to a variety of different conclusions regarding the forces that bind metal carbonyls.

Studies into charge and bond migration in metal carbonyls have typically focused on determining the relative importance of σ- and π-donation in stabilizing metal carbonyls, though no consensus has been reached. Most of this controversy has surrounded the question of whether and to what extent σ-donation contributes to the bond energies and C−O bond properties in metal carbonyls. Early computational studies on select species have indicated that σ-donation is essential to bond formation,[168, 167, 191, 122] while others suggest it is essentially non-existent.[141, 220] Comparative studies across a number of species have been particularly illumining in this respect. The charge decomposition analysis (CDA) studies of Frenking *et al.*[92, 386, 260] indicated σ-donation is always more significant than π-donation for stabilization of the M−CO bond, and that the relative importance of π-donation decreases from anionic to neutral to cationic systems. They also emphasized the importance of orbital polarization in stabilizing metal carbonyls regardless of charge,[386] and for effecting blue shifts in υ_{CO} for cationic systems.[260]. On the basis of their Mulliken population analyses, Barnes, Bauschlicher, and coworkers have also argued that π-donation plays a minimal role in cationic metal carbonyls, where electrostatic and polarization effects tend to dominate the interaction.[32, 27] Others have put forward similar arguments.[220]

The description of metal–carbonyl bonding that has emerged from energy decomposition analysis (EDA), constrained space orbital variation (CSOV),[18] as well as other approaches for analysis of M−CO binding energies is somewhat different. All of these methods proceed by running constrained computations on metal carbonyls and analyzing the changes in ΔE_{bind} as various constraints are removed. CSOV studies of a variety of metal carbonyls by Bagus, Bauschlicher, *et al.*[18, 19, 33] indicated that π-donation and metal orbital polarization each contributed to binding energies more significantly than σ-donation in most cases, though they found σ- and π-donation to be on the same order in $Fe(CO)_6$.[31] Other results have indicated that σ-electrons contribute the lion's share of the bonding energy between an Fe cluster and CO.[45] Similarly, a series of Morokuma EDA[285, 286] studies of

$Cr(CO)_6$ indicated electrostatics drive bonding through penetration of CO 5σ-electrons into the Cr valence space, though orbital polarization and π-donation were also found to be important.[229, 95] Another EDA study found that complex charge (paradoxically) promotes bond covalency, that σ-donation dominates cations, and that the importance of π-donation increases as a species becomes more anionic.[100] This is in contrast with previous results that suggested certain cationic metal carbonyls are bound by electrostatics.[30, 276, 27, 411]

While the preceding literature survey has focused on molecular metal carbonyls, a brief discussion of current models of the interaction between extended metal systems and CO helps to situate this work within a broader context. Much as the DCD model serves as a paradigm for molecular metal carbonyls, the Blyholder model[44, 43] provides the basis for understanding the metal-carbonyl interaction in extended systems. This model is similar to the DCD model in content, explaining the M−CO bond in terms of charge transfer, although only π-donation was considered in its original formulations. Subsequent studies have expanded upon and refined the Blyholder model, indicating that orbital polarization, σ-donation, and π-donation all seem to play important roles in the formation of M−CO bonds and shifts in υ_{CO}.[294, 314, 129] Suffice it to say, similar interactions promote the formation of M−CO bonds whether the metal in question is a single atom or an extended surface; in both system classes, the relative importance of these interactions is contested.

Taken together, the extant computational literature indicates that electrostatics, orbital polarization, σ-donation, and π-donation can all contribute significantly to binding in metal carbonyls, although the interplay between these features is subtle, depending on the system of interest and the computational methods employed. Most of this literature focuses on understanding contributions to electronic binding energies of these complexes. Still, the properties of the C−O bond are frequently discussed as well, and these are typically inferred on the basis of the ΔE_{bind} decomposition. If a given component of the physics is the major contribution to ΔE_{bind}, it is assumed to also drive shifts in υ_{CO}. Such an analysis is problematic because C−O bond properties do not correlate well with ΔE_{bind}. In particular the magnitude of υ_{CO} has been shown to vary independently of that of ΔE_{bind}.[119, 386, 403] Only a few direct investigations into the sources of C−O properties in metal carbonyls have been completed.[141, 260, 21] The largest two of these focused on cationic systems, indicating that electrostatic and polarization effects, rather than σ-donation as suggested by the DCD model, drive blue shifts in υ_{CO}.[141, 260] Beyond these, a comprehensive and direct investigation into the properties of the C−O bond in metal carbonyls is absent from the literature.

3.0.3 Scope of the Current Study

Our primary purpose is to provide a coherent model of υ_{CO} shifts in molecular metal carbonyls. This is a vast topic, and we choose to limit the scope of our investigation to metal monocarbonyls (MCOs). Relative to polycarbonyls, which have also been the subject of much research, MCOs carry two major advantages for our purposes: (1) these systems better approximate the metal surface–CO interaction relevant to heterogeneous catalysis[44, 18,

33, 144] and (2) the smaller size of MCOs admits the use of more sophisticated electronic structure methods.

Still, even limited to three-atom MCO systems, computational modeling of transition metal chemistry proves formidable with density functional theory (DFT).[85] It was therefore important to select MCO systems expected to possess relatively straightforward electronic structure. Furthermore, because the effects of overall charge bear significantly on vibrational frequency shifts in these systems,[441] we consider isoelectronic series of anionic, neutral, and cationic complexes. With these two concerns in mind we have modeled the MCO complexes of all first-row atoms and ions that are expected to have a low-lying configuration with either a half- or completely-filled 3*d*-shell. This includes the neutral complexes of V, Cr, Mn, Ni, Cu, and Zn, as well as the singly ionized systems that are isoelectronic to them. We did not consider $GaCO^+$ even though it is isoelectronic with $CuCO^-$ and ZnCO, as Ga is not a transition metal.

We analyze the properties of the C−O bond in these systems using the adiabatic EDA approach of Head-Gordon and coworkers,[266, 267] discussed in more detail in Section 3.1.2 below. This EDA scheme differs from the Morokuma[285, 286] methods discussed above in that it is fully variational, allowing for geometry optimizations and harmonic vibrational frequency computations at each stage in the decomposition. The CSOV method,[18] allows for variational decomposition of fragment polarization and charge transfer, but can exhibit non-additivity and can require multiple iterations to approach a self-consistent result.[33] As demonstrated by Bagus and Pacchioni for CO adsorbed to Au clusters, the CSOV method can be used to decompose $\Delta\upsilon_{CO}$ directly,[21] though most previous uses of EDA schemes, including CSOV, did not analyze the properties of CO in these complexes.[33, 45, 100, 19, 18, 31, 229, 30] In the case of Ref. 21, υ_{CO} was analyzed by fixing the M−CO distance before constructing potential energy curves as a function of r_{CO} that could be used to approximate υ_{CO}, leading to discrepancies between their decomposition analysis and the frequency shift they determined through unconstrained computations. In contrast to these methods, we are able to determine normal modes for MCOs through diagonalization of the full Hessian matrix at each stage in our decomposition. This leads to a more physically meaningful and direct analysis of $\Delta\upsilon_{CO}$ in the systems of interest.

The remainder of this manuscript is organized as follows. In Section 3.1 we describe in more detail our computational procedures and EDA scheme. We then provide validation for our DFT treatment of the systems of interest through comparison to coupled-cluster computations and experimental results (Section 3.2). Having demonstrated the fidelity of our DFT results for these systems, we report EDA results that provide a general model for the physical content of binding energies and frequency shifts in MCO cations, anions, and neutrals in Sections 3.3.2-3.3.4. Finally, we consider some anomalous results (Section 3.4) and conclude with a presentation of a general model for carbonyl binding that includes these outlying systems.

3.1 Computational methods

The metal carbonyl (MCO) species of interest were computationally studied using both correlated wave function and density functional theory (DFT) approaches. Geometric parameters and harmonic vibrational frequencies were evaluated using the def2-TZVPD basis set,[417, 336] while the larger def2-QZVPD basis[420, 336] was employed for single-point energy (SPE) computations at the def2-TZVPD geometries. Harmonic vibrational frequencies were determined through diagonalization of the full Hessian matrix, and optimized structures were confirmed to be local minima by the absence of imaginary frequencies. Self-consistent field (SCF) iterations were converged to a DIIS error of at most 10^{-8} Hartree, with tighter convergences of 10^{-10} Hartree being achieved in most cases. Solutions to the Hartree–Fock and Kohn–Sham equations were confirmed to be stable with respect to occupied–virtual mixing. All computations were performed using Q-Chem 5.0.[361]

Electron correlation was incorporated into our computational treatments using both wave function and DFT approaches. In the former case, unrestricted Hartree-Fock reference wave functions were correlated using coupled-cluster theory with single, double, and perturbative triple excitations [CCSD(T)].[333] Coupled-cluster iterations were taken to be converged when the changes in energy passed below 10^{-8} Hartree and those in the magnitude of the T-amplitudes below 10^{-6}. Unrestricted DFT computations were completed using the ωB97X-V exchange-correlation functional, a combinatorially optimized, range-separated hybrid generalized gradient approximation (GGA) developed by Mardirossian and Head-Gordon.[270] This functional is particularly suitable for the present study because it has been shown to outperform other hybrid GGAs in modeling both transition metal and main-group chemistry[377, 140, 101, 68, 147]. A large (99, 590) integration grid was used in the quadrature for the exchange-correlation potential to ensure the quality of the results.

3.1.1 Dipole moments

The dipole moment ($\vec{\mu}$) of isolated CO was determined as a function of its bond length to assist in the interpretation of the EDA results. The ωB97X-V/def2-TZVPD dipole moments were evaluated using linear response theory as implemented in the Q-Chem package.[361] This particular density functional was previously shown to predict dipole moments with high fidelity across a wide range of main group chemical systems.[148] In the present work we further validate the CO dipole moment from ωB97X-V against that obtained using CCSD(T). Because analytic gradients of the energy with respect to orbital rotations were not available for this theory, CCSD(T) dipole moments were obtained using a two-point central finite differences approach to approximate

$$\vec{\mu} = \frac{dE}{d\vec{F}}, \tag{3.1}$$

where E is the CCSD(T) internal energy, and $\vec{F}$ is an external electric field. Field strengths of $\vec{F} = \pm 1 \times 10^{-4}$ a.u. were used in this analysis, following previous work.[148]

3.1.2 Energy decomposition analysis

The adiabatic absolutely localized molecular orbital energy decomposition analysis (ALMO-EDA) of Mao, Horn, and Head-Gordon[266, 267] was used to parse bond lengths, binding energies, and harmonic vibrational frequencies of MCO complexes into contributions from permanent electrostatics, orbital polarization, and charge transfer. While those interested in the details of these terms and their computational implementation should consult the relevant references, a brief overview of the physical content of these terms is helpful at present.

The influence of frozen orbital interactions (permanent electrostatics, Pauli repulsion, and dispersion) on the binding of two molecular or atomic fragments is determined by performing a geometry optimization of the overall complex subject to the constraint that the individual fragment orbitals are determined in isolation and not allowed to relax. The potential energy surface (PES) defined by these constraints is referred to as the frozen (FRZ) surface, and the FRZ contribution to the binding energy (ΔE^{FRZ}) is obtained as the difference between the optimal energy on FRZ surface (E^{FRZ}) and the energy of the isolated fragments, *viz.*

$$\Delta E^{\mathrm{FRZ}} = E^{\mathrm{FRZ}} - \sum_A E_A, \tag{3.2}$$

where E_A is the isolated energy of fragment A. Note that this definition means stable complexes will have negative binding energies. FRZ contributions to single-fragment observables like bond lengths and harmonic frequencies are evaluated similarly:

$$\Delta\Omega^{\mathrm{FRZ}} = \Omega^{\mathrm{FRZ}} - \Omega_0. \tag{3.3}$$

Here, Ω^{FRZ} and Ω_0 are the values of the observable on the FRZ and isolated surfaces, and $\Delta\Omega^{\mathrm{FRZ}}$ is the FRZ contribution to the value of the observable.

The effects of polarization (POL) are incorporated by allowing each individual fragment's orbitals to relax in the presence of the other fragment, although mixing between two orbitals on different fragments is forbidden. This amounts to optimizing the supersystem energy by varying the coefficients of the AO-to-MO matrix subject to the constraint that this matrix is fragment-block-diagonal. The POL contribution to an observable ($\Delta\Omega^{\mathrm{POL}}$) is then obtained as

$$\Delta\Omega^{\mathrm{POL}} = \Omega^{\mathrm{POL}} - \Omega^{\mathrm{FRZ}}, \tag{3.4}$$

where Ω^{POL} is the value of the observable on the POL surface.

Finally, the effects of charge transfer (CT) are obtained as the difference between the structure and properties obtained on the unconstrained PES and those of the POL surface. The CT contribution to an observable of interest ($\Delta\Omega^{\mathrm{CT}}$) is obtained from Ω^{POL} and the value of the observable for the minimum energy structure on the unconstrained surface (Ω^{FULL}) using

$$\Delta\Omega^{\mathrm{CT}} = \Omega^{\mathrm{FULL}} - \Omega^{\mathrm{POL}}. \tag{3.5}$$

In the complete basis set limit, the distinction between POL and CT becomes blurred, so it is important to consider the effects of basis set superposition error (BSSE) between the fragments. Previous studies using ALMO-EDA have indicated that this effect is minimal up through augmented triple-ζ bases.[173, 267] All EDA computations in the present work employ the def2-TZVPD basis, so we assume the BSSE will not be significant on the basis of these previous results.

As defined in the adiabatic EDA scheme, CT is not divided into independent contributions from forward- and back-donation, unlike other EDA schemes. Due to the controversy surrounding the relative importance of these contributions in MCOs, we further analyzed our results by obtaining complementary occupied-virtual pairs (COVPs) of fragment orbitals, following the work of Khaliullin *et al.*[205, 206] These computations used the (vertical) ALMO-EDA scheme of Head-Gordon and coworkers,[207, 205, 206, 174] which is similar to the adiabatic scheme outlined above, except that the FRZ and POL results are obtained through single point computations using the geometry as optimized on the unconstrained surface. These COVPs represent the most energetically significant CT interactions in the complex. As indicated above, analysis of molecular properties on the basis of the decomposition of energies, as occurs in COVP, is inherently indirect and our analysis of the specific influences of forward- and backward-donation on the basis of COVP results should therefore be treated with caution relative to the adiabatic EDA results that probe geometries and frequencies directly.

In our application of the adiabatic EDA framework, we define the MCO complexes as a supersystem of a metal atom/ion and a neutral, singlet CO molecule. A number of relatively low-energy spin states can be realized for many of the metals of present interest. In this study, spin states were determined on the basis of their computed harmonic CO vibrational frequency (ω_{CO}) and its agreement with experimental values. In most cases this also corresponded to the energetic minimum among the set of possible spin states for a given MCO complex. The few exceptions are noted as they are discussed at length below.

3.2 Validation of density functional theory

In this work we use energy decomposition analysis (EDA) to provide quantitative and qualitative insights into the physical content of vibrational Stark effects in MCO complexes. The FRZ, POL, and CT contributions (defined above) to bonding in these systems are not physically observable, and so they cannot be compared to experimental results. Furthermore, while a variety of EDA schemes have been developed for DFT and partially correlated wave function theories,[396] EDA for highly correlated, more trustworthy wave function methods like coupled-cluster theory has yet to be realized. Hence, the ωB97X-V structures and properties obtained on the FRZ and POL surfaces cannot be directly validated either by comparison to experiment or to higher-level, systematic theories. Instead, we evaluate the performance of the ωB97X-V functional through its treatment of MCO complexes on unconstrained PESs, as this is a necessary condition for the validity of the remaining results from

the EDA. Specifically, we compare ωB97X-V binding energies, bond lengths, and harmonic frequency shifts against those obtained using CCSD(T). We further confirm the quality of our DFT treatment through comparison to experimental frequency shifts. Data used in these comparisons can be found in Table 3.1.

The ωB97X-V predictions for compound geometries exhibit high fidelity to CCSD(T) results we have obtained. For isolated CO, the ωB97X-V/def2-TZVPD equilibrium bond length is 1.126 Å, in good agreement with both our CCSD(T) result (1.133 Å) and the experimental value of 1.128 Å.[132] For MCO complexes, better agreement is obtained in predictions for the C−O bond lengths ($r_{\mathrm{C-O}}$) than those for the M−C bonds ($r_{\mathrm{M-C}}$) in both absolute and relative terms, though the agreement for both parameters is excellent. The mean absolute errors for the ωB97X-V $r_{\mathrm{M-C}}$ and $r_{\mathrm{C-O}}$ values, relative to those for CCSD(T), are 0.020(18) Å and 0.006(5) Å, respectively, where uncertainties are standard deviations. These correspond to relative errors of 1 % for M−C bonds and 0.5 % for C−O bonds. Both theories yield linear geometries for most complexes in this study, though CrCO, $CrCO^-$, and CuCO are all predicted to be bent. We discuss MCO bending at length in Section 3.4.0.3 below; here we simply note that ωB97X-V overbends complexes by 2.6–6.2° relative to CCSD(T) for the few bent complexes in this study.

Comparisons between the ωB97X-V and CCSD(T) binding energies found in Table 3.1 were obtained through single-point computations using the def2-QZVPD basis set and include corrections to account for vibrational zero-point energies (VZPE), unless otherwise indicated; additional binding energies with the def2-TZVPD basis and without the VZPE correction can be found in Table 3.2. For about half of the compounds studied herein, chemical accuracy (agreement within 1 kcal mol^{-1}) between CCSD(T) and ωB97X-V was achieved, while for $CrCO^-$, $FeCO^+$, $CuCO^-$, and ZnCO discrepancies of about 1–4 kcal mol^{-1} were obtained. In certain cases the disagreement is egregious: the isoelectronic $CrCO^+$ and $TiCO^-$ systems exhibit errors of 40 and 50 kcal mol^{-1}, respectively, with ωB97X-V underbinding the complexes relative to CCSD(T). Absent experimental values for these binding energies, we cannot say with certainty which (if either) value is likely to be correct, although the ωB97X-V energies are closer to the absolute values obtained for the isoelectronic VCO complex, as well as most other MCOs in this study. The errors for the remaining compounds—MnCO, $CoCO^-$, NiCO, and $NiCO^-$—range from 9–12 kcal mol^{-1}. Where they exist, discrepancies between energies obtained with these two theories are not systematic: depending on the identity of the metal atom, ωB97X-V may either overbind or underbind the MCO complex relative to CCSD(T).

Shifts in the ω_{CO} upon complex formation ($\Delta\omega_{\mathrm{CO}}$), evaluated using ωB97X-V and CCSD(T), are also compared to experimental CO frequency shifts in Table 3.1. Our frequency anaylsis yields normal modes that, in general, depend on the coordinates of all three atoms in the MCO complex. By ω_{CO}, then, we mean the frequency of the high-energy vibrational mode, which consists almost entirely of a stretching of the C−O bond, even if M moves slightly as well; we will not worry about this distinction in the remainder of the manuscript. Computed vibrational frequencies were not corrected for anharmonicity in the CO bond, rendering comparison of absolute frequencies to experimental results inappropriate. Instead, we com-

Table 3.1: Computational and experimental data for MCO complexes of specified multiplicity (M), organized into isoelectronic series. Geometric parameters and harmonic vibrational frequencies were computed using the indicated method with the def2–TZVPD basis set. Unless noted otherwise, binding energies were determined using def2–QZVPD single-point computations on these geometries and include corrections for vibrational zero-point energies. Binding energies are calculated according to Eq. 3.2, such that a negative value indicates a stable complex, unlike some other conventions. Harmonic frequency shifts are reported relative to isolated CO, and experimental values were obtained from species in Ne matrices and obtained from values in Ref. 441, unless noted otherwise

Species	M	M−C Length (Å)		C−O Length (Å)		Binding Energy (kcal mol^{-1})		CO Frequency Shift (cm^{-1})		
		CCSD(T)	ωB97X-V	CCSD(T)	ωB97X-V	CCSD(T)	ωB97X-V	CCSD(T)	ωB97X-V	Expt
$TiCO^-$	4	2.020	1.997	1.175	1.175	-80.51	-29.20	-319.2	-388.4	-350.9
VCO	6	1.992	1.996	1.150	1.144	-17.18	-17.58	-169.6	-197.6	-210.2
$CrCO^+$	6	2.169	2.165	1.123	1.117	-60.68	-21.51	77.7	77.0	60.0
VCO^-	5	1.955	1.944	1.172	1.172	-19.20	-19.22	-304.3	-376.7	-334.1
CrCO	7	2.179	2.189	1.137	1.134	-2.31	-2.49	-87.6	-119.4	-122.4
$MnCO^+$	7	2.575	2.556	1.123	1.115	-9.78[a]	-9.68[a]	80.5	97.5	7.2[b]
$CrCO^-$	6	2.155	2.168	1.165	1.171	0.93	-1.70	-461.3	-447.7	-462.8
MnCO	6	2.004	2.008	1.163	1.151	23.87[a]	12.59[a]	-211.1	-195.1	-185.8
$FeCO^+$	4	1.876	1.934	1.130	1.120	-36.08	-33.58	-0.6	45.0	-17.8
$CoCO^-$	3	1.709	1.707	1.195	1.174	-5.49	-17.29	-325.8	-336.0	-320.6
NiCO	1	1.649	1.680	1.157	1.146	-39.52	-30.58	-138.6	-115.3	-134.2
$CuCO^+$	1	1.928	1.923	1.121	1.114	-33.16	-33.17	102.8	114.3	93.6
$NiCO^-$	2	1.718	1.670	1.170	1.169	-27.20	-19.61	-366.5	-260.0	-280.2
CuCO	2	1.910	1.963	1.138	1.134	-6.27	-5.44	-86.9	-124.2	-111.1
$ZnCO^+$	2	2.316	2.330	1.121	1.114	-15.50	-14.90	96.7	113.4	–
$CuCO^-$	3	1.837	1.865	1.181	1.182	11.76	8.71	-377.4	-399.1	-394.6
ZnCO	3	1.955	1.947	1.165	1.162	56.34	54.49	-253.8	-261.5	-288.6[c]

[a] Binding energy single points computed using the def2–TZVPD basis set

[b] Frequency obtained from Ar_3MnCO. Matrix-perturbation was estimated to depress this value by 68.6 cm^{-1}, suggesting a gas-phase value of 7.2 cm^{-1}. See Ref. 341 and discussion in text.

[c] Ref. 187

Table 3.2: Electronic, vibrational zero point, and binding energies for first-row transition metal monocarbonyls. Geometries and vibrational frequencies were determined using the def2-TZVPD basis set, and complex single-point energies using bases indicated in the table. Energies in kcal/mol.

Species	CCSD(T)					ωB97X-V				
	TZVPD			QZVPD		TZVPD			QZVPD	
	D_e	VZPE	D_0	D_e	D_0	D_e	VZPE	D_0	D_e	D_0
CO	–	6.17	–	–	–	–	6.40	–	–	–
$TiCO^-$	-60.82	7.83	-59.16	-82.17	-80.51	-32.05	7.44	-31.01	-30.24	-29.20
VCO	-18.09	7.66	-16.59	-18.68	-17.18	-19.26	7.73	-17.94	-18.90	-17.58
$CrCO^+$	-22.14	7.84	-20.47	-62.35	-60.68	-23.27	8.12	-21.55	-23.23	-21.51
VCO^-	-22.42	7.34	-21.25	-20.37	-19.20	-22.51	7.56	-21.35	-20.38	-19.22
CrCO	-2.83	6.89	-2.10	-3.03	-2.31	-3.19	7.09	-2.51	-3.18	-2.49
$MnCO^+$	-11.35	7.74	-9.78	-11.52	-9.95	-11.27	7.99	-9.68	-10.96	-9.38
$CrCO^-$	-0.21	6.09	-0.29	1.01	0.93	-2.77	6.42	-2.74	-1.72	-1.70
MnCO	22.12	7.92	23.87	18.83	18.75	10.78	8.21	12.59	11.04	12.85
$FeCO^+$	-36.02	8.15	-34.04	-38.05	-36.08	-35.94	8.43	-33.92	-35.61	-33.58
$CoCO^-$	-5.96	7.54	-4.8	-6.86	-5.49	-22.20	7.88	-20.72	-18.77	-17.29
NiCO	-38.09	8.71	-35.55	-42.06	-39.52	-33.53	8.76	-31.17	-32.94	-30.58
$CuCO^+$	-32.10	8.14	-30.12	-35.14	-33.16	-35.25	8.52	-33.14	-35.29	-33.17
$NiCO^-$	-19.35	6.87	-18.65	-27.90	-27.20	-25.02	8.21	-23.21	-21.42	-19.61
CuCO	-6.64	7.37	-5.44	-7.47	-6.27	-6.27	7.42	-5.25	-6.46	-5.44
$ZnCO^+$	-16.24	7.97	-14.42	-17.32	-15.50	-16.90	8.22	-15.08	-16.72	-14.90
$^1CuCO^-$	-1.75	6.41	-1.51	-1.43	-1.19	-1.98	6.69	-1.69	-1.30	-1.01
$^3CuCO^-$	9.43	6.79	10.05	11.14	11.76	6.24	7.03	6.87	8.08	8.71
^1ZnCO	-0.34	6.27	-0.24	-0.43	-0.34	-0.21	6.41	-0.20	-0.18	-0.18
^3ZnCO	54.05	7.97	55.85	54.53	56.34	52.93	8.24	54.77	52.65	54.49

pare shifts in the CO frequency upon binding to metal atoms under the assumption that anharmonic effects in free and bound CO are similar. Experimental shifts were determined as

$$\Delta\upsilon_{CO} = \upsilon_{CO}^{bound} - \upsilon_{CO}^{free} \tag{3.6}$$

using a value of $\upsilon_{CO}^{free} = 2140.8\,cm^{-1}$ obtained in a Ne matrix by Liang and Andrews.[251] Unless noted otherwise in Table 3.1, values of υ_{CO}^{bound} for MCO complexes were obtained from experiments performed in Ne matrices. Experimentally, these matrices depress υ_{CO} in metal carbonyls by 5–15 cm^{-1}.[441] This perturbation is relatively small, and we expect these absolute matrix effects to approximately cancel in determining $\Delta\upsilon_{CO}$ through Eq. 3.6. Small errors in this approximation should not affect our results significantly, since we are concerned with overarching trends in MCOs.

Without including corrections for anharmonicity or matrix effects, ωB97X-V values of ω_{CO} have a mean absolute error of $21.4(147)\,cm^{-1}$ with respect to experimental shifts, marginally better than the $24.0(201)\,cm^{-1}$ discrepancy between CCSD(T) and experiment.

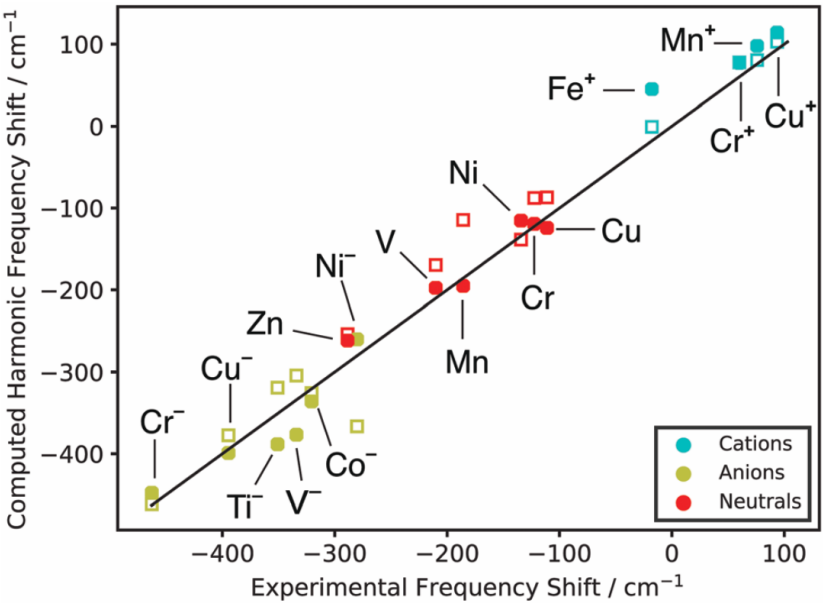

Figure 3.2: Comparison of experimental and computational CO frequency shifts in MCO complexes of different charge. ωB97X-V (solid circles) performs well against CCSD(T) (open squares) and experimental frequency shifts (solid line) for species of different charge. Computations performed using the def2-TZVPD basis set. The experimental value for $MnCO^+$ has been corrected for matrix effects following Ref. 341.

The CCSD(T) and ωB97X-V frequency shifts agree with each other within 31.2(271) cm^{-1}. These results are visualized in Figure 3.2. There is a slight tendency for our computed frequencies to blue-shift relative to experiment, exhibited by mean signed errors of 6.1 and 8.9 cm^{-1} in the ωB97X-V and CCSD(T) frequency shifts, respectively. *Prima facie*, the most egregious errors between our computations and experiment are for $MnCO^+$ and $FeCO^+$, and these are discussed at length in Section 3.4 below.

While CCSD(T) is the *bona fide* gold standard for modeling the electronic structure of single reference systems, it is known to break down in systems that exhibit significant multireference character and/or strong correlation.[344, 189, 56] Results from at least one study suggest that transition metal carbonyls are well-treated with single reference methods,[189] lending credence to our computational methodologies. Still, the potential for these difficulties means that we are not completely guaranteed of the trustworthiness of our DFT results, even in the systems where excellent agreement with CCSD(T) was obtained. For the same reason, however, discrepancies between ωB97X-V and CCSD(T) need not necessarily be taken as a failure of the density functional. Indeed, due to the well-known difficulties in determining the electronic structure of transition metals, any individual computation on

these systems should be treated with caution, even when state-of-the-art methods are used. The bulk of our analysis of MCO compounds does not pivot on any single result but is derived from a number of results for similar species. We submit, therefore, that the overall agreement between our computational methods and available experimental results lends credence to our DFT treatment on the whole, even if any individual result may be erroneous. Hence, we proceed with optimistic caution in analyzing the bonding in MCO systems using EDA results from the ωB97X-V density functional.

3.3 Bonding in MCO complexes

After briefly analyzing the computed dipolar properties of free CO, we establish a general model for MCO binding by first considering the most straightforward cationic, anionic, and neutral systems, treating more complicated systems later. Specifically, the "normal" systems are taken to be those where a metal binds CO in a linear fashion on a PES containing the asymptote of its electronic ground state. The remaining systems, which either exhibit a non-linear geometry or bind CO through an excited electronic state on the metal, are incorporated into our general model of MCO binding in Section 3.4 below.

3.3.1 Isolated carbon monoxide

Modeling isolated CO is a straightforward but necessary precursor to analyzing physical and chemical features of MCO binding. The equilibrium electric dipole moment ($\vec{\mu}_e$) of CO is particularly important for analyzing the interactions between the M and CO fragments on the FRZ and POL surfaces. At equilibrium, ωB97X-V predicts a CO dipole moment of 0.0884 D oriented toward the O atom (with negative charge on C), in qualitative agreement with the experimental value of $\vec{\mu}_e = 0.1222$ D.[288]. Our CCSD(T)/def2-TZVPD prediction of 0.1288 D enjoys even closer agreement with experiment. The discrepancy between CCSD(T) and ωB97X-V predictions of μ_e is not surprising as theoretical treatments of the CO dipole moment are known to depend sensitively on the amount of electron correlation and the size of the basis set that is employed in the computation.[358]

The dipolar properties of CO near its equilibrium bond length are particularly interesting. On the ωB97X-V PES, the CO dipole moment decreases as the bond is stretched, and a dipole-free structure is obtained with $r_{\mathrm{C-O}} = 1.149$ Å (Figure 3.3). This dipole-free structure is destabilized by less than 1 kcal/mol relative to the energetic minimum. As the CO bond continues to stretch beyond 1.149 Å, the dipole moment increases in magnitude, but with a sign opposite that at equilibrium. Similarly, low-energy compressions of CO from its equilibrium structure increase μ_e. While CCSD(T) predictions of near-equilibrium dipole moments, also shown in Figure 3.3, give a zero-dipole structure with a slightly higher relative energy of 2 kcal/mol, and a markedly higher zero-dipole bond length of 1.173 Å, the qualitative features of stretching and compression are the same. These trends confirm earlier studies of the CO electric dipole moment function determined from experimental vibrational

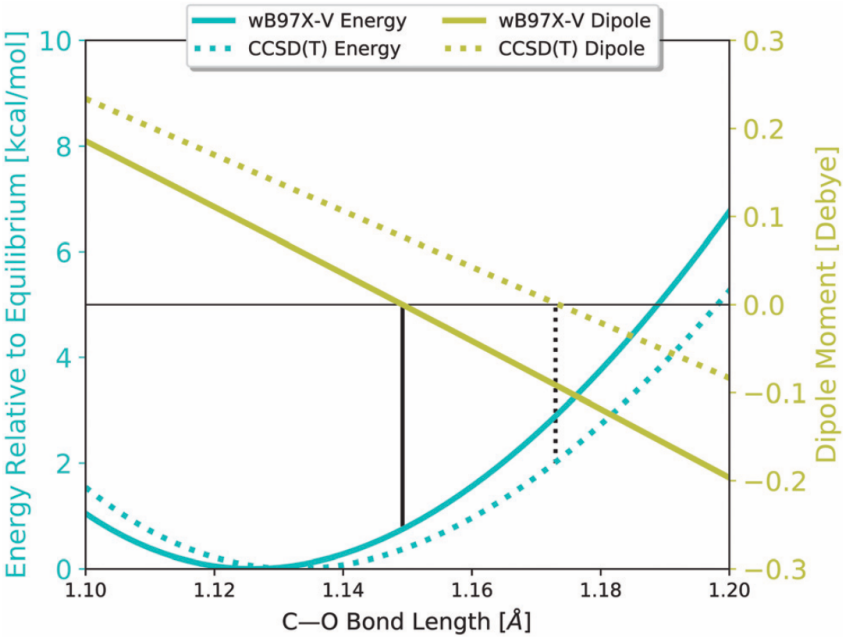

Figure 3.3: Binding energy of isolated CO relative to that at the equilibrium bond length, plotted with the absolute dipole moment of CO, both as a function of distance. Results using ωB97X-V/def2-TZVPD (solid) and CCSD(T)/def2-TZVPD (dashed) are compared. The dipole moment vector is oriented from O to C, such that a positive dipole moment corresponds to the localization of negative charge on the carbon atom. Vertical black lines indicate bond lengths where CO exhibits no permanent electric dipole. Energies, dipole moments, and bond lengths are in units of kcal/mol, debye, and angstom, respectively.

frequencies,[65] and are consistent with the moderately large electric polarizability that has been computed for CO.[76]

Thus, computation and experiment provide a similar picture of CO: stretching and compressing the C−O bond on small length scales causes only minor increases in the electronic energy of the system, accompanied by noticeable changes in μ_e. Intriguingly, small, low-energy perturbations to the C−O bond length can change the magnitude—indeed, the sign—of the molecular dipole moment. These features of the electronic structure of CO provide critical insight into the bonding of MCO systems.

3.3.2 Anionic complexes (M = Ti^-, V^-, Cr^-, Co^-, Ni^-, Cu^-)

Relative to neutral and cationic species, theoretical treatments of MCO anions are relatively sparse in the literature. In decompositions of both ΔE_{bind} and $\Delta\omega_{\text{CO}}$, binding in various

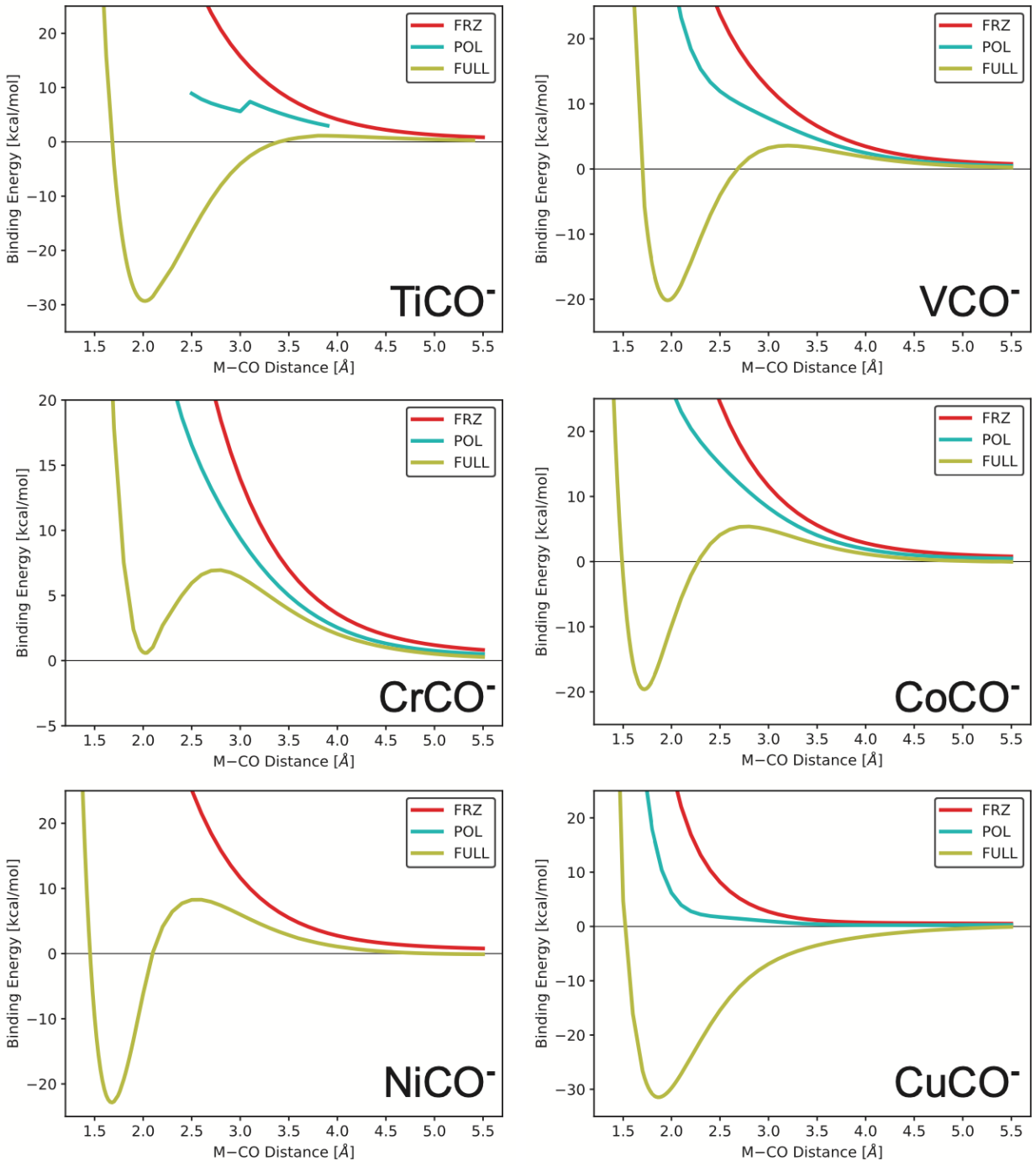

Figure 3.4: Frozen, polarized, and unconstrained potential energy surfaces for MCO anions considered in this study. The energetic zero is defined as the energy of infinitely separated M^- and CO fragments. Missing data for the POL surfaces of $TiCO^-$ and $NiCO^-$ are due to SCF convergence errors.

Table 3.3: Geometric parameters for selected transition metal monocarbonyls of multiplicity M on different adiabatic EDA surfaces. Values obtained using the ωB97X-V density functional with the def2–TZVPD basis set; this theory predicts the bond length of isolated CO to be 1.126 Å. Missing entries indicate a lack of a bound structure on a given surface.

Species	M	M−C Length (Å)			C−O Length (Å)			MCO Angle (Degree)		
		FRZ	POL	FULL	FRZ	POL	FULL	FRZ	POL	FULL
$TiCO^-$	4	–	–	1.997	–	–	1.175	–	–	180.0
VCO	6	5.582	2.698	1.996	1.126	1.122	1.144	168.2	179.9	179.9
$CrCO^+$	6	2.751	2.362	2.165	1.117	1.114	1.117	180.0	180.0	180.0
VCO^-	5	–	–	1.944	–	–	1.144	–	–	180.0
CrCO	7	5.807	5.373	2.189	1.126	1.126	1.134	180.0	152.0	152.7
$MnCO^+$	7	3.594	2.704	2.556	1.120	1.116	1.115	179.4	180.0	180.0
$CrCO^-$	6	–	4.959	2.168	–	1.126	1.171	–	85.2	134.1
MnCO	6	–	–	2.008	–	–	1.151	–	–	180.0
$FeCO^+$	4	2.774	2.214	1.934	1.117	1.113	1.120	180.0	179.9	179.8
$CoCO^-$	3	–	–	1.707	–	–	1.174	–	–	179.9
NiCO	1	2.332	1.937	1.680	1.123	1.118	1.146	180.0	179.7	179.9
$CuCO^+$	1	2.390	2.052	1.923	1.114	1.112	1.114	180.0	180.0	180.0
$NiCO^-$	2	–	–	1.670	–	–	1.169	–	–	179.9
CuCO	2	4.535	4.427	1.963	1.26	1.126	1.134	144.7	130.5	145.7
$ZnCO^+$	2	3.297	2.398	2.330	1.119	1.114	1.114	180.0	180.0	180.0
$CuCO^-$	3	–	4.562	1.865	–	1.127	1.182	–	99.6	180.0
ZnCO	3	3.287	2.456	1.946	1.124	1.120	1.162	180.0	180.0	180.0

MCO^- systems is along the lines of the DCD model, and so this subset of systems forms a natural starting point for our discussion of metal–carbonyl bonding.

Our computational results indicate that the physical components of the FRZ term (electrostatics, Pauli repulsion, and dispersion) are insufficient to bind anionic MCOs, indicated by the lack of stable bound structures on the FRZ surface. In order to confirm the repulsion between the M^- and CO fragments, we computed rigid-CO dissociation curves for these systems. We present the FRZ surface for each of these, displayed as the red curves in Figure 3.4, as an example of this. These results indicate that the (M^-)−CO interaction is everywhere repulsive on the FRZ surface. Pauli forces are exclusively destabilizing, and dispersion and electrostatics are insufficient to bind anionic MCOs.

Given the previous result that C−O stretching eventually reverses the sign of its dipole moment (Figure 3.3), it is interesting to consider whether MCO anions with sufficiently long C−O bonds are bound on their FRZ surfaces. While results for all MCO anions mentioned above are not included, this possibility is explored for VCO^-. As seen in Figure 3.5, C−O stretching does result in marginal decreases in fragment repulsion, as expected, but this is insufficient for a bound structure on the FRZ surface to be realized, even when perturbations

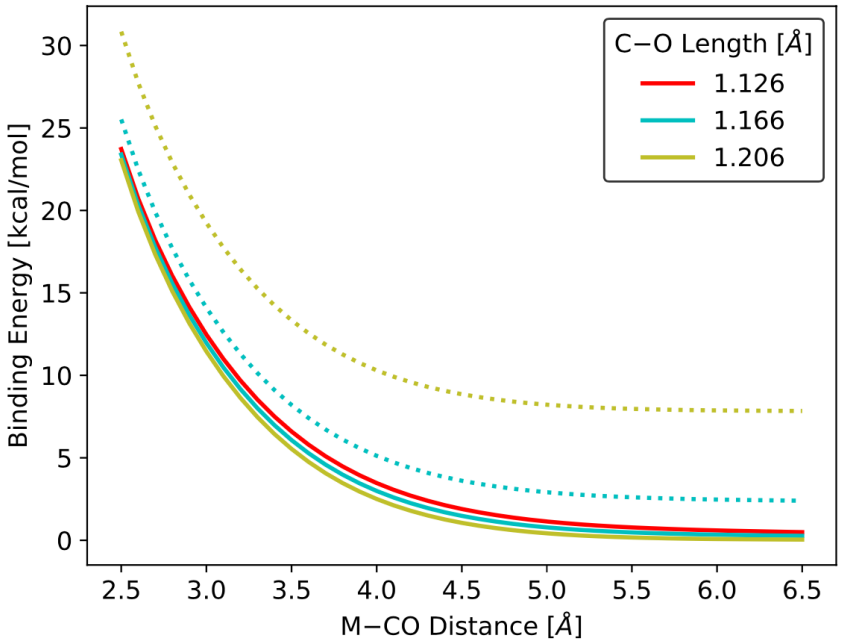

Figure 3.5: Potential energy surfaces for VCO^- dissociation at different values of r_{C-O}. All dissociations are rigid in the C−O bond length. The energetic zero for solid lines is defined as infinitely separated V^- and Co fragments, where the isolated fragment value for r_{C-O} is given by the colors in the legend. Dashed lines are rescaled such that the energetic zero corresponds to infinitely separated V^- and CO with $r_{C-O} = 1.126\,\text{Å}$.

to the C−O bond were significant ($\Delta r \approx 0.08\,\text{Å}$, which corresponds to $\Delta E \approx 10\,\text{kcal mol}^{-1}$ for isolated CO). We rationalize this lack of binding on the basis of both Pauli repulsion between the fragments and the distortion energy that accompanies CO stretching. The $3d$- and (if occupied) $4s$-orbitals of metal anions are relatively diffuse and therefore hinder a close approach be- tween the two fragments, overpowering the small but stabilizing charge-dipole interaction between the metal anion and stretched CO. Continued stretching of CO is not expected to overme this Pauli repulsion, as linear increases in the CO dipole moment correspond to quadratic increases in the CO fragment energy, rendering the energetic costs of increasing the dipole insurmountable. Hence, metal anions are unable to bind CO through the physical interactions included in the FRZ term of our EDA, in spite of the dipolar properties of CO described in the main text.

When we include POL effects, the picture of MCO^- binding is largely the same. Most of the POL surfaces do not possess local minima, the exceptions being $CrCO^-$ and $CuCO^-$, which form weakly bound van der Waals (vdW) complexes. As both of these systems exhibit exceptional behavior in other respects as well, a full discussion of their binding is deferred to Section 3.4 below. Despite the formation of vdW complexes in two of the six systems,

short range interactions between metal anions and CO are energetically unfavorable on POL surfaces, exemplified by that for $CoCO^-$ in Figure 3.4 and the remaining systems in Figure S1.[†] Rationalization of this behavior follows that provided in the preceding paragraph: the effects of intramolecular orbital relaxation are unable to overcome the energetic penalties of Pauli repulsion.

This leaves on explanation for the formation of anionic MCO complexes: charge transfer. As illustrated for $CoCO^-$ in Figure 3.4 and the remaining anionic systems through the data in Tables 3.3 and 3.4, short-range, bound complexes are observed on the unconstrained PESs for all of the MCO^- species considered herein. In the "normal" cases of $TiCO^-$, VCO^-, $CoCO^-$, and $NiCO^-$, we compute sizable binding energies of -22–$32\,\mathrm{kcal\,mol^{-1}}$. The computed binding energies of $CrCO^-$ and $CuCO^-$ are small by comparison; indeed, $CuCO^-$ is predicted to be metastable with respect to infinitely separated, ground state Cu^- and CO fragments. Again, discussion of these anomalies is found in Section 3.4 below. The importance of CT in MCO anions is further highlighted by the shape of the unconstrained PES in Figure 3.4. As the Co^- and CO fragments approach each other from infinite separation, the interaction is repulsive until $r_{\mathrm{Co-CO}} \lesssim 2.3\,\text{Å}$. This initial repulsion is a feature of most of the other anions in this study as well (see discussion in the ESI[†]). Despite differences in binding energies and PES morphologies, the six anionic MCO complexes of this study are unified by large red shifts in ω_{CO} upon binding. We compute these to be on the order of 300–$500\,\mathrm{cm^{-1}}$, in agreement with experimental results (Table 3.4) as discussed above.

The coupled occupied-valence pair (COVP) analysis[207, 205] provides a first-order estimate to the contributions of forward- and back-donation to the overall energy stabilization due to charge transfer. COVP analysis may also provide insight into the sources of shifts in ω_{CO}, but we advise caution here for the reasons described above. Results from this procedure, presented in Figure 3.6, indicate that the back-donation from the metal anions into unoccupied CO orbitals is the predominant mode of charge transfer for the MCO^- systems we considered, as many have argued previously.[441] Chemical interpretation of this result is routine: negative charge renders the metal anion reluctant to accept additional electron density from CO while enhancing the extent of back donation. Stated differently, the M−CO bond in these systems can be considered a dative covalent bond.

While our results show CT is necessary to bind the MCO anions, the physical interactions included in the FRZ and POL terms are obviously present in the physical systems. In particular, we expect electrostatic and polarization effects to help stabilize the final complexes, as previous EDA results have indicated.[100] But the lack of binding on the FRZ and POL surfaces indicates that electrostatics, dispersion, and polarization do not play a fundamental role in anionic MCO complexes. As such, these systems serve as paradigmatic examples of the DCD model of metal-ligand binding, where electron donation between the ligands dominates both ΔE_{bind} and $\Delta \upsilon_{\mathrm{CO}}$.

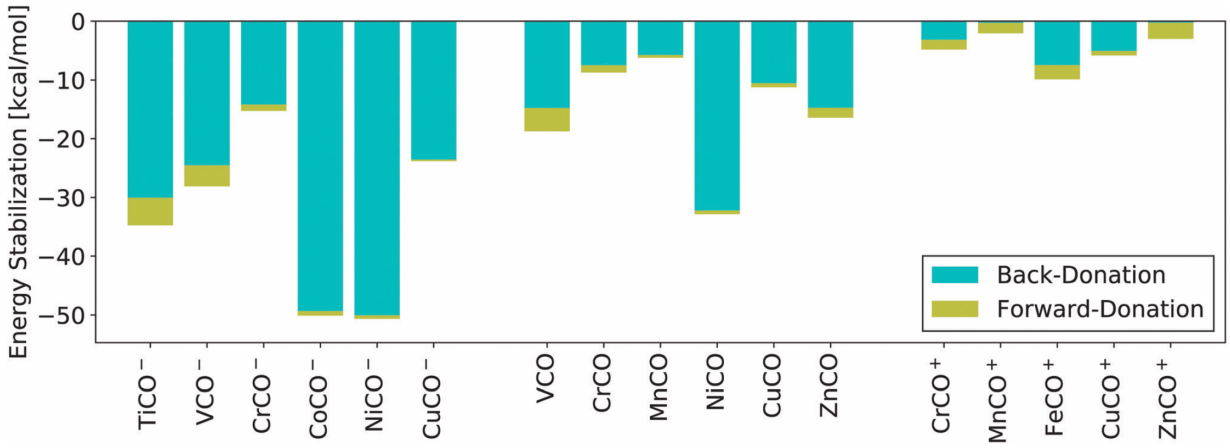

Figure 3.6: Coupled occupied-valence pair (COVP) analysis for selected transition metal monocarbonyls. Energy stabilization due to charge transfer is separated into contributions from forward- (CO → M) and back-donation (M → CO).

3.3.3 Cationic complexes (M = Cr^+, Mn^+, Fe^+, Cu^+, Zn^+)

In contrast to the anionic MCO complexes, where charge transfer effects are responsible for binding, electrostatics and polarization play more important roles for MCO cations. Indeed, among the salient features of the data in Table 3.3 is the formation of closely bound complexes on the FRZ surfaces of all of the MCO^+ species in the scope of this study. This is unsurprising given the electrostatic properties of isolated CO (*vide supra*): a permanent charge–dipole interaction stabilizes the cationic complex relative to the isolated fragments. Furthermore, the effects of Pauli repulsion are expected to be diminished in the cationic systems, where metal 3*d*- and/or 4*s*-orbitals are more compact relative to those in the corresponding anions.

Altogether, the physics included on the FRZ surface results in binding energies of −2–8 kcal mol^{-1}, up to nearly a quarter of the total binding energies for these species. The binding of MCO cations on the FRZ surface is accompanied by moderate compressions in r_{C-O} of 0.006–0.012 Å (Table 3.3) and blue shifts in ω_{CO} of 55–115 cm^{-1} (Table 3.5). These results can be rationalized using Figure 3.3, which demonstrates that compression of CO increases the magnitude of its dipole moment, leading to a stronger electrostatic interaction with the metal cation. This CO compression may also be interpreted as a strengthening of the CO bond with an accompanying increase in ω_{CO}, ranging from 50–115 cm^{-1} in the present systems.

Inclusion of the effects of intraatomic orbital relaxation on the POL surface leads to further compression of the C−O bond and additional blue shifts in ω_{CO}. The effects of POL on the C−O bond are less marked than the effects of FRZ interactions, with additional bond compressions and harmonic frequency shifts of 0.002–0.005 Å and 25–50 cm^{-1}, respectively.

Table 3.4: Adiabatic energy decomposition analysis of binding energies (kcal mol^{-1}) for metal monocarbonyls of a specified spin multiplicity (M). FRZ, POL, and CT values are incremental, as defined in Section 3.1.2 of the text, and computations were performed using the ωB97X-V density functional with the def2–TZVPD basis set. Positive binding energies indicate that a complex is metastable with respect to ground state fragments, and missing entries a lack of a bound structure at a given level of theory

Species	M	δ(FRZ)	δ(POL)	δ(CT)	δ(Total)
$TiCO^-$	4	–	–	-32.05	-32.05
VCO	6	-0.03	-0.36	-18.88	-19.27
$CrCO^+$	6	-5.27	-11.76	-6.24	-23.27
VCO^-	5	–	–	-22.51	-22.51
CrCO	7	-0.04	-0.01	-3.15	-3.20
$MnCO^+$	7	-2.24	-6.19	-2.84	-11.27
$CrCO^-$	6	–	-0.91	-1.85	-2.76
MnCO	6	–	–	–	10.8
$FeCO^+$	4	-4.88	-17.57	-13.49	-35.94
$CoCO^-$	3	–	–	-22.20	-22.20
NiCO	1	33.96	-30.41	-37.09	-33.54
$CuCO^+$	1	-8.27	-20.01	-6.97	-35.25
$NiCO^-$	2	–	–	-25.02	-25.02
CuCO	2	-0.07	-0.02	-6.19	-6.28
$ZnCO^+$	2	-2.95	-9.77	-4.18	-16.90
$CuCO^-$	3	–	40.39	-34.14	6.25
ZnCO	3	87.44	-3.07	-31.44	52.93

These effects can be understood as a continuation of the FRZ surface effects just described, where removing the constraint on orbital relaxation allows for additional flexibility in the geometry of CO. Others have also noted that polarization can effect C−O bond contractions in MCO cations.[386] While the impact of POL on the properties of CO is relatively small, it drives significant changes to the binding energies in MCO^+: indeed, POL makes the dominant contribution to binding in these systems, providing 6–20 kcal mol^{-1} of stabilization, about half of the overall binding energies (Table 3.4). Relaxation of the frozen-orbital constraint also impacts the complex geometries significantly, giving rise to 0.3–0.9 Å decreases in M−C bond lengths (Table 3.3). Taken together, the significant POL effects in the overall MCO^+ complex and the minimal effects on the properties of CO suggest that the bulk of the fragment polarization occurs on the metal cations, which redistribute their $3d$-/$4s$-orbitals to allow for a closer approach between the fragments, resulting in greater energetic stabilization.

Charge transfer effects provide an additional 3–7 kcal mol^{-1} stabilization to the M−CO bond, a contribution of similar magnitude to that from FRZ interactions in most cases. CT also decreases r_{M-C} in cations by a few tenths of an angstrom. In two of the five systems (M

Table 3.5: Adiabatic energy decomposition analysis of harmonic vibrational frequencies (cm^{-1}) for metal monocarbonyls of a specified spin multiplicity (M). FRZ, POL, and CT values are incremental, as defined in Section 3.1.2 of the text, and computations were performed using the ωB97X-V density functional with the def2–TZVPD basis set. Missing entries a lack of a bound structure at a given level of theory

Species	M	δ(FRZ)	δ(POL)	δ(CT)	δ(Total)	Expt.
$TiCO^-$	4	–	–	-388.4	-388.4	-350.9
VCO	6	-0.8	40.3	-237.0	-197.5	-210.2
$CrCO^+$	6	86.9	25.0	-34.9	77.0	60.0
VCO^-	5	–	–	-376.7	-376.7	-334.1
CrCO	7	-0.2	0.0	-119.2	-119.4	-122.4
$MnCO^+$	7	56.0	33.3	8.6	97.9	7.2
$CrCO^-$	6	–	-0.2	-447.6	-447.8	-462.8
MnCO	6	–	–	–	-195.2	-185.8
$FeCO^+$	4	84.5	42.0	-81.5	45.0	-17.8
$CoCO^-$	3	–	–	-336.0	-336.0	-320.6
NiCO	1	31.1	69.6	-216.0	-115.3	-134.2
$CuCO^+$	1	114.6	32.3	-32.6	114.3	93.6
$NiCO^-$	2	–	–	-260.0	-260.0	-280.2
CuCO	2	0.2	-0.3	-124.1	-124.2	-111.1
$ZnCO^+$	2	60.0	50.3	3.0	113.3	–
$CuCO^-$	3	–	-5.6	-393.4	-399.1	-394.6
ZnCO	3	15.6	40.9	-318.0	-261.5	-288.6

= Mn^+ and Zn^+), CT gives rise to incremental blue shifts in ω_{CO}. However, in the remaining three cations (M = Cr^+, Fe^+, and Cu^+), we compute that CT actually leads to 30–80 cm^{-1} incremental *red shifts* in ω_{CO}. While they do not report directly on $\Delta\omega_{CO}$, the COVP results for cations in Figure 3.6 indicate that these three systems exhibit greater back-donation than both $MnCO^+$ and $ZnCO^+$, where the CT effect on ω_{CO} is negligible.

Our results for the decomposition of $\Delta\omega_{CO}$ in cationic MCOs provide direct contradiction to the standard application of the DCD model for these systems. As noted above, this framework attributes MCO blue shifts to CT, specifically a decreased occupation of the 5σ-orbital on CO. Previous results have already indicated that these blue shifts were not due to CT as argued in the DCD model.[141, 260] Our data not only confirm that blue-shifts are due to permanent electrostatics and orbital polarization, but go on to demonstrate that CT effects, where appreciably present, actually *diminish* the amount of blue-shifting observed in non-classical metal carbonyls. While values of $\Delta\omega_{CO}^{CT} = 8.6$ and 3.0 cm^{-1} for $MnCO^+$ and $ZnCO^+$ suggest that some minimal amount of ω_{CO} blue-shifting due to CT may be possible, the magnitude of these shifts is too small to be decisive. Hence, the DCD explanation for ω_{CO} blue shifts is not only incorrect, but qualitatively wrong for most if not all of the relevant

cationic MCO systems.

The careful reader will remember that our results for MCO cations exhibited the worst agreement with experiment among our dataset, due to particularly egregious results for $MnCO^+$ and $FeCO^+$. It is therefore sensible to ask again whether we can trust the qualitative trends indicated by our results. It seems that matrix effects account for the discrepancy in $MnCO^+$, though disagreement for $FeCO^+$ persists (see Section 3.4.0.2 for details). In any case, the results for $FeCO^+$, suggest we *underestimate* the CT red-shifting. For now it is therefore sufficient to note that these results, along with the close agreement for the other cations (Table 3.1) make it clear that CT does actually promote red-shifting in non-classical metal carbonyls, in contrast to the paradigm of the DCD model.

In summary, a number of overall trends for MCO cations stand out from our dataset. The most notable of these is the significance of FRZ and POL effects in determining $\Delta\omega_{CO}$ and ΔE_{bind}, especially in light of the fact that these are effectively absent in the description of the anionic systems provided above. Polarization plays the dominant role in energetic stabilization of MCO cations. While CT contributions to both the relative and absolute values of ΔE_{bind} and $\Delta\omega_{CO}$ are diminished in cations relative to MCO anions, CT is still an important feature of MCO cations despite previous indications otherwise.[276] A competition between blue-shifts due to FRZ and POL interactions and red-shifts due to CT results in the overall frequencies that are observed experimentally. This is similar to the case of certain hydrogen-bonding systems, where FRZ interactions promote blue-shifting in the C−H bond that is mitigated by the effects of POL and CT.[265]

Our model of cation binding indicates that FRZ and POL interactions drive moderate to large values of ΔE_{bind} and significant blue shifts in ω_{CO}. CT provides additional stabilization to these complexes and also attenuates the blue-shifting tendencies of interaction with the cation. Additional subtleties in the trends in ΔE_{bind}, r_{M-C}, and ω_{CO} for MCO cations can be understood in terms of the orbital occupation of the isolated metal fragment. As suggested by the CT results, discussed in the main text, two classes of MCO cations are apparent in our data set. These are $MnCO^+$ and $ZnCO^+$ on the one hand and $CrCO^+$, $FeCO^+$, and $CuCO^+$ on the other. In the former case the coupled occupied-valence pair (COVP) analysis indicates that back-donation is all but absent, whereas it contributes to the stability and ω_{CO} red-shifting in the latter. The extent of back-donation is correlated with r_{M-C} (see Table 3.3): longer M−C bonds diminish spatial overlap between the orbitals involved in back-donation.

It seems plausible that electron configuration of the isolated metal cation, particularly the occupancy of the diffuse 4*s*-orbital, governs the closeness of CO approach in the complex. In ground state $^6Cr^+$, $^4Fe^+$, and $^1Cu^+$, the 4*s*-orbital is unoccupied, allowing for relatively short M−C bonds. Similarly short M−C bonds are prevented by the occupation of the 4*s*-orbital in the ground state configurations of $^7Mn^+$ and $^2Zn^+$. Within each of these two classes of metal cations, the ordering of the M−C bond lengths follows the general trend of decreasing atomic radius across the periodic table due to increasing nuclear charge. In essence, metal electron configurations determine the closeness of M−CO approach and thereby the extent of spatial orbital overlap, which controls the amount of back-donation in the complex. This

analysis cannot account for the cation frequency shifts in their entirety. For instance the red shift in $FeCO^+$ due to charge transfer is significantly larger than that for $CuCO^+$, despite similar M−C bond lengths. Still, metal cation electron configurations and their influence on r_{M-C} can serve as a touchstone for understanding the nature of charge transfer in their carbonyl complexes.

3.3.4 Neutral complexes (M = V, Cr, Mn, Ni, Cu, Zn)

The binding motifs of neutral MCO complexes mediate between those of their cationic and anionic counterparts, exhibiting moderate $\Delta\upsilon_{CO}$ red-shifts on the order of 100–300 cm^{-1}. In some ways this reflects the fact that the physical underpinnings of MCO bonds share motifs with both MCO^- and MCO^+ systems. Despite similarities to both of the cases considered previously, the neutral systems present interesting physical phenomena not present in either set of charged systems.

Similar to the cationic systems, bound structures exist on the FRZ surfaces for all of the neutral complexes considered in this study. But where FRZ cations were more tightly bound with binding energies on the order of −2–10 kcal mol^{-1}, there is a tendency for neutral metals to form vdW complexes on their FRZ surfaces, indicated by r_{M-C} values of 4.5–5.8 Å and binding energies on the order of hundredths of kcal mol^{-1} (Tables 3.3 and 3.4, respectively). Absent the permanent electrostatic interactions that govern the FRZ surfaces of charged complexes, neutral MCO complexes are loosely bound by dispersion interactions in their FRZ structures. NiCO and ZnCO are somewhat exceptional, having shorter M−C bonds, though they must still be dispersion-bound as there is no permanent electrostatic contribution and the Pauli term is always repulsive.[174] These two compounds, as well as MnCO, are further interesting in that their metal atoms bind CO through an electronically excited state; this behavior is discussed in Section 3.4.0.1 below. In the species that form vdW complexes (M = V, Cr, Mn, and Cu), $\Delta\omega_{CO}$ values for FRZ structures are negligible (Table 3.5). Small blue shifts (15–30 cm^{-1}) are found in NiCO and ZnCO, indicating that the shortening (and strengthening) of the C−O bond increases the strength of dispersion interactions with the metal atom, possibly through charge reorganization in CO.

Polarization effects vary significantly across the neutral species in this study: in some cases, the effects are negligible, while in others they are substantial. The structures, binding energies, and frequency shifts in CrCO, MnCO, and CuCO are largely unperturbed by intramolecular orbital relaxation. In the other three systems (VCO, NiCO, and ZnCO), POL decreases the length of the M−C bond, stabilizes the complexes slightly, and leads to blue shifts in ω_{CO}. The effect on the complex geometry is startlingly large for VCO, where $r^{FRZ}_{V-C} = 5.582$ Å and $r^{POL}_{V-C} = 2.698$ Å—POL leads to a nearly 3 Å contraction in r_{M-C}! Polarization-derived decreases in r_{M-C} for VCO and NiCO are likely due to the unoccupied metal 4*s*-orbital in these systems, which allows a closer approach between the fragments. In the other species, Pauli repulsion between the CO orbitals and the diffuse 4*s*-shell prevents a close approach between the two fragments absent the effects of CT. ZnCO is an exception to this rule because its binding occurs through an excited Zn atom electron configuration

(Section 3.4.0.1). In accordance with the trends seen on the FRZ surfaces, close binding on POL surfaces is accompanied by blue shifts in ω_{CO}. Blue shifts of 40.3, 69.6, and 40.9 cm^{-1} are seen for VCO, NiCO, and ZnCO, respectively.

Neutral MCOs are generally more complicated than their ionic counterparts, such that producing a coherent model of their binding is more difficult. Still, as in the cationic species, the magnitude of both ΔE_{bind} and $\Delta\omega_{CO}$ generally correlates with the occupancy of the 4*s*-orbital. VCO and NiCO, which do not have 4*s*-electrons, exhibit the most significant CT contributions to their binding. Charge transfer in these two complexes leads to more than 200 cm^{-1} red shifts in ω_{CO} (Table 3.5) and large decreases in ΔE_{bind} (Table 3.4). The contribution to ΔE_{bind} is particularly large for NiCO, where an exceptionally short (1.680 Å) M−C bond creates significant overlap between the fragment orbitals, resulting in nearly 40 kcal mol^{-1} of additional complex stabilization. Single occupation of the 4*s*-orbitals in CrCO and CuCO directly limits forward donation and, more importantly, indirectly limits back donation by diminishing the overlap between the relevant orbitals. Hence, less significant stabilization energies (3–6 kcal mol^{-1}) and frequency shifts (120–125 cm^{-1}) are seen in most neutral as compared to ionic MCOs.

Overall, CT strengthens the binding in neutral MCO complexes significantly, relative to the FRZ and POL effects. As a result, all of the neutral metals we studied bind CO covalently in unconstrained computations. Figure 3.6 indicates that these charge transfer effects are dominated by back-donation, similar to the anionic MCO systems. The charge transfer stabilization in these systems ranges from 3–37 kcal mol^{-1} (Table 3.4) and is roughly correlated with the M−C bond length (Table 3.3) in the complex. Again ZnCO provides a clear exception to this trend, and this is because Zn binds CO from an electronically excited triplet state, discussed in the following section.

3.4 Anomalous behavior in MCO compounds

The preceding results and discussion indicate that the binding motifs in MCO compounds, including the resulting shift in ω_{CO} depends largely on the overall charge, electron configuration, and atomic number of the metal atom. Trends based on these features provide a coherent description of the majority of the compounds in our dataset. Still, a few of the systems under consideration exhibit unique binding modes that warrant further analysis and discussion.

3.4.0.1 Electronically excited metal atoms: MnCO, NiCO, $CuCO^-$, and ZnCO

The electronic structure in the majority of the MCO complexes of this study can be understood as a perturbation to that of the ground electronic states of the isolated M and CO fragments. In MnCO, NiCO, $CuCO^-$, and ZnCO, however, this is not the case; in these systems the orbitals in the MCO complex are derived from the interaction between CO and an electronically excited metal atom. The concept of bond preparation, commonly

Table 3.6: Binding energies and frequency shifts for MCO complexes that form from bond prepared metal atoms, computed at the ωB97X-V/def2-TZVPD level of theory. Electronic binding energies (D_e) with respect to both ground ($\Delta E_{\text{bind}}^{\text{grd}}$) and bond-prepared ($\Delta E_{\text{bind}}^{\text{bp}}$) fragments are reported. Experimental CO vibrational frequency shifts ($\Delta\nu_{\text{CO}}^{\text{expt}}$), reproduced from Table 3.1, allow unambiguous identification of experimental species. Energies and frequency shifts are in units of kcal/mol and cm^{-1}, respectively.

Species	$\Delta E_{\text{bind}}^{\text{grd}}$	$\Delta E_{\text{bind}}^{\text{bp}}$	$\Delta\omega_{\text{CO}}$	$\Delta\nu_{\text{CO}}^{\text{expt}}$
^{6}MnCO	10.8	-25.3	-195.1	-188.8
^{3}NiCO	-10.9	–	-58.0	–
^{1}NiCO	-33.5	-71.5	-115.3	-134.2
^{1}CuCO^{-}	-1.7	–	-35.2	–
^{3}CuCO^{-}	6.2	-34.8	-399.1	-394.6
^{1}ZnCO	-0.20	–	0.4	–
^{3}ZnCO	52.9	-35.9	-261.5	-288.6

employed in cluster models,[301, 369, 368, 404] is helpful in the analysis of these systems and is invoked repeatedly below. Simply put, we must first prepare the metal atom/ion for binding through electronic excitation to a state that can interact with the adsorbate, CO in this case, appropriately. For three of these systems, this results in MCO compounds that are only metastable relative to the isolated ground state fragments. In the remaining system, NiCO, the final complex is bound with respect to the ground state fragments, though the electronic structure is particularly complicated due to multiple low-lying electronic configurations.

The isoelectronic Cu^- and Zn atoms bind CO similarly, although differences due to the charge in the resulting complex like those seen above (Section 3.3) persist. Both metals have ground state $[Ar]4s^23d^{10}$ electronic configurations that form dispersion-bound vdW MCO complexes with negligible $\Delta\omega_{\text{CO}}$ values according to our ωB97X-V computations (Table 3.6). These results comport with chemical intuition—stable, fully occupied $4s$ and $3d$ subshells render the metal atoms unlikely to interact with the CO orbitals—but fail to account for the large υ_{CO} red shifts of 394.6 and 288.6 cm^{-1} that have been experimentally observed for $CuCO^-$[439] and ZnCO,[187] respectively. Interestingly, the study that reported the CO stretching frequency for $CuCO^-$ included mixed-basis B3LYP computational results for $^{1}CuCO^-$ that gave a frequency shift of $-331.2\,\text{cm}^{-1}$ in qualitative agreement with their experimental result. Subsequent DFT studies[423, 144] also determined a singlet ground state for $CuCO^-$. We obtain a similar result of $-350.1\,\text{cm}^{-1}$ using the B3LYP functional and the def2-TZVPD basis. Yet the inability of both CCSD(T) and ωB97X-V to predict this value for $CuCO^-$ calls the B3LYP results into question.

To investigate alternative binding modes, we obtained CCSD(T) and ωB97X-V results for $^{3}CuCO^-$ and ^{3}ZnCO. Results from these computations exhibit excellent agreement with the experimental $\Delta\upsilon_{\text{CO}}$ results for $CuCO^-$ and ZnCO, suggesting it may be these high-

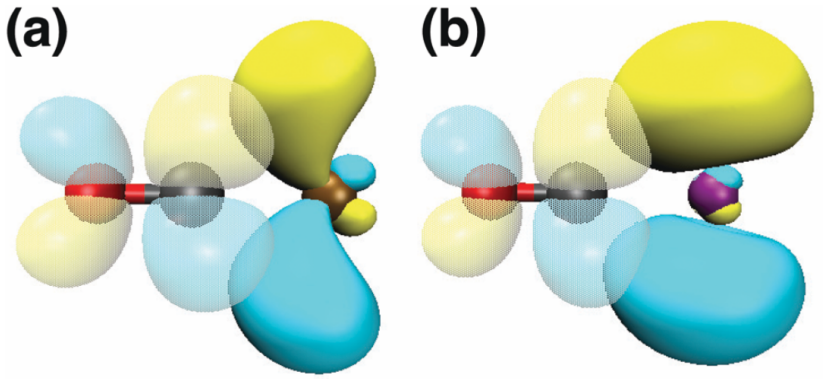

Figure 3.7: COVP orbitals for $\pi^* \leftarrow 4p$ back-donation from M to CO for (a) $CuCO^-$ and (b) ZnCO. This is the dominant CT interaction in these systems.

spin species that have been observed experimentally. Indeed, the experimental work that first identified ZnCO assigned the absorption at 1852.2 cm^{-1} to ^{3}ZnCO on the basis of BP86 calculations.[187] However, as indicated in Table 3.6, these triplet complexes are destabilized with respect to the ground state fragments by 6.3 and 52.9 kcal mol^{-1}, respectively. The metastability of these complexes also explains other aspects of the experimental results. Specifically, the magnitude of the $CuCO^-$ peak was found to decrease relative to those of other species upon matrix annealing,[439] and both $CuCO^-$ and ZnCO peaks disappeared entirely after a period of broadband radiation.[439, 187] To the best of our knowledge, the present study provides the first indication that the observed signals for $CuCO^-$ come from the triplet complexes. Furthermore, where previous (singlet) computations led researchers to conclude that $CuCO^-$ exhibited a bent structure,[439, 423] the present results predict a linear geometry for this species, as well as ZnCO. Experimentally, our results suggest the Cu^- and Zn atoms undergo electronic excitation to metastable triplet states (bond preparation) during metal vaporization and prior to reaction with CO. Something similar likely occurs in the preparation of alkaline earth metal carbonyls, where excitations into the $(n-1)d$-orbitals facilitate bonding.[424, 425]

Working from the conclusion that experimental results for $CuCO^-$ and ZnCO concern triplet states obtained through a bond-prepared $[Ar]4s^14p^13d^{10}$ configuration on the metal, the decomposition of the binding properties for these species follows the general trends for anionic and neutral species as described above. Unlike the other anions in this study, $^3CuCO^-$ forms a vdW complex on its POL surface, although this result is not particularly significant. More interestingly, the extent of CT is significantly enhanced in these two systems. lndeed, $CuCO^-$ and ZnCO exhibit the the largest υ_{CO} red shifts in each of their charge categories (Table 3.5). The highly diffuse $4p$-orbital exhibits significantly greater spatial and energetic overlap with the CO π^*-orbital than do the more contracted metal $3d$-orbitals (Figure 3.7).

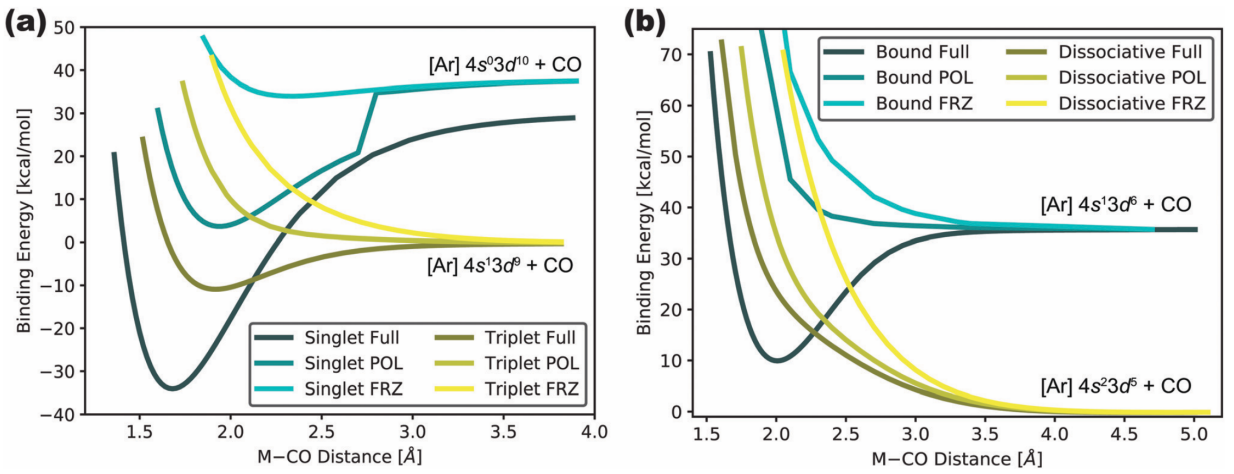

Figure 3.8: Potential energy surfaces for the energy decomposition analysis of (a) NiCO and (b) MnCO. In both cases the most tightly bound MCO complex is formed through the interaction of an electronically excited metal atom and ground state CO. See text for discussion of the discontinuity and asymptotes in $^1\Sigma^+$ NiCO dissociation and the absence of FRZ and POL surfaces for bound MnCO.

These features allow a much stronger mixing between the donor–acceptor orbitals in the $\pi^* \leftarrow 4p$ interaction, and a significant CT effect ensues. CT energy stabilizations for unconstrained computations on $CuCO^-$ and ZnCO are also among the largest in anions and neutrals, respectively (Table 3.4), but even so are not significant enough to overcome the initial promotion energy to obtain the triplet metal atoms from the ground state singlets. Previous studies had debated the importance of 4*p*-orbitals in metal–carbonyl bonding, finding that 4*p*-repolarization can be an important mechanism for diminishing interfragment repulsion, but that CT from 4*p*-orbitals was insignificant compared to other CT interactions.[375, 31, 100] For most cases in the present study, analysis of the COVP orbitals supports the conclusion that $\pi^* \leftarrow 4p$ back-donation is relatively unimportant. But our results for $CuCO^-$ and ZnCO suggest that, at least in some cases, the 4*p*-orbitals actually play a defining role in the M−CO bond.

The modes of complex formation for MnCO and NiCO are similar in some ways, though additional complications arise. As in the two cases above, the experimentally observed structures (as determined by the υ_{CO} shift upon complex formation) are formed through the interaction of a ground state CO molecule and an electronically excited, bond-prepared metal atom. For Ni, the ground state $[Ar]4s^13d^9$ configuration excites to $[Ar]4s^03d^{10}$ upon NiCO formation, while for Mn, $[Ar]4s^23d^5$ excites to $[Ar]4s^13d^6$ (Figure 3.8). In both cases the 4*s*-electron excites into the $3d_{z^2}$ orbital, rendering the 4*s*-orbital singly occupied such that $4s \leftarrow 5\sigma$ forward-donation becomes possible.[33, 30, 175] These bond-preparing excitations also significantly diminish the Pauli repulsion in the complex, which is known to be a significant

barrier to bond formation in metal carbonyls.[33, 120] Hence electronic excitations on Ni and Mn facilitate binding, as in the cases of Cu^- and Zn considered above.

For NiCO, both the ground (^{3}Ni) and excited (^{1}Ni) metal atoms can bind CO, although a more favorable interaction occurs through the excited state. This is in qualitative agreement with the coupled-cluster study of NiCO electronic states by Schaefer, *et al.*.[175] There has been disagreement as to the geometry of ^{3}NiCO: this same coupled-cluster study predicted a linear, $^3\Delta$ NiCO structure as the lowest lying NiCO excited state[175], while DFT studies had predicted a bent structure.[119, 120, 321] Similar to other density functionals, ωB97X-V functional predicts a bent $^3A'$ NiCO structure for triplet NiCO. However, the ωB97X-V barrier to linearity is a mere $0.1\,\mathrm{kcal\,mol^{-1}}$, two orders of magnitude smaller than the binding energy of ^{3}NiCO, rendering this discrepancy largely inconsequential.

The PESs for these interactions [Figure 3.8(a)] suggest that two different modes of binding occur for these structures. In $^1\Sigma^+$NiCO, a vdW complex forms on the FRZ surface as seen for other neutral systems, in contrast to an earlier CSOV result that indicated a repulsive FRZ interaction for ^{1}NiCO.[33] POL and CT further stabilize the M−CO interaction by 30 and $37\,\mathrm{kcal\,mol^{-1}}$ increments, respectively (Table 3.4). This leads to an overall complex binding energy of $-33.5\,\mathrm{kcal\,mol^{-1}}$ with respect to (ground state) ^{3}Ni and CO (Table 3.6). $^3A'$ NiCO by contrast, forms vdW complexes on the FRZ and POL surfaces, and a moderately bound ($\Delta E_{\mathrm{bind}} = -10.8\,\mathrm{kcal\,mol^{-1}}$) complex on the FULL surface. We note again that the ωB97X-V structure for $^3A'$ NiCO used in this EDA is bent, in contrast with the CCSD(T) result. Regardless of this discrepancy, the difference in the phenomenology of ^{1}NiCO and ^{3}NiCO binding as predicted by ωB97X-V is likely due to the occupation of the $4s$-orbital in ^{3}Ni, which extends the range of Pauli repulsion, overpowering any dispersion-based attraction between the fragments. Its absence in ^{1}Ni allows the latter effect to dominate, and bound FRZ and POL structures can be obtained.

The $^1\Sigma^+$NiCO surfaces in Figure 3.8(a) are unusual and deserve further comments. In particular, there is an $8\,\mathrm{kcal\,mol^{-1}}$ gap between the asymptotes of the full surface and the FRZ/POL surfaces; this is clearly unphysical. Mulliken population analysis reveals charge delocalization errors[81] on the full surfaces that can explain these artifacts. Partial anionic character on Ni spuriously lifts too much degeneracy from the Ni $3d$-orbitals, giving rise to two distinct asymptotes for the triplet surfaces, as well as the discontinuity in the POL surface, in Figure 3.8(a). Examination of molecular orbitals on this surface explains the source of this discontinuity (Figure 3.9). In the limit of a large separation between the fragments, the $3d$-orbitals in ^{3}Ni will be 10-fold degenerate. The degeneracy in these orbitals is lifted upon approach of the CO adsorbate. The plots in Figure 3.9 indicate that this degeneracy is first lifted as the $3d_{z^2}$-orbital polarizes, likely due to the CO 5σ-electrons, and then is further lifted as the $3d_{xz}$- and $3d_{yz}$-orbitals polarize to accommodate the π-electrons. The discontinuity in the POL surface in Figure 3.8(a) is apparently due to the lifting of this degeneracy as CO approaches ^{1}Ni from $r_{\mathrm{M-C}} = 2.8\,\text{Å}$. All FRZ computations yielded binding energies on the "upper" surface, which corresponds to a 1Ni atom with 2- and 8-fold degeneracy among the $3d$-orbitals. The persistence of this degeneracy across the $r_{\mathrm{M-C}}$ values of interest is due to the mechanics of the FRZ computation, which completes the SCF

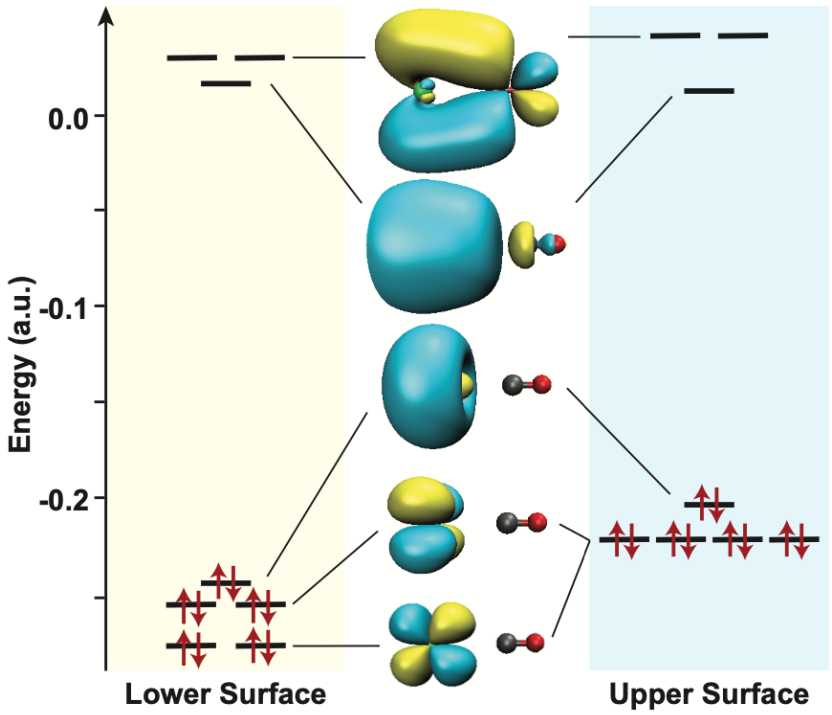

Figure 3.9: Molecular orbital diagram for POL surface of ^{1}NiCO (*cf.* Figure 3.8). The orbitals on the lower and upper surfaces were obtained with $r_{\mathrm{M-C}} = 2.7$ and 2.8 Å, respectively.

iterations for each fragment independently of the other (i.e. intramolecular relaxation due to the presence of other fragments is prevented).

Notably, none of our computations recover the 10-fold degeneracy of the Ni d-orbitals at large values of $r_{\mathrm{M-C}}$, and both asymptotes are therefore spurious. This feature of our computational approach, due to charge delocalization errors, does not necessarily invalidate the results obtained in the short M−C regime. As the energies of all optimized structures were found to be stable with respect to rotations between the occupied and virtual orbital subspaces, we take these results to be legitimate. Using these results, the binding energies presented in Table 3.4 were obtained with respect to the isolated fragments, which lie slightly above the energy of the upper asymptote in Figure 3.8(a).

Delocalization errors notwithstanding, the phenomenology of the $^1\Sigma^+$Ni−CO bond is distinct from that in the other neutral species. Specifically, we find that ^{1}Ni is able to bind CO closely and strongly on both the FRZ and POL surfaces, and furthermore that binding impacts ω_{CO} on these surfaces. This is in marked contrast to the previously discussed neutral species, where FRZ and POL structures were identified as vdW complexes. The compact d^{10}- and empty 4s-shells on Ni likely serve to diminish Pauli repulsion and increase the ability of the CO 5σ lone pair to penetrate into the Ni core, stabilizing the Ni−CO bond, as occurs

in other systems.[95] Similar effects were seen for V (nominally a $4s^0 3d^5$ configuration), which binds CO on the POL but not the FRZ surface, but the more compact d^{10}-core in Ni facilitates an ever closer approach between the fragments (Table 3.3), and thereby a stronger interaction at all stages of the EDA.

Likewise, an excited ^{6}Mn electron configuration leads to the MnCO structure that has been observed experimentally, though in this case both the ground and excited configurations exhibit the same (hextet) spin multiplicity. Computationally, we consider the MnCO binding event to consist first of a bond-preparing excitation from the ground state [Ar] $4s^2 3d^5$ configuration to an excited [Ar] $4s^1 3d^6$ state through a $4s \rightarrow 3d_{z^2}$ promotion ($\Delta E = 36.1\,\mathrm{kcal\,mol^{-1}}$), followed by interaction with an approaching CO molecule. The bond-prepared binding energy of the resulting complex is $-25.3\,\mathrm{kcal\,mol^{-1}}$, leading to an overall destabilization of $10.8\,\mathrm{kcal\,mol^{-1}}$ with respect to isolated ground-state Mn and CO. Figure 3.8(b) presents the ground and excited state potential energy surfaces for MnCO. Unlike in the case for the ground state ^{3}Ni atom, no tightly bound structure was obtained for ground state Mn, although a very weakly bound ($\Delta E_{\mathrm{bind}} < 0.2\,\mathrm{kcal\,mol^{-1}}$) vdW complex was found to be stable on all three surfaces. Analogous to the case for ^{1}NiCO examined in detail above, the electronic difference between these two structures was found to be a result of (lifted) degeneracy among the Mn 3*d*-orbitals.

The excited FRZ and POL surfaces were found to be everywhere dissociative, so the entirety of ΔE_{bind}, geometry changes, and $\Delta\omega_{\mathrm{CO}}$ are attributed to CT in Tables 3.3, 3.4 and 3.5. In contrast to the results discussed for $^1\Sigma^+$NiCO in the preceding paragraphs, the nature of the Mn−CO bond is highly similar to that for the other neutral species of this study: FRZ and POL interactions are insufficient to overcome Pauli repulsion, and a bound structure can only be obtained once the effects of CT are included.

Despite subtle differences in the details of these four complexes, the binding motifs of NiCO, MnCO, $CuCO^-$, and ZnCO are unified by the necessity of bond preparation to achieve the ground state complex. In some cases, this insight into the complex formation clears up previous discrepancies between experimental and computational results. Once the metal excitation has been accounted for, the EDA for these systems indicates that MCO binding typically follows the trends determined for the systems of the same charge as presented in Sections 3.3.2 and 3.3.4 above.

3.4.0.2 Discrepancies with cations: $MnCO^+$ and $FeCO^+$

The results for $MnCO^+$ and $FeCO^+$ stand out among those for the rest of the species in Table 3.1 for two reasons: (1) unlike the other cations, experimental results for these systems do not exhibit significant blue shifts in υ_{CO} and (2) the *prima facie* disagreement between theory and experiment is the greatest for these two complexes. This disagreement warrants a closer examination of the experimental results for $MnCO^+$ and $FeCO^+$.

Reed and Duncan report experimental values for $\Delta\upsilon_{\mathrm{CO}}$ for $Ar_3(MnCO^+)$ using mass-selected infrared photodissociation spectroscopy.[341] The dissociation spectrum contains two peaks at $2106\,\mathrm{cm^{-1}}$ and $2148\,\mathrm{cm^{-1}}$, which they attribute to $Ar_3(^5MnCO^+)$ and

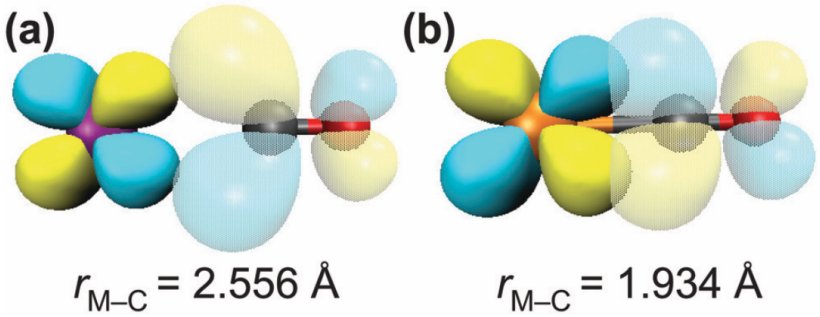

Figure 3.10: COVP orbitals for the most significant back-donation interactions in (a) $MnCO^+$ and (b) $FeCO^+$. Metal–carbon bond lengths influence the strength of the interaction and thereby the extent of CT effects on ΔE_{bind} (Table 3.4) and $\Delta\omega_{\text{CO}}$ (Table 3.5).

$Ar_3(^7MnCO^+)$ on the basis of B3LYP/def2-TZVPP computations. They report additional computational results (at the same level of theory) that indicate that the perturbation due to two Ar atoms red-shifts the CO frequency by 68.6 cm^{-1}. Hence, the experimental result for the $MnCO^+$ frequency shifts in Table 3.1 should be corrected by 68.6 cm^{-1} in order to remove the effects of the Ar atoms and better facilitate comparison to the computational results. This correction gives value of $\Delta\upsilon_{\text{CO}} = 75.8\,\text{cm}^{-1}$, in much better agreement with the CCSD(T) and ωB97X-V $\Delta\omega_{\text{CO}}$ values of 80.5 and 97.9 cm^{-1}, respectively, as well as the general trend for cations. This also suggests that the anomalously small υ_{CO} blue-shift reported for $MnCO^+$ in Ref. 341 is due to the effects of the Ar atoms present in the experiment, rather than the physics inherent to this MCO complex. Hence, $MnCO^+$ is not as exceptional as it first appears, and the general analysis of Section 3.3.3 carries over to this case.

It is more difficult to reconcile the disagreement between our density functional treatment and the experimental results for $FeCO^+$. Comparison of experimental results for $FeCO^+$ in Ne[440] and Ar[442] matrices indicates that matrix effects are non-trivial for this system: the value of υ_{CO} in solid Ar is red-shifted by 41.5 cm^{-1} relative to that in solid Ne. Hence, we expect the Ne matrix value of 2123.0 cm^{-1} to be noticeably red-shifted from its value in vacuum. This matrix effect may be significant enough to account for the 17.2 cm^{-1} difference between CCSD(T) and experiment, though gas phase determination of υ_{CO} would be necessary to know for sure. It is, however, exceedingly unlikely that this effect can explain the much larger 62.8 cm^{-1} discrepancy for ωB97X-V, the largest in our data set (Table 3.1).

Furthermore, $\Delta\upsilon_{\text{CO}}$ for $FeCO^+$ is lower than we would expect based on the analysis of the other cationic complexes above. According to the results in Table 3.5, the contributions of FRZ and POL interactions to $\Delta\omega_{\text{CO}}$ are similar to those in the other cationic systems considered herein. Instead, $FeCO^+$ stands out because of a relatively large 81.5 cm^{-1} red shift due to charge transfer. We also note that $r_{\text{M–C}} = 1.934$ Å in $FeCO^+$ (Table 3.1), a

much shorter bond length than most of the other cations, a result of the low-spin of the complex. This close M−CO approach, and the resulting increase in the overlap of orbitals between the two fragments, facilitates a greater amount of back-donation than in the other cations.[120] Comparison of the COVP orbitals for $MnCO^+$ ($r_{M-C} = 2.556$ Å), where the CT effect is small, and $FeCO^+$ supports this line of reasoning (Figure 3.10). (Despite a similarly small value for r_{M-C}, a comparable amount of back-donation does not occur for $CuCO^+$ because the additional nuclear charge on Cu^+ diminishes both the spatial and energetic overlap between the metal 3*d*- and CO $2\pi^*$-orbitals.) Such an analysis is also supported by the COVP results in Figure 3.6, which show significant energetic stabilization due to back-donation for $FeCO^+$.

Experimental red-shifting of υ_{CO} for $FeCO^+$[440] obscures the reality that the underlying physics for this system is along the lines of that for the other cations, which all exhibit υ_{CO} blue-shifting. FRZ and POL interactions that increase υ_{CO} compete against the tendency of CT to decrease υ_{CO}. In all cases, including $FeCO^+$, the observed υ_{CO} reports on the overall balance of these interactions.

3.4.0.3 Bending in MCO complexes

Finally, we consider metal atoms and ions that form non-linear MCO complexes on their unconstrained PESs. While metal monocarbonyls tend to be linear (see Table 3.3), exceptions to this rule have been known for some time. Indeed, a number of previous computational studies have indicated that the equilibrium structures of CrCO[119, 120, 321, 220, 209, 210, 46] and CuCO[119, 120, 29, 439, 321, 423, 188] are non-linear, although at least one wave function (MRCI) study found a linear ground state for CrCO.[186] Two DFT studies of $CrCO^-$ reported predictions that $CrCO^-$ is linear.[9, 144] In agreement with the former consensus and in contrast to the latter results, below we report bent ground-state structures for CrCO, $CrCO^-$, and CuCO on the basis of CCSD(T) and ωB97X-V computations (Table 3.7). (Electronically excited states of these and other MCO compounds have also been found to adopt bent structures, [120, 321, 210, 46] but are not of present interest.) Historically, this MCO bending has been rationalized on the basis that bent geometries diminish the repulsion between the CO 5σ- and metal $3d_{z^2}$- and 4*s*-orbitals.[119, 120] Our results expand upon this understanding of non-linear MCO complexes.

The geometric data in Table 3.3 indicate that a variety of mechanisms can promote the linearity of an MCO bond. A linear geometry is obtained for the majority of anionic systems, which are bound almost entirely by CT ($CrCO^-$ is an exception and will be treated below). This suggests that the most favorable orbital overlap is achieved in a linear arrangement, and thus we expect CT to promote linearity in the majority of systems. For the cationic systems, a linear complex is obtained on each of the EDA surfaces. At both the FRZ and POL levels, metal cations bind CO through a favorable charge-dipole interaction (Section 3.3.3) that is maximized when the complex has a linear arrangement. Thus in cations both electrostatic and CT effects promote linear complexes.

Table 3.7: CCSD(T) and ωB97X-V bond angles (degree) for bent MCO complexes of multiplicity M

Species	M	CCSD(T)	ωB97X-V
CrCO	6	157.9	152.7
$CrCO^-$	7	136.7	134.1
CuCO	2	151.9	145.7

The picture is somewhat more complicated in neutral systems, where vdW complexes are found to form on the FRZ and/or POL surfaces in some cases (Section 3.3.4). Most vdW complexes on the FRZ/POL surfaces (taken as those with M−C bonds at least 4 Å) are bent. As constraints are removed from the computations, some neutral complexes linearize, while others (CrCO and CuCO) do not. As Fournier observed,[119, 120] there is a correlation between the 4*s* occupation of a metal and the linearity of its resulting MCO complex: neutral complexes without a 4*s*-electron tend to be linear, while those with 4*s*-electrons bend, presumably to minimize Pauli repulsion between 4*s*- and 5σ-orbitals. Fournier used this trend to argue that, to the right of V in the transition metal series, low-spin MCO complexes are linear, while high-spin complexes are bent.[120] The linear structure we obtain for ^{1}NiCO, for instance, is an example of this trend. Unlike Fournier, however, we find a bound, linear, and high-spin structure for MnCO, although this structure is only metastable with respect to the ground state fragments (Figure 3.8). The high-spin ^{3}ZnCO is also linear, presumably to maximize the overlap between the Zn 4*p*- and CO 2π^*-orbitals that is critical to binding in this case as shown in Section 3.4.0.1.

Among neutral complexes, this leaves CrCO and CuCO as our case studies in MCO bending, for which we report ωB97X-V bond angles of 152.7° and 145.7°, respectively (Table 3.7). Relative to the other complexes in our dataset, each of these compounds is weakly bound ($\Delta E_{\text{bind}} \approx -3$–$6\,\text{kcal mol}^{-1}$ [Table 3.4]). CT is necessary to allow close approach between the two fragments, and even so these three systems have uncharacteristically large M−C bond lengths, on account of repulsion from the 4*s*-electron(s) (Table 3.3). Analysis of the COVP orbitals in these complexes, presented for CrCO in Figure 3.11, indicates unique CT interactions for these bent systems. The major forward-donation in these systems occurs through CT from the CO 5σ-orbital into the $3d_{z^2}$- or 4*s*-orbitals for CrCO and CuCO, respectively, similar to the previously considered cases [Figure 3.11(a)]. The primary back-donation, however, is a $2\pi^* \leftarrow 3d_{z^2}$ interaction [Figure 3.11(b)], which is forbidden in the linear complex on the grounds of orbital symmetry. This explains how $\Delta\omega_{\text{CO}}$ in these two complexes is comparable to similar systems despite longer M−C lengths which would otherwise diminish the extent of CT: three different metal orbitals are able to donate into the CO 2π^*-orbital and weaken the bond, unlike in linear complexes.

We finally consider $CrCO^-$, the only bent ion in our series, for which we report an ωB97X-V bond angle of 134.1° (Table 3.7). At least one previous study reported a linear structure for this system,[9] and to the best of our knowledge the present results are the

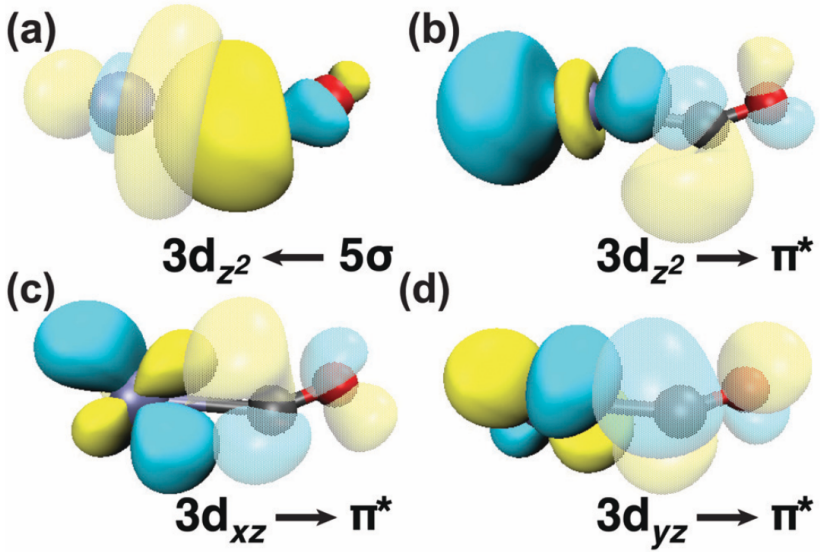

Figure 3.11: Most significant COVP orbitals for CrCO: (a) forward-donation and (b)-(d) back-donation. Repulsion between the CO 5σ- and Cr $4s$-electrons alters the complex geometry and orbital interactions.

first indication of a bent structure for $CrCO^-$. Unlike its neutral counterpart and similar to the other anions, $CrCO^-$ does not form a bound structure on the FRZ surface, though a vdW complex forms when POL effects are included. The COVP orbitals for this species are very similar to those depicted for its neutral counterpart in Figure 3.11, indicating the same, non-standard mode of CT discussed above. We therefore motivate the bent structure of $CrCO^-$ as for the neutral species above: bending diminishes σ-repulsion and leads to orbital repolarization to compensate for lost CT stabilization. The destabilizing effects of σ-repulsion are further evident in the fact that $\Delta E_{\text{bind}} = -1.7\,\text{kcal}\,\text{mol}^{-1}$ for this complex, much smaller than that for other MCO anions.

It is interesting to compare the structure of $CrCO^-$ to the isoelectronic species MnCO and to $CuCO^-$, which also exhibits a doubly occupied $4s$-orbital. Both of these complexes are found to be linear in this study on the basis of CCSD(T) and ωB97X-V computations. All previous literature reports of $CuCO^-$ reported a bent structure;[439, 423] some computations on MnCO indicated this species was bent[120], and others that it was linear.[321] Bending in MCO complexes occurs to diminish σ-repulsion between the fragments, but comes at the energetic cost of diminishing the overlap of the standard $2\pi^* \leftarrow 3_{d_\pi}$ back-donation that stabilizes these complexes. MCO bending is then the result of two competing interactions between the fragment orbitals. In MnCO it seems sensible to us that linearity is achieved through diminished σ-repulsion vis-à-vis the isoelectronic $CrCO^-$. By contrast, the linearity of $CuCO^-$ almost certainly results from the unique $2\pi^* \leftarrow 4p$ donation that stabilizes this

system. The energetic contribution of this interaction, maximized in the linear geometry, prevents bending despite what we assume to be a significant amount of σ-repulsion on the basis of the bent structure for CuCO that we already discussed above. Mutual comparison of CrCO, MnCO, and $CuCO^-$ indicates that the interplay between the interactions that either promote or prevent bending can be quite subtle.

Following Fournier,[120] we understand MCO bending to result from a complicated interplay between minimizing orbital repulsion and maximizing CT stabilization. For Cr and Cu, the singly-occupied $4s$-orbital and the half- and fully-occupied $3d$-shells, respectively, repel the CO 5σ-electrons sufficiently to promote bending. We also report the first bent structure for $CrCO^-$, predicted by both CCSD(T) and ωB97X-V, and rationalize this result along the same lines as has been done for neutral systems that are bent. The juxtaposition of these examples against the linear monocarbonyls of Mn and Cu^- elucidates that changes in either the extent of σ-repulsion or the nature of the CT interactions can dramatically alter MCO complex geometries.

3.5 Conclusions

Despite the various exceptional cases considered above, a unified picture of MCO binding on the basis of metal charge and orbital occupation emerges from our dataset. The most significant barrier to M−CO bond formation comes from Pauli repulsion due to interactions between the CO 5σ-electrons and metal valence electrons. Various mechanisms can be employed to overcome this repulsion, and the nature of these interactions bears on various experimental observables, like ΔE_{bind} and $\Delta\upsilon_{\text{CO}}$. System charge determines the interplay between these interactions in predictable ways:

- In anions, permanent electrostatics and Pauli repulsion both inhibit binding, and the latter effect is enhanced by diffuse valence orbitals on the metal. These interactions prevent binding absent the inclusion of charge effects, specifically CO ← M back-donation. This leads to large values for ΔE_{bind} in most cases and red-shifted values for υ_{CO} in all of them.

- In cations, permanent electrostatic interactions overcome the destabilizing effects of Pauli repulsion, and orbital polarization facilitates the strengthening of the electrostatic interactions and decreases Pauli repulsion. These effects coincide with C−O bond compression and result in υ_{CO} blue-shifting, which is mitigated by the effects of charge transfer. Polarization of metal valence orbitals contributes about half of ΔE_{bind} for cations.

- Neutral systems exhibit more complicated binding motifs than either ionic system. Charge transfer is the major driving force behind ΔE_{bind}, and compounds are only weakly bound in its absence. Overall υ_{CO} red-shifting is due to charge transfer, though these effects are attenuated by orbital polarization in select cases.

While the significance of charge transfer varies across systems, its effects can hardly ever be neglected in theoretical treatments of MCOs. As has been suggested elsewhere,[220] the lion's share of charge transfer effects on ΔE_{bind} in these systems seems to result from back-donation. Still, we reiterate that caution should be exercised in using parsings of ΔE_{bind} as a proxy for direct analysis of $\Delta\omega_{\text{CO}}$. To a first approximation, this understanding of charge transfer confirms the DCD model, which accounts for M−CO binding through synergistic forward- and back-donation. However, charge transfer almost always promotes υ_{CO} red-shifting, even in systems where overall blue-shifts are observed. This conclusion, informed by previous results,[141, 260] directly contradicts the DCD model's picture of υ_{CO} blue-shifts. The DCD model is particularly inapplicable to MCO cations, where permanent electrostatics and orbital polarization play dominant roles.

In select systems, fragment repulsion is overcome by more complicated binding motifs, such as (1) electronic excitations on the metal atom (M = Mn, Ni, Cu^-, Zn) and (2) complex bending (M = Cr, Cr^-, Cu). These features arise through a complicated interplay of orbital interactions, rendering prediction of electronic excitations or complex geometries unlikely.

While we have focused our efforts on understanding the binding of molecular MCOs, the interaction of CO with an extended metal surface is of considerable interest in the broader scientific community. The triatomic MCO system is obviously a crude model for the surface–CO interaction as it neglects the presence of the metal band structure, which can perturb all of the interactions analyzed herein. We can begin to understand the exact nature of this perturbation with reference to cluster models, which help bridge the gap between MCOs and extended systems. These models suggest that σ-repulsion and metal-to-CO π-donation play the dominant role in the surface–CO bond,[20, 165, 299, 22] although σ-donation can also be important in some systems.[299] Additionally, as the size of the cluster increases, CO polarization and CT effects vary little with cluster size, while changes to the nature of electrostatic effects and metal orbital polarization can impact binding energies significantly.[165, 299] In effect, the metal cluster is more polarizable than an individual atom, enabling more efficient reduction of σ-repulsion.[299] These cluster results suggest that POL may play a much more significant role in extended systems than it does in our present analysis of MCOs, while the nature of CT may remain less changed.

Finally, we note the performance of the ωB97X-V density functional on systems containing first-row transition metals. Results from this functional compare favorably to CCSD(T) predictions of MCO geometries and binding energies in most cases, as well as both experimental and CCSD(T) CO frequency shifts. In cases like $CuCO^-$ and $CrCO^-$, ωB97X-V and CCSD(T) predict qualitatively different geometries and spin states than other DFT treatments, indicating the importance of high-level computations. These results are promising and broadly in line with benchmarks for this functional on other transition metal and main group chemical systems.[140, 101, 68] Of course, caution should be exercised in using ωB97X-V and other density functionals to study systems with transition metal atoms, particularly when the case of interest is known or expected to exhibit multireference character. But the present study indicates that state-of-the-art density functionals like ωB97X-V can provide valuable insight into the binding of transition metal systems.

Part II

Progress towards salmon-safe tires: Identifying the mechanism of ozonation for rubber and 6PPD

Chapter 4

Mechanisms of ozonation for natural rubber and PPDs

4.1 Introduction

Rubber tires are essential across various sectors, including transportation and agriculture. Indeed, tire manufacturers produced 19 million tons of rubber in 2019, and continued global industrialization is expected to increase tire demand, requiring nearly 23 million tons annually by 2024.[337] Maximization of the longevity of tires is a form of sustainability, reducing the annual flow of tires to landfills and other waste streams. This and other pressures have led the development of highly effective rubber additives that protect rubber from degradation during manufacture and use,[180] most notably *p*-phenylenediamines (PPDs).[84, 235] Unfortunately, these additives aggravate various toxicity endpoints for both human and environmental health.[79, 13, 14, 431, 39, 360] 6PPD (*N*-(1,3-dimethylbutyl)-*N*′-phenyl-*p*-phenylenediamine), the most ubiquitous of these compounds,[16] has recently gained notoriety due to the extreme aquatic toxicity of its quinone transformation product (6PPDQ) to coho salmon[399, 41, 398] and other aquatic species.[166, 410, 54] As a result, replacement of 6PPD tires has become an extremely pressing problem in green chemistry.

This poses a formidable challenge as rubber compounds are susceptible to attack from numerous reactive species—peroxyl radicals, alkyl radicals, ozone—and 6PPD protects rubber compounds from each of these degradation pathways.[170, 246, 130] Degradation due to peroxyl and alkyl radicals (collectively, "oxidation processes") is relatively well- characterized,[180] and research into alternative antioxidants was underway well before the discovery of 6PPD quinone and its toxicity.[380, 105, 64, 4, 307, 351, 390, 429, 389, 106, 428] The O_3 chemistry of PPDs and the development of safer antiozonants are more elusive. Broadly speaking, it is believed that 6PPD protects tires in two distinct but overlapping ways:[179] (1) kinetic scavenging that consumes O_3 before it is able to react with the tire[84, 112, 340] and (2) subsequent formation of a protective film that prevents ozone permeation past the surface of the tire.[112, 10, 11] Not observed in all PPDs,[340] these protective films are

likely comprised of PPD reaction products,[10, 11, 234] although details are poorly understood. Furthermore, an early and significant body of research into the ozone chemistry of PPDs failed to identify quinone byproducts, indicating that this work is incorrect or (at best) incomplete. Reinvestigation of the mechanism of 6PPD ozonation is imperative to understanding the kinetics of its ability to scavenge ozone, the likely products that lead to film formation, and the pathway to 6PPD quinone.

Herein, we report the first investigation into the mechanism of PPD ozonation since the discovery of its toxic quinone byproduct.[399] Others have laid seeds for this work through detection of potential intermediates[217, 359] and developing broad-strokes proposals of the pathway.[399, 217, 359] We continue this work through high-level computational analysis of the ozonation pathways of PPDs. Comparative analysis of the barrier heights for various PPD ozonation pathways demonstrates that the route to the quinone is uniquely accessible, linking the toxicity of PPDs directly to their function as antiozonants. Throughout this study, mechanistic proposals are derived from ozonation mechanisms in related systems (Section 4.1.1), and our computational protocol follows best practices for O_3 modeling (Section 4.1.2). We benchmark our methodology against existing methods (Section 4.3) before presenting mechanistic results for ozonation of a rubber surrogate (4.5) and PPDs (Section 4.6). We conclude (Section 4.7) by discussing the implications of this work for the development of alternatives to 6PPD.

4.1.1 Ozonation mechanisms

While the O_3 chemistry of PPDs is under-explored, the literature contains a vast body of work on ozonation reactions in similar systems. Recent reviews and monographs provide a through treatment of this chemistry in a wide array of systems.[374, 116] Here, we provide an overview of critical aspects of ozonation chemistry in alkenes, amines, and aromatic systems, which are all relevant to understanding the reactions of O_3 with rubber systems and/or PPDs.

Alkenes. Generally speaking, ozone reacts with unsaturated systems to produce scission products of the parent substrate.[116] The overall reaction pathway is uncontroversial: ozone adds to the olefins to form so-called primary ozonides, which may decompose or rearrange to form (secondary) ozonides, ultimately resulting in scission of the original olefin to two carbonyl products. This pathway explains the degradation of rubber upon exposure to ozone.[340, 10, 438]

Despite this consensus, two distinct proposals for the mechanism of primary ozonide formation have gained popularity: A concerted addition across the double bond (Criegee mechanism)[90] and a stepwise addition, where ozone reacts with an olefin to form a biradical intermediate which may subsequently collapse to the ozonide (DeMore mechanism).[97] Consensus increasingly indicates that the Criegee mechanism prevails in simple (*i.e.* less substituted, electronically symmetric) systems,[133, 350, 224, 128] while both steric and electronic effects of olefin substituents increase the importance of DeMore channels.[107, 350,

213] In extreme cases, steric hindrance prevents formation of the primary ozonide completely, and the initial ozonation of alkenes results in epoxide formation.[107] Recent theoretical work indicates that solvent effects can make stepwise mechanisms dominant in systems where they otherwise would not be.[228]

Amines. The reactivity between amines and O_3 is generally understood as a nucleophilic attack of N toward O_3,[23, 25, 365] and this pathway is particularly important in tertiary amines.[24, 253] Depending on the substitution pattern of the parent amine, reaction products may include *N*-oxides, nitrones, hydroxylamines, nitroso-alkanes, and nitroalkanes, and dealkylated amines.[178, 277, 253, 365] Amines may also react with ozone through insertion into the N−H bond.[405] The N lone pair plays a critical role in amine reactivity towards O_3, such that more highly substituted aliphatic amines exhibit increased O_3 reactivity.[365] By the same token, these reactions are highly sensitive to pH, as amine protonation eliminates the reaction channel.[82, 253] Even in the most favorable systems and conditions, high barrier heights for N−O bond formations[405] can limit these reactions relative to other available ozonation pathways.[25]

Aromatics. Reference to the O_3 chemistry of aromatic systems like anilines and phenols also enhances our understanding of its reactivity in PPDs. In both former types of systems, ozonation reactions produce manifold products, and a broad array of mechanistic pathways have been suggested.[291, 151, 320, 391, 394] Motifs common to the preceding functional groups are present here as well: primary ozonide formation,[290, 394] nucleophilic attack of ozone from heteroatoms like N[391] or the aromatic ring,[320, 392] and ring cleavage reactions[151, 290, 394] have all been reported in aromatic systems. These initial ozonation steps often produce intermediates that are themselves reactive towards O_3.[178] Electron donating groups activate reactions between aromatic carbons and O_3, resulting in highly oxidized aromatic products like quinones.[290, 335, 320, 394]

PPDs. Historically, work on PPD ozonation has emphasized formation of N−O oxides, analogous to ozonation of amines, resulting in dinitrone products for PPD ozonation.[340, 234, 233, 63, 60] In the case of 6PPD, this assignment was recently repudiated on the basis of two-dimensional nuclear magnetic resonance spectroscopy,[399] and quinones are now understood to form instead,[359, 414] representing about 10 % of the product distribution for 6PPD.[177] Beyond this, a great number of reaction products have been determined experimentally,[340, 234, 233, 217, 359] though mechanistic details of these transformations are not always clear. A few recent studies have emphasized the formation of quinone diimines (QDIs) in the various ozonation pathways of PPDs, including the formation of 6PPDQ.[63, 217, 359] Even still, the stepwise mechanism of C−O bond formation in PPDs is completely unexplored to the best of our knowledge, despite the ultimate necessity of this motif in the production of 6PPDQ.

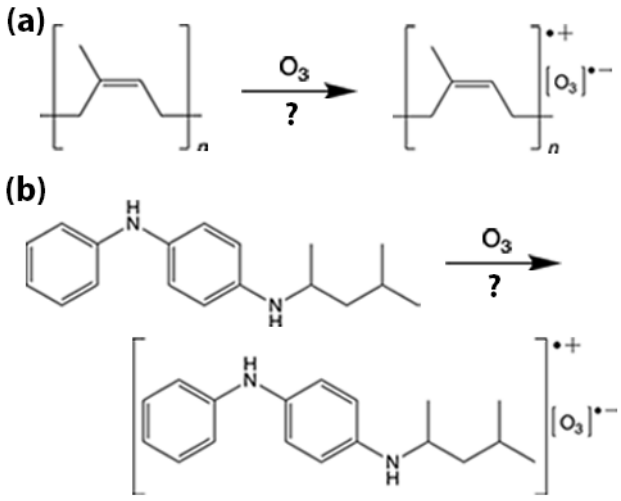

Figure 4.1: Ozone charge transfer complexes for (a) natural rubber and (b) 6PPD have been proposed by a number of authors (see text).

Charge transfer mechanisms. For each of the classes of reactions discussed above, a number of authors argue that ozonation reactions are initiated by one-electron charge transfer (CT) to form biradical, zwitterionic pre-reaction complexes (Figure 4.1). Examples for alkenes,[435, 61, 62, 353] amines,[23, 25, 289, 253, 365] aromatics,[290, 391] and PPDs[330, 63, 338, 60] can be found at the indicated references. Such proposals are defended on the basis of a strong correlation between substrate ionization potential and O_3 reaction rates,[435, 60] electron spin resonance (ESR) spectra that presence of radicals in the reaction mixture,[63] or details of product distributions.[353, 253] Some have expressed skepticism about these CT intermediates, which have not been isolated experimentally, though theoretical literature analyzing this proposal is sparse.[235, 242, 365] Often, these proposals posit that electron transfer is the rate determining step of ozonation, so the existence of these complexes for olefins and PPDs is of present interest.

4.1.2 Modeling ozone chemistry

Accurate modeling of the electronic structure of ozone (O_3) is a formidable challenge in quantum chemistry, and many generally reliable methods have been shown to yield (sometimes catastrophically) bad predictions for O_3 chemistry.[298] Beginning with some of the earliest theoretical work, O_3 was generally accepted to have a biradical ground state.[136, 159] Subsequent work has called this once-settled conclusion into question. At least one multireference study indicated that the ground state of O_3 is a "regular" (*i.e.* closed-shell) singlet, with authors arguing that the electronic structure of O_3 can be completely captured

without reference to biradical character.[200] Ozone is a difficult modeling problem because the truth lies somewhere between these two extremes, and a number of researchers have quantified the degree of biradical character in O_3, with values ranging from 16–49 %.[135, 280, 281, 109, 50] Regardless of the exact degree of biradical character, it is clear that O_3 is a genuinely multireference (MR) system. As a result, much of the highest quality theoretical literature on O_3 chemistry resorts to one of a number of MR schemes.[350, 308]

Nevertheless, many single-reference (SR) approaches to O_3 modeling have been reported.[12, 87, 89, 69, 70, 419, 224, 15, 287, 243, 405, 59] Errors in these predictions can be substantial. As Wheeler *et al.* have noted, generally respectable SR methodologies predict barrier heights with discrepancies in excess of $10\,\mathrm{kcal\,mol^{-1}}$ for small systems like C_2H_2 and C_2H_4, and even the generally reliable CCSD(T) (coupled-cluster with single, double, and perturbative triple excitations) method gives unsatisfactory results.[419] To take just one relevant example, these high-level methods predict divergent results for the initial step of O_3 addition to olefins.[350, 224, 128] In order to systematically approach the fully correlated limit, inclusion of explicit triple and perturbative quadruple excitations (the CCSDT(Q) method) is necessary.[419, 437, 405] While Trogolo *et al.* report results of this quality for a number of small systems, the $\mathcal{O}(N^9)$ scaling of this method excludes its use for the present systems.

Instead, systems of present interest require treatment with either less computationally demanding wave function approaches or density functional approximations (DFAs). A number of DFA treatments of ozone chemistry have been reported.[69, 70, 405, 392, 365] Generally speaking, however, out-of-the box DFA treatments are unable to predict ozone reaction energies with consistent fidelity,[405] while more success can be expected for barrier heights, where correlation treatments converge more rapidly than reaction energies.[437] Hybrid density functionals generally exhibit the best performance for both overall thermodynamics and transition energies.[405] Spin projection schemes[197] are known to improve DFA results for related systems,[241] and this approach has been used to model O_3 chemistry in select systems.[350, 365] On the other hand, novel low-scaling wave function approaches like regularized orbital-optimized second-order Møller–Plesset perturbation theory (κ-OOMP2) effectively treat radical species in other contexts,[240, 364, 342] though their use for O_3 chemistry has not been previously explored.

4.2 Computational methods

Methods of electron correlation. In the present study, we consider the ωB97X-V[269] and ωB97M-V[268] density functional approximations (DFAs), as well as regularized orbital-optimized second-order Møller–Plesset perturbation theory (κ-OOMP2)[240] in our modeling of O_3 reactivity. These density functionals were chosen on the bases that hybrids outperform other classes of DFAs for O_3 chemistry[405] and that ωB97X-V and ωB97M-V, specifically, have been shown to yield highly accurate predictions for thermochemistry and reaction barrier heights.[272] On the other end of the spectrum, we also explore the use of κ-OOMP2[240]

as a low-scaling wave function method for modeling O_3 chemistry. Though unexplored in this context, κ-OOMP2 is able to successfully treat strong correlation in other systems when combined with spin projection,[241] as discussed further below.

Spin projection. Yamaguchi's approximate spin projection (AP) method[197] was used to address spin contamination in both DFA and κ-OOMP2 computations. Procedurally, the degree of spin contamination in the singlet reference state is represented by the parameter

$$\alpha = \frac{{}^1\langle \hat{\mathbf{S}}^2 \rangle_{\mathrm{SC}}}{{}^3\langle \hat{\mathbf{S}}^2 \rangle - {}^1\langle \hat{\mathbf{S}}^2 \rangle_{\mathrm{SC}}}, \tag{4.1}$$

where ${}^1\langle \hat{\mathbf{S}}^2 \rangle_{\mathrm{SC}}$ and ${}^3\langle \hat{\mathbf{S}}^2 \rangle$ are the expectation values of the total spin operator for the spin-contaminated (SC) singlet reference state and a high-spin triplet state, respectively. This parameter is then used to project energetic contributions from the high-spin state out of the targeted singlet reference, affording the corrected energy

$${}^1E_{\mathrm{AP}} = {}^1E_{\mathrm{SC}} + \alpha \left({}^1E_{\mathrm{SC}} - {}^3E \right) \tag{4.2}$$

using the energies of the triplet and spin-contaminated singlet reference states, ${}^3E$ and ${}^1E_{\mathrm{SC}}$. Both SC and AP energies are reported for all reactive oxygen species, including ozone, singlet oxygen, and various intermediates and transition states that were determined to resemble these molecules on the basis of the values of $\langle \hat{\mathbf{S}}^2 \rangle$ for computed reference states.

Exploring potential energy surfaces. Single-point energies were evaluated using either the def2-TZVPP[417] or def2-QZVPPD[420] basis set, as indicated in the text below. Exchange–correlation integrals were evaluated using fine-mesh (99,590) Lebedev integration grids.[237, 236] Self-consistent field (SCF) iterations were to at least 1×10^{-8} a.u. in all cases, and a tighter threshold of 1×10^{-10} a.u. was achieved where possible. Unrestricted reference states and stability analysis were used to confirm ground electronic state configurations were obtained in all cases. Where included, molecular orbitals were obtained as intrinsic bonding orbitals (IBOs),[218] using a recently reported implementation.[134]

All geometries utilized in this work were optimized using the ωB97X-V density functional with the def2-TVZPP basis, and stationary points were obtained using gradient and energy thresholds of 3×10^{-4} and 1×10^{-6} a.u., respectively. While algorithms for structural optimization on spin projection surfaces have been reported,[214, 350] all geometric properties and harmonic vibrational frequencies have been obtained on the (spin-contaminated) singlet energy surfaces. Initial structures for transition state optimizations were obtained using either the freezing string method[35, 362] or constrained optimizations near the expected transition structure. Harmonic frequencies for each optimized structure were determined through diagonalization of the full Hessian matrix, and stationary points were characterized as local minima or transition states based on the presence or absence of a single imaginary frequency in this analysis. These harmonic frequencies were also used to calculate vibrational zero point energy (VZPE) corrections for all relevant species. All computations were completed using the Q-Chem package.[361]

Energy decomposition analysis. The adiabatic energy decomposition analysis (EDA) of Head-Gordon and coworkers[266] was used to evaluate the formation of charge transfer (CT) complexes. Interactions between fragments defined as substrate radical cations ($X^{\cdot+}$) and ozone radical anion ($O_3^{\cdot-}$) were treated using a hierarchy of mathematical constraints that model frozen electrostatics (FRZ), orbital polarization (POL), and CT contributions to overall binding energies. A full description of this formalism and the components of the different potential energy surfaces may be found elsewhere.[174, 266, 264] Incremental energy contributions are defined as

$$\Delta E_{\mathrm{FRZ}} = E_{\mathrm{FRZ}} - \sum_{\alpha} E_{\alpha} \tag{4.3}$$

$$\Delta E_{\mathrm{POL}} = E_{\mathrm{POL}} - E_{\mathrm{FRZ}} \tag{4.4}$$

$$\Delta E_{\mathrm{CT}} = E_{\mathrm{FULL}} - E_{\mathrm{POL}}, \tag{4.5}$$

where E_{FRZ}, E_{POL}, and E_{FULL} and the minimum energies on the frozen, polarization, and unconstrained PESs, respectively, and the E_{α} are the energies of the radical ion fragments in unconstrained computations.

For present purposes, it is critical to note that E_{POL} contains all terms of the standard (*e.g.* Born–Oppenheimer, non-relativistic, *etc.*) physical model, but explicitly forbids CT between fragments. By evaluating the energetics of radical ionic fragments on this surface relative to an unconstrained computation, we can determine the feasibility of CT complex formation.

Surrogate molecules. The structural optimization procedures outlined above are computationally expensive, bordering on intractability for 6PPD and for large polymeric units of natural rubber (*cis*-polyisoprene, **NR**). We have therefore used surrogate molecules for each of these compounds in our exploration of the potential energy surfaces (PESs) of ozone reaction and the characterization of stationary points. Specifically, we have used 2-methyl-2-butene (2M2B, **1**) and 4-aminodiphenylamine (4ADPA, **2**) as stand-ins for natural rubber and 6PPD, respectively (Figure 4.2). We have also modeled select key PPD reaction steps using *N*-methyl-*N*′-phenyl-*p*-phenylenediamine (MePPD, **3**) to account for the known effects of *N*-alkylation on PPD ozonation rates.[84, 235] While subtle energetic differences between these surrogates and their parent molecules may exist, we anticipate critical features of the PESs are preserved.

Conformer specifications Our computational work utilized a number of distinct isomers and conformers for all derivatives of 4-aminodiphenylamine (4ADPA, **2**) and *N*-methyl-*N*′-phenyl-*p*-phenylenediamine (MePPD, **3**), and only results corresponding to the minimum-energy conformers are reported in the main text. We include structural details for each conformer in the molecular coordinate (`.xyz`) files accompanying the SI, and energies for these in the corresponding spreadsheet. The labeling scheme for these conformers is defined

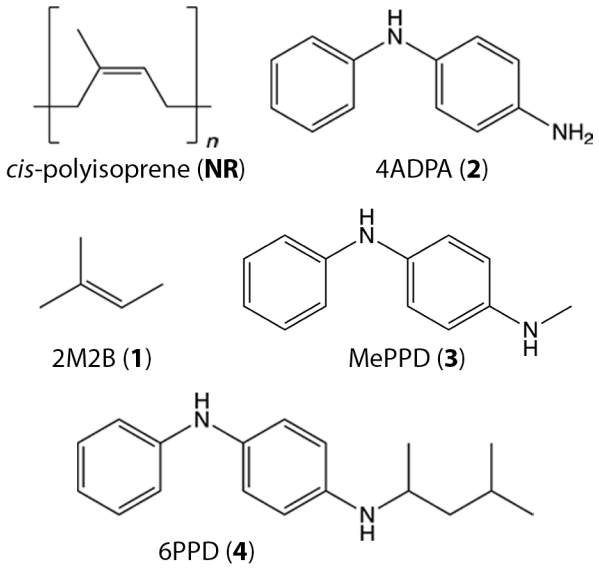

Figure 4.2: Substrates used in modeling ozone reactivity. Primary exploration of potential energy surfaces was completed using **1** and **2**, as surrogates for **NR** and **4**. Select modeling was completed for compound **3** to better understand experimental results for ozonation kinetics.

in Figures 4.3-4.6. Conformers for quinone diimine (QDI) structures follow the same ordering, though they are not explicitly included in the figures below.

4.3 Benchmarking methods for modeling O_3 chemistry

In their study of the convergence of the coupled-cluster hierarchy for ozone, Trogolo *et al.* report a set of reaction energies that we use as a highly accurate benchmark for ozone chemistry.[405] Their results consist of CCSDT(Q) energies extrapolated to the complete basis set (CBS) limit for three cycloadditions (C_2H_4, C_2H_2, HCN), two insertion reactions (HCl, NH_3), two linear additions ($N(CH_3)_3$ and Br^-), and three ozone scission reactions (O_3, $N(CH_3)_3O_3$, BrO_3^-). Across these species, van der Waals (vdW) complexation energies, transition state barrier heights, and overall reaction energies are included for all of the listed reaction types except ozone scission, where only the overall reaction energy is reported. Benchmark comparisons to these high-level CC reaction energies and barrier heights for the ωB97X-V and ωB97M-V density functionals as well as the κ-OOMP2 approach are found in Table 4.1, and comparisons for vdW complexes in Table S1.

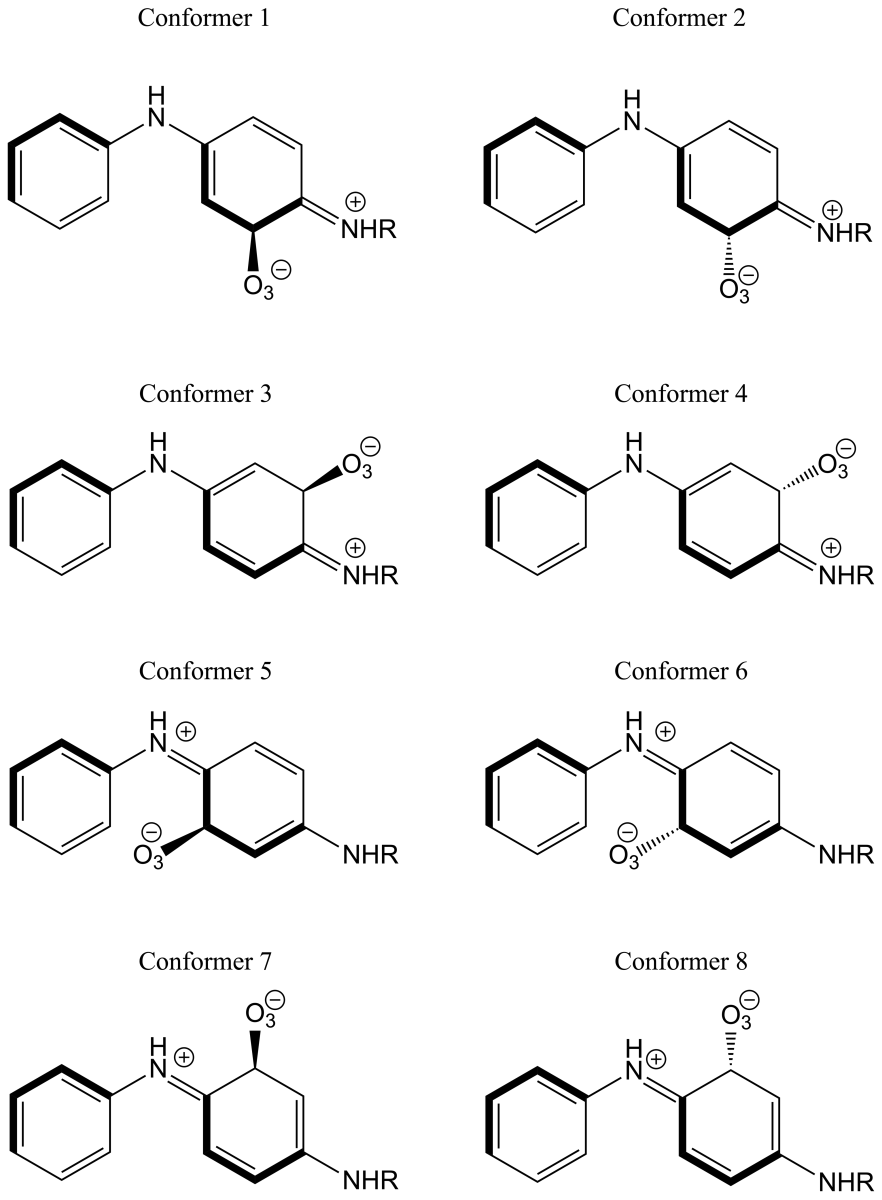

Figure 4.3: Definition of conformer labeling for PPD DeMore adducts. R = H (4ADPA), Me (MePPD).

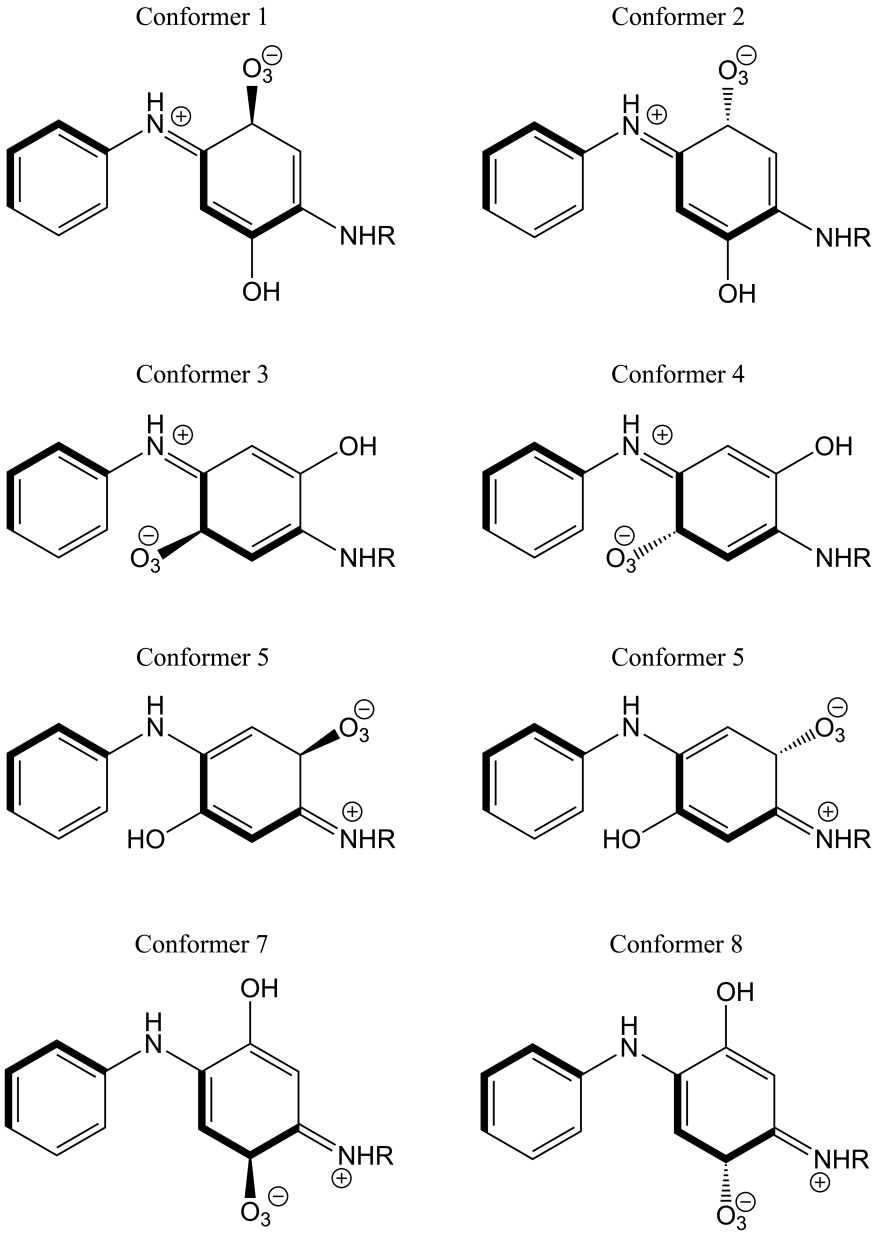

Figure 4.4: Definition of conformer labeling for PPD-OH DeMore adducts. R = H (4ADPA), Me (MePPD).

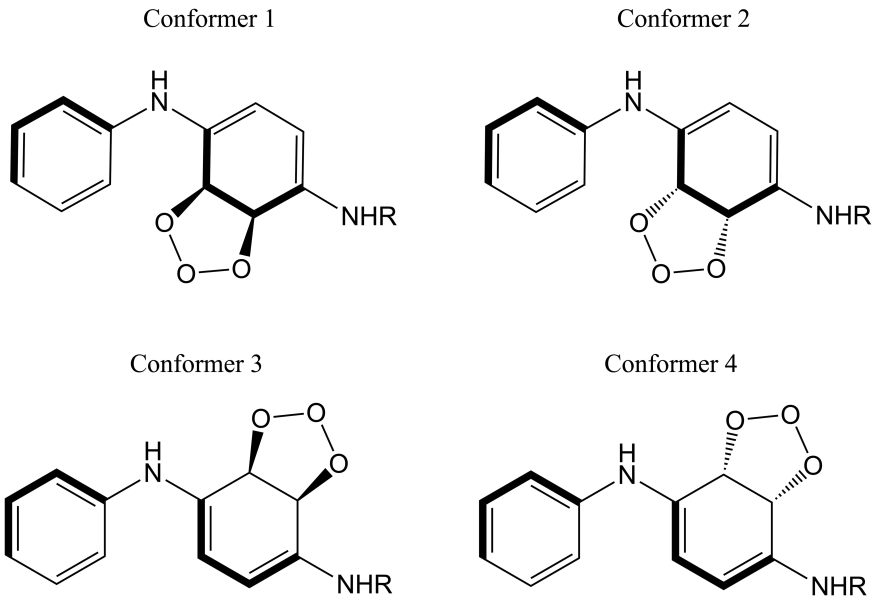

Figure 4.5: Definition of conformer labeling for PPD primary ozonides. R = H (4ADPA), Me (MePPD).

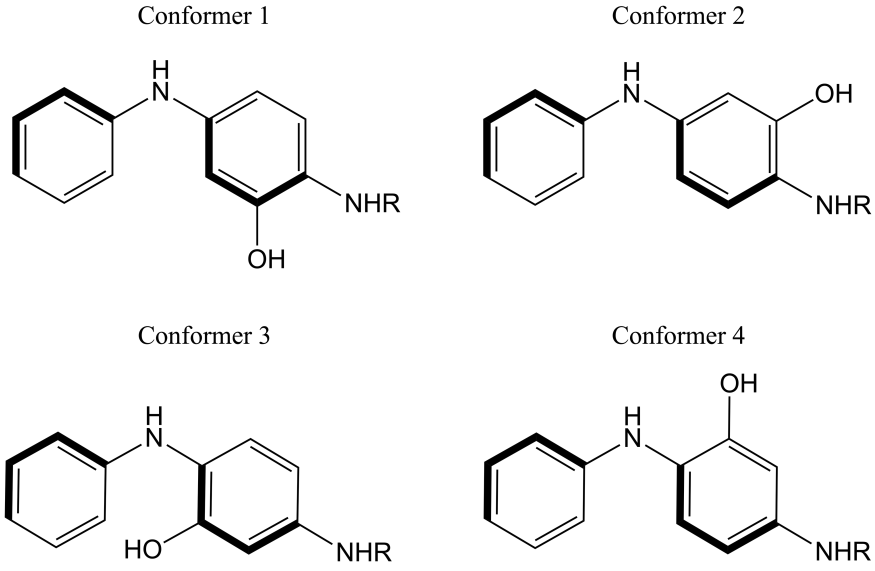

Figure 4.6: Definition of conformer labeling for hydroxylated PPDs. R = H (4ADPA), Me (MePPD).

Table 4.1: Errors in spin-contaminated (SC) and approximate projection (AP) single-point energies for benchmark ozonation reactions. Reference values are CCSDT(Q) results extrapolated to the CBS limit obtained from Ref. 405.

	Error in ΔE (kcal mol^{-1})								ΔE_{ref}
	def2-TZVPP				def2-QZVPPD				CBS
	ωB97X-V		ωB97M-V		ωB97X-V		ωB97M-V		CCSDT(Q)
Substrate	SC	AP	SC	AP	SC	AP	SC	AP	
	Ozone Addition/Insertion Barrier Heights								
C_2H_4	1.06	8.71	-0.80	5.69	1.38	9.12	-0.51	5.96	3.01
C_2H_2	-0.08	7.57	-2.02	4.47	0.21	7.95	-1.75	4.71	7.65
HCN	0.27	7.92	-1.31	5.18	0.69	8.43	-0.88	5.59	17.92
HCl	-0.59	3.71	-1.86	1.92	0.16	4.57	-1.04	2.76	20.23
NH_3	1.46	6.12	0.08	4.87	1.99	6.91	0.61	5.60	23.13
$N(CH_3)_3$	2.64	10.29	0.59	7.08	2.62	10.36	0.56	7.03	10.33
Br^-	0.47	8.12	-2.14	4.35	0.19	7.93	-2.18	4.29	9.73
RMSD	1.25	7.73	1.46	5.01	1.38	8.07	1.23	5.29	–
	Ozone Addition/Insertion Reaction Energies								
C_2H_4	-9.28	-1.64	-8.93	2.24	-8.67	-0.93	-8.32	-1.86	-56.19
C_2H_2	-9.32	-1.67	-9.21	2.72	-8.79	-1.05	-8.69	-2.23	-63.01
HCN	-9.55	-1.90	-9.26	2.77	-8.89	-1.15	-8.57	-2.11	-19.39
HCl	-5.64	2.01	-8.42	1.93	-5.38	2.36	-8.09	-1.63	-4.99
NH_3	-7.99	-0.35	-9.66	3.16	-7.14	0.60	-8.76	-2.30	-12.13
$N(CH_3)_3$	-18.50	-0.11	-16.17	2.52	-18.40	0.04	-16.03	2.58	-12.09[a]
Br^-	-7.60	5.13	-7.73	3.50	-7.73	5.24	-7.54	3.87	5.15
RMSD	10.42	2.38	10.25	2.76	10.07	2.29	9.81	2.46	–
	$^1O_2$ Scission Reaction Energies								
O_3	-21.59	-2.99	-19.80	-0.89	-21.11	-2.58	-19.29	-0.47	49.83
$N(CH_3)_3O_3$	-20.02	-1.46	-17.64	1.27	-20.40	-1.80	-18.02	0.80	-9.20[a]
BrO_3^-	-17.62	0.94	-15.93	2.99	-20.09	-1.48	-18.31	0.50	15.72

[a] Computed indirectly *via* addition of partial reaction channels. See Ref. 405 for details.

4.3.1 Hybrid density functionals

As in previous work,[350] significant spin contamination was found on the singlet DFA potential energy surfaces (PESs) for reactive oxygen species, which we addressed through Yamaguchi's approximate projection scheme.[197] Comparison of the results from spin contaminated (SC) and approximate projection (AP) energies highlight the complexities of strong correlation in ozone systems. Specifically, these data are conclusive that SC predictions of barrier heights consistently outperform their AP counterparts, while AP schemes are necessary in order to achieve accurate predictions of reaction energies for ozone reactions. While necessary for all reaction energies, AP corrections are especially important when $^1O_2$ is a product, as SC errors can approach 20 kcal mol^{-1}, even with the def2-QZVPPD set, which closely approximates the CBS limit.[420] These errors are so egregious that SC predictions for both ωB97X-V and ωB97M-V reactions energies are qualitatively incorrect in some cases,

even predicting the wrong sign for the thermicity of Br^- ozone addition and then BrO_3^- dissociation to BrO^- and $^1O_2$.

The discrepancy between performance for ΔE_{rxn} and ΔE_{TS} is troubling, and we discuss the theoretical basis for this in Section S1.3. Here, we note simply that the best performance on ΔE_{TS} is achieved using spin-contaminated structures, where def2-QZVPPD RSMDs for ωB97X-V and ωB97M-V are 1.38 and 1.23 kcal mol^{-1}, respectively. Both DFAs even predict energies within the bounds of chemical accuracy for select SC transition structures. AP schemes are necessary to achieve tolerable predictions of ΔE_{rxn} for these funtionals, resulting in RMSDs of 2.29 and 2.46 kcal mol^{-1} for reactions that do not produce $^1O_2$. AP-ωB97M-V energies are particularly accurate for O_3 scission reactions, and chemical accuracy is achieved in all cases. For ωB97X-V, AP errors are 1.48–2.58 kcal mol^{-1} in magnitude.

The disparity in the accuracy of predictions for barrier heights and reaction energies, as well as the poor performance of κ-OOMP2, stems from changes in the extent of multireference character of various species across the ozonation PES. Stationary points corresponding to reactant states exhibit strong correlation and spin symmetry breaking due to the biradicaloid nature of O_3. In formation of a vdW complex, the electronic structure of O_3 does not change drastically, and both SC and AP schemes treat the complexation energy in a balanced way. As a result, all methods achieve chemical accuracy, *i.e.* errors less than 1 kcal mol^{-1}, for predictions of ΔE_{vdW} (Table 4.3). The situation is materially different for computations of ΔE_{rxn}, where the reaction products do not exhibit the same multireference character as the reactants, evidenced by a lack of spin symmetry breaking on the unrestricted singlet surface across methods. This imbalance results in SC predictions of ΔE_{rxn} that are generally 7–9 kcal mol^{-1} too exothermic. The magnitude of these errors mirrors the size of AP corrections for O_3, which are -7.7 and -6.5 kcal mol^{-1} for ωB97X-V and ωB97M-V, respectively. Hence, the use of AP corrections brings results for these DFAs in closer agreement with the CCSDT(Q) results and explains why SC methods that are effective at predicting ΔE_{vdW} fail for ΔE_{rxn}.

By contrast, the AP scheme overestimates the barrier heights of ozonation reactions by a similar magnitude in the majority of cases, while the SC values generally hover around 1 kcal mol^{-1}. Indeed, even sub-chemical accuracy is achieved with SC barrier heights in about half of the included systems, suggesting a balance in the degree of correlation errors in reactants and transition states is present on the SC but not the AP surfaces. It is difficult to explain this solely on the basis of spin contamination, as the transition structures for cycloaddition and linear addition are spin pure, and therefore unaffected by a spin correction. Nevertheless, SC predictions of ΔE_{TS} exhibit a similarly high degree of accuracy as they do for the insertion reactions of HCl and NH_3, where the transition structures are spin-polarized. Indeed, AP corrections uniformly reduce the accuracy of computed ΔE_{TS}, regardless of the spin-polarization of a given transition structure. These results would be unintuitive if one expected the extent of spin-polarization in DFA calculations to match those of exact wavefunction theory. However, the exact Kohn-Sham DFT orbitals are expected to be unrestricted in general,[325] and we remind the reader that the extent of spin-contamination in DFT is measured for the fictitious reference system of non-interacting electrons, rather

Table 4.2: Effect of regularizer strength (κ) on performance of κ-OOMP2 for benchmark ozonation reactions. Empty columns for approximate projection (AP) results indicate an absence of spin polarization for all relevant species and the given method. CCSDT(Q)/CBS results obtained from Ref. 405

	Error in ΔE (kcal mol^{-1})								ΔE_{ref}
	def2-TZVPP						def2-QZVPPD		CBS
κ	0.80		1.10		1.45		1.45		CCSDT(Q)
Substrate	SC	AP	SC	AP	SC	AP	SC	AP	
Ozone Addition/Insertion Barrier Heights									
C_2H_4	8.32	18.31	0.96	–	-0.52	–	-1.30	–	3.01
C_2H_2	8.81	18.79	1.40	–	-0.10	–	-0.86	–	7.65
HCN	10.51	20.50	2.59	–	0.58	–	-0.04	–	17.92
HCl	13.54	23.52	6.11	–	4.16	–	3.32	–	20.23
NH_3	11.43	21.42	5.52	–	4.60	–	4.15	–	23.13
$N(CH_3)_3$	6.78	16.76	1.57	–	1.17	–	0.08	–	10.33
Br^-	7.19	17.17	2.48	–	2.63	–	0.51	–	9.73
RMSD	9.78	19.63	3.51	–	2.60	–	2.10	–	–
Ozone Addition/Insertion Reaction Energies									
C_2H_4	-17.31	-7.33	-13.98	–	-5.40	–	-5.11	–	-56.19
C_2H_2	-14.46	-4.47	-10.98	–	-2.36	–	-2.66	–	-63.01
HCN	-9.85	0.14	-7.69	–	-0.31	–	-0.74	–	-19.39
HCl	-3.06	6.93	-1.92	–	4.12	–	2.86	–	-4.99
NH_3	-7.70	2.29	-5.13	–	2.34	–	2.55	–	-12.13
$N(CH_3)_3$	0.10	10.08	1.56	–	7.95	–	7.24	–	-12.09
Br^-	7.33	17.31	3.28	–	4.39	–	1.52	–	5.15
RMSD	10.20	8.59	7.73	–	4.47	–	3.84	–	–
$^1O_2$ Scission Reaction Energies									
O_3	-31.87	-7.62	-22.45	-8.99	-11.13	1.69	-6.96	5.53	49.83
$N(CH_3)_3O_3$	-25.21	-0.96	-21.39	-7.93	-13.26	-0.45	-13.24	7.24	-9.20
BrO_3^-	-17.76	6.49	-15.30	-1.84	-8.57	4.25	-11.72	1.52	15.72

than the physical system of interacting electrons.

4.3.2 Wave function approaches

Recent developments in electronic structure theory have led to orbital optimization techniques that provide tractable alternatives to DFAs on the one hand and high-level CC or multireference approaches on the other. Orbital-optimized MP2 (OOMP2) has proven particularly promising, and regularization schemes like κ-OOMP2 have been shown to perform

well across a variety of radical and closed shell systems.[342, 364, 240] The strength of the regularizer (κ) has been shown to strongly influence the performance of the κ-OOMP2 method, and different values of κ are appropriate for different applications.[240, 364, 342] In particular, like OOMP2 itself ($\kappa \to \infty$), overly weak regularizers (κ too large) have been shown to result in artificial symmetry restoration in strongly correlated systems. Stronger regularizers (lower κ values) are necessary to recover essential spin polarization that is associated with systems exhibiting strong correlation. At the other extreme, excessively strong regularization leads to artificial symmetry-breaking, as is well-known for mean-field Hartree-Fock (i.e. $\kappa = 0$).[342].

Given previous indications that O_3 possesses both static and dynamic correlation,[350, 419, 405] we present results for $\kappa = 0.80$, 1.10, and 1.45.[342] Benchmark predictions evaluated at each of these values of are presented in Table 4.2. For the weaker two regularizers ($\kappa = 1.10$, 1.45), the stable reference state of O_3 was not spin-polarized and the AP scheme was only used for reactions producing $^1O_2$, which remained polarized. Both SC and AP results are included for $\kappa = 0.80$, which preserved broken symmetry for O_3. On the basis of def2-TZVPP results, the best performance is obtained with $\kappa = 1.45$, and we only obtain def2-QZVPPD results with this regularizer strength. In the larger basis, this method yields RMSDs for ΔE_{rxn} and ΔE_{TS} of 5.12 and 2.10 kcal mol^{-1} relative to CCSDT(Q)/CBS results. In some cases, errors for individual entries are nearly exact, while disagreement in the reaction energy for $N(CH_3)_3$ is in excess of 10 kcal mol^{-1}. As for the DFAs, AP is necessary to achieve reasonable agreement for O_3 scission reactions, but even here it exhibits errors in excess of 1 kcal mol^{-1}.

Our observations for O_3 and other similar molecules are that the generally recommended [240] value of $\kappa = 1.45$ results in loss of spin-polarization in the reference determinant for O_3 and related species. This behavior persists with $\kappa = 1.10$ (which has been recommended to preserve essential symmetry breaking in transition metal systems.[342]), and spin-polarization is finally obtained with $\kappa = 0.8$ (i.e. very strong regularization). Interestingly this persistence of symmetry restoration indicates that electron correlation effects in ozone (specifically at its most stable geometry) are not as strong as in strongly correlation systems such as C_{36} where spin-polarization is recovered in κ-OOMP2 with far weaker regularization,[239] or in transition-metal containing systems.[342] In other words, the k-OOMP2 results suggest that O_3 at its equilibrium geometry is not actually strongly correlated because it does not exhibit *essential* symmetry breaking for κ values in the recommended range.[342]

As a corollary, the use of too-strong regularizers overly dampens the effects of dynamic correlation, and this effect is apparently significant for the O_3 systems here, such that $\kappa = 0.8$ results in poor agreement with benchmark energies (Table 4.2). Instead, the best agreement with CCSDT(Q) benchmarks[405] is achieved with $\kappa = 1.45$. Even still, the ωB97X-V and ωB97M-V DFAs outperform κ-OOMP2. In particular, none of the tested parameterizations of κ-OOMP2 achieve chemical accuracy for the thermodynamics of O_3 splitting ($O_3 \to {}^1O_2 + O(3\,p)$), which has been put forth as a test system for ozone modeling.[405] As a result, we do not use κ-OOMP2 for any of the main results of this paper, despite its success for other strongly correlated systems.

Table 4.3: Errors in spin-contaminated (SC) and approximate projection (AP) single-point energies for benchmark van der Waals (vdW) complexation energies. For κ-OOMP2 (κ = 1.45) results, no spin polarization was observed for O_3 or any vdW complex, so "SC" does not apply and AP corrections are identically zero. Reference values are CCSDT(Q) results extrapolated to the CBS limit obtained from Ref. 405. Highlighted boxes represent the best performing methodology for a given parameter at a given basis set truncation.

	Error in ΔE (kcal mol^{-1})										ΔE_{ref}
	def2-TZVPP					def2-QZVPPD					CBS
	ωB97X-V		ωB97M-V		κ-OOMP2	ωB97X-V		ωB97M-V		κ-OOMP2	CCSDT(Q)
Substrate	SC	AP	SC	AP	–	SC	AP	SC	AP	–	
vdW Complexation Energies											
C_2H_4	-0.05	-0.76	-0.10	0.40	-0.40	0.23	-0.38	0.20	-0.12	-0.71	-2.01
C_2H_2	-0.10	-0.70	-0.13	0.34	-0.38	0.15	-0.36	0.13	-0.11	-0.61	-1.83
HCN	-0.12	-0.04	-0.09	0.09	-0.32	0.10	0.31	0.16	0.33	-0.57	-1.96
HCl	-0.10	-0.06	-0.10	0.05	-0.37	0.28	0.45	0.33	0.50	-0.26	-2.23
NH_3	-0.32	-0.12	-0.38	0.04	-0.40	0.20	0.52	0.19	0.53	-0.40	-2.75
$N(CH_3)_3$	-0.27	-0.91	-0.38	0.59	-1.01	0.31	-0.20	0.27	0.07	-1.16	-3.80
Br^-	-3.34	-1.33	-4.09	2.75	0.41	-1.80	0.45	-2.28	-0.80	0.07	-6.13
RMSD	1.27	0.72	0.96	1.56	0.52	0.71	0.39	0.89	0.43	0.63	–

While the energetics of many reactions are stable across a wide range of values of the regularizer strength κ, other systems exhibit a strong κ-dependence. More specifically, the tuning of the regularizer strength is important in systems with essential spin symmetry breaking as weak regularizers can lead to spurious resymmetrization.[342] This occurs for O_3 with the recommended value of κ = 1.45,[240] and even at the stronger value of κ = 1.1, which has been recommended to preserve essential symmetry breaking in transition metal systems.[342] Increasing the regularizer strength further to $\kappa = 0.8$ recovers a broken symmetry solution, which is the physically correct single-reference picture for a biradicaloid system like O_3.[135, 280, 281, 109, 50] Nevertheless, as discussed in Section 4.3.2 above, this results in poor performance. It seems, then, that for O_3 chemistry you cannot have your cake and eat it too. Strong κ-OOMP2 regularizers lead to HF-like results, and therefore capture the static correlation intrinsic to O_3 and its derivatives, but fail to account for the dynamic correlation in this system, leading to poor results. On the other hand, weakly regularized κ-OOMP2 eliminates the (physically correct) spin polarization in the reference determinant, but can capture dynamic correlation, providing better results overall.

4.3.3 Benchmark values for vdW complexes

In contrast to transition structures and reaction energies, both spin contaminated and approximate projection (AP)[197] schemes yield adequate results for van der Waals (vdW) complexation energies (ΔE_{vdW}) with O_3 (Table 4.3). Reference values obtained from Ref. 405 were computed using CCSDT(Q) and extrapolated to the complete basis set limit. Results using the ωB97X-V[269] and ωB97M-V[268] density functionals, as well as the κ-OOMP2 method (κ = 1.45),[240] are within chemical accuracy for almost all species. Furthermore,

while not employed here for the sake of simplicity, we expect even better agreement could be achieved with use of counterpoise corrections (CPCs) to correct for the basis set superposition error (BSSE) that arises in these computations.[49] When the def2-TZVPP basis set[417] is used, the errors for the Br^- complex are significantly larger than other species, reflecting the necessity of diffuse orbitals in modeling anions. Significantly improved performance is achieved with the def2-QZVPPD set.[420] While values of ΔE_{vdW} do not play a role in the main work of this study, these results provide additional insight into discrepancies in the performance of spin-contaminated (SC) and approximately spin-projected (AP) methods in modeling O_3 chemistry.

4.3.4 Method selection.

Overall, the ωB97X-V and ωB97M-V DFAs perform surprisingly well for these systems, exceeding even the good expectations for hybrid density functionals established in previous work.[405] Each of these methods outperforms κ-OOMP2, where a regularizer balancing the effects of static and dynamic correlation could not be achieved (Section S1.2). Based on these results, DFAs are used for the analysis that follows. The discrepancy between ωB97X-V and ωB97M-V performance is smaller than the overall errors of each of these methods relative to CCSDT(Q), such that the choice between these two methods is unlikely to make a material difference. On the basis of performance with the truncated def2-TZVPP basis set, which we use for systems below, we focus on results from ωB97X-V. Though not the primary purpose of this work, we emphasize here the importance of establishing an effective protocol for DFT modeling of ozone transition states and reaction energies, which are notoriously difficult problems in electronic structure theory.

4.4 EDA of radical ion complexes

As documented in Section 4.1.1, a number of authors argue that explicit $X \rightarrow O_3$ one-electron transfer initiates ozonation chemistry for a wide variety of substrates X. We have used adiabatic energy decomposition analysis (EDA) to analyze this reactivity for 2M2B (**1**) and 4ADPA (**2**) as representative examples of alkenes/unsaturated polymers and PPDs, respectively.

CT complexes between **1** and ozone on the series of ωB97X-V/ def2-TZVPP EDA surfaces indicate that these structures are highly unstable relative to neutral fragments (Figure 4.7). The initial promotion to ionized fragments in this system is energetically expensive, with $\Delta E_{\text{IP}} = 145.2\,\text{kcal mol}^{-1}$. This result is physically reasonable on the basis of experimental results[252] for the first ionization energy of **1** and the electron affinity of ozone, 200.4 and $48.5\,\text{kcal mol}^{-1}$, respectively, yielding $\Delta E_{\text{IF}}^{\text{expt}} = 151.9\,\text{kcal mol}^{-1}$. Interactions between these ionized fragments on the FRZ and POL surfaces are unable to compensate for the high promotion energy, yielding structures that are destabilized by 50.3 and $40.5\,\text{kcal mol}^{-1}$, respectively, relative to the neutral fragments. Upon relaxation of all constraints, spontaneous

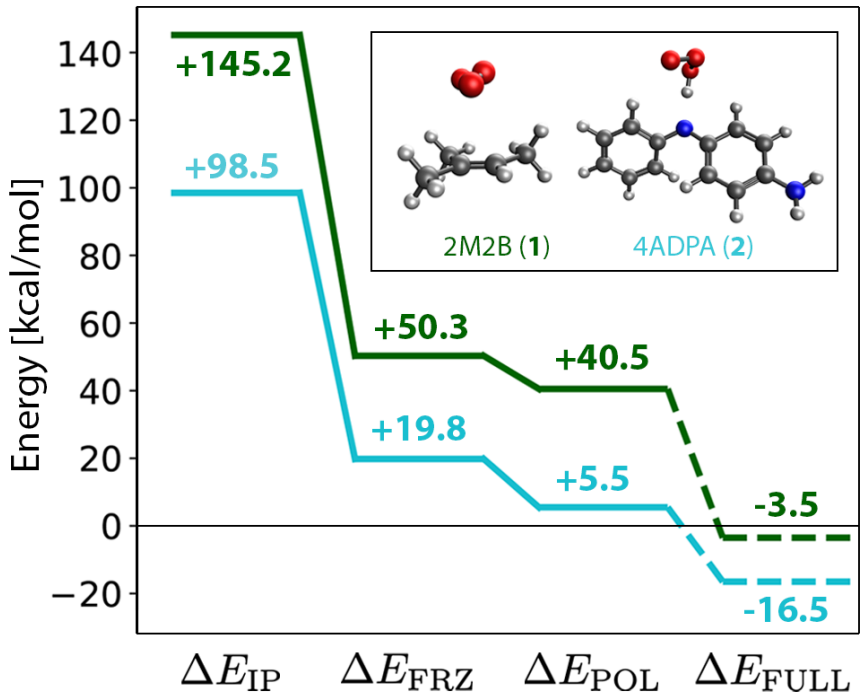

Figure 4.7: Energy decomposition analysis for CT complexes of 2M2B (**1**, top line) and 4ADPA (**2**, bottom line) with O_3. Structural minima for biradical zwitterionic CT complexes could not be found on unconstrained surfaces, where spontaneous charge transfer (indicated by dashed lines) resulted in charge-neutral fragments and the structures shown in the inset. The zero of energy corresponds to the optimal geometry of isolated neutral fragments.

charge transfer results in a neutral van der Waals (vdW) complex between **1** and O_3 (Figure 4.7, inset). The inability of this approach to locate a structural minimum on the $[\mathbf{1}]^{\cdot+}[O_3]^{\cdot-}$ surface indicates that this complex cannot form spontaneously, and the vdW complex will preferentially form instead.

The situation is similar for **2**, which we take to be representative for other PPDs where these CT complexes have been repeatedly proposed.[63, 60] Ionization energies for PPDs are generally lower than those for olefins,[63] and here we compute $\Delta E_{\mathrm{IP}}^{\mathrm{comp}} = 98.5\,\mathrm{kcal\,mol^{-1}}$ for **2**. This lower energetic penalty results in CT complexes that are less energetically unfavorable than those for **1**, with ΔE_{FRZ} and ΔE_{POL} of 19.8 and 5.5 $\mathrm{kcal\,mol^{-1}}$, respectively (Figure 4.7). They are nonetheless still above the zero of energy corresponding to neutral fragments, and so here too relaxation of the CT constraint results in spontaneous electron transfer to afford neutral fragments. Upon subsequent geometry optimization cycles, the neutralized O_3 molecule abstracts a proton from **2** as depicted in the inset of Figure 4.7. While the energy cost to form $[\mathbf{2}]^{\cdot+}[O_3]^{\cdot-}$ on the POL surface is relatively small, it is still

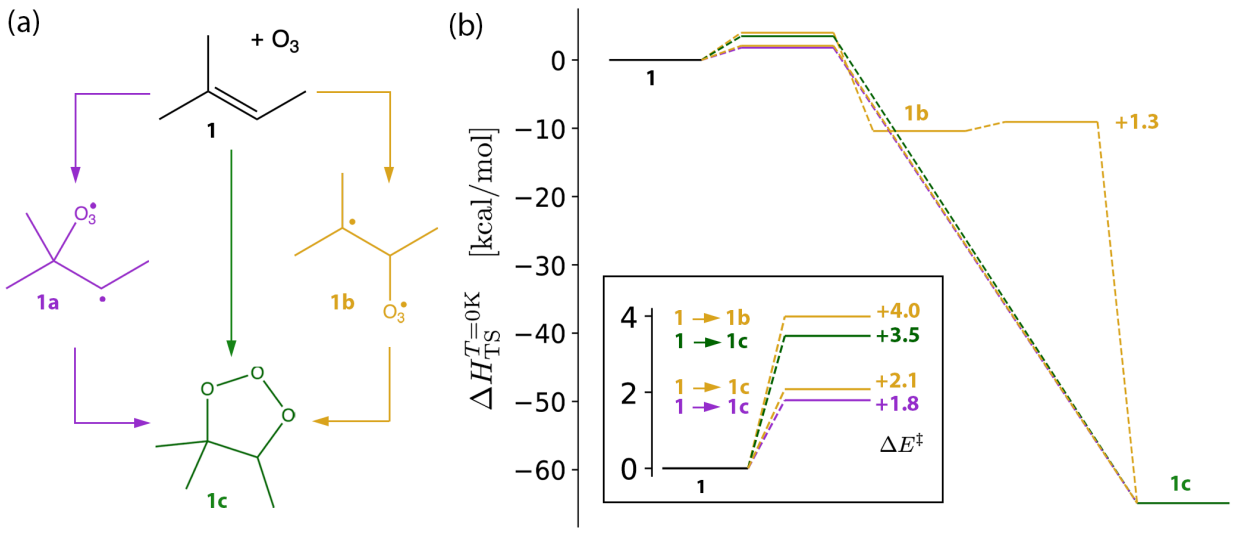

Figure 4.8: Mechanistic possibilities for the formation of the 2-methyl-2-butene (**1**) primary ozonide (**1c**). In addition to the symmetric addition of O_3 to **1** ($\Delta H_{TS}^{T=0\,K} = 3.5\,kcal\,mol^{-1}$) and the true DeMore pathway through **1b** ($\Delta H_{TS}^{T=0\,K} = 4.0\,kcal\,mol^{-1}$), two asymmetric additions ($\Delta E^{\ddagger} = 1.8$ and $2.1\,kcal\,mol^{-1}$) *without* isolable DeMore intermediates were identified.

unbound. Spontaneous reversion to neutral fragments upon relaxation of the constraints used to force formation of the CT complex indicates that such complexes do not form for these systems.

Taken together, the results of Figure 4.7 indicate that CT complexes like those described above do not form in the ozone reactions of **1** and **2**. Inasmuch as these compounds are representative of olefins and PPDs more broadly, this conclusion carries over, and one-electron charge transfer should not be relied upon to explain the kinetics of ozone chemistry for olefins and PPDs, as is common (*cf.* Section 4.1.1).

4.5 Mechanisms of natural rubber ozonation

Having eliminated the possibility of a CT mechanism for **1**, two possibilities remain: concerted (Criegee) and stepwise (DeMore) addition of O_3 across the **1** double bond. Conceptually, two distinct DeMore pathways exist for **1**, corresponding to initial reactions forming secondary (**1a**) and tertiary (**1b**) carbon radicals (Figure 4.8[a]). Each of these structures may then collapse to the primary ozonide (**1c**). Therefore, we expect at least three distinct transition structures on the **1**–O_3 PES.

The Criegee mechanism for addition of O_3 to **1**, where the symmetric formation of two C−O bonds was unambiguously confirmed with vibrational analysis, possesses a barrier

height of 3.5 kcal mol^{-1} on the ωB97X-V/def2-TZVPP surface. Analysis of the DeMore structures **1a** and **1b** was more complicated. While a structure corresponding to **1a** with a single imaginary frequency corresponding to the formation of the C2$-$O$_3$ bond was identified, intrinsic reaction coordinate (IRC) analysis[127, 354] on this structure identified it as a saddle point connecting the vdW complex and primary ozonide **1c**. Hence, this structure actually represents an asymmetric pseudo-Criegee structure, with a barrier of 1.8 kcal mol^{-1}. An otherwise similar structure that initially forms the C3$-$O$_3$ bond with a barrier of 2.1 kcal mol^{-1} was also identified. These structures are DeMore-like in the asymmetric formation of C$-$O bonds, but they do not result in true DeMore intermediates, *i.e.* local minima on the ωB97X-V/def2-TZVPP surface. Nevertheless, asymmetric addition to the double bond in **1** is more favorable than symmetric addition by approximately 1.7 kcal mol^{-1} at the ωB97X-V/def2-TZVPP level.

In addition to these three transition structures, a true DeMore pathway exists for the tertiary radical intermediate **1b**, where IRC analysis does identify a local minimum for this species. The ωB97X-V/def2-TZVPP barrier height for this **1** $\rightarrow$ **1b** is 4.0 kcal mol^{-1}, meaning this will be a minor pathway relative to the Criegee and pseudo-Criegee structures reported above. A second transition structure ($\Delta E^{\ddagger}$ = 1.3 kcal mol^{-1}) was identified for the collapse of **1b** $\rightarrow$ **1c**. Hence, a true DeMore pathway does exist for **1**, but this is not expected to be favorable under the conditions of this model. It is possible that solvation effects could stabilize this pathway, as has been observed in other systems,[228] but we do not explore this here.

Overall, the lowest energy pathway for **1** ozonation is an asymmetric Criegee addition, which possesses a barrier height of a mere 1.8 kcal mol^{-1} at the ωB97X-V/def2-TZVPP level. This and other small barrier heights for this system underscore one difficulty of developing rubber antiozonants. Candidate molecules must possess even smaller transition structure energies in order to effectively scavenge O$_3$. As seen below, PPDs are among the few molecules that achieve this threshold of reactivity.

4.6 Mechanisms of PPD ozonation

PPDs are highly reactive substrates in oxygen and ozone chemistry, and a number of potential pathways for the reaction of ozone with these compounds can be imagined.[217, 359] This panoply of reaction intermediates is reminiscent of the ozone chemistry of aniline[391] and phenolic systems,[291] complicating efforts to identify the mechanism of quinone formation. While a few overarching frameworks have been suggested,[399, 217] no stepwise mechanisms for 6PPD quinone formation have been proposed. We begin the analysis of PPD ozonation with discussion of the kinetics and thermodynamics of ozonation steps for 4ADPA (**2**) in Section 4.6.1, demonstrating that the particularly high activity of PPDs toward O$_3$ stems from direct interactions with the PPD ring system. We then consider the effects of N-alkylation on the kinetics of key ozonation steps in Section 4.6.2. Finally, we discuss proposals that PPD quinones form through quinone diimines (QDIs) in Section 4.6.3.

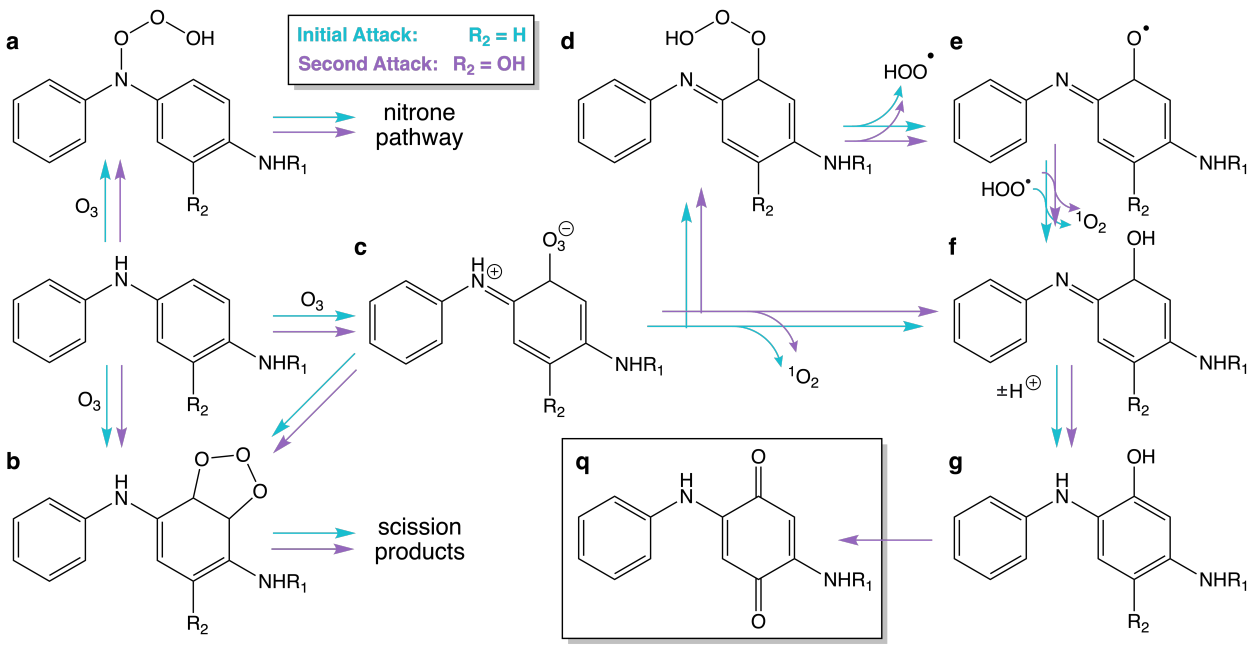

Figure 4.9: Selected reaction pathways for PPDs and ozone. In general, each structure represents a collection of regioisomers. Two sequential additions of ozone to the PPD ring system can afford hydroquinone **g** (R_2 = OH), which is readily oxidized to quinone **q**. R_1 = H, Me, and 1,3-dimethylbutyl correspond to 4-ADPA (**2**), *N*-Me-PPD (**3**), and 6PPD (**4**), respectively.

4.6.1 Ozonation of 4ADPA

Charge transfer mechanisms aside (Section 4.4), we consider a number of initial steps for the reactivity between 4-ADPA (**2**) and O_3, including linear addition of O_3 to N atoms, insertion of O_3 into N−H bonds, and both Criegee (concerted) and Demore (stepwise) addition to the aromatic ring (Figure 4.9). In all cases, a number of regioisomers and conformers were considered. While energetic data for each of these can be found in the SI, here we present transformation energies for only the most stable conformers and select other structures of interest.

Of considered steps, direct interaction between PPD amines and O_3 corresponds to the least favorable transition structures, contrary to historical and prevailing opinion (Figure 4.10).[340, 234, 233, 63, 60] Insertions into the N−H bond exhibited lower barrier heights than N additions, but even these were 17.7 and 13.9 kcal mol^{-1} for terminal and central amines **2a**, respectively (Figures 4.9 and 4.10). Such high barriers are consistent with the high value of the benchmark quality result for NH_3 insertion (ΔE_{TS} = 23.1 kcal mol^{-1}) from Trogolo *et al.*[405] Experimental evidence also supports the conclusion that N−O bond formation is not the major path of ozone consumption in PPDs. Reported ozonation rates

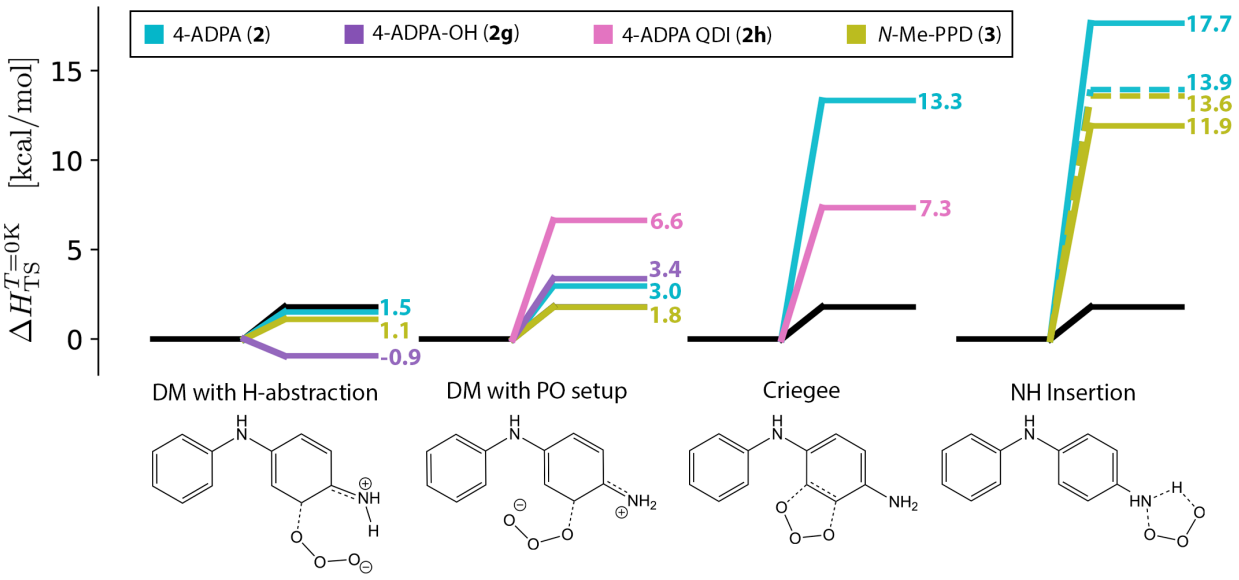

Figure 4.10: Vibrationally corrected barrier heights for PPD ozonation pathways compared to the minimum barrier pathway for 2M2B ozonation (**1**, solid black lines). Transition structures are shown for 4-ADPA transformations. For N−H insertion reactions, solid and dashed lines correspond to insertion at terminal and central N atoms, respectively. DeMore (DM) additions of O_3 to the rings of 4-ADPA (**2**), 4-ADPA-OH (**2g**), and MePPD (**3**) are the only transformations that are kinetically competitive with **1** ozonation. DeMore TSs with secondary H-abstraction interactions show additional stabilization.

for alkyl amines increase from 9.3×10^4 to $4.1 \times 10^6\,M^{-1}\,s^{-1}$ with alkyl substitution.[327, 289, 253] Assuming this is the primary mechanism in PPDs, we might generously expect ozonation rates similar to secondary aliphatic amines, *e.g.* diethylamine where $k = 3.9 \times 10^5\,M^{-1}\,s^{-1}$.[253] By contrast, ozonation rates of PPDs are 1–2 orders of magnitude faster, with 6PPD around $2 \times 10^7\,M^{-1}\,s^{-1}$.[60] More active channels are necessary to explain this reactivity.

Direct interaction with the phenylene diamine ring results in more stable—thereby, more accessible—transition structures. Among these interactions, concerted addition of ozone to the ring system, which has been proposed for other electron-rich aromatics,[290, 394] to form primary ozonide **2b** is the least favorable interaction. While conducive of a faster reaction than N−H insertion, the barrier for the minimum energy Criegee transition structure of $\Delta E_{TS} = 13.3\,kcal\,mol^{-1}$ is still insufficient to compete with the ozonation of **1**. Asymmetric, DeMore-like addition to the ring system[394] is significantly more accessible, with barrier heights ranging from 1.5–7.0 $kcal\,mol^{-1}$. Conformational details of these transition structures explain the range of ΔE_{TS} values in these systems and provide significant insight into the reactivity of PPDs and likely fate of these structures.

Each of the most stable DeMore transition structures in **2** is stabilized by a secondary interaction with O_3. The lowest energy structure ($\Delta E_{TS} = 1.5\,\text{kcal mol}^{-1}$) is actively forming a C−O bond with the 2-position in the phenylene diamine ring and is stabilized by a secondary interaction that primes the intermediate to then form the 1,2-primary ozonide. Additional low-lying DeMore transition structures are stabilized through a secondary interaction between ozone and an amine hydrogen. Vibrational analysis indicates that these structures correspond to a normal coordinate forming C−O bonds at the 2- and 3-positions in the ring, but the resulting intermediates are primed for amine H abstraction, ultimately affording the hydroperoxy imine, **2d**. In both types of DeMore transition structures—those set up for primary ozonide formation and for H abstraction—**2** ozonation pathways initiated through interaction with the C atoms of the phenylene diamine ring are significantly more accessible than interactions with PPD amine groups.

These transition structures indicate that transformations from various isomers of DeMore adduct **2c** to primary ozonide **2b** and hydroperoxy-imine **2d** represent the most significant early stage intermediates of **2** ozonation. As a result, the reactivity of these compounds determines the distribution of the products for the overall reaction between **2** and ozone. 1,2-Primary ozonide **2b** is expected to decompose into open-chain scission products[291, 290, 391] similar to the wide variety of experimentally determined PPD ozonation products.[359] While not the focus of the present study, the wax-like structure of these products (especially in the 6PPD system, which has a longer alkyl tail) makes them potential candidates for the film formation mechanism of PPDs in tires.[340] For our present purposes, the opening of the PPD ring is the most salient feature of these products, making them poor candidates for the formation of **2** quinone, and we do not consider them further.

Formation of **2d**, on the other hand, is a promising step towards the quinone, forming a necessary C−O bond and preserving the ring structure. This species is primed for the loss of hydroperoxy radical ($HOO^{\cdot}$) to form alkoxy radical **2e**,[290, 391, 392] which may abstract $H^{\cdot}$ from $HOO^{\cdot}$ producing $^1O_2$. This reaction affords hydroxyl imine **2f**, which may rearomatize to form hydroxyl-4ADPA (**2g**) with catalytic amounts of H^+.[391] It is also possible that alkoxy radical **2e** immediately recombines with $HOO^{\cdot}$ and loses H_2O to promptly form the quinone **2q**, as has been suggested in other systems.[335] Due to the difficulty of identifying transition structures, we do not report barrier heights for these transformations. Still, overall reaction energies (Table 4.4 and Figure 4.11) indicate that each individual step is thermodynamically feasible. The citations for each step also provide literature precedent for each of these transformations in similar systems, though other pathways from **2d** to **2g** can also be imagined.[290, 320, 394]

Regardless of the particular steps, production of hydroxyl-4ADPA **2g** through direct **2**–O_3 interaction is the salient feature of this mechanistic proposal. This motif is analogous to ozonation of anilines[391], catechols,[320] and pyrazoles,[392] where hydroxylated aromatics are significant products. Furthermore, recent experimental work identified the presence of **2g** in snow samples collected along major roadways.[359] These hydroxyl inetermediates aid the function of PPDs in tires, as these derivatives possess similar reactivity towards O_3 as their parent compounds.[178] Indeed, addition of ozone to **2g** to form hydroxylated DeMore

Table 4.4: Vibrationally corrected barrier heights and reaction energies for PPD ozonation on both SC- and AP-ωB97X-V/def2-TZVPP surfaces. SC energies are more accurate for ΔE_{TS}, while AP energies are more accurate for ΔE_{rxn} (Section 4.3). Results for the lowest energy 2M2B (**1**) ozonation pathway are included for reference. All values are at 0 K. [Units: kcal mol^{-1}]

	SC		AP	
Reaction	ΔH_{TS}	ΔH_{rxn}	ΔH_{TS}	ΔH_{rxn}
1 → **1c**	1.8	-64.9	4.0	-56.2
2 → **2a**	13.9	-20.4	21.8	-11.7
2 → **2b**	13.3	-30.1	22.0	-21.4
2 → **2c**	1.5	-2.8	6.8	5.8
2c → **2d**	–	-20.3	–	-20.4
2d → **2f**	–	-16.5	–	-5.6
2f → **2g**	–	-28.1	–	N/A
2g → **2c′**	-0.9	-1.3	3.9	5.9
3 → **3a**	11.9	-22.7	22.2	-14.0
3 → **3c**	1.1	-3.6	6.3	3.8
2h → **2i**	7.3	-8.3	16.0	0.8
2h → **2j**	6.6	-49.2	8.4	-40.6

intermediate **2c′** proceeds with a minimum barrier height of -0.9 kcal mol^{-1}, significantly lower than the minimum barrier for **2**. Because **2g** is even more reactive toward O_3 than **2**, an initial ozonation of **2** to form **2g** "commits" the substrate to a second ozonation. Each of the reaction pathways available to **2c** presumably exists for **2c′**, which may decompose into scission products through primary ozonide **2b′** or form hydroquinone **2g′** through **2d′** (Figure 4.9). This hydroquinone can slowly oxidize to 4ADPA quinone **2q** at ambient conditions[297] or more rapidly through further reaction with O_3.[335, 394] Though not shown in Figure 4.9, adduct **2c′** may alternatively abstract the *ipso* H from the ring to form the quinone, similar to the mechansim proposed for phenolates.[394]

Overall, this cascade of reactions results in a molecular mechanism for the formation of 4ADPA quinone (**2q**) from **2** through a series of kinetically and thermodynamically favorable transformations. The initial nucleophilic attack of O_3 by the PPD ring has not been previously proposed, but critically occurs with a barrier height lower than that for 2M2B ozonation (Section 4.5). Additionally, consumption of two molar equivalents of O_3 is consistent with experimental results.[177] Thus, this channel allows kinetic scavenging of ozone, even for aryl PPD **2**.

4.6.2 Effects of N-alkylation

It is well-known that alkyl-aryl PPDs (like 6PPD) are more reactive toward ozone than aryl PPDs like our surrogate compound **2**.[84, 235, 179] Still, inclusion of the 6PPD alkyl chain

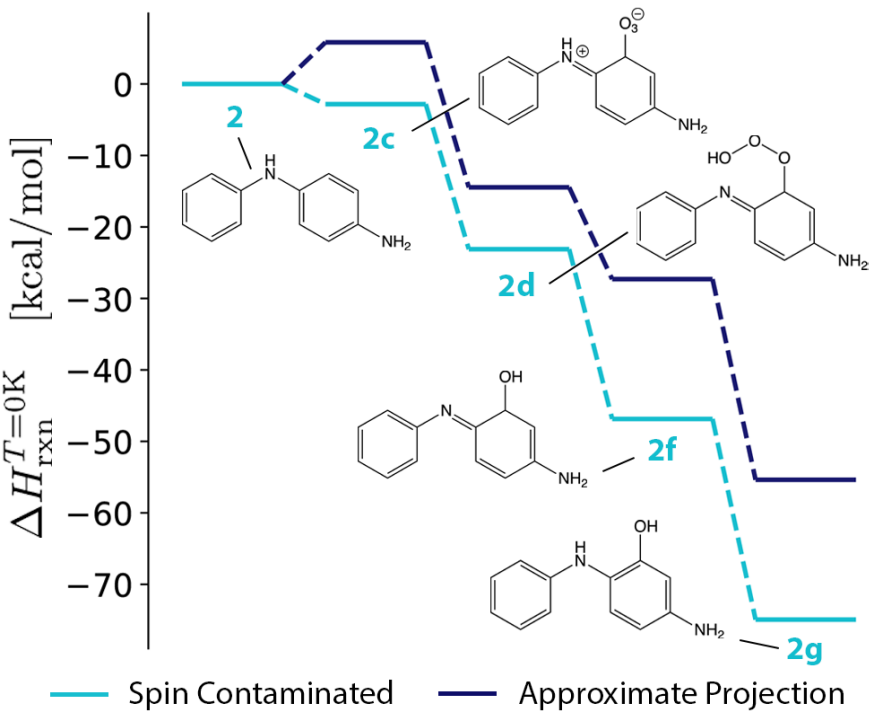

Figure 4.11: Vibrationally correct reaction energies ($\Delta H_{\mathrm{rxn}}^{T=0\,\mathrm{K}}$) for steps from 4ADPA (**2**) to 4ADPA-OH (**2g**) at the SC- and AP-ωB97X-V/def2-TZVPP levels. Following the initial ozonation step to form **2c**, both methods indicate a strongly exothermic reaction cascade.

into our model system would result in a nearly 50 % increase in the size of our system as well as introducing a significant degree of conformational flexibility. We therefore model the kinetic effects of alkylation using *N*-Me-PPD (**3**), which is more computationally tractable and should capture the lion's share of the relevant effects.

Many authors attribute increased ozonation rates to more stable interactions with the nitrogen atom,[179] but we have already noted that these are not significant reaction channels for **2**. N−H insertion pathways remain uncompetitive in **3**. Unsurprisingly, alkylation of the terminal amine does not affect that barrier height for insertion into the central N−H bond significantly, and we have $\Delta E_{\mathrm{TS}} = 13.6\,\mathrm{kcal\,mol^{-1}}$ for this reaction. Methylation of the terminal nitrogen does increase the reactivity of its N−H bond considerably, resulting in an insertion barrier of $11.9\,\mathrm{kcal\,mol^{-1}}$ (*cf.* the barrier of $17.7\,\mathrm{kcal\,mol^{-1}}$ in **2**), but the resulting barrier is still relatively large.

Instead, the experimental effects of alkylation can be attributed to additional stability in the interactions between ozone and the ring system, mediated through the N atom's connection to the π-system. The DeMore-plus-H-abstraction transition structures that lead to hydroperoxy imine **3d** at the methylated amine are particularly stable, with a minimum

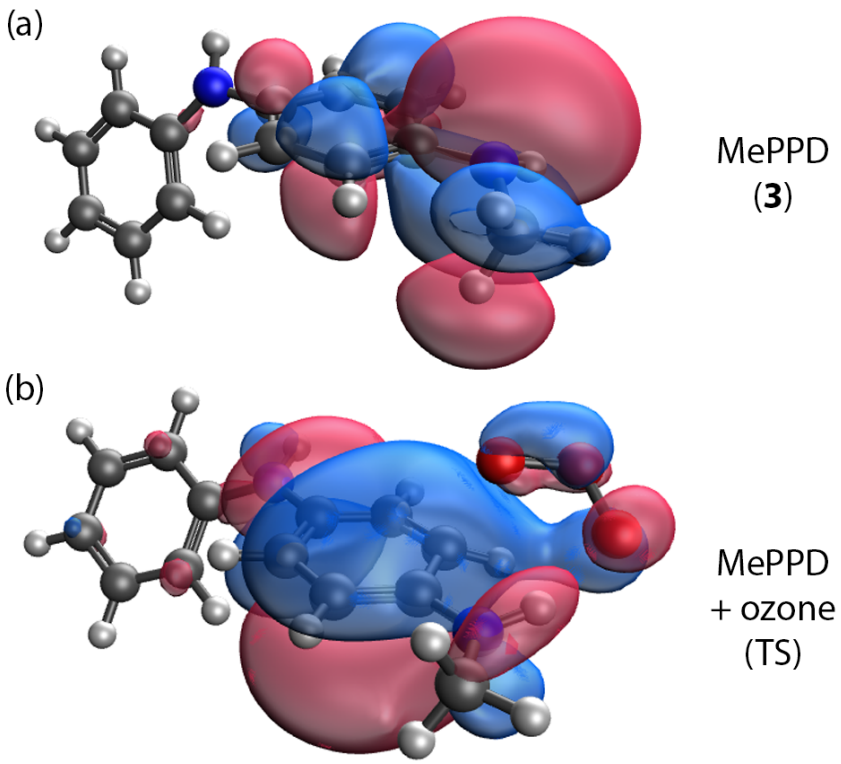

Figure 4.12: Intrinsic bonding orbitals (IBOs) for (a) MePPD (**3**), showing delocalization of N lone pair stabilized by methyl hyperconjugation and (b) DeMore-like TS for **3** with a secondary interaction between the amine H and O_3.

barrier height of $\Delta E_{TS} = 1.1\,\text{kcal mol}^{-1}$ relative to isolated fragments. This stabilization can be understood with reference to the "lone pair" (LP) orbital on the terminal N atom in **3** (Figure 4.12[a]). Hyperconjugation of the methyl C−H density supports interactions through the ring π-system in **3**, resulting in significant delocalization of the amine LP through the ring. In the transition structure for O_3 addition (Figure 4.12[b]), this orbital clearly exhibits the nascent interaction between the floating O_3 and the amine H, even though the normal mode consists entirely of C3−O bond formation.

The role of amine H atoms in achieving this high degree of ozone reactivity has gone unrecognized in previous work on PPD systems. While barrier heights for certain other DeMore structures (like the precursors to 1,2-primary ozonides) are competitive, stabilization from H abstraction leads to particularly active reaction channels. As seen above (Section 4.6.1), these channels are connected to quinone formation, and there is an inextricable link between the activity of 6PPD as an antiozonant and its toxicity through the quinone.

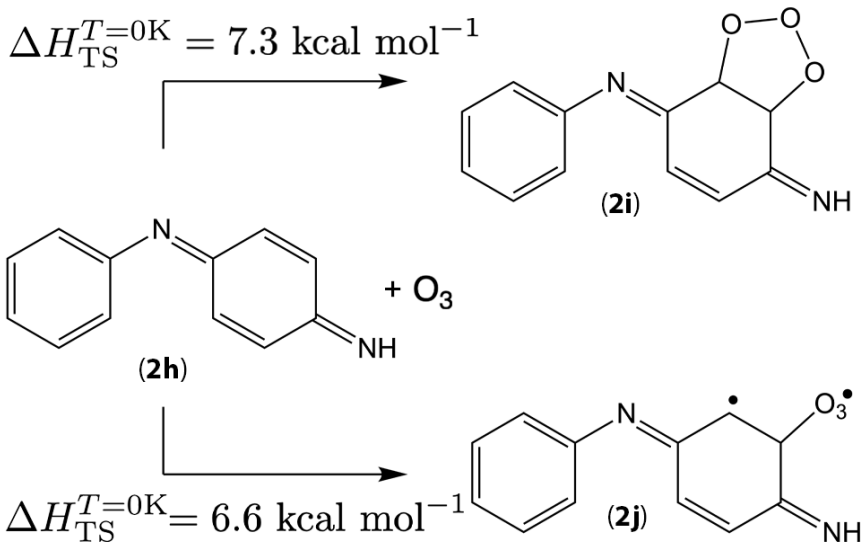

Figure 4.13: Reaction pathways for ring ozonation in 4ADPA QDI (**2h**). Neither primary ozonide **2i** nor DeMore intermediate **2j** is likely to result in products conducive to quinone formation.

4.6.3 Pathways through the quinone diimine

While the preceding discussion provides strong evidence for one pathway to PPD quinones, alternative mechanisms are present in the literature. Indeed, recent experimental evidence has been interpreted to suggest quinone formation proceeds through the 6PPD quinone diimine (QDI).[217] Specifically, mass spectrometry of the ozonation products of 6PPD resultsd in a peak with an integrated mass of 283.1798 Da, which the authors attributed to the $[M+H]^+$ ion of 6PPD QDI-OH. This interpretation is supported by a body of work detailing the *in situ* formation of 6PPD QDI itself,[246, 130] and others have proposed similar chemistry.[359] We evaluate the possibility of 6PPD QDI ozonation to form 6PPDQ through the QDI with reference to the model 4-ADPA QDI (**2h**), assuming once again this system captures the fundamental chemistry.

Analogous to both **2** and **3** as discussed in Sections 4.6.1 and 4.6.2 above, **2h** possesses transition structures corresponding to both Criegee (concerted) and DeMore-like (stepwise) addition of O_3 to the QDI ring system (Figure 4.13). These two pathways are similarly facile in the QDI system. Quantitatively, the minimum barrier for concerted addition to **2h** is 7.3 kcal mol^{-1}, compared to 6.6 kcal mol^{-1} for DeMore addition. It is noteworthy that the absence of amine H atoms in **2h** corresponds to the absence of extremely low barrier ozonation pathways as were seen for **2** and **3**, underscoring the importance of H-abstraction for PPD ozonation. Instead, in the case of **2h** DeMore adducts, the most stable DeMore transitions are accompanied instead by secondary interactions with an additional C atom in

the PPD ring. Hence, as far as ring interactions in with **2h** are concerned, the significant pathways will progress through primary ozonides, ultimately resulting in scission products. In particular, it is difficult to see how these structures could result in quinone formation.

It therefore seems more likely that the experimentally determined[217] 6PPD QDI-OH forms through the oxidation of 6PPD-OH (**4g**) to the QDI, rather than the hydroxylation of the QDI. These considerations also indicate that the QDI is unlikely to be a precursor to the quinone. All of the results of the present study suggest, instead, that a direct attack of the 6PPD ring initiating the pathway to the quinone occurs through 6PPD-OH, which exhibits increased reactivity toward ozone than even the parent 6PPD.

4.7 Implications for non-toxic PPD design

The preceding mechanistic work highlights the vulnerability of rubber to degradation by ozone and explains the distinct ability of PPDs to afford protection against this degradation. As identified through analysis of key, rate-determining steps in the mechanism of PPD ozonation, critical features of this chemistry that result in the formation of highly toxic 6PPD quinone should inform ongoing work to identify replacements for 6PPD.

The mechanistic work in this report has dispelled a number of reports in the literature that suggest the ozonation of both alkene and PPD systems is initialized by one-electron transfer from the subtrate to ozone.[435, 61, 62, 353] This provides theoretical backing to the perhaps obvious conclusion that predicting ozonation capacity is more complicated than determining ionization potentials, even if this parameter is relatively predictive within a single class of molecules.[60] Instead, the subtlety of the mechanistic results above indicate that atomistic details of reactivity must be taken into account.

Under the previous paradigm that ozonation of PPDs is facilitated through their N atoms,[340, 234, 233] prevention of quinone formation through deactivation of the aromatic ring system is a logical approach to reduce the toxicity of 6PPD. The results above, however, demonstrate direct attack by the aromatic ring is significantly more favorable, suggesting that such approaches will be unsuccessful, as they will poison the antiozonant capacity of 6PPD. The discovery of the importance of secondary interaction with amine H atoms for stabilizing transition structures suggests the necessity of these atoms also has bearing on PPD design. Specifically, while compounds that lack the potential for these reactions may still exhibit reactivity towards O_3 (*e.g.* 6PPD QDI[359]), these reactions are unlikely to afford kinetic protection against rubber ozonation.

Present results indicate that activation of the PPD ring significantly increase activity toward O_3 (Figure 4.10). This is seen first in the minor increase in reactivity upon *N*-alkylation, which has been known for some time,[84, 235, 179] and then by the significant increase upon hydroxylation. Though ring activation improves antiozonant performance, it also facilitates the reactions that can ultimately produce PPD quinones. This is perhaps the most important result of this study, in that it provides a direct, atomistic link between the function of 6PPD as an antiozonant and its aquatic toxicity through the quinone.[399, 41,

398, 166, 410, 54] While this suggests an obvious difficulty in continued use of the PPDs on the market today, all is not lost. Atomistic details of PPDs that support rapid reactivity with O_3 provide principles for rational design of effective antiozonants, informing ongoing efforts to develop non-toxic alternatives for tires.

Bibliography

[1] Carlo Adamo, Matthias Ernzerhof, and Gustavo E Scuseria. "The meta-GGA functional: Thermochemistry with a kinetic energy density dependent exchange-correlation functional". In: *The Journal of Chemical Physics* 112.6 (2000), pp. 2643–2649.

[2] Lucas E Aebersold et al. "Efficacy of density functionals and relativistic effective core potentials for lanthanide-containing species: The Ln54 molecule set". In: *Journal of Chemical Theory and Computation* 13.6 (2017), pp. 2831–2839. DOI: 10.1021/acs.jctc.6b01223.

[3] J. Allison, A. Mavridis, and J. F. Harrison. "The gas phase chemistry of bare and ligated transition metal ions: Correlations of reactivity with electronic structure–I. M^+ and MCO^+". In: *Polyhedron* 7 (1988), pp. 1559–1572. DOI: 10.1016/S0277-5387(00)81782-9.

[4] V. Ambrogi et al. "Natural antioxidants for polypropylene stabilization". In: *Polymer Degradation and Stability* 96.12 (2011), pp. 2152–2158. ISSN: 0141-3910. DOI: https://doi.org/10.1016/j.polymdegradstab.2011.09.015.

[5] Paul T. Anastas and John C. Warner. *Green Chemistry: Theory and Practice*. Oxford, UK: Oxford University Press, 1998.

[6] D Andrae et al. "Energy-adjusted ab initio pseudopotentials for the second and third row transition elements". In: *Theoretica chimica acta* 77.2 (1990), pp. 123–141. DOI: 10.1007/BF01114537.

[7] D Andrae et al. "Energy-adjusted ab initio pseudopotentials for the second and third row transition elements: Molecular test for M_2 (M = Ag, Au) and MH (M = Ru, Os)". In: *Theoretica chimica acta* 78.4 (1991), pp. 247–266. DOI: 10.1007/BF01112848.

[8] D. Andrae et al. "Energy-adjusted *ab initio* pseudopotentials for the second and third row transition elements". In: *Theor. Chim. Acta* 77 (1990), pp. 123–141. DOI: 10.1007/bf01114537.

[9] Lester Andres et al. "Reactions of laser-ablated chromium atoms, cations, and electrons with CO in excess argon and neon: Infrared spectra and density functional calculations on neutral and charged unsaturated chromium carbonyls". In: *J. Phys. Chem. A* 107 (2003), pp. 561–569. DOI: 10.1021/jp026955g.

[10] J.C. Andries, D.B. Ross, and H.E. Diem. "Ozone attack and antiozonant protection of vulcanized natural rubber. A surface study by attenuated total reflectance spectroscopy". In: *Rubber Chem. Technol.* 48 (1975), pp. 41–49. DOI: 10.5254/1.3545038.

[11] J.C. Andries et al. "A surface study of ozone attack and antiozonant protection of carbon black loaded natural rubber compounds". In: *Rubber Chem. Technol.* 52 (1979), pp. 823–837. DOI: 10.5254/1.3535244.

[12] Josep M. Anglada, Ramon Crehuet, and Josep Maria Bofill. "The Ozonolysis of Ethylene: A Theoretical Study of the Gas-Phase Reaction Mechanism". In: *Chemistry – A European Journal* 5 (1999), pp. 1809–1822. DOI: 10.1002/(SICI)1521-3765(19990604)5:6<1809::AID-CHEM1809>3.0.CO;2-N.

[13] E.H. El-Ansary, M.E.K. Ahmed, and H.W. Clague. "Systemic toxicity of *para*-phenylenediamine". In: *The Lancet* 321.8337 (1983), p. 1341. DOI: 10.1016/S0140-6736(83)92456-X.

[14] Dr. S. Anuradha et al. "Acute Renal Failure Following para-Phenylenediamine (PPD) Poisoning: A Case Report and Review". In: *Renal Failure* 26.3 (2004), pp. 329–332. DOI: 10.1081/JDI-200026722.

[15] Somaie Asgharzade and Morteza Vahedpour. "Mechanism and thermodynamics of multichannel 1:1 ammonia and ozone tropospheric oxidation reaction". In: *Progress in Reactin Kinetics and Mechanism* 38 (2013), pp. 266–282.

[16] Robert O. Babbit. *The Vanderbilt Rubber Handbook*. 14th ed. R.T. Vanderbilt Company, 2010.

[17] G. B. Bachelet, D. R. Hamann, and M. Schlüter. "Pseudopotentials that work: From H to Pu". In: *Phys. Rev. B* 26 (8 1982), pp. 4199–4228. DOI: 10.1103/PhysRevB.26.4199.

[18] Paul S. Bagus, K. Hermann, and Charles W. Bauschlicher. "A new analysis of charge transfer and polarization for ligand–metal bonding: Model studies of Al_4CO and Al_4NH_3". In: *J. Chem. Phys.* 80 (1984), pp. 4378–4386. DOI: 10.1063/1.447215.

[19] Paul S. Bagus, Klaus Hermann, and Charles W. Bauschlicher. "On the nature of the bonding of lone pair ligands to a transition metal". In: *J. Chem. Phys.* 81 (1984), pp. 1966–1974. DOI: 10.1063/1.447818.

[20] Paul S. Bagus, Constance J. Nelin, and Charles W. Bauschlicher. "Bonding of CO to metal surfaces: A new interpretation". In: *Phys. Rev. B* 28 (1983), pp. 5423–5438. DOI: 10.1103/PhysRevB.28.5423.

[21] Paul S. Bagus and Gianfranco Pacchioni. "On the origin of bonding and vibrational frequency shifts for CO adsorbed on neutral, cationic and anionic gold clusters". In: *J. Phys. Conf. Ser* 117 (2008), p. 012003. DOI: 10.1088/1742-6596/117/1/012003.

[22] Paul S. Bagus and Gianfranco Pacchioni. "The contribution of metal sp electrons to the chemisorption of CO: theoretical studies of CO on Li, Na, and Cu." In: *Surface Science* 278 (1992), pp. 427–436. DOI: 10.1016/0039-6028(92)90678-Y.

[23] Philip S. Bailey and John E. Keller. "Ozonation of amines. III. *t*-Butylamine". In: *J. Org. Chem.* 33 (1968), pp. 2680–2684. DOI: 10.1021/jo01271a014.

[24] Philip S. Bailey, Duane A. Lerdal, and Thomas P. Carter. "Ozonation of nucleophiles. 9. Tertiary amines". In: *J. Org. Chem.* 43 (1978), p. 266202664. DOI: 10.1021/jo00407a022.

[25] Philip S. Bailey, Lloyd M. Southwick, and Thomas P. Carter. "Ozonation of nucleophiles. 8. Secondary amines". In: *J. Org. Chem.* 43 (1978), pp. 2657–2662. DOI: 10.1021/jo00407a021.

[26] Leslie A. Barnes and Charles W. Bauschlicher. "Theoretical studies of the transition metal–carbonyl systems MCO and $M(CO)_2$, M = Ti, Sc, and V". In: *J. Chem. Phys.* 91 (1989), pp. 314–330. DOI: 10.1063/1.457519.

[27] Leslie A. Barnes, Marzio Rosi, and Charles W. Bauschlicher. "Theoretical studies of the first- and second-row transition-metal mono- and dicarbonyl positive ions". In: *J. Chem. Phys.* 93 (June 1990), pp. 609–624. DOI: 10.1063/1.459508.

[28] Rodney J Bartlett and Monika Musiał. "Coupled-cluster theory in quantum chemistry". In: *Reviews of Modern Physics* 79.1 (2007), p. 291.

[29] Charles W. Bauschlicher. "An ab initio study of CuCO". In: *J. Chem. Phys.* 100 (1994), pp. 1215–1218. DOI: 10.1063/1466651.

[30] Charles W. Bauschlicher. "Transition metal–ligand bonding. II". In: *J. Chem. Phys.* 84 (Aug. 1986), pp. 260–267. DOI: 10.1063/1.450179.

[31] Charles W. Bauschlicher and Paul S. Bagus. "The metal–carbonyl bond in $Ni(CO_4)$ and $Fe(CO)_5$: A clear-cut analysis". In: *J. Chem. Phys.* 81 (Nov. 1984), pp. 5889–5898. DOI: 10.1063/1.447589.

[32] Charles W. Bauschlicher, Stephen R. Langhoff, and Leslie A. Barnes. "Bonding in zerovalent Ni compounds: NiN_2 and $Ni(N_2)_4$ compared with NiCO and $Ni(CO)_4$". In: *Chem. Phys.* 129 (1989), pp. 431–437. DOI: 10.1016/0301-0104(89)85012-8.

[33] Charles W. Bauschlicher et al. "The nature of the bonding in XCO for X=Fe, Ni, andCu". In: *J. Chem. Phys.* 85 (Aug. 1986), pp. 354–364. DOI: 10.1063/1.451610.

[34] Axel D Becke. "Density-functional exchange-energy approximation with correct asymptotic behavior". In: *Physical review A* 38.6 (1988), p. 3098.

[35] Andrew Behn et al. "Efficient exploration of reaction paths via a freezing string method". In: *J. Chem. Phys.* 135 (2011), p. 224108. DOI: 10.1063/1.3664901.

[36] Harrison M Bergman et al. "Copper (III) Metallacyclopentadienes via Zirconocene Transfer and Reductive Elimination to an Isolable Phenanthrocyclobutadiene". In: *Journal of the American Chemical Society* (2022).

[37] Andreas Bergner et al. "*Ab initio* energy-adjusted pseudopotentials for elements of groups 13-17". In: *Mol. Phys.* 80 (6 1993), pp. 1431–1441.

[38] Gaston Berthier. "Extension de la méthode du champ moléculaire self-consistent à l'étude des états à couches incompletes". In: *Comptes Rendus Hebdomadaires des Séances de l'Académie des Sciencies* 238 (1954), pp. 91–93.

[39] Manuj Kr. Bharali and Karabi Dutta. "Testicular toxicity of para-phenylenediamine after subchronic topical application in rat". In: *International Journal of Environmental Health Research* 22.3 (2012), pp. 270–278. DOI: 10.1080/09603123.2011.634388.

[40] Asmit Bhowmick, Sudhir C Sharma, and Teresa Head-Gordon. "The importance of the scaffold for de novo enzymes: a case study with kemp eliminase". In: *Journal of the American Chemical Society* 139.16 (2017), pp. 5793–5800. DOI: 10.1021/jacs.6b12265.

[41] Stephanie I. Blair, Clyde H. Barlow, and Jenifer K. McIntyre. "Acute cerebrovascular effects in juvenile coho salmon exposed to roadway runoff". In: *Canadian Journal of Fisheries and Aquatic Sciences* 78.2 (2021), pp. 103–109.

[42] P. E. Blöchl. "Projector augmented-wave method". In: *Phys. Rev. B* 50.24 (1994), pp. 17953–17979. DOI: 10.1103/PhysRevB.50.17953.

[43] G. Blyholder and Marvin C. Allen. "Infrared spectra and molecular orbital model for carbon monoxide adsorbed on metals". In: *J. Am. Chem. Soc.* 91 (1969), pp. 3158–3162. DOI: 10.1021/ja01040a009.

[44] George Blyholder. "Molecular orbital view of chemisorbed carbon monoxide". In: *J. Phys. Chem.* 68 (1964), pp. 2772–2777. DOI: 10.1021/j100792a006.

[45] George Blyholder and Michael Lawless. "An energy criterion for determining relative σ and π contributions in transition metal–carbonyl bonding". In: *J. Am. Chem. Soc.* 114 (1992), pp. 5828–5832. DOI: 10.1021/ja00040a052.

[46] Vladimir I. Bolshakov et al. "The performance of the new $6-31G^{\#\#}$ basis set: Molecular structures and vibrational frequencies of transition metal carbonyls". In: *J. Comput. Chem.* 28 (2007), pp. 778–782. DOI: 10.1002/jcc.20596.

[47] Pedro Borlido et al. "Validation of pseudopotential calculations for the electronic band gap of solids". In: *J. Chem. Theory Comput.* 16 (6 2020), pp. 3620–3627. DOI: 10.1021/acs.jctc.0c00214.

[48] Max Born and J Robert Oppenheimer. "On the quantum theory of molecules". In: *Ann. Phys. Leipzig* 84 (1927), p. 457.

[49] S.F. Boys and F. Bernardi. "The calculation of small molecular interactions by the differences of separate total energies. Some procedures with reduced errors". In: *Mol. Phys.* 19 (1970), pp. 553–66. DOI: 10.1080/00268977000101561.

[50] Benoît Braïda, Sérgio E. Galembeck, and Philippe C. Hiberty. "Ozone and other 1,3-dipoles: Toward a quantitative measure of diradical character". In: *J. Chem. Theory Comput.* 13 (2017), pp. 3228–3235. DOI: 10.1021/acs.jctc.7b00399.

[51] A. D. Brathwaite, Z.D. Reed, and M. A. Duncan. "Infrared photodissociation spectroscopy of copper carbonyl cations". In: *J. Phys. Chem. A* 115 (2011), pp. 10461–10469. DOI: 10.1021/jp206102z.

[52] Éric Brémond et al. "Range-separated hybrid density functionals made simple". In: *The Journal of Chemical Physics* 150.20 (2019), p. 201102.

[53] L. Brillouin. "Act. Sci. Ind." In: vol. 159. Hermann, 1934.

[54] Markus Brinkmann et al. "Acute toxicity of the tire rubber-derived chemical 6PPD-quinone to four fishes of commercial, cultural, and ecological importance". In: *Environ. Sci. Technol. Lett.* 9 (2022), pp. 333–338. DOI: 10.1021/acs.estlett.2c00050.

[55] Kieth A. Bruckner and Shang-Keng Ma. "Correlation energy of an electron gas with a slowly varying high density". In: *Physical Review* 165.1 (1968), p. 18.

[56] Ireneusz W. Bulik, Thomas M. Henderson, and Gustavo E. Scuseria. "Can single-reference coupled cluster theory describe static correlation?" In: *J. Chem. Theory Comput.* 11 (2015), pp. 3171–3179. DOI: 10.1021/acs.jctc.5b00422.

[57] Oleksandr S Bushuyev et al. "What should we make with CO2 and how can we make it?" In: *Joule* 2.5 (2018), pp. 825–832. DOI: 10.1016/j.joule.2017.09.003.

[58] Xiaoyan Cao and Michael Dolg. "Pseudopotentials and modelpotentials". In: *Wiley Interdisciplinary Reviews: Computational Molecular Science* 1.2 (2011), pp. 200–210. DOI: 10.1002/wcms.28.

[59] Alejandro L. Cardona et al. "Experimental and theoretical kinetic studies of the ozonolysis of select allyl sulfides (H_2C=$CHCH_2SR$, R = CH_3, CH_3CH_2): The effect of nascent OH radicals". In: *J. Phys. Chem. A* 126 (2022), pp. 6751–6761. DOI: 10.1021/acs.jpca.2c04547.

[60] Franco Cataldo. "Early stages of p-phenylenediamine antiozonants reaction with ozone: Radical cation and nitroxyl radical formation". In: *Poly. Degrad. Stab.* 147 (2018), pp. 132–141. DOI: 10.1016/j.polymdegradstab.2017.11.020.

[61] Franco Cataldo. "Ozone interaction with conjugated polymers—I. Polyacetylene". In: *Polymer Degradation and Stability* 60.2 (1998), pp. 223–231. DOI: 10.1016/S0141-3910(97)00068-2.

[62] Franco Cataldo. "Ozone interaction with conjugated polymers—II. Polyphenylacetylene". In: *Polymer Degradation and Stability* 60.2 (1998), pp. 233–237. DOI: 10.1016/S0141-3910(97)00069-4.

[63] Franco Cataldo et al. "On the early reaction stages of ozone with N,N′-substituted p-phenylenediamines (6PPD, 77PD) and N,N′,N″-substituted-1,3,5-triazine "Durazone®": An electron spin resonance (ESR) and electronic absorption spectroscopy study". In: *Poly. Degrad. Stab.* 111 (2015), pp. 223–231.

[64] Pierfrancesco Cerruti et al. "Effect of natural antioxidants on the stability of polypropylene films". In: *Polymer Degradation and Stability* 94.11 (2009), pp. 2095–2100. ISSN: 0141-3910. DOI: https://doi.org/10.1016/j.polymdegradstab.2009.07.023.

[65] C. Chackerian et al. "Experimental determination of the $^1\Sigma^+$ state electric dipole moment function of carbon monoxide up to a large internuclear separation". In: *Can. J. Phys.* 62 (1984), pp. 1579–1585. DOI: 10.1139/p84-202.

[66] Jeng-Da Chai and Martin Head-Gordon. "Long-range corrected hybrid density functionals with damped atom–atom dispersion corrections". In: *Physical Chemistry Chemical Physics* 10.44 (2008), pp. 6615–6620.

[67] Bun Chan. "Formulation of small test sets using large test sets for efficient assessment of quantum chemistry methods". In: *J. Chem. Theory Comput.* 14 (8 2018), pp. 4254–4262. DOI: 10.1021/acs.jctc.8b00514.

[68] Bun Chan, Peter M. W. Gill, and Masanari Kimura. "Assessment of DFT methods for transition metals with the TMC151 compilation of data sets and comparison with accuracies for main-group chemistry". In: *J. Chem. Theory Comput.* 15 (2019), pp. 3610–3622. DOI: 10.1021/acs.jctc.9b00239.

[69] Wai-To Chan and I.P. Hamilton. "Mechanisms for the ozonolysis of ethene and propene: Reliability of quantum chemical predictions". In: *J. Chem. Phys.* 118 (2003), p. 1688. DOI: 10.1063/1.1531104.

[70] Wait-To Chan, Chang'e Wang, and John D. Goddard. "Concerted and stepwise reaction mechanisms for the addition of ozone to acetylene: A computational study". In: *J. Phys. Chem. A* 111 (2007), pp. 4792–4803. DOI: 10.1021/jp0633188.

[71] T.C. Chang et al. "Accuracy and limitations of the pseudopotential method". In: *Theoretica chimica acta* 34.4 (1974), pp. 263–275. DOI: 10.1007/BF02399014.

[72] J. Chatt and L. A. Duncanson. "Olefin co-ordination compounds. Part III. Infra-red spectra and structure: Attempted preparation of acetylene complexes". In: *J. Chem. Soc.* (1953), pp. 2939–2947. DOI: 10.1039/JR9530002939.

[73] Lan Cheng et al. "Bond dissociation energies for diatomic molecules containing 3d transition metals: benchmark scalar-relativistic coupled-cluster calculations for 20 molecules". In: *J. Chem. Theory Comput.* 13.3 (2017), pp. 1044–1056.

[74] Tao Cheng, Hai Xiao, and William A Goddard III. "Full atomistic reaction mechanism with kinetics for CO reduction on Cu (100) from ab initio molecular dynamics free-energy calculations at 298 K". In: *Proceedings of the National Academy of Sciences* 114.8 (2017), pp. 1795–1800. DOI: 10.1073/pnas.1612106114.

[75] Francesco Cherubini. "The biorefinery concept: using biomass instead of oil for producing energy and chemicals". In: *Energy conversion and management* 51.7 (2010), pp. 1412–1421. DOI: 10.1016/j.enconman.2010.01.015.

[76] Ove Christiansen, Christof Hätig, and Jürgen Gauss. "Polarizabilities of CO, HF, Ne, BH, and CH^+ from ab initio calculations: Systematic studies of electron correlation, basis set errors, and vibrational contributions". In: *J. Chem. Phys.* 109 (1998), pp. 4745–4757. DOI: 10.1063/1.477086.

[77] Ove Christiansen et al. "Excitation energies of H2O, N2 and C2 in full configuration interaction and coupled cluster theory". In: *Chemical physics letters* 256.1-2 (1996), pp. 185–194.

[78] Phillip A. Christiansen, Yoon S. Lee, and Kenneth S. Pitzer. "Improved ab initio effective core potentials for molecular calculations". In: *J. Chem. Phys.* 71 (1979), p. 4445. DOI: 10.1063/1.438197.

[79] King-Thom Chung et al. "Mutagenicity and toxicity studies of p-phenylenediamine and its derivatives". In: *Toxicology Letters* 81.1 (1995), pp. 23–32. DOI: 10.1016/0378-4274(95)03404-8.

[80] Rachel Clune et al. "Competence and confidence: addressing inequity among incoming chemistry graduate students through a week-long mathematics intervention". In: *ChemRxiv* (2022). DOI: 10.26434/chemrxiv-2022-dl84f.

[81] Aron J. Cohen, Paula Mori-Sánchez, and Weitao Yang. "Challenges for density functional theory". In: *Chem. Rev.* 112 (2012), pp. 289–320. DOI: 10.1021/cr200107z.

[82] H. Corrodi and E. Hardegger. "Die konfiguration des colchicins und verwandter verbindungen". In: *Helv. Chem. Acta* 38 (1955), pp. 2030–2033. DOI: 10.1002/hlca.19550380743.

[83] F. Albert Cotton and Geoffrey Wilkinson. *Advanced Inorganic Chemistry*. 5th ed. New York, New York: John Wiley & Sons, Inc., 1988, pp. 58–62. ISBN: 0-471-849979.

[84] William L. Cox. "Chemical antiozonants and factors affecting their utility". In: *Rubber Chem. Technol.* 32 (1959), pp. 364–378. DOI: 10.5254/1.3542401.

[85] Christopher J. Cramer and Donald G. Truhlar. "Density functional theory for transition metals and transition metal chemistry". In: *Phys. Chem. Chem. Phys.* 11 (2009), pp. 10757–10816. DOI: 10.1039/b907148b.

[86] Dieter Cremer. "Møller–Plesset perturbation theory: from small molecule methods to methods for thousands of atoms". In: *Wiley Interdisciplinary Reviews: Computational Molecular Science* 1.4 (2011), pp. 509–530.

[87] Dieter Cremer, Ramon Crehuet, and Joseph Anglada. "The ozonolysis of acetylene–A quantum chemical investigation". In: *J. Am. Chem. Soc.* 123 (2001), pp. 6127–6141. DOI: 10.1021/ja010166f.

[88] Dieter Cremer and Zhi He. "Sixth-Order Møller- Plesset Perturbation Theory On the Convergence of the MP n Series". In: *The Journal of Physical Chemistry* 100.15 (1996), pp. 6173–6188.

[89] Dieter Cremer et al. "The ozone–acetylene reaction: Concerted or non-concerted reaction mechanism? A quantum chemical investigation". In: *Chem. Phys. Lett.* 347 (2001), pp. 268–276. DOI: 10.1016/S0009-2614(01)01032-6.

[90] Rudolf Criegee. "Mechanism of ozonolysis". In: *Angew. Chem. Chem., Int. Ed. Engl.* 14 (11 1975), pp. 745–752. DOI: 10.1002/anie.197507451.

[91] Leonardo A. Cunha et al. "Relativistic orbital-optimized density functional theory for accurate core-level spectroscopy." In: *J. Phys. Chem. Lett.* 13 (2022), pp. 3438–3449. DOI: 10.1021/acs.jpclett.2c00578.

[92] Stefan Dapprich and Gernot Frenking. "Investigation of donor–acceptor interactions: A charge decomposition anlaysis using fragment molecular orbitals". In: *J. Phys. Chem.* 99 (Mar. 1994), pp. 9352–9362. DOI: 10.1021/j100023a009.

[93] Donald J Darensbourg and Andrew D Yeung. "Thermodynamics of the carbon dioxide–epoxide copolymerization and kinetics of the metal-free degradation: a computational study". In: *Macromolecules* 46.1 (2013), pp. 83–95. DOI: 10.1021/ma3021823.

[94] Donald J Darensbourg et al. "Dramatic behavioral differences of the copolymerization reactions of 1, 4-cyclohexadiene and 1, 3-cyclohexadiene oxides with carbon dioxide". In: *Macromolecules* 48.6 (2015), pp. 1679–1687. DOI: 10.1021/acs.macromol.5b00172.

[95] Ernest R. Davidson et al. "The transition metal–carbonyl bond". In: *Acc. Chem. Res.* 26 (1993), pp. 628–635. DOI: 10/1021/ar0036a004.

[96] Wibe A De Jong et al. "Fully relativistic correlated benchmark results for uranyl and a critical look at relativistic effective core potentials for uranium". In: *Theoretical Chemistry Accounts* 107.1 (2001), pp. 22–26. DOI: 10.1007/s002140100293.

[97] W.B. DeMore. "Arrhenius constants for the reactions of ozone with ethylene and acetylene". In: *Int. J. Chem. Kinet.* 1 (1969), pp. 209–220. DOI: 10.1002/kin.550010207.

[98] M. J. S. Dewar. In: *Bull. Soc. Chim. Fr.* 18 (1951), pp. C71–C79.

[99] David W DeWulf, Tuo Jin, and Allen J Bard. "Electrochemical and surface studies of carbon dioxide reduction to methane and ethylene at copper electrodes in aqueous solutions". In: *Journal of the Electrochemical Society* 136.6 (1989), p. 1686. DOI: 10.1149/1.2096993.

[100] Axel Diefenbach, F. Matthias Bickelhaupt, and Gernot Frenking. "The nature of the transition metal–carbonyl bond and the question about the valence orbitals of transition metals. A bond-energy decomposition analysis of $TM(CO)_6{}^q$ ($TM^q = Hf^{2-}$, Ta^-, W, Re^+, Os^{2+}, Ir^{3+})". In: *J. Am. Chem. Soc.* 122 (June 2000), pp. 6449–6458. DOI: 10.1021/ja000663g.

[101] Sebastian Dohm et al. "Comprehensive thermochemical benchmark set of realistic closed-shell metal organic reactions". In: *J. Chem. Theory Comput.* 14 (5 2018), pp. 2596–2608. DOI: 10.1021/acs.jctc.7b01183.

[102] M Dolg, H Stoll, and H Preuss. "Energy-adjusted ab initio pseudopotentials for the rare earth elements". In: *The Journal of chemical physics* 90.3 (1989), pp. 1730–1734. DOI: 10.1063/1.456066.

[103] M Dolg et al. "Energy-adjusted abinitio pseudopotentials for the first row transition elements". In: *The Journal of chemical physics* 86.2 (1987), pp. 866–872. DOI: 10.1063/1.452288.

[104] Michael Dolg and Xiaoyan Cao. "Relativistic pseudopotentials: their development and scope of applications". In: *Chemical reviews* 112.1 (2012), pp. 403–480. DOI: 10.1021/cr2001383.

[105] M. S. Dopico-García et al. "Natural extracts as potential source of antioxidants to stabilize polyolefins". In: *Journal of Applied Polymer Science* 119.6 (2011), pp. 3553–3559. DOI: https://doi.org/10.1002/app.33022.

[106] K. Doudin et al. "New genre of antioxidants from renewable natural resources: Synthesis and characterisation of rosemary plant-derive antioxidants and their performance in polyolefins". In: *Polymer Degradation and Stability* 130 (2016), pp. 126–134. DOI: 10.1016/j.polymdegradstab.2016.05.030.

[107] Peter Dowideit and Clemens von Sonntag. "Reaction of ozone with ethene and its methyl- and chlorine-substituted derivatives in aqueous solution". In: *Environ. Sci. Technol.* 32 (1998), pp. 1112–1119. DOI: 10.1021/es971044j.

[108] Aseem Dubey and Akhilesh Arora. "Advancements in carbon capture technologies: A review". In: *Journal of Cleaner Production* (2022), p. 133932. DOI: 10.1016/j.jclepro.2022.133932.

[109] Thom H. Dunninrg et al. "Insights into the electronic structure of molecules from generalized valence bond theory". In: *J. Phys. Chem. A* 120 (2016), pp. 1763–1778. DOI: 10.1021/acs.jpca.5b12335.

[110] Kenneth G Dyall. "Interfacing relativistic and nonrelativistic methods. I. Normalized elimination of the small component in the modified Dirac equation". In: *J. Chem. Phys.* 106.23 (1997), pp. 9618–9626.

[111] Pablo Echenique and José Luis Alonso. "A mathematical and computational review of Hartree–Fock SCF methods in quantum chemistry". In: *Molecular Physics* 105.23-24 (2007), pp. 3057–3098.

[112] E.R. Erickson et al. "The reaction of ozone with SBR rubbers". In: *Rubber Chem. Technol.* 32 (1959), pp. 1062–1079. DOI: 10.5254/1.3542467.

[113] Walter C Ermler et al. "A binitio effective core potentials including relativistic effects. II. Potential energy curves for Xe2, Xe+ 2, and Xe* 2". In: *The Journal of Chemical Physics* 69.3 (1978), pp. 976–983. DOI: 10.1063/1.436650.

[114] Walter C. Ermler et al. "AB initio effective core potentials including relativistic effects. A procedure for the inclusion of spin-orbit coupling in molecular wavefunctions". In: *Chemical Physics Letters* 81.1 (1981), pp. 70–74. ISSN: 0009-2614. DOI: https://doi.org/10.1016/0009-2614(81)85329-8. URL: https://www.sciencedirect.com/science/article/pii/0009261481853298.

[115] E Fermi. "A statistical method for the determination of some atomic properties and the application of this method to the periodic system of element". In: *Z. Phys* 48 (1928), pp. 73–79.

[116] Thomas J. Fisher and Patrick H. Dussault. "Alkene ozonolysis". In: *Tetrahedron* 73 (30 2017), pp. 4233–4258. DOI: 10.1016/j.tet.2017.03.039.

[117] V. Fock. "'Selfconsistent field' mit Austausch für Natrium". In: *Z. Physik* 62 (1930), pp. 795–805.

[118] V. Fock. "Näherungsmethode zur Lösung des quantenmechanischen Mehrkörper- problems". In: *Z. Physik* 62 (1930), pp. 126–148.

[119] René Fournier. "Theoretical study of linear and bent CrCO, NiCO, and CuCO". In: *J. Chem. Phys.* 98 (Feb. 1993), pp. 8041–8050. DOI: 10.1063/1.464559.

[120] René Fournier. "Theoretical study of the monocarbonyls of first-row transition metal atoms". In: *J. Chem. Phys.* 99 (Aug. 1993), pp. 1801–1815. DOI: 10.1063/1.465297.

[121] Garnot Frenking and Nikolaus Fröhlich. "The nature of bonding in transition-metal compounds". In: *Chem. Rev.* 100 (Jan. 2000), pp. 717–774. DOI: 10.1021/cr9804011.

[122] Regina F. Frey and Ernest R. Davidson. "Analysis of the bond energy of ScCO". In: *J. Chem. Phys.* 90 (1989), pp. 5541–5554. DOI: 10.1063/1.456407.

[123] M. Fuchs et al. "Pseudopotential study of binding properties of solids within generalized gradient approximations: The role of core-valence exchange correlation". In: *Phys. Rev. B* 57 (4 1998), pp. 2134–2145. DOI: 10.1103/PhysRevB.57.2134. URL: https://link.aps.org/doi/10.1103/PhysRevB.57.2134.

[124] P Fuentealba et al. "On the reliability of semi-empirical pseudopotentials: simulation of Hartree–Fock and Dirac-Fock results". In: *Journal of Physics B: Atomic and Molecular Physics (1968-1987)* 16.11 (1983), p. L323. DOI: 10.1088/0022-3700/16/11/001.

[125] P Fuentealba et al. "Pseudopotential calculations for alkaline-earth atoms". In: *Journal of Physics B: Atomic and Molecular Physics* 18.7 (1985), p. 1287. DOI: 10.1088/0022-3700/18/7/010.

[126] P. Fuentealba et al. "Pseudopotential calculations for alkaline-earth atoms". In: *J. Phys. B: At. Mol. Phys.* 18 (1985), pp. 1287–1296. DOI: 10.1088/0022-3700/18/7/010.

[127] Kenichi Fukui. "Formulation of the reaction coordinate". In: *J. Phys. Chem.* 74 (1970), pp. 4161–4163. DOI: 10.1021/j100717a029.

[128] Oleg B. Gadzhiev et al. "Quantum chemical study of the initial step of ozone addition to the double bond of ethylene". In: *J. Phys. Chem. A* 116 (42 2012), pp. 10420–10434. DOI: 10.1021/jp307738p.

[129] Kareem M. Gameel, Icell M. Sharafeldin, and Nageh K. Allam. "First=principles descriptors of CO chemisorption on Ni and Cu surfaces". In: *Phys. Chem. Chem. Phys.* 21 (2019), pp. 11476–11487. DOI: 10.1039/c9cp00881k.

[130] Anton Gatial et al. "On the dehydrogenation of N, N'-substituted p-phenylenediamine antioxidants. II. N-Phenyl-N'-(α-methylbenzyl)-p-phenylenediamine (SPPD)". In: *Vibrational Spectroscopy* 44 (2006), pp. 1–8. DOI: 10.1016/j.vibspec.2006.06.011.

[131] Oliver Geden, Vivian Scott, and James Palmer. "Integrating carbon dioxide removal into EU climate policy: Prospects for a paradigm shift". In: *Wiley Interdisciplinary Reviews: Climate Change* 9.4 (2018), e521. DOI: 10.1002/wcc.521.

[132] O. R. Gilliam, Charles M. Johnson, and Walter Gordy. "Microwave spectroscopy in the region from two to three millimeters". In: *Phys. Rev.* 78 (1950), pp. 140–147. DOI: 10.1103/PhysRev.78.140.

[133] JZ Gillies et al. "The ozonolysis of ethylene. microwave Spectrum, molecular structure, and dipole moment of ethylene primary ozonide (1, 2, 3-trioxolane)". In: *Journal of the American Chemical Society* 110.24 (1988), pp. 7991–7999. DOI: 10.1021/ja00232a007.

[134] Martí Gimferrer et al. "Oxidation State Localized Orbitals: A Method for Assigning Oxidation States Using Optimally Fragment-Localized Orbitals and a Fragment Orbital Localization Index". In: *J. Chem. Theory Comput.* 18.1 (2022), pp. 309–322. DOI: 10.1021/acs.jctc.1c01011.

[135] Vassiliki-Alexandra Glezakou et al. "Analysis of bonding patterns in the valence isoelectronic series O_3, S_3, SO_2, and OS_2 in terms of oriented quasi-atomic molecular orbitals". In: *J. Phys. Chem. A* 114 (2010), pp. 8923–8931. DOI: 10.1021/jp105025d.

[136] William A. Goddard et al. "Generalized valence bond description of bonding in low-lying states of molecules". In: *Acc. Chem. Res.* 6 (1973), pp. 368–376. DOI: 10.1021/ar50071a002.

[137] S. Goedecker and K. Maschke. "Transferability of pseudopotentials". In: *Phys. Rev. A* 45 (1 1992), pp. 88–93. DOI: 10.1103/PhysRevA.45.88.

[138] S. Goedecker, M. Teter, and J. Hutter. "Separable dual-space Gaussian pseudopotentials". In: *Phys. Rev. B* 54 (3 1996), pp. 1703–1710. DOI: 10.1103/PhysRevB.54.1703.

[139] Stefan Goedecker and Santanu Saha. "Eliminating core electrons in electronic structure calculations: Pseudopotentials and PAW potentials". In: *Handbook of Solid State Chemistry*. Ed. by Richard Dronskowski, Shinichi Kikkawa, and Andreas Stein. Wiley-VCH Verlag GmbH & Co, 2017. Chap. 2, pp. 29–58.

[140] Lars Goerigk et al. "A look at the density functional theory zoo with the advanced GMTKN55 database for general main group thermochemistry, kinetics and noncovalent interactions". In: *Phys. Chem. Chem. Phys.* 19 (2017), pp. 32184–32215. DOI: 10.1039/c7cp04913g.

[141] Alan S. Goldman and Karsten Krogh-Jespersen. "Why do cationic carbon monoxide complexes have high C−O stretching force constants and short C−O bonds? Electrostatic effects, not σ-bonding". In: *J. Am. Chem. Soc.* 118 (Aug. 1996), pp. 12159–12166. DOI: 10.1021/ja960876z.

[142] Jason D Goodpaster, Alexis T Bell, and Martin Head-Gordon. "Identification of possible pathways for C–C bond formation during electrochemical reduction of CO2: new theoretical insights from an improved electrochemical model". In: *The journal of physical chemistry letters* 7.8 (2016), pp. 1471–1477. DOI: 10.1021/acs.jpclett.6b00358.

[143] Stefan Grimme. "Semiempirical GGA-type density functional constructed with a long-range dispersion correction". In: *Journal of computational chemistry* 27.15 (2006), pp. 1787–1799.

[144] Gennady L. Gutsev, Lester Andrews, and Charles W. Bauschlicher. "3d-Metal monocarbonyls MCO, MCO^+, and MCO^- (M = Sc to Cu): comparative bond strengths and catalytic ability to produce CO_2 in reactions with CO". In: *Chem. Phys.* 290 (2003), pp. 47–58. DOI: 10.1016/S0301-0104(03)00097-1.

[145] Jürgen Hafner. "Ab-initio simulations of materials using VASP: Density-functional theory and beyond". In: *Journal of Computational Chemistry* 29.13 (2008), pp. 2044–2078. DOI: 10.1002/jcc.21057.

[146] P Hafner and WHE Schwarz. "Molecular spinors from the quasi-relativistic pseudopotential approach". In: *Chemical Physics Letters* 65.3 (1979), pp. 537–541. DOI: 10.1016/0009-2614(79)80287-0.

[147] Diptarka Hait and Martin Head-Gordon. "How accurate are static polarizability predictions from density functional theory? An assessment over 132 species at equilibrium geometry". In: *Phys. Chem. Chem. Phys.* 20 (2018), pp. 19800–19810. DOI: 10.1039/c8cp03569e.

[148] Diptarka Hait and Martin Head-Gordon. "How accurate is density functional theory at predicting dipole moments? An assessment using a new database of 200 benchmark values". In: *J. Chem. Theory Comput.* 14 (Mar. 2018), pp. 1969–1981. DOI: 10.1021/acs.jctc.7b01252.

[149] G. G. Hall. "The molecular orbital theory of chemical valency VIII. A method of calculating ionization potentials". In: 205 (1083 1951), pp. 541–552. DOI: 10.1098/rspa.1951.0048.

[150] D. R. Hamann, M. Schlüter, and C. Chiang. "Norm-Conserving Pseudopotentials". In: *Phys. Rev. Lett.* 43 (20 1979), pp. 1494–1497. DOI: 10.1103/PhysRevLett.43.1494.

[151] Frederik Hammes et al. "Mechanistic and kinetic evaluation of organic disinfection by-product and assimilable organic carbon (AOC) formation during the ozonation of drinking water". In: *Water Research* 40 (2006), pp. 2275–2286. DOI: 10.1016/j.watres.2006.04.029.

[152] Sharon Hammes-Schiffer. "Theoretical perspectives on non-Born–Oppenheimer effects in chemistry". In: *Philosophical Transactions of the Royal Society A* 380.2223 (2022), p. 20200377.

[153] D. R. Hartree. "The Wave Mechanics of an Atom with a Non-Coulomb Central Field. Part II. Some Results and Discussion". In: *Mathematical Proceedings of the Cambridge Philosophical Society* 24.1 (1928), pp. 111–132. DOI: 10.1017/S0305004100011920.

[154] Douglas R Hartree. *The calculation of atomic structures*. John Wiley & Sons, 1957.

[155] C. Hartwigsen, S. Goedecker, and J. Hutter. "Relativistic separable dual-space Gaussian pseudopotentials from H to Rn". In: *Phys. Rev. B* 58 (1998), pp. 3641–3662. DOI: 10.1103/PhysRevB.58.3641.

[156] P Jeffrey Hay and Richard L Martin. "Theoretical studies of the structures and vibrational frequencies of actinide compounds using relativistic effective core potentials with Hartree–Fock and density functional methods: UF 6, NpF 6, and PuF 6". In: *The Journal of chemical physics* 109.10 (1998), pp. 3875–3881. DOI: 10.1063/1.476988.

[157] P Jeffrey Hay and Willard R Wadt. "Ab initio effective core potentials for molecular calculations. Potentials for K to Au including the outermost core orbitals". In: *J. Chem. Phys.* 82.1 (1985), pp. 299–310. DOI: 10.1063/1.448975.

[158] P Jeffrey Hay, Willard R Wadt, and Luis R Kahn. "Ab initio effective core potentials for molecular calculations. II. All-electron comparisons and modifications of the procedure". In: *The Journal of Chemical Physics* 68.7 (1978), pp. 3059–3066. DOI: 10.1063/1.436172.

[159] P. Jeffrey Hay, Thom H. Dunning, and William A. Goddard. "Configuration interaction studies of O_3 and O_3^+. Ground and excited states". In: *J. Chem. Phys.* 62 (1975), pp. 3912–3924. DOI: 10.1063/1.430306.

[160] Trygve Helgaker, Poul Jørgensen, and Jeppe Olsen. "Configuration-Interaction Theory". In: *Molecular Electronic-Structure Theory*. John Wiley & Sons, Ltd, 2000. Chap. 11, pp. 523–597. ISBN: 9781119019572. DOI: https://doi.org/10.1002/9781119019572.ch11. eprint: https://onlinelibrary.wiley.com/doi/pdf/10.1002/9781119019572.ch11.

[161] Trygve Helgaker, Poul Jørgensen, and Jeppe Olsen. "Coupled-Cluster Theory". In: *Molecular Electronic-Structure Theory*. John Wiley & Sons, Ltd, 2000. Chap. 13, pp. 648–723. ISBN: 9781119019572. DOI: https://doi.org/10.1002/9781119019572.ch13.

[162] Trygve Helgaker, Poul Jørgensen, and Jeppe Olsen. "Perturbation Theory". In: *Molecular Electronic-Structure Theory*. John Wiley & Sons, Ltd, 2000. Chap. 13, pp. 724–816. ISBN: 9781119019572. DOI: https://doi.org/10.1002/9781119019572.ch14.

[163] Trygve Helgaker, Poul Jørgensen, and Jeppe Olsen. "Second Quantization". In: *Molecular Electronic-Structure Theory*. John Wiley & Sons, Ltd, 2000. Chap. 1, pp. 1–33. ISBN: 9781119019572. DOI: https://doi.org/10.1002/9781119019572.ch1.

[164] Hans Hellmann. "A new approximation method in the problem of many electrons". In: *J. Chem. Phys.* 3.1 (1935), pp. 61–61. DOI: 10.1063/1.1749559.

[165] Klaus Hermann, Paul S. Bagus, and Constance J. Nelin. "Size dependence of surface cluster models: CO adsorbed on Cu(100)". In: *Phys. Rev. B* 35 (1987), pp. 9467–9473. DOI: 10.1103/physrevb.35.9467.

[166] Kyoshiro Hiki et al. "Acute Toxicity of a Tire Rubber-Derived Chemical, 6PPD Quinone, to Freshwater Fish and Crustacean Species". In: *Environ. Sci. Technol. Lett.* 8.9 (2021), pp. 779–784.

[167] I. H. Hillier and V. R. Saunders. "Ab initio calculation of the bonding in nickel tetracarbonyl". In: *J. Chem. Soc. D* (1971), pp. 642–643. DOI: 10.1039/C29710000642.

[168] I. H. Hillier and V. R. Saunders. "Ab initio molecular orbital calculations of transition metal complexes". In: *Mol. Phys.* 22 (1971), pp. 1025–1034. DOI: 10.1080/00268977100103341.

[169] Pierre Hohenberg and Walter Kohn. "Inhomogeneous electron gas". In: *Physical review* 136.3B (1964), B864.

[170] Sung W. Hong and Chung-Yuan Lin. "Improving flex fatigue and dynamic ozone crack resistance through antidegradamts". In: *Rubber World* (2000), pp. 36–41.

[171] Y. Hori. "Electrochemical CO2 Reduction on Metal Electrodes". In: *Modern Aspects of Electrochemistry*. Ed. by Constantinos G. Vayenas, Ralph E. White, and Maria E. Gamboa-Aldeco. New York, NY: Springer New York, 2008, pp. 89–189. ISBN: 978-0-387-49489-0. DOI: 10.1007/978-0-387-49489-0_3. URL: https://doi.org/10.1007/978-0-387-49489-0_3.

[172] Yoshio Hori et al. "Selective formation of C2 compounds from electrochemical reduction of CO2 at a series of copper single crystal electrodes". In: *The Journal of Physical Chemistry B* 106.1 (2002), pp. 15–17. DOI: 10.1021/jp013478d.

[173] Paul R. Horn and Martin Head-Gordon. "Polarization contributions to intermolecular interactions revisited with fragment electric-field response functions". In: *J. Chem. Phys.* 143 (2015), p. 114111. DOI: 10.1063/1.4930534.

[174] Paul R. Horn, Yuezhi Mao, and Martin Head–Gordon. "Defining the contributions of permanent electrostatics, Pauli repulsion, and dispersion in density functional theory calculations of intermolecular interaction energies". In: *J. Chem. Phys.* 144 (2016), p. 114107. DOI: 10.1063/1.4942921.

[175] Luboš Horný et al. "The low-lying electronic excited states of NiCO". In: *J. Chem. Phys.* 121 (2004), pp. 1412–1418. DOI: 10.1063/1.1760073.

[176] Lianrui Hu and Hui Chen. "Assessment of DFT methods for computing activation energies of Mo/W-mediated reactions". In: *J. Chem. Theory Comput.* 11 (10 2015), pp. 4601–4614. DOI: 10.1021/acs.jctc.5b00373.

[177] Ximin Hu et al. "Transformation product formation upon heterogeneous ozonation of the tire rubber antioxidant 6ppd (N-(1,3-dimethylbutyl)-N'-phenly-p-phenylene diamine". In: *Environ. Sci. Technol. Lett.* 9 (2022), pp. 413–419. DOI: 10.1021/acs.estlett.2c00187.

[178] Uwe Hübner, Urs von Gunten, and Martin Jekel. "Evaluation of the persistence of transformation products from ozonation of trace organic compounds – A critical review". In: *Water Research* 68 (2015), pp. 150–170. DOI: 10.1016/j.watres.2014.09.051.

[179] N. M. Huntink, R. N. Datta, and J. W. M. Noordermeer. "Addressing Durability of Rubber Compounds". In: *Rubber Chemistry and Technology* 77 (2004), pp. 476–511. DOI: 10.5254/1.3547833.

[180] Nicolaas Maria Huntink. *Durability of rubber products: Development of new anti-degradants for long-term protection*. Enschede : Twente University Press, 2003, pp. 1–207.

[181] Chun-Fang Huo et al. "Structures and energies of $[Co(CO)_n]^m$ ($m = 0, 1+, 1-$) and $HCo(CO)_n$: Density functional studies". In: *J. Phys. Chem. A* 106 (2002), pp. 12161–12169. DOI: 10.1021/jp0270710.

[182] M. M. Hurley et al. "*Ab initio* relativistic effective potentials with spin-orbit operators. II. K through Kr". In: *J. Chem. Phys.* 84 (1986), pp. 6840–6853. DOI: 10.1063/1.450689.

[183] Jürg Hutter et al. "CP2K: Atomistic simulations of condensed matter systems". In: *WIREs Computational Molecular Science* 4.1 (2014), pp. 15–25. DOI: https://doi.org/10.1002/wcms.1159. eprint: https://wires.onlinelibrary.wiley.com/doi/pdf/10.1002/wcms.1159. URL: https://wires.onlinelibrary.wiley.com/doi/abs/10.1002/wcms.1159.

[184] G Igel-Mann, H Stoll, and H Preuss. "Pseudopotentials for main group elements (IIIa through VIIa)". In: *Molecular Physics* 65.6 (1988), pp. 1321–1328. DOI: 10.1080/00268978800101811.

[185] Benjamin G Janesko, Thomas M Henderson, and Gustavo E Scuseria. "Screened hybrid density functionals for solid-state chemistry and physics". In: *Physical Chemistry Chemical Physics* 11.3 (2009), pp. 443–454. DOI: 10.1039/B812838C.

[186] Gwang-Hi Jeung and Stéphane Haettel. "Are metal–CO molecules linear? ScCO, TiCO, VCO, and CrCO cases studied in MRCI method compared with DFT method". In: *Int. J. Quantum Chem.* 61 (1997), pp. 547–550. DOI: 10.1002/(SICI)1097-461X(1997)61:3<547::AID-QUA23>3.0.CO;2-4.

[187] Ling Jiang, Yun-Lei Teng, and Qiang Xu. "Reactions of laser-ablated zinc and cadmium atoms with CO: Infrared spectra of the $Zn(CO)_x$ ($x = 1 - 3$), $CdCO^-$, and $Cd(CO)_2$ molecules in solid neon". In: *J. Phys. Chem. A* 110 (2006), pp. 7092–7096. DOI: 10.1021/jp0614852.

[188] Ling Jiang and Qiang Xu. "Infrared spectroscopic and theoretical studies on the reactions of copper atoms with carbon monoxide and nitric oxide molecules in rare-gas matrices". In: *J. Phys. Chem. A* 111 (2007), pp. 2690–2696. DOI: 10.1021/jp067050w.

[189] Wanyi Jiang, Nathan J. DeYonker, and Angela K. Wilson. "Multireference character for 3d transition-metal-containing molecules". In: *J. Chem. Theory Comput.* 8 (2012), pp. 3171–3179. DOI: 10.1021/acs.jctc.5b00422.

[190] Ryosuke Jinnouchi and Alfred B Anderson. "Electronic structure calculations of liquid-solid interfaces: Combination of density functional theory and modified Poisson-Boltzmann theory". In: *Physical Review B* 77.24 (2008), p. 245417. DOI: 10.1103/PhysRevB.77.245417.

[191] Jeffrey B. Johnson and W. G. Klemperer. "A molecular orbital analysis of electronic structure and bonding in chromium hexacarbonyl". In: *J. Am. Chem. Soc.* 99 (1977), pp. 7132–7137. DOI: 10.1021/ja00464a006.

[192] John-Paul Jones, GK Surya Prakash, and George A Olah. "Electrochemical CO2 reduction: recent advances and current trends". In: *Israel Journal of Chemistry* 54.10 (2014), pp. 1451–1466. DOI: 10.1002/ijch.201400081.

[193] RO Jones and O Gunnarsson. "Density-functional formalism: Sources of error in local-density approximations". In: *Physical review letters* 55.1 (1985), p. 107.

[194] Matthew Jouny, Wesley Luc, and Feng Jiao. "General techno-economic analysis of CO2 electrolysis systems". In: *Industrial & Engineering Chemistry Research* 57.6 (2018), pp. 2165–2177. DOI: 10.1021/acs.iecr.7b03514.

[195] Zarko P Jovanov et al. "Opportunities and challenges in the electrocatalysis of CO2 and CO reduction using bifunctional surfaces: A theoretical and experimental study of Au–Cd alloys". In: *Journal of Catalysis* 343 (2016), pp. 215–231. DOI: 10.1016/j.jcat.2016.04.008.

[196] Petr Jurečka et al. "Benchmark database of accurate MP2 and CCSD(T) complete basis set limit interaction energies of small model complexes, DNA base pairs, and amino acid pairs". In: *Phys. Chem. Chem. Phys.* 8 (17 2006), pp. 1985–1993. DOI: 10.1039/B600027D.

[197] K.Yamaguchi et al. "A spin correction procedure for unrestricted Hartree-Fock and Møller-Plesset wavefunctions for singlet diradicals and polyradicals". In: *Chem. Phys. Lett.* 149 (1988), pp. 537–542. DOI: 10.1016/0009-2614(88)80378-6.

[198] Luis R Kahn, Paul Baybutt, and Donald G Truhlar. "Ab initio effective core potentials: Reduction of all-electron molecular structure calculations to calculations involving only valence electrons". In: *The Journal of Chemical Physics* 65.10 (1976), pp. 3826–3853. DOI: 10.1063/1.432900.

[199] Luis R Kahn and William A Goddard III. "Ab initio effective potentials for use in molecular calculations". In: *The Journal of Chemical Physics* 56.6 (1972), pp. 2685–2701. DOI: 10.1063/1.1677597.

[200] Apostolos Kalemos and Aristides Mavridis. "Electronic structure and bonding of ozone". In: *J. Chem. Phys.* 129 (2008), p. 054312. DOI: 10.1063/1.2960629.

[201] Runhua Kang et al. "How accurate can a local couped cluster approach be in computing the activation energies of late-transition-metal-catalyzed reactions with Au, Pt, and Ir?" In: *J. Chem. Theory Comput.* 8 (9 2012), pp. 3119–3127. DOI: 10.1021/ct3003942.

[202] Amir Karton, Shauli Daon, and Jan M. L. Martin. "W4-11: A high-confidence benchmark dataset for computational thermochemistry dervied from first-principles W4 data". In: *Chem. Phys. Lett.* 510 (2011), pp. 165–178. DOI: 10.1016/j.cplett.2011.05.007.

[203] Martin Kaupp et al. "Pseudopotential approaches to Ca, Sr, and Ba hydrides. Why are some alkaline earth MX2 compounds bent?" In: *The Journal of chemical physics* 94.2 (1991), pp. 1360–1366. DOI: 10.1063/1.459993.

[204] David P Keller et al. "The effects of carbon dioxide removal on the carbon cycle". In: *Current climate change reports* 4.3 (2018), pp. 250–265. DOI: 10.1007/s40641-018-0104-3.

[205] Rustam Z. Khaliullin, Alexis T. Bell, and Martin Head-Gordon. "Analysis of charge transfer effects in molecular complexes based on absolutely localized molecular orbitals". In: *J. Chem. Phys.* 128 (2008), p. 184112. DOI: 10.1063/1.2912041.

[206] Rustam Z. Khaliullin, Alexis T. Bell, and Martin Head-Gordon. "Electron donation in the water–water hydrogen bond". In: *Chem. Eur. J.* 15 (2009), pp. 851–855. DOI: 10.1002/chem.200802107.

[207] Rustam Z. Khaliullin et al. "Unraveling the origin of intermolecular interactions using absolutely localized molecular orbitals". In: *J. Phys. Chem. A* 111 (2007), pp. 8753–8765. DOI: 10.1021/jp073685z.

[208] Md Golam Kibria et al. "Electrochemical CO2 reduction into chemical feedstocks: from mechanistic electrocatalysis models to system design". In: *Advanced Materials* 31.31 (2019), p. 1807166. DOI: 10.1002/adma.201807166.

[209] Joonghan Kim, Yoon Sup Lee, and Hyotcherl Ihee. "Density function and ab initio studies on structures and energies of the ground state of CrCO". In: *Int. J. Quantum Chem.* 107 (2007), pp. 458–463. DOI: 10.1002/qua.21099.

[210] Joonghan Kim et al. "Density functional and ab initio study of $Cr(CO)_n$ ($n = 1 - 6$) complexes". In: *J. Phys. Chem. A* 111 (2007), pp. 4697–4710. DOI: 10.1021/jp066081o.

[211] Barbara Kirchner, Philipp J di Dio, and Juerg Hutter. "Real-world predictions from ab initio molecular dynamics simulations". In: *Multiscale Molecular Methods in Applied Chemistry* (2011), pp. 109–153. DOI: 10.1007/128_2011_195.

[212] Barbara Kirchner, Philipp J. di Dio, and Jürg Hutter. "Real-World Predictions from Ab Initio Molecular Dynamics Simulations". In: *Multiscale Molecular Methods in Applied Chemistry*. Ed. by Barbara Kirchner and Jadran Vrabec. Berlin, Heidelberg: Springer Berlin Heidelberg, 2012, pp. 109–153. ISBN: 978-3-642-24968-6. DOI: 10.1007/128_2011_195. URL: https://doi.org/10.1007/128_2011_195.

[213] D.P. Kiryukhin, B.E. Krisyuk, and A.V. Maiorov. "Kinetics and mechanism of ozone addition to tetrafluoroethylene and hexafluoropropylene". In: *Russian Chemical Bulletin* 70 (2021), pp. 132–139. DOI: 10.1007/s11172-021-3067-9.

[214] Yasutaka Kitagawa et al. "Approximately spin-projected geometry optimization method and its application to di-chromium systems". In: *Chem. Phys. Lett.* 442 (2007), pp. 445–450. DOI: 10.1016/j.cplett.2007.05.082.

[215] Leonard Kleinman. "Relativistic norm-conserving pseudopotential". In: *Phys. Rev. B* 21 (1980), pp. 2630–2631. DOI: 10.1103/PhysRevB.21.2630.

[216] Leonard Kleinman. "Relativistic norm-conserving pseudopotential". In: *Phys. Rev. B* 21 (6 1980), pp. 2630–2631. DOI: 10.1103/PhysRevB.21.2630.

[217] Philipp Klöckner et al. "Organic markers of tire and road wear particles in sediments and soils: Transformation products of major antiozonants as promising candidates". In: *Environ. Sci. Technol.* 55 (2021), pp. 11723–11732. DOI: 10.1021/acs.est.1c02723.

[218] Gerald Knizia. "Intrinsic atomic orbitals: An unbiased bridge between quantum theory and chemical concepts". In: *J. Chem. Theory Comput.* 9 (2013), pp. 4834–4843. DOI: 10.1021/ct400687b.

[219] Walter Kohn and Lu Jeu Sham. "Self-consistent equations including exchange and correlation effects". In: *Physical review* 140.4A (1965), A1133.

[220] Constantine Koukounas, Stavros Kardahakis, and Aristides Mavridis. "Electronic and geometric structure of the 3d-transition metal monocarbonyls MCO, M = Sc, Ti, V, and Cr". In: *J. Chem. Phys.* 123 (Aug. 2005), p. 074327. DOI: 10.1063/1.949199.

[221] M. Krack. "Pseudopotentials for H to Kr optimized for gradient-corrected exchange-correlation functions". In: *Theor. Chem. Acc.* 114 (2005), pp. 145–152. DOI: 10.1007/s00214-005-0655-y.

[222] G. Kresse and J. Hafner. "Ab initio molecular dynamics for open-shell transition metals". In: *Phys. Rev. B* 48.17 (1993), pp. 13115–13118. DOI: 10.1103/PhysRevB.48.13115.

[223] G. Kresse and D. Joubert. "From ultrasoft pseudopotentials to the projector augmented- wave method". In: *Phys. Rev. B* 59 (1999), pp. 1758–1775. DOI: 10.1103/PhysRevB.59.1758.

[224] B. E. Krisyuk and A. V. Maiorov. "Competition between the concerted and nonconcerted addition of ozone to a double bond". In: *Russian Journal of Physical Chemistry B* 5 (2011), pp. 790–796. DOI: 10.1134/S1990793111090065.

[225] W. Küchle et al. "Ab initio pseudopotentials for Hg through Rn". In: *Mol. Phys.* 74.6 (1991), pp. 1245–1263. DOI: 10.1080/00268979100102941.

[226] Kendra P Kuhl et al. "New insights into the electrochemical reduction of carbon dioxide on metallic copper surfaces". In: *Energy & Environmental Science* 5.5 (2012), pp. 7050–7059. DOI: 10.1039/C2EE21234J.

[227] Thomas D. Kühne et al. "CP2K: An electronic structure and molecular dynamics software package - Quickstep: Efficient and accurate electronic structure calculations". In: *The Journal of Chemical Physics* 152.19 (2020), p. 194103. DOI: 10.1063/5.0007045. eprint: https://doi.org/10.1063/5.0007045. URL: https://doi.org/10.1063/5.0007045.

[228] Manoj Kumar et al. "Multiple stable isoprene–ozone complexes reveal complex entrance channel dynamics in the isoprene + ozone reaction". In: *J. Am. Chem. Soc.* 142 (24 2020), pp. 10806–10813. DOI: 10.1021/jacs.0c02360.

[229] Kathryn L. Kunze and Ernest R. Davidson. "Energetics and electronic structure of chromium hexacarbonyl". In: *J. Phys. Chem.* 96 (1992), pp. 2129–2141. DOI: 10.1021/j100184a022.

[230] Werner Kutzelnigg. "The relativistic many body problem in molecular theory". In: *Physica Scripta* 36 (1987), p. 416. DOI: 10.1088/0031-8949/36/3/007.

[231] L. A. LaJohn et al. "Ab initio relativistic effective potentials with spin–orbit operators. III. Rb through Xe". In: *The Journal of Chemical Physics* 87 (1987), pp. 2812–2824. DOI: 10.1063/1.453069.

[232] Alexei A Lapkin et al. "Screening of new solvents for artemisinin extraction process using ab initio methodology". In: *Green Chemistry* 12.2 (2010), pp. 241–251. DOI: 10.1039/B922001A.

[233] R. P. Lattimer et al. "Mechanisms of ozonation of N-(1,3-Dimethylbutyl)-N'-phenyl-p-phenyl- enediamine". In: *Rubber Chemistry and Technology* 56.2 (1983), pp. 431–439. DOI: 10.5254/1.3538136.

[234] R.P. Lattimer et al. "Mechanisms of ozonation of N, N'-di-(1-methylheptyl)-p-phenylenediamine". In: *Rubber Chem. Technol.* 53 (1980), pp. 1170–1190. DOI: 10.5254/1.3535087.

[235] Robert W. Layer. "Reaction of ozone with p-phenylenediamine and related compounds". In: *Rubber Chem. Technol.* 39 (1966), pp. 1584–1592. DOI: 10.5254/1.3547073.

[236] V. I. Lebedev. "Quadratures on a sphere". In: *USSR Computational Mathematics and Mathematical Physics* 16 (2 1976), pp. 10–24. DOI: 10.1016/0041-5553(76)90100-2.

[237] V. I. Lebedev. "Values of the nodes and weights of ningth to seventeenth order gauss-markov quadrature formulae invariant under the octahedron group with inversion". In: *USSR Computational Mathematics and Mathematical Physics* 15 (1 1975), pp. 44–51. DOI: 10.1016/0041-5553(75)90133-0.

[238] Chengteh Lee, Weitao Yang, and Robert G Parr. "Development of the Colle-Salvetti correlation-energy formula into a functional of the electron density". In: *Physical review B* 37.2 (1988), p. 785.

[239] Joonho Lee and Martin Head-Gordon. "Distinguishing artificial and essential symmetry breaking in a single determinant: Approach and application to the C 60, C 36, and C 20 fullerenes". In: *Phys. Chem. Chem. Phys.* 21.9 (2019), pp. 4763–4778.

[240] Joonho Lee and Martin Head-Gordon. "Regularized orbital-optimized second-order Møller–Plesset perturbation theory: A reliable fifth-order-scaling electron correlation model with orbital energy dependent regularizers". In: *J. Chem. Theory Comput.* 14 (2018), pp. 5203–5219. DOI: 10.1021/acs.jctc.8b00731.

[241] Joonho Lee and Martin Head-Gordon. "Two single-reference approaches to singlet biradicaloid problems: Complex, restricted orbitals and approximate spin-projection combined with regularized orbital-optimized Møller-Plesset perturbation theory". In: *J. Chem. Phys.* 150 (2019), p. 244106. DOI: 10.1063/1.5097613.

[242] Minju Lee et al. "Development of prediction models for the reactivity of organic compounds with ozone in aqueous solution by quantum chemical calculations: The role of delocalized and localized molecular orbitals". In: *Environ. Sci. Technol.* 49 (2015), pp. 9925–9935. DOI: 10.1021/acs.est.5b00902.

[243] Richmond Lee and Michelle L. Coote. "Mechanistic insights into ozone-initiated oxidative degradation of saturated hydrocarbons and polymers". In: *Phys. Chem. Chem. Phys.* 18 (2016), pp. 24663–24671. DOI: 10.1039/C6CP05064F.

[244] Matthew L Leininger et al. "Is Mo/ller–Plesset perturbation theory a convergent ab initio method?" In: *The Journal of Chemical Physics* 112.21 (2000), pp. 9213–9222.

[245] Thierry Leininger et al. "The accuracy of the pseudopotential approximation: Non-frozen-core effects for spectroscopic constants of alkali fluorides XF (X= K, Rb, Cs)". In: *Chem. Phys. Lett.* 255 (1996), pp. 274–280. DOI: 10.1016/0009-2614(96)00382-X.

[246] Gui-Yang Li and J.L. Koenig. "FTIR imaging of oxidation of polyisoprene. 2. The role of *N*-phenyl-*N*′-dimethylbutyl-*p*-phenylenediamine antioxidant". In: *Poly. Degrad. Stab.* 81 (2003), pp. 377–385. DOI: 10.1016/S0141-3910(03)00109-5.

[247] Wan-Lu Li et al. "Critical role of thermal fluctuations for CO binding on electrocatalytic metal surfaces". In: *JACS Au* 1.10 (2021), pp. 1708–1718.

[248] Wan-Lu Li et al. "Optimized pseudopotentials and basis sets for semiempirical density functional theory for electrocatalysis applications". In: *J. Phys. Chem. Lett.* 12 (2022), pp. 10304–10309. DOI: acs.jpclett.1c02918.

[249] Zhendong Li, Yunlong Xiao, and Wenjian Liu. "On the spin separation of algebraic two-component relativistic Hamiltonians". In: *J. Chem. Phys.* 137.15 (2012), p. 154114.

[250] Zhenwei Li, James R Kermode, and Alessandro De Vita. "Molecular dynamics with on-the-fly machine learning of quantum-mechanical forces". In: *Physical review letters* 114.9 (2015), p. 096405. DOI: 10.1103/PhysRevLett.114.096405.

[251] Binyong Liang and Lester Andrews. "Reactions of laser-ablated Ag and Au atoms with carbon monoxide: Matrix infrared spectra and density functional calculations on $Ag(CO)_n$ ($n = 2, 3$), $Au(CO)_n$ ($n = 1, 2$) and $M(CO)_n^+$ ($n = 1 - 4$; M=AgAu)". In: *J. Phys. Chem. A* 104 (2000), pp. 9156–9164. DOI: 10.1021/jp001833e.

[252] Sharon G. Lias et al. "NIST Chemistry WebBook, NIST Standard Reference Database Number 69". In: ed. by P.J. Linstrom and W.G. Mallrd. Gaithersburg, MD: National Institute of Standards and Technology. Chap. Ion Energetics Data. DOI: 10.18434/T4D303.

[253] Sungeun Lim, Christa S. McArdell, and Urs von Gunten. "Reactions of aliphatic amines with ozone: Kinetics and mechanisms". In: *Water Research* 157 (2019), pp. 514–528. DOI: 10.1016/j.watres.2019.03.089.

[254] Christianna N. Lininger et al. "Challenges for density functional theory: calculation of CO adsorption on electrocatalytically relevant metals". In: *Phys. Chem. Chem. Phys.* 23 (15 2021), pp. 9394–9406. DOI: 10.1039/D0CP03821K.

[255] Gerald Lippert, Jürg Hutter, and Michele Parrinello. "A hybrid Gaussian and plane wave density functional scheme". In: *Molecular Physics* 92.3 (1997), pp. 477–488. DOI: 10.1080/002689797170220. eprint: https://doi.org/10.1080/002689797170220. URL: https://doi.org/10.1080/002689797170220.

[256] Wenjian Liu and Daoling Peng. "Exact two-component Hamiltonians revisited". In: *J. Chem. Phys.* 131.3 (2009), p. 031104.

[257] R.C. Lochan and Martin Head-Gordon. "Orbital-optimized opposite-spin scaled second-order correlation: An economical method to improve the description of open-shell molecules". In: *J. Chem. Theory Comput.* 3 (2007), pp. 988–1003. DOI: 10.1063/1.2718952.

[258] Jun-Bo Lu et al. "Norm-conserving pseudopotentials and basis sets to explore actinide chemistry in complex environments". In: *Journal of Chemical Theory and Computation* 17.6 (2021), pp. 3360–3371. DOI: 10.1021/acs.jctc.1c00026.

[259] Jun-Bo Lu et al. "Norm-conserving pseudopotentials and basis sets to explore lanthanide chemistry in complex environments". In: *J. Chem. Theory Comput.* 15 (11 2019), pp. 5987–5997. DOI: 10.1021/acs.jctc.9b00553.

[260] Anthony J. Lupinetti et al. "Theoretical analysis of the bonding between CO and positively charged atoms". In: *J. Phys. Chem. A* 101 (Aug. 1997), pp. 9551–9559. DOI: 10.1021/jp9726571.

[261] G. Makov and M. C. Payne. "Periodic boundary conditions in ab initio calculations". In: *Phys. Rev. B* 51.7 (1995), pp. 4014–4022. DOI: 10.1103/PhysRevB.51.4014. URL: https://link.aps.org/doi/10.1103/PhysRevB.51.4014.

[262] Samuel Manzer et al. "Fast, accurate evaluation of exact exchange: The occ-RI-K algorithm". In: *The Journal of chemical physics* 143.2 (2015), p. 024113. DOI: 10.1063/1.4923369.

[263] Samuel F Manzer, Evgeny Epifanovsky, and Martin Head-Gordon. "Efficient implementation of the pair atomic resolution of the identity approximation for exact exchange for hybrid and range-separated density functionals". In: *Journal of chemical theory and computation* 11.2 (2015), pp. 518–527. DOI: 10.1021/ct5008586.

[264] Y. Mao et al. "From intermolecular interaction energies and observable shifts to component contributions and back again: A tale of variational energy decomposition analysis". In: *Ann. Rev. Phys. Chem.* 72 (2021), pp. 641–666. DOI: 10.1146/annurev-physchem-090419-115149.

[265] Yuezhi Mao and Martin Head-Gordon. "Probing blue-shifting hydrogen bonds with adiabatic energy decomposition analysis". In: *Chem. Phys. Lett.* 10 (2019), pp. 3899–3905. DOI: 10.1021/acs.jpclett.9b01203.

[266] Yuezhi Mao, Paul R. Horn, and Martin Head–Gordon. "Energy decomposition analysis in an adiabatic picture". In: *Phys. Chem. Chem. Phys.* 19 (2017), pp. 5944–5958. DOI: 10.1039/C6CP08039A.

[267] Yuezhi Mao et al. "On the computational characterization of charge-transfer effects in noncovalently bound molecular complexes". In: *J. Chem. Theory Comput.* 14 (2018), pp. 2401–2417. DOI: 10.1021/acs.jctc.7b01256.

[268] N. Mardirossian and M. Head-Gordon. "ωB97M-V: A combinatorially optimized, range-separated hybrid, meta-GGA density functional with VV10 nonlocal correlation". In: *J. Chem. Phys.* 144 (2016), p. 214110. DOI: 10.1063/1.4952647.

[269] N. Mardirossian and M. Head-Gordon. "ωB97X-V: A 10-parameter, range-separated hybrid, generalized gradient approximation density functional with nonlocal correlation, designed by a survival-of-the-fittest strategy". In: *Phys. Chem. Chem. Phys.* 16 (21 2014), pp. 9904–9924. DOI: 10.1039/C3CP54374A.

[270] Narbe Mardirossian and Martin Head-Gordon. "ωB97X-V: A 10-parameter, range-separated hybrid, generalized gradient approximation density functional with nonlocal correlation, dsigned by a survival-of-the-fittest strategy". In: *Phys. Chem. Chem. Phys.* 16 (2014), pp. 9904–9924. DOI: 10.1039/c3cp54374a.

[271] Narbe Mardirossian and Martin Head-Gordon. "Mapping the genome of meta-generalized gradient approximation density functionals: The search for B97M-V". In: *J. Chem. Phys.* 142.7 (2015), p. 074111.

[272] Narbe Mardirossian and Martin Head-Gordon. "Thirty years of density functional theory in computational chemistry: An overview and extensive assessment of 200 density functionals". In: *Mol. Phys.* 115 (June 2017), pp. 2315–2372. DOI: 10.1080/00268976.2017.1333644.

[273] Narbe Mardirossian et al. "Use of the rVV10 nonlocal correlation functional in the B97M-V density functional: Defining B97M-rV and related functionals". In: *J. Phys. Chem. Lett.* 8 (1 2017), pp. 35–40. DOI: 10.1021/acs.jpclett.6b02527.

[274] Jan ML Martin and Golokesh Santra. "Empirical double-hybrid density functional theory: A 'third way'in between WFT and DFT". In: *Israel Journal of Chemistry* 60.8-9 (2020), pp. 787–804.

[275] Ángel Martín, Alexander Navarrete, and María Dolores Bermejo. "Applications of supercritical technologies to CO2 reduction: Catalyst development and process intensification". In: *The Journal of Supercritical Fluids* 134 (2018), pp. 141–149. DOI: 10.1016/j.supflu.2017.11.021.

[276] A. Mavridis, J. F. Harrison, and J. Allison. "On the electrostatic bonding of CO to the monocations of the first-row transition elements". In: *J. Am. Chem. Soc.* 111 (1989), pp. 2482–2487. DOI: 10.1021/ja00189a019.

[277] Daniel L. McCurry, Amanda N. Quay, and William A. Mitch. "Ozone promotes chloropicrin formation by oxidizing amines to nitro compounds". In: *Environ. Sci. Technol.* 50 (2016), pp. 1209–1217. DOI: 10.1021/acs.est.5b04282.

[278] Simon C. McKenzie et al. "Efficient method for calculating effective core potential integrals". In: *J. Phys. Chem. A* 122 (11 2018), pp. 3066–3075. DOI: 10.1021/acs.jpca.7b12679.

[279] Bernhard Metz, Hermann Stoll, and Michael Dolg. "Small-core multiconfiguration-Dirac–Hartree–Fock-adjusted pseudopotentials for post-d main group elements: Application to PbH and PbO". In: *The Journal of Chemical Physics* 113.7 (2000), pp. 2563–2569. DOI: 10.1063/1.1305880.

[280] Evangelos Miliordos, Klaus Ruedenberg, and Sotiris S. Xantheas. "Unusual inorganic biradicals: A theoretical analysis". In: *Angew. Chem.* 125 (2013), pp. 5848–5851. DOI: 10.1002/ange.201300654.

[281] Evangelos Miliordos and Sotiris S. Xantheas. "On the bonding nature of ozone (O_3) and its sulfur-substituted analogues SO_2, OS_2, and S_3: Correlation between their biradical character and molecular properties". In: *J. Am. Chem. Soc.* 136 (2014), pp. 2808–2817. DOI: 10.1021/ja410726u.

[282] C. Møller and M.S. Plesset. "Note on an approximation treatment for many-electron systems". In: *Phys. Rev.* 46.7 (1934), pp. 618–622. DOI: 10.1103/PhysRev.46.618.

[283] Klaus A. Moltved and Kasper P. Kepp. "Chemical bond energies of 3d transition metals studied by density functional theory". In: *J. Chem. Theory Comput.* 14 (7 2018), pp. 3479–3492. DOI: 10.1021/acs.jctc.8b00143.

[284] Joseph H Montoya et al. "Materials for solar fuels and chemicals". In: *Nature materials* 16.1 (2017), pp. 70–81. DOI: 10.1038/nmat4778.

[285] Keiji Morokuma. "Molecular orbital studies of hydrogen bonds. III. C=O···H−O hydrogen bond in $H_2CO\cdots H_2O$ and $H_2CO\cdots 2\,H_2O$". In: *J. Chem. Phys.* 55 (1971), pp. 1236–1244. DOI: 10.1063/1.1676210.

[286] Keiji Morokuma. "Why do molecules interact? The origin of electron donor–acceptor complexes, hydrogen bonding, and proton affinity". In: *Acc. Chem. Res.* 10 (1977), pp. 294–300. DOI: 10.1021/ar50116a004.

[287] S. Hosein Mousavipour, Maryam Mortazavi, and Omid Hematti. "Multichannel RRKM-TST and direct-dynamics CVT study of the reaction of hydrogen sulfide with ozone". In: *J. Phys. Chem. A* 2013 (2013), pp. 6744–6756. DOI: 10.1021/jp404738d.

[288] J. S. Muenter. "Electric dipole moment of carbon monoxide". In: *J. Mol. Spec.* 55 (1975), pp. 490–491. DOI: 10.1016/0022-2852(75)90287-8.

[289] Florinella Muñoz and Clemens von Sonntag. "The reactions of ozone with tertiary amines including complexing agents nitrilotriacetic acid (NTA) and ethylenediaminetetraacetic acid (EDTA) in aqueous solution". In: *J. Chem. Soc., Perkin Tans.* 2 (2000), pp. 2029–2033. DOI: 10.1039/b004417m.

[290] Eino Mvula, Sergej Naumov, and Clemens von Sonntag. "Ozonolysis of lignin models in aqueous solution: Anisole, 2,3-dimethoxybenzene, 1,4-dimethoxybenzene, and 1,3,5-trimethoxybenzene". In: *Environ. Sci. Technol.* 43 (2009), pp. 6275–6282. DOI: 10.1021/es900803p.

[291] Eino Mvula and Clemens von Sonntag. "Ozonolysis of phenols in aqueous solution". In: *Organic & Biomolecular Chemistry* 1 (10 2003), pp. 1749–1756. DOI: 10.1039/B301824P.

[292] F. Neese et al. "Assessment of orbital-optimized, spin-component scaled second-order many-body perturbation theory for thermochemistry and kinecits". In: *J. Chem. Theory Comput.* 5 (2009), pp. 3060–3073. DOI: 10.1021/ct9003299.

[293] Jörg Neugebauer and Matthias Scheffler. "Adsorbate-substrate and adsorbate- adsorbate interactions of Na and K adlayers on Al(111)". In: *Phys. Rev. B* 46.24 (Dec. 1992). Publisher: American Physical Society, pp. 16067–16080. DOI: 10.1103/PhysRevB.46.16067. URL: https://link.aps.org/doi/10.1103/PhysRevB.46.16067 (visited on 11/09/2022).

[294] Anders Nilsson and Lars Gunnar Moody Pettersson. "Chemical Bonding on Metal Surfaces". In: *Model Systems in Catalysis: Single Crystals to Supported Enzyme Mimics*. Ed. by Robert Rioux. New York, NY: Springer New York, 2010, pp. 253–274. ISBN: 978-0-387-98049-2. DOI: 10.1007/978-0-387-98049-2_12. URL: https://doi.org/10.1007/978-0-387-98049-2_12.

[295] George A Olah, Alain Goeppert, and GK Surya Prakash. "Chemical recycling of carbon dioxide to methanol and dimethyl ether: from greenhouse gas to renewable, environmentally carbon neutral fuels and synthetic hydrocarbons". In: *The Journal of organic chemistry* 74.2 (2009), pp. 487–498. DOI: 10.1021/jo801260f.

[296] Jeppe Olsen et al. "Surprising cases of divergent behavior in Mo/ller–Plesset perturbation theory". In: *The Journal of chemical physics* 105.12 (1996), pp. 5082–5090.

[297] Izabela Owsik and Bożena Kolarz. "The oxidation of hydroquinone to p-benzoquinone catalysed by Cu(II) ions immobilized on acrylic resins with aminoguanidyl groups: Part 1". In: *Journal of Molecular Catalysis A: Chemical* 178 (2002), pp. 63–71. DOI: 10.1016/S1381-1169(01)00299-0.

[298] Mathias Pabst et al. "A worrisome failure of the CC2 coupled-cluster method when applied to ozone". In: *Chem. Phys. Lett.* 495 (2010), pp. 135–140. DOI: 10.1016/j.cplett.2010.06.023.

[299] Gianfranco Pacchioni and Paul S. Bagus. "Cluster calculations of CO chemisorbed on the bridge site of Pd(100)". In: *J. Chem. Phys.* 93 (1990), pp. 1209–1214. DOI: 10.1063/1.459185.

[300] Luis Fernandez Pacios and P. A. Christiansen. "*Ab initio* relativistic effective potentials with spin-orbit operators. I. Li through Ar". In: *J. Chem. Phys.* 82 (1985), pp. 2664–2671. DOI: 10.1063/1.448263.

[301] Itai Panas et al. "On the cluster convergence of chemisorption energies". In: *Chem. Phys. Lett.* 149 (1988), pp. 265–272. DOI: 10.1016/0009-2614(88)85024-3.

[302] Ewa Papajak et al. "Efficient Diffuse Basis Sets: cc-pV x Z+ and maug-cc-pV x Z". In: *Journal of chemical theory and computation* 5.5 (2009), pp. 1197–1202. DOI: 10.1021/ct800575z.

[303] Ewa Papajak et al. "Perspectives on basis sets beautiful: Seasonal plantings of diffuse basis functions". In: *Journal of chemical theory and computation* 7.10 (2011), pp. 3027–3034. DOI: 10.1021/ct200106a.

[304] Robert G Parr and Yang Weitao. "Density-functional theory". In: *Density-Functional Theory of Atoms and Molecules*. Oxford University Press, 1995. Chap. 3. DOI: 10.1093/oso/9780195092769.003.0005.

[305] Robert G Parr and Yang Weitao. "The Kohn–Sham method: Basic principles". In: *Density-Functional Theory of Atoms and Molecules*. Oxford University Press, 1995. Chap. 7. DOI: 10.1093/oso/9780195092769.003.0005.

[306] W. Pauli. "Über den Zusammenhang des Abschlusses der Elektronengruppen im Atom mit der Komplexstruktur der Spektren". In: *Z. Physik* 31 (1925), pp. 765–783.

[307] Mercedes A. Peltzer et al. "Evaluation of the melt stabilization performance of hydroxytyrosol (3,4-dihydroxy-phenylethanol) in polypropylene". In: *Polymer Degradation and Stability* 95 (2010), pp. 1636–1641. DOI: 10.1016/J.POLYMDEGRADSTAB.2010.05.021.

[308] Fabio E. Penotti and David L. Cooper. "Combining rival π-space descriptions of O_3 and of SO_2". In: *Int. J. Quantum Chem.* 116 (2016), pp. 718–730. DOI: 10.1002/qua.25094.

[309] J. P. Perdew, K. Burke, and M. Ernzerhof. "Generalized gradient approximation made simple". In: *Phys. Rev. Lett.* 77 (18 1996), pp. 3865–3868. DOI: 10.1103/PhysRevLett.77.3865.

[310] John P Perdew, Kieron Burke, and Matthias Ernzerhof. "Generalized gradient approximation made simple". In: *Physical review letters* 77.18 (1996), p. 3865.

[311] John P Perdew and Karla Schmidt. "Jacob's ladder of density functional approximations for the exchange-correlation energy". In: *AIP Conference Proceedings*. Vol. 577. 1. American Institute of Physics. 2001, pp. 1–20.

[312] John P. Perdew, Matthias Ernzerhof, and Kieron Burke. "Rationale for mixing exact exchange with density functional approximations". In: *The Journal of Chemical Physics* 105.22 (1996), pp. 9982–9985. DOI: 10.1063/1.472933.

[313] Kirk A Peterson et al. "Systematically convergent basis sets with relativistic pseudopotentials. II. Small-core pseudopotentials and correlation consistent basis sets for the post-d group 16–18 elements". In: *The Journal of Chemical Physics* 119.21 (2003), pp. 11113–11123. DOI: 10.1063/1.1622924.

[314] Lars Gunnar Moody Pettersson. "A molecular perspective on the *d*-band model: Synergy between experiment and theory". In: *Top. Catal.* 57 (2014), pp. 2–13. DOI: 10.1007/s11244-013-0157-4.

[315] Roberto Peverati and Donald G Truhlar. "Screened-exchange density functionals with broad accuracy for chemistry and solid-state physics". In: *Physical Chemistry Chemical Physics* 14.47 (2012), pp. 16187–16191. DOI: 10.1039/C2CP42576A.

[316] James C. Phillips. "Energy-Band Interpolation Scheme Based on a Pseudopotential". In: *Phys. Rev.* 112 (3 1958), pp. 685–695. DOI: 10.1103/PhysRev.112.685.

[317] James C. Phillips and Leonard Kleinman. "New Method for Calculating Wave Functions in Crystals and Molecules". In: *Phys. Rev.* 116 (2 1959), pp. 287–294. DOI: 10.1103/PhysRev.116.287.

[318] Warren E Pickett. "Pseudopotential methods in condensed matter applications". In: *Computer Physics Reports* 9.3 (1989), pp. 115–197. DOI: 10.1016/0167-7977(89)90002-6.

[319] K. Pierloot, P. Verbeke, and L. G. Vanquickenborne. "Electronic spectra of the d^6 binary carbonyl complexes $Mn(CO)_6^+$, $Cr(CO)_6$, and $V(CO)_6^-$: An ab initio analysis". In: *Inorg. Chem.* 28 (1988), pp. 3059–3063. DOI: 10.1021/ic00314a039.

[320] Elizabeth A Pillar-Little, Robert C Camm, and Marcelo I Guzman. "Catechol oxidation by ozone and hydroxyl radicals at the air–water interface". In: *Environmental science & technology* 48.24 (2014), pp. 14352–14360. DOI: 10.1021/es504094x.

[321] Julien Pilme, Bernard Silvi, and Mohammad Esmail Alikhani. "Structure and stbaility of M−CO, M = first-transition-row metal: An application of density functional theory and topological approaches". In: *J. Phys. Chem. A* 107 (2003), pp. 4506–4514. DOI: 10.1021/jp027203p.

[322] Russell M Pitzer and Nicholas W Winter. "Electronic-structure methods for heavy-atom molecules". In: *The Journal of Physical Chemistry* 92.11 (1988), pp. 3061–3063.

[323] Patrik Pollak and Florian Weigend. "Segmented contracted error-consistent basis sets of double-and triple-ζ valence quality for one-and two-component relativistic all-electron calculations". In: *J. Chem. Theory Comput.* 13.8 (2017), pp. 3696–3705.

[324] J. A. Pople and R. K. Nesbet. "Self-consistent orbitals for radicals". In: *J. Chem. Phys.* 22 (1953), pp. 571–572. DOI: 10.1063/1.1740120.

[325] John A Pople, Peter MW Gill, and Nicholas C Handy. "Spin-unrestricted character of Kohn-Sham orbitals for open-shell systems". In: *Int. J. Quantum Chem.* 56.4 (1995), pp. 303–305.

[326] E.I. Proynov, A. Vela, and D.R. Salahub. "Nonlocal correlation functional involving the Laplacian of the density". In: *Chemical Physics Letters* 230.4 (1994), pp. 419–428. DOI: https://doi.org/10.1016/0009-2614(94)01189-3.

[327] William A Pryor, David H Giamalva, and Daniel F Church. "Kinetics of ozonation. 2. Amino acids and model compounds in water and comparisons to rates in nonpolar solvents". In: *J. Am. Chem. Soc.* 106.23 (1984), pp. 7094–7100. DOI: 10.1021/ja00335a038.

[328] Peter Psarras et al. "Slicing the pie: how big could carbon dioxide removal be?" In: *Wiley Interdisciplinary Reviews: Energy and Environment* 6.5 (2017), e253. DOI: 10.1002/wene.253.

[329] George D. Purvis and Rodney J. Bartlett. "A full coupled-cluster singles and doubles model: The inclusion of disconnected triples". In: *The Journal of Chemical Physics* 76.4 (1982), pp. 1910–1918. DOI: 10.1063/1.443164. eprint: https://doi.org/10.1063/1.443164. URL: https://doi.org/10.1063/1.443164.

[330] Chen-Ze Qi, Tian-Min Wang, and Xian-Man Zhang. "Protection mechanisms of *p*-phenylenediamine-type antiozonants". In: *Rubber Chemistry and Technology* 71 (4 1998), pp. 722–729. DOI: 10.5254/1.3538500.

[331] Jinli Qiao et al. "A review of catalysts for the electroreduction of carbon dioxide to produce low-carbon fuels". In: *Chemical Society Reviews* 43.2 (2014), pp. 631–675. DOI: 10.1039/C3CS60323G.

[332] Hua-Li Qin et al. "Computational and experimental comparison of diphosphane and diene ligands in the Rh-catalysed carboxylation of organoboron compounds with CO 2". In: *Green Chemistry* 16.6 (2014), pp. 3224–3229. DOI: 10.1039/C4GC00243A.

[333] Krishnan Raghavachari et al. "A fifth-order perturbation comparison of electron correlation theories". In: *Chemical Physics Letters* 157.6 (1989), pp. 479–483. ISSN: 0009-2614. DOI: https://doi.org/10.1016/S0009-2614(89)87395-6. URL: https://www.sciencedirect.com/science/article/pii/S0009261489873956.

[334] Mohammad Rahimi et al. "Electrochemical carbon capture processes for mitigation of CO 2 emissions". In: *Chemical Society Reviews* (2022). DOI: 10.1039/D2CS00443G.

[335] Maaike K Ramseier and Urs von Gunten. "Mechanisms of phenol ozonation—kinetics of formation of primary and secondary reaction products". In: *Ozone: science & engineering* 31.3 (2009), pp. 201–215. DOI: 10.1080/01919510902740477.

[336] Dmitrij Rappoport and Filipp Furche. "Property-optimized Gaussian basis sets for molecular response calculations". In: *J. Chem. Phys.* 133 (2010), p. 134105. DOI: 10.1063/1.3484283.

[337] Smithers Rapra. *Global tire manufacturing output to grow 3.4% year-on-year to 2024*. https://www.smithers.com/resources/2019/jun/global-tire-manufacturing-output-to-grow-by-2024. Accessed: 2021-01-04. 2019.

[338] Peter Rapta et al. "A variety of oxidation products of antioxidants based on N,N'-substituted *p*-phenylenediamines". In: *Polymer Degradation and Stability* 94.9 (2009), pp. 1457–1466. DOI: 10.1016/j.polymdegradstab.2009.05.003.

[339] Thomáš Rauch, Miguel A. L. Marques, and Silvana Botti. "Electronic structure of molecules, surfaces, and molecules on surfaces with the local modified Becke–Johnson exchange–correlation potential". In: *J. Chem. Theory Comput.* 17 (8 2021), pp. 4746–4755. DOI: 10.1021/acs.jctc.1c00255.

[340] S.D. Razumovskii and L.S. Batashova. "Mechanism of protection against ozone by *N*-phenyl-*N′*-isopropyl-*p*-phenylenediamine". In: *Rubber Chem. Technol.* 43 (1970), pp. 1340–1348. DOI: 10.5254/1.3547334.

[341] Zach D. Reed and Michael A. Duncan. "Infrared spectroscopy and structures of manganese carbonyl cations, $Mn(CO)_n^+$(n=1−9)". In: *J. Am. Soc. Mass. Spectrom.* 21 (2010), pp. 739–749. DOI: 10.1016/j.jasms.2010.01.022.

[342] Adam Rettig et al. "Revisiting the orbital energy-dependent regularization of the orbital-optimized second-order Møller–Plesset theory". In: *J. Chem. Theory Comput.* 18 (2022), pp. 5382–5392. DOI: 10.1021/acs.jctc.2c00641.

[343] A. M. Ricks, Z. E. Reed, and M. A. Duncan. "Infrared spectroscopy of mass-selected metal carbonyl cations". In: *J. Mol. Spectrosc.* 266 (2011), pp. 63–74. DOI: 10.1016/j.jms.2011.03.006.

[344] David Rinaldo et al. "Density functional localized orbital corrections for transition metals". In: *J. Chem. Phys.* 129 (2008), p. 164108. DOI: 10.1063/1.2974101.

[345] C. C. J. Roothaan. "New developments in molecular orbital theory". In: *Rev. Mod. Phys.* 23 (1951), pp. 69–89. DOI: 10.1103/RevModPhys.23.69.

[346] R. B. Ross et al. "Ab initio relativistic effective potentials with spin–orbit operators. IV. Cs through Rn". In: *The Journal of Chemical Physics* 93 (1990), pp. 6654–6670. DOI: 10.1063/1.458934.

[347] Elliot Rossomme et al. "Electronic structure calculations permit identification of the driving forces behind frequency shifts in transition metal monocarbonyls". In: *Physical Chemistry Chemical Physics* 22.2 (2020), pp. 781–798. DOI: 10.1039/C9CP04643G.

[348] Lindsay E Roy, P Jeffrey Hay, and Richard L Martin. "Revised basis sets for the LANL effective core potentials". In: *Journal of chemical theory and computation* 4.7 (2008), pp. 1029–1031. DOI: 10.1021/ct8000409.

[349] Thomas V. Russo, Richard L. Martin, and P. Jeffrey Hay. "Effective core potentials for DFT calculations". In: *J. Phys. Chem.* 99 (1995), pp. 17085–17087. DOI: 10.1021/j100047a007.

[350] Toru Saito et al. "Multireference character of 1,3-dipolar cycloaddition of ozone with ethylene and acrylonitrile". In: *J. Phys. Chem. A* 114 (2010), pp. 12116–12123. DOI: 10.1021/jp108302y.

[351] María Dolores Samper et al. "The potential of flavonoids as natural antioxidants and UV light stabilizers for polypropylene". In: *Journal of Applied Polymer Science* 129 (2013), pp. 1707–1716. DOI: 10.1002/APP.38871.

[352] Trond Saue. "Relativistic Hamiltonians for chemistry: A primer". In: *ChemPhysChem* 12.17 (2011), pp. 3077–3094.

[353] Kurt Schank et al. "Ozonation of 1,1,2,2-tetraphenylethene revisited: Evidence for electron-transfer oxygenations". In: *Helvetica Chemica Acta* 83 (2000), pp. 801–826. DOI: 10.1002/(SICI)1522-2675(20000412)83:4<801::AID-HLCA801>3.0.CO;2-6.

[354] Michael W. Schmidt, Mark S. Gordon, and Michel Dupuis. "The intrinsic reaction coordinate and the rotational barrier in silaethylene". In: *J. Am. Chem. Soc.* 107 (1985), pp. 2585–2589. DOI: 10.1021/ja00295a002.

[355] K. J. P. Schouten et al. "A new mechanism for the selectivity of C_1 and C_2 species in the electrochemical reduction of carbon dioxide on copper electrodes". In: *Chem. Sci.* 2 (2011), pp. 1902–1909. DOI: 10.1039/C1SC00277E.

[356] WH Schwarz. "The general form of pseudopotential operators". In: *Theoretica chimica acta* 23.2 (1971), pp. 147–154. DOI: 10.1007/BF00526428.

[357] Peter Schwerdtfeger. "The pseudopotential approximation in electronic structure theory". In: *Chem. Phys. Chem.* 12 (2011), pp. 3143–3155.

[358] Gustavo E. Scuseria et al. "The dipole moment of carbon monoxide". In: *J. Chem. Phys.* 94 (1991), pp. 6660–6663. DOI: 10.1063/1.460293.

[359] Bettina Seiwert et al. "Abiotic oxidative transformation of 6-PPD and 6-PPD quinone from tires and occurrence of their products in snow from urban roads and in municipal wastewater". In: *Water Research* 212 (2022), p. 118122. DOI: 10.1016/j.watres.2022.118122.

[360] Enayatollah Seydi et al. "The effects of para-phenylenediamine (PPD) on the skin fibroblast cells". In: *Xenobiotica* 49.10 (2019), pp. 1143–1148. DOI: 10.1080/00498254.2018.1541264.

[361] Yihan Shao et al. "Advances in molecular quantum chemistry contained in the Q-Chem 4 program package". In: *Mol. Phys.* 113.2 (2015), pp. 184–215. DOI: 10.1080/00268976.2014.952696. eprint: https://doi.org/10.1080/00268976.2014.952696. URL: https://doi.org/10.1080/00268976.2014.952696.

[362] Shaama Mallikarjun Sharada et al. "Automated transition state searches without evaluating the Hessian". In: *J. Chem. Theory Comput.* 8 (2012), pp. 5166–5174. DOI: 10.1021/ct300659d.

[363] Isaiah Shavitt and Rodney J. Bartlett. *Many-Body Methods in Chemistry and Physics: MBPT and Coupled-Cluster Theory*. Cambridge Molecular Science. Cambridge University Press, 2009. DOI: 10.1017/CBO9780511596834.

[364] James Shee et al. "Revealing the nature of electron correlation in transition metal complexes with symmetry breaking and chemical intuition". In: *J. Chem. Phys.* 154 (2021), p. 194109. DOI: 10.1063/5.0047386.

[365] Qunfang Shen, Yong Dong Liu, and Rugang Zhong. "Degradation mechanisms of simple aliphatic amines under ozonation: A DFT study". In: *Environ. Sci.: Processes Impacts* 23 (2021), pp. 480–490. DOI: 10.1039/D0EM00476F.

[366] David E. Sherwood and Michael B. Hall. "Theoretical study of vibrational interaction coordinates and π bonding in chromium hexacarbonyl. Comparison with cobalt hexacyanide and nickel tetracarbonyl". In: *Inorg. Chem.* 19 (1980), pp. 1805–1809. DOI: 10.1021/ic50208a077.

[367] Eric L. Shirley et al. "Extended norm-conserving pseudopotentials". In: *Phys. Rev. B* 40 (6 1989), pp. 3652–3660. DOI: 10.1103/PhysRevB.40.3652.

[368] P.E.M. Siegbahn, M.A. Nygren, and U. Wahlgren. "The use of the cluster model for the calculation of chemisorption energies". In: *Cluster Models for Surface and Bulk Phenomena*. Ed. by Gianfranco Pacchioni, Paul S. Bagus, and Fulvio Parmigiani. New York: Plenum Press, 1992, pp. 267–279.

[369] Per E. M. Siegbahn, Lars G. M. Pettersson, and Ulf Wahlgren. "A theoretical study of atomic fluorine chemisorption on the Ni(100) surface". In: *J. Chem. Phys.* 94 (1991), pp. 4024–4030. DOI: 10.1063/1.460679.

[370] Meenesh R Singh, Ezra L Clark, and Alexis T Bell. "Effects of electrolyte, catalyst, and membrane composition and operating conditions on the performance of solar-driven electrochemical reduction of carbon dioxide". In: *Physical Chemistry Chemical Physics* 17.29 (2015), pp. 18924–18936. DOI: 10.1039/C5CP03283K.

[371] J. C. Slater. "The Theory of Complex Spectra". In: *Phys. Rev.* 34 (10 1929), pp. 1293–1322. DOI: 10.1103/PhysRev.34.1293.

[372] American Chemical Society. *12 Principles of Green Chemistry*. https://www.acs.org/content/acs/en/greenchemistry/principles/12-principles-of-green-chemistry.html. Accessed: 2022-11-22.

[373] American Chemical Society. *What is Green Chemistry?* https://www.acs.org/content/acs/en/greenchemistry/what-is-green-chemistry.html. Accessed: 2022-11-22.

[374] Clemens von Sonntag and Urs von Gunten. *Chemistry of Ozone in Water and Wastewater Treatment: From Basic Principles to Applications*. London: IWA Puvlishing, 2012.

[375] Dale Spangler et al. "Geometry and electronic structure of $(CO)_3NiCH_2$. A model transition-metal carbene". In: *J. Am. Chem. Soc.* 103 (1981), pp. 3985–3990. DOI: 10.1021/ja00404a004.

[376] Manuel Sparta and Frank Neese. "Chemical applications carried out by local pair natural orbital based coupled-cluster methods". In: *Chem. Soc. Rev.* 43 (2014), pp. 5032–5041. DOI: 10.1039/c4cs00050a.

[377] Marc Steinmetz et al. "Accurate Thermochemistry for Large Molecules with Modern Density Functionals". In: *Density Functionals: Thermochemistry*. Ed. by Erin R. Jonhson. Cham: Springer International Publishing, 2015, pp. 1–23. ISBN: 978-3-319-19692-3. DOI: 10.1007/128_2014_543. URL: https://doi.org/10.1007/128_2014_543.

[378] Jonathan Stevens. "Virtually going green: The role of quantum computational chemistry in reducing pollution and toxicity in chemistry". In: *Physical Sciences Reviews* 2.7 (2017), p. 20170005. DOI: doi:10.1515/psr-2017-0005. URL: https://doi.org/10.1515/psr-2017-0005.

[379] Walter J Stevens et al. "Relativistic compact effective potentials and efficient, shared-exponent basis sets for the third-, fourth-, and fifth-row atoms". In: *Canadian Journal of Chemistry* 70.2 (1992), pp. 612–630. DOI: 10.1139/v92-085.

[380] R. M. Suffield, S. H. Dillman, and J. E. Haworth. "Evaluation of antioxidant performance of a natural product in polyolefins". In: *Journal of Vinyl and Additive Technology* 10.1 (2004), pp. 52–56. DOI: 10.1002/vnl.20007.

[381] J. Sun, A. Ruzsinszky, and J. P. Perdew. "Strongly constrained and appropriately normed semilocal density functional". In: *Phys. Rev. Lett.* 115 (2015), p. 036402. DOI: 10.1103/PhysRevLett.115.036402.

[382] Jianwei Sun et al. "Self-consistent meta-generalized gradient approximation within the projector-augmented-wave method". In: *Physical Review B* 84.3 (2011), p. 035117. DOI: 10.1103/PhysRevB.84.035117.

[383] Yihua Sun and Hui Chen. "Performance of density functionals for activation energies of Re-catalyzed organic reactions". In: *J. Chem. Theory Comput.* 10 (2 2014), pp. 579–588. DOI: 10.1021/ct4010855.

[384] Yuanyuan Sun and Hui Chen. "Performance of density functionals for activation energies of Zr-mediated reactions". In: *J. Chem. Theory Comput.* 9 (11 2013), pp. 4735–4743. DOI: 10.1021/ct400432x.

[385] Attila Szabo and Neil S Ostlund. *Modern quantum chemistry: introduction to advanced electronic structure theory*. Courier Corporation, 2012.

[386] Robert K. Szilagyi and Gernot Frenking. "Structure and bonding of the isoelectronic hexacarbonyls $[Hf(CO)_6]^{2-}$, $[Ta(CO)_6]^{-}$, $W(CO)_6$, $[Re(CO)_6]^{+}$, $[Os(CO)_6]^{2+}$, and $[Ir(CO)_6]^{3+}$: A theoretical study". In: *Organometallics* 16 (Aug. 1997), pp. 4807–4815. DOI: 10.1021/om970671e.

[387] Hengxin Tan et al. "Effect of Hartree–Fock pseudopotentials on local density functional theory calculations". In: *Phys. Chem. Chem. Phys.* 20 (2018), pp. 18844–18849. DOI: 10.1039/C8CP00990B.

[388] Dean J Tantillo. *Faster, catalyst! react! react! Exploiting computational chemistry for catalyst development and design*. 2016. DOI: 10.1021/acs.accounts.6b00249.

[389] Dóra Tátraaljai, Enikő Földes, and Béla Pukánszky. "Efficient melt stabilization of polyethylene with quercetin, a flavonoid type natural antioxidant". In: *Polymer Degradation and Stability* 102 (2014), pp. 41–48. DOI: 10.1016/j.polymdegradstab.2014.02.010.

[390] Dóra Tátraaljai et al. "Processing stabilisation of PE with a natural antioxidant, curcumin". In: *European Polymer Journal* 49.6 (2013), pp. 1196–1203. DOI: 10.1016/j.eurpolymj.2013.02.018.

[391] Agnes Tekle-Röttering et al. "Ozonation of anilines: Kinetics, stoichiometry, product identification and elucidation of pathways". In: *Water Res.* 98 (1 2016), pp. 147–159. DOI: 10.1016/j.watres.2016.04.001P.

[392] Agnes Tekle-Röttering et al. "Reactions of pyrrole, imidazole, and pyrazole with ozone: kinetics and mechanisms". In: *Environmental Science: Water Research & Technology* 6.4 (2020), pp. 976–992. DOI: 10.1039/c9ew01078e.

[393] Edward Teller. "On the stability of molecules in the Thomas-Fermi theory". In: *Reviews of Modern Physics* 34.4 (1962), p. 627.

[394] Peter R. Tentscher, Marc Bourgin, and Urs von Gunten. "Ozonation of *para*-substituted phenolic compounds yields *p*-benzoquinones, other cyclic α,β-unsaturated ketones, and substituted catechols". In: *Environ. Sci. Technol.* 52 (2018), pp. 4763–4773. DOI: 10.1021/acs.est.8b00011.

[395] Michael Teter. "Additional condition for transferability in pseudopotentials". In: *Phys. Rev. B* 48 (8 1993), pp. 5031–5041. DOI: 10.1103/PhysRevB.48.5031.

[396] Jonathan Thirman and Martin Head-Gordon. "An energy decomposition analysis for second-order Moller-Plesset perturbation theory based on absolutely localized molecular orbitals". In: *J. Chem. Phys.* 143 (2015), p. 084124. DOI: 10.1063/1.4929479.

[397] Llewellyn H Thomas. "The calculation of atomic fields". In: *Mathematical proceedings of the Cambridge philosophical society*. Vol. 23. 5. Cambridge University Press. 1927, pp. 542–548.

[398] Zhenyu Tian et al. "6PPD-Quinone: Revised toxicity assessment and quantification with a commercial standard". In: *Environ. Sci. Technol. Lett.* 9 (2 2022), pp. 140–156. DOI: 10.1021/acs.estlett.1c00910.

[399] Zhenyu Tian et al. "A ubiquitous tire rubber-derived chemical induces acute mortality in coho salmon". In: *Science* 371 (2021), pp. 185–189. DOI: 10.1126/science.abd6951.

[400] William C Topp and John J Hopfield. "Chemically motivated pseudopotential for sodium". In: *Physical Review B* 7.4 (1973), p. 1295. DOI: 10.1103/PhysRevB.7.1295.

[401] J. R. Trail and R. J. Needs. "Norm-conserving Hartree–Fock pseudopotentials and their asymptotic behavior". In: *J. Chem. Phys.* 122 (2005), p. 014112. DOI: 10.1063/1.1829049.

[402] JR Trail and RJ Needs. "Smooth relativistic Hartree–Fock pseudopotentials for H to Ba and Lu to Hg". In: *The Journal of chemical physics* 122.17 (2005), p. 174109. DOI: 10.1063/1.1888569.

[403] Benoît Tremblay and Laurent Manceron. "Evaluation of CO coordination energies from spectroscopic data: On the use of vibrational isotopic effects". In: *Inorg. Chem.* 47 (2008), pp. 4531–4535. DOI: 10.1021/ic701960t.

[404] Luciano Triguero et al. "Calculations of hydrogen chemisorption energies on optimized copper clusters". In: *Chem. Phys. Lett.* 237 (1995), pp. 550–559. DOI: 10.1016/0009-2614(95)00353-6.

[405] Daniela Trogolo, J. Samuel Arey, and Peter R. Tentscher. "Gas-phase ozone reactions with a structurally diverse set of molecules: Barrier heights and reaction energies evaluated by coupled cluster and density functional theory calculations". In: *J. Phys. Chem. A* 123 (2 2019), pp. 517–536. DOI: 10.1021/acs.jpca.8b10323.

[406] Mark E Tuckerman. "Ab initio molecular dynamics: basic concepts, current trends and novel applications". In: *Journal of Physics: Condensed Matter* 14.50 (2002), R1297. DOI: 10.1088/0953-8984/14/50/202.

[407] Joost VandeVondele and Jürg Hutter. "An efficient orbital transformation method for electronic structure calculations". In: *The Journal of Chemical Physics* 118.10 (2003), pp. 4365–4369. DOI: 10.1063/1.1543154. eprint: https://doi.org/10.1063/1.1543154. URL: https://doi.org/10.1063/1.1543154.

[408] Joost VandeVondele and Jürg Hutter. "Gaussian basis sets for accurate calculations on molecular systems in gas and condensed phases". In: *The Journal of Chemical Physics* 127.11 (2007), p. 114105. DOI: 10.1063/1.2770708. eprint: https://doi.org/10.1063/1.2770708. URL: https://doi.org/10.1063/1.2770708.

[409] Joost VandeVondele et al. "Quickstep: Fast and accurate density functional calculations using a mixed Gaussian and plane waves approach". In: *Computer Physics Communications* 167.2 (2005), pp. 103–128. ISSN: 0010-4655. DOI: https://doi.org/10.1016/j.cpc.2004.12.014. URL: https://www.sciencedirect.com/science/article/pii/S0010465505000615.

[410] Shubham Varshney et al. "Toxicological effects of 6PPD and 6PPD quinone in zebrafish larvae". In: *Journal of Hazardous Materials* 424 (2022), p. 127623. DOI: 10.1016/j.jhazmat.2021.127623.

[411] Achim Veldkamp and Gernot Frenking. "Theoretical studies of organometallic compounds. 6. Structures and bond energies of $M(CO)_n^+$, MCN, and $M(CN)^{2-}$ (M = Ag, Au; $n = 1 - 3$)". In: *Organometallics* 12 (1993), pp. 4613–4622. DOI: 10.1021/om0035a054.

[412] Sumit Verma et al. "A gross-margin model for defining technoeconomic benchmarks in the electroreduction of CO2". In: *ChemSusChem* 9.15 (2016), pp. 1972–1979. DOI: 10.1002/cssc.201600394.

[413] S. H. Vosko, L. Wilk, and M. Nusair. "Accurate spin-dependent electron liquid correlation energies for local spin density calculations: A critical analysis". In: *Can. J. Phys.* 58 (8 1980), pp. 1200–1211. DOI: 10.1139/p80-159.

[414] Wei Wang et al. "Beyond substituted *p*-phenylenediamine antioxidants: Prevalence of their quinone derivative in $PM_{2.5}$". In: *Environ. Sci. Technol.* 56 (2022), pp. 10629–10637. DOI: 10.1021/acs.est.2c02463.

[415] Simon P Webb, Tzvetelin Iordanov, and Sharon Hammes-Schiffer. "Multiconfigurational nuclear-electronic orbital approach: Incorporation of nuclear quantum effects in electronic structure calculations". In: *The Journal of chemical physics* 117.9 (2002), pp. 4106–4118. DOI: 10.1063/1.1494980.

[416] John D. Weeks and Stuart A. Rice. "Use of Pseudopotentials in Atomic-Structure Calculations". In: *The Journal of Chemical Physics* 49.6 (1968), pp. 2741–2755. DOI: 10.1063/1.1670479.

[417] Florian Weigend and Reinhart Ahlrichs. "Balanced basis sets of split valence, triple zeta valence, and quadruple valence quality for H to Rn: Design and assessment of accuracy". In: *Phys. Chem. Chem. Phys.* 7 (15 2005), pp. 3297–3305. DOI: 10.1039/B508541A.

[418] Steven E Wheeler et al. "Noncovalent interactions in organocatalysis and the prospect of computational catalyst design". In: *Accounts of Chemical Research* 49.5 (2016), pp. 1061–1069. DOI: 10.1021/acs.accounts.6b00096.

[419] Steven E. Wheeler, Daniel H. Ess, and Ken N. Houk. "Thinking out of the black box: Accurate barrier heights of 1,3-dipolar cycloadditions of ozone with acetylene and ethylene". In: *J. Phys. Chem. A* 112 (8 2008), pp. 1798–1807. DOI: 10.1021/jp710104d.

[420] Florian Wiegend, Filipp Furche, and Reinhart Ahlrichs. "Gaussian basis sets of quadruple zeta valence quality for atoms H-Kr". In: *J. Chem. Phys.* 119 (2003), p. 12753. DOI: 10.1063/1.1627293.

[421] Tabbi Wilberforce et al. "Progress in carbon capture technologies". In: *Science of The Total Environment* 761 (2021), p. 143203. DOI: 10.1016/j.scitotenv.2020.143203.

[422] Alex Willand et al. "Norm-conserving pseudopotentials with chemical accuracy compared to all-electron calculations". In: *J. Chem. Phys.* 138 (2013), p. 104109. DOI: 10.1063/1.4793260.

[423] Guisheng Wu et al. "Density functional investigation on copper carbonyl complexes". In: *J. Mol. Struct.: THEOCHEM* 637 (Oct. 2003), pp. 101–107. DOI: 10.1016/S0166-1280(03)00424-X.

[424] Xuan Wu et al. "Barium as honorary transition metal in action: Experimental and theoretical study of $Ba(CO)^+$ and $Ba(CO)^-$". In: *Angew. Chem. Int. Ed.* 57 (2018), pp. 3974–3980. DOI: 10.1002/anie.201713002.

[425] Xuan Wu et al. "Observation of alkaline earth complexes $M(CO)_8$ (M = Ca, Sr, or Ba) that mimic transition metals". In: *Science* 361 (2018), pp. 912–916. DOI: 10.1126/science.aau0839.

[426] Yujing Wu et al. "Accuracy trade-off between one-electron and excitonic spectra of cuprous halides in first-principles calculations". In: *J. Chem. Phys.* 154 (2021), p. 134704. DOI: 10.1063/5.0043999.

[427] Christoph van Wüllen. "On the use of common effective core potentials in density functional calculations. I. Test calculations on transition-metal carbonyls". In: *International journal of quantum chemistry* 58.2 (1996), pp. 147–152. DOI: 10.1002/(SICI)1097-461X(1996)58:2<147::AID-QUA3>3.0.CO;2-Y.

[428] Huimin Xia et al. "Natural antioxidant from bamboo leaves for the processing stability of polypropylene". In: *Journal of Thermal Analysis and Calorimetry* 146 (2021), pp. 1657–1665. DOI: 10.1007/s10973-020-10115-0.

[429] Mingliang Xin et al. "Dihydromyricetin: An effective non-hindered phenol antioxidant for linear low-density polyethylene stabilisation". In: *J. Therm. Anal. Calorim.* 114 (2013), pp. 1167–1175. DOI: 10.1007/s10973-013-3169-1.

[430] Wenhua Xu et al. "Rare-earth monocarbonyls MCO: Comprehensive infrared observations and a transparent theoretical interpretation for M = Sc; Y; La−Lu". In: *Chem. Sci.* 3 (2012), pp. 1548–1554. DOI: 10.1039/c2sc00998f.

[431] Tetsuo Yamano and Mitsuru Shimizu. "Skin sensitization potency and cross-reactivity of p-phenylenediamine and its derivatives evaluated by non-radioactive murine local lymph node assay and guinea-pig maximization test". In: *Contact Dermatitis* 60.4 (2009), pp. 193–8. DOI: 10.1111/j.1600-0536.2008.01500.x.

[432] Jing Yang, Liang Z. Tan, and Andrew M. Rappe. "Hybrid functional pseudopotentials". In: *Phys. Rev. B* 97 (8 2018), p. 085130. DOI: 10.1103/PhysRevB.97.085130.

[433] Sheng-Che Yang, Timm Lankau, and Chin-Hui Yu. "A theoretical study of the nornicotine-catalyzed Mannich reaction in wet solvents and water". In: *Green Chemistry* 16.8 (2014), pp. 3999–4008. DOI: 10.1039/C4GC01021C.

[434] Yang Yang et al. "Development of a practical multicomponent density functional for electron-proton correlation to produce accurate proton densities". In: *The Journal of Chemical Physics* 147.11 (2017), p. 114113. DOI: 10.1063/1.4996038.

[435] Xian-Man Zhang and Qinyan Zhu. "Olefinic ozonation electron transfer mechanism". In: *J. Org. Chem.* 62 (17 1997), pp. 5934–5938. DOI: 1.

[436] Yan Zhao and Donald G Truhlar. "Density functionals with broad applicability in chemistry". In: *Accounts of chemical research* 41.2 (2008), pp. 157–167.

[437] Yan Zhao et al. "Thermochemical kinetics for multireference systems: Addition reactions of ozone". In: *J. Phys. Chem. A* 113 (2009), pp. 5786–5799. DOI: 10.1021/jp811054n.

[438] Tingting Zheng et al. "Study on the ozone aging mechanism of natural rubber". In: *Poly. Degrad. Stab.* 186 (2021), p. 109514. DOI: 10.1016/j.polymdegradstab.2021.109514.

[439] Mingfei Zhou and Lester Andrews. "Infrared spectra and density functional calculations of $Cu(CO)_{1\text{-}4}^{+}$, $Cu(CO)_{1\text{-}3}$, and $Cu(CO)_{1\text{-}3}^{-}$ in solid neon". In: *J. Chem. Phys.* 111 (1999), pp. 4548–4557. DOI: 10.1063/1.479216.

[440] Mingfei Zhou and Lester Andrews. "Reactions of laser-ablated iron atoms and cations with carbon monoxide: Infrared spectra of $FeCO^{+}$, $Fe(CO)^{2+}$, $Fe(CO)_x$, and $Fe(CO)_x^{-}$ ($x = 1 - 4$) in solid neon". In: *J. Chem. Phys.* 110 (1999), pp. 10370–10379. DOI: 10.1063/1.478970.

[441] Mingfei Zhou, Lester Andrews, and Charles W. Bauschlicher Jr. "Spectroscopic and theoretical investigations of vibrational frequencies in binary unsaturated transition-metal carbonyl cations, neutrals, and anions". In: *Chem. Rev.* 101 (June 2001), pp. 1931–1961. DOI: 10.1021/cr990102b.

[442] Mingfei Zhou, George V. Chertihin, and Lester Andrews. "Reactions of laser-ablated iron atoms with carbon monoxide: Infrared spectra and density functional calculations of Fe_xCO, $Fe(CO)_x$ and $Fe(CO)_x^{-}$ ($x = 1, 2, 3$) in solid argon". In: *J. Chem. Phys.* 109 (1998), pp. 10893–10904. DOI: 10.1063/1.477785.

[443] Tom Ziegler, Vincenzo Tschinke, and Charles Ursenbach. "Thermal stability and kinetic lability of the metal–carbonyl bond. A theoretical study on $M(CO)_6$ (M = Cr, Mo, W), $M(CO)_5$ (M = Fe, Ru, Os), and $M(CO_4)$ (M = Ni, Pd, Pt)". In: *J. Am. Chem. Soc.* 109 (1987), pp. 4825–2837. DOI: 10.1021/ja00250a013.

Appendix A

Additional Work

In addition to the work completed and presented in the preceding chapters, I have conducted additional research in collaboration with other theoretical and experimental scientists, and also engaged in piloting a mathematics instruction program for incomining physical chemistry graduate students.

As indicated in Chapter 2, the potential hazards of PPs for main group chemistry was rediscovered in work benchmarking methods for application of DFT to catalysis systems. This body includes a number of papers theoretical papers where I conducted benchmark studies of PP errors that would ultimately lead to the work in Chapter 2. These works include a general paper on the applicability of DFT to the many challenges posed by electrocatalytic systems[254], a paper examining how thermal fluctuations influence CO binding sites on coinage metals,[247] and finally a paper developing a GTH pseudopotential fit to the B97M-rV density functiona.[248] This work is ongoing, and we continue to look into alternative corrections that increase the reliability of PPs.

I have also contributed computational support to experimental chemists who have synthesized novel cycloalkenes that exhibit extreme degrees of antiaromaticity.[36] Here, my work involved applying the nucleus independent chemical shift (NICS) formalism to quantify the degree of antiaromaticity in these novel compounds relative to existing molecules like benzene, napthalene, and various cyclobutadienes.

Finally, outside of my research activities, I worked with other graduate students (Orion Cohen, Avishek Das, Dipti Jasrasaria, and later Rachel Clune) to co-found a mathematics bootcamp for incoming physical chemistry students. This process included the development of material covering a wide variety of advanced undergraduate topics in mathematics, including multivariable calculus, differential equations, linear algebra, probability and statistics, and scientific computing. Together, we leverage this material and taught two 30-person cohorts of physical chemistry students in week-long intensive programs before the start of the semester. We examined the effects of the bootcamp through self-reported surveys, finding among other things that this program eliminated prior gender gaps in student confidence upon entering graduate school. We have summarized these and other findings in a paper that is currently under review, and in the meantime can be found on ChemRxiv.[80]